

AUTONOMOUS UNIVERSITY OF MADRID

DOCTORAL THESIS

---

**Mechanical and Electromechanical Study  
of Ferro-Electrets Films for Water  
Immersion Ultrasonic Transducers**

---

*Author:*

Julio QUIRCE AGUILAR

*Supervisor:*

Dr. Tomás Enrique GÓMEZ  
ÁLVAREZ-ARENAS

*A thesis submitted in fulfillment of the requirements  
for the degree of Doctor of Philosophy*

*in the*

Advanced Materials and Nanotechnology

November 28, 2022



## Declaration of Authorship

I, Julio QUIRCE AGUILAR, declare that this thesis titled, "Mechanical and Electromechanical Study of Ferro-Electrets Films for Water Immersion Ultrasonic Transducers" and the work presented in it are my own. I confirm that:

- This work was done wholly or mainly while in candidature for a research degree at this University.
- Where any part of this thesis has previously been submitted for a degree or any other qualification at this University or any other institution, this has been clearly stated.
- Where I have consulted the published work of others, this is always clearly attributed.
- Where I have quoted from the work of others, the source is always given. With the exception of such quotations.
- I have acknowledged all main sources of help.

Signed:

---

Date:

---

You can find the most recent pdf version of the thesis at this url:  
[https://github.com/JulioQuirceA/Thesis\\_manuscript/blob/main/Thesis\\_Julio\\_Quirce\\_Aguilar.pdf](https://github.com/JulioQuirceA/Thesis_manuscript/blob/main/Thesis_Julio_Quirce_Aguilar.pdf)  
or pressing [here](#) as I anticipate that even though it has been revised numerous times there will still be typos to correct. The paper under revision will also be included.  
If you find any errors when reading the document do not hesitate to contact me so that I can correct them.

Thank you very much!



*"And once the storm is over, you won't remember how you made it through, how you managed to survive. You won't even be sure, whether the storm is really over. But one thing is certain. When you come out of the storm, you won't be the same person who walked in."*

Haruki Murakami



AUTONOMOUS UNIVERSITY OF MADRID

## *Abstract*

Doctor of Philosophy

### **Mechanical and Electromechanical Study of Ferro-Electrets Films for Water Immersion Ultrasonic Transducers**

by Julio QUIRCE AGUILAR

The motivation for this work is the development of ultrasonic transducers for quantitative echography. In this regard, the thesis aims to study the role of polypropylene Ferroelectret Films (FF) as an active layer for ultrasound transducers operating in water immersion. These type of polymers present a cellular structure and a strong piezoelectric response, they were introduced in the '80s, and since then, they have been used and researched mostly for air-coupled transducers and pressure sensors but not for water immersion or medical transducers.

The starting point of this thesis was the unexpected fact that the piezoelectric response was observed when the film was submerged in water. These preliminary results show that the film can operate as an ultrasonic transmitter and receiver with unforeseen features such as short impulse response and large bandwidth, contrary to the air-coupled behavior. This feature is of great interest for quantitative echography.

The observed differences between the response of the FF transducer air-coupled and FF transducer water-coupled explained above motivated the study of the thickness resonances at different loads, which was performed by studying the ultrasonic transmission coefficient spectra.

The main results point out that FF conserves the mechanical resonances, although they are slightly displaced while immersed, but the electromechanical resonances are lost. We provide an explanation for this behavior.

Taking advantage of all the knowledge developed about the FF, different ultrasound transducers were manufactured with the aim of being used for resonant quantitative echography. Also, different designs and paths of fabrication were explored (flat and spherical aperture).

The lack of electromechanical resonances suggested the possibility of designing, fabricating, and testing hydrophones with a very flat band. Results are compared against PVDF hydrophones manufactured with the same design.

Finally, five cartilage phantoms were manufactured to test the spectroscopy ultrasound technique with conventional ultrasonic transducers as a proof of concept.



UNIVERSIDAD AUTÓNOMA DE MADRID

## *Resumen*

Doctor en Física

### **Estudio Mecánico y Electromecánico de Láminas de Ferroelectreto para Transductores Ultrasónicos Acoplados en Agua**

por Julio QUIRCE AGUILAR

La motivación de este trabajo es el desarrollo de transductores de ultrasonidos para la ecografía cuantitativa. En este sentido, la tesis pretende estudiar el papel de las láminas de ferroelectret construidas con polipropileno como capa activa para transductores de ultrasonidos que operan en inmersión en agua. Este tipo de polímeros presentan una estructura celular y una fuerte respuesta piezoeléctrica. Fueron introducidos en los años 80, y desde entonces, han sido utilizados e investigados principalmente para transductores acoplados al aire y sensores de presión, pero no para transductores de inmersión en agua o médicos.

El punto de partida de esta tesis fue el hecho inesperado de observar la respuesta piezoeléctrica con las láminas de ferroelectreto (LF) cuando estos estaban sumergidos en el agua. Estos resultados preliminares muestran que estas láminas pueden funcionar como transmisor y receptor de ultrasonidos con características no previstas, como una respuesta de impulso corta y un gran ancho de banda, al contrario que el comportamiento de estas láminas cuando están acopladas al aire. Esta característica es de gran interés para la ecografía cuantitativa. Las diferencias observadas entre la respuesta de las LF montadas en un transductor acoplado al aire y acoplado al agua, motivaron el estudio de las resonancias de espesor en estos medios. Este análisis se llevó a cabo mediante el estudio de los espectros de los coeficientes de transmisión. Los principales resultados señalan que las LF conservan las resonancias mecánicas cuando están sumergidas, aunque están ligeramente desplazadas, pero las resonancias electromecánicas se pierden. Se presenta una explicación para este comportamiento.

Aprovechando todo el conocimiento desarrollado sobre las LF, se fabricaron diferentes transductores de ultrasonidos con el objetivo de ser utilizados para la ecografía cuantitativa resonante. También se exploraron diferentes diseños y vías de fabricación (apertura plana y esférica).

La ausencia de resonancias electromecánicas sugirió la posibilidad de diseñar, fabricar y probar hidrófonos con una banda muy plana. Los resultados se comparan con hidrófonos de PVDF fabricados con el mismo diseño.

Por último, se produjeron cinco phantoms de cartílago para probar la técnica de ultrasonidos por espectroscopia con transductores de ultrasonidos convencionales como prueba de concepto.



## Acknowledgements

This acknowledgment part makes me nostalgic for the previous four years and forces me to reflect on all that has happened. I suppose, I should thank everyone who assisted me with my thesis. Still, most of them are the same people who have encouraged me to continue with this and other projects, and some of the most important to me don't speak English, and I want them to read this directly from my hands rather than through Google Translate. So I Will continue in Spanish.

Cuando comencé el doctorado, obviamente, no sabía a lo que me estaba enfrentando y casi que pensaba que esta experiencia simplemente sería una más, en la cual se aprende mogollón de conocimiento técnico que muy probablemente nunca vaya a usar. Afortunadamente, estaba completamente confundido para sorpresa de nadie. Ya que, aunque sea cierto el hecho de que he aprendido mogollón e incluso puede que cosas útiles, no creo que represente en absoluto todo lo que me llevo en la mochila el día que salí del CSIC.

Si esto está sucediendo, no puede ser de otra manera que, con la inestimable ayuda de mi familia, en concreto mis padres. No por el apoyo durante estos últimos cuatro años, que también, si no, en haber tenido éxito, desde la difícil empresa de haberme mantenido con vida hasta que después de tantos años de convivencia sean las primeras personas que me vengan a la cabeza para agradecer. ¡Muchas gracias! El siguiente párrafo quiero dedicárselo a los amigos, por no hacer la pandemia aburrida, por las risas, por escuchar, por tener siempre las peores ideas, no os doy la turra, pero ya sabéis que siempre lo mejor está por llegar. ¡¡Y no se olviden el frontal!!

Tampoco me olvido de todo el mundo que conocí en el instituto, en especial a mis compis de despacho, muchas gracias por la ayuda, lo aprendido, y las conversaciones que no tenían fin.

Probablemente este sea el agradecimiento más repetido desde el origen de las tesis hasta ahora, y es agradecer a mi supervisor, Tomás. Es una obviedad, especialmente para los que me conocen, que esto no hubiera ido a ningún sitio sin su ayuda. Al principio de la tesis pensaba, "Wow imagínate saber todo lo que sabe el... Sería increíble", bueno, pues cuatro años después sigo pensando lo mismo.

En último lugar y no por ello menos importante me gustaría agradecer a la "escalada" por ser esa vía de escape, por enseñarme a tener paciencia, que dedicar más horas no es sinónimo de tener mejores resultados, por enseñarme que con la única persona que me tengo que comparar es con mi yo del pasado y sobre todo que la vida no trata de ser el mejor en todo, si no el más feliz en todo.





# Contents

<b>Declaration of Authorship</b>	<b>iii</b>
<b>Abstract</b>	<b>vii</b>
<b>Resumen</b>	<b>ix</b>
<b>Acknowledgements</b>	<b>xi</b>
<b>1 Introduction</b>	<b>1</b>
1.1 Motivation . . . . .	1
1.2 General Objetives . . . . .	3
1.3 Piezoelectricity & piezoelectric materials . . . . .	4
1.4 Ferroelectrets . . . . .	6
1.4.1 Ferroelectret fabrication . . . . .	9
1.4.2 Ferroelectret piezoelectric response . . . . .	11
<b>2 Thickness resonance</b>	<b>15</b>
2.1 Sring analogy $\lambda/4$ and $\lambda/2$ . . . . .	15
2.2 Transmission and reflection at single interface . . . . .	17
2.3 Transmission and reflection at two interface . . . . .	19
2.4 Transmission and reflection at n interface . . . . .	27
<b>3 Inverse problem</b>	<b>29</b>
3.1 Algorithms, Simulated Annealing . . . . .	29
3.2 Phantom Interferometry . . . . .	31
<b>4 Publications</b>	<b>37</b>
4.1 Journals SCI . . . . .	37
4.1.1 Paper 1, IEEE Transactions on Ultrasonics, Ferroelectrics, and Frequency Control, 2021. . . . .	37
4.1.2 Paper 2, Applied Sciences, 2021 . . . . .	37
4.1.3 Paper 3, Polymers (Basel), 2021. . . . .	37
4.1.4 Paper 4, IEEE Transactions on Ultrasonics, Ferroelectrics, and Frequency Control, 2022. . . . .	37
4.2 IEEE International Ultrasonics Symposium (IUS) publications . . . . .	88
4.2.1 IUS 2019, Glasgow, UK. . . . .	88
4.2.2 IUS 2021, Xi'an, China. . . . .	88
4.2.3 IUS 2021, Xi'an, China. . . . .	88
4.3 International Congress on Ultrasonics (ICU) . . . . .	101
4.3.1 ICU 2019, Bruges, Belgium. . . . .	101
4.3.2 ICU 2019, Bruges, Belgium. . . . .	101

<b>5 Conclusions and Future work</b>	<b>115</b>
5.1 Conclusions . . . . .	115
5.2 Future work . . . . .	118
<b>6 Conclusiones y Trabajo Futuro</b>	<b>119</b>
6.1 Conclusiones . . . . .	119
6.2 Trabajo Futuro . . . . .	122
<b>Bibliography</b>	<b>123</b>

# List of Figures

1.1	Schematic of ferroelectret material where $P_s$ is the polarization direction [18]	5
1.2	Power from body-driven sources; total power for each action is included in parenthesis [46]	8
1.3	Nondestructive testing of a piece of wood using air-coupled transducers in transmission operation [51].	8
1.4	Position sensing. a) The voltage data plot harvested from the eight-channel electrodes when pixel (III-b) was subjected to a force. b) Histogram depiction derived from the case of (a), inset schematic represents the action of pressing the pixel (III-b) [58]	9
1.5	Electric response of the sleeping monitor to successive motions [62]	9
1.6	Heart rate variability and sleep tracker based on ferroelectrets by Emfit	9
1.7	. Production of a cellular structure by stretching a filler-loaded polymer (process 1) or foaming by a physical blowing agent (supercritical carbon dioxide, CO <sub>2</sub> ) [25]	10
1.8	Schematic sketch of a cellular polymer film (left picture), the charge generation by dielectric-barrier discharges inside the voids (middle picture) and the trapping of charges of different polarities at the upper and lower void surfaces (right picture) [25].	10
1.9	Negative tip-to-plane corona charging [66].	11
1.10	Energy Conversion Mechanisms of FENG. (a) Charge distribution and giant dipoles of the ferroelectret nanogenerator (FENG) after micro plasma discharging, showing that the upper and lower surfaces of voids are oppositely charged. (b,c) Direct electromechanical interaction effect. (b) Pressed by a human hand on the surface of FENG. (c) Pressure is released, and giant dipoles restore their original sizes. (d,e) Reverse electromechanical interaction effect. (d) Giant dipoles further expand as positive potential is applied. (e) Giant dipoles shrink as negative potential is applied. [67]	11
1.11	Schematic dependence of the piezoelectric activity and the elastic stiffness on sample density and cross sections of the corresponding cellular structures [68]	12
1.12	Schematic representation of: (a) truss-like and (b) eye-shaped geometrical structures [69]	13
1.13	Model based on charged parallel polymeric and gaseous layers [70]	13
2.1	Scheme, where each wave is shown as a vertical line, with its mathematical equation next to it, and the direction of propagation is shown by an arrow.	19
2.2	Coefficient of transmission through a wall made of different materials. The wall is immersed in water.	25
2.3	Coefficient of reflection through a wall made of different materials. The wall is immersed in water.	26
3.1	The image is from the book Simulated Annealing - Advances, Applications and Hybridizations [82]	30

3.2	The image is from the book Simulated Annealing - Advances, Applications and Hybridizations [82] . . . . .	31
3.3	The blue dots represent the experimental data and the yellow line the solution of the inverse problem. . . . .	32
3.4	Thickness of the phantoms measured by two different methods, on y axis ultrasound spectroscopy is used and on the x axis a micrometer is used . . . . .	34
3.5	On the top left, echoes in time domain with the 1 MHz Transducer. On the top right, coefficient modulus of reflection On the bottom left, echoes in time domain with the 5 MHz Transducer. On the bottom right, coefficient modulus of reflection . . . . .	35
3.6	On the top left, echoes in time domain with the 1 MHz Transducer. On the top right, coefficient modulus of reflection On the bottom left, echoes in time domain with the 5 MHz Transducer. On the bottom right, coefficient modulus of reflection . . . . .	36

# List of Tables

1.1	Types of polymers ferroelectret and its piezoelectric coefficient $d_{33}$ . . .	6
1.2	Comparative table of some properties of PVDF vs Cellular PP [40]. . .	7



## Chapter 1

# Introduction

### 1.1 Motivation

Ferroelectret film is an extraordinary piezoelectric material with remarkable features such as flexibility, a high  $d_{33}$  piezoelectric coefficient, and a very low acoustic impedance. Its early stage of development also merits keeping an eye on.

Ferroelectret film has proved that it is a good choice for sophisticated sensors and transducers for air-coupled transmission. This is something that we can see in the piezoelectric materials portion of this thesis. Due to the dearth of published information regarding the performance of FF in water immersion, in particular, the mechanical and piezoelectric properties added to the short pulse response, as well as the hypothesis that it is reasonable to anticipate that some of the properties are advantageous for water immersion, we were motivated to conduct research on the behavior of FF in these conditions.

The majority of piezoelectric transducers are designed for water-coupled operation because one of the largest markets, medicine, operates in the human body, whose mechanical properties are comparable to water. In situations where other piezoelectric materials have performance limitations, therefore, a comprehensive understanding of the FF is required to construct devices that can contribute to this sector. The range of applications for a piezoelectric polymer is quite broad, so in this dissertation, we investigate the FF strengths while submerged and compare their performance to that of conventional technology.

There is a lot of well-established and well-known technology that can be transferred to the FF, considering its limitations and enhancing its features. One example of this could be the replacement of PVDF with FF for these applications where low frequencies are required. The non-Contact Resonant Ultrasound Spectroscopy (NC-RUS) technique has been demonstrated to be very robust for non-contact and non-destructive material characterization [1][2][3]. This method will study the FF properties of both water and air as outer media. This approach has several benefits over others, including mechanical testing and atomic force microscopy. First, after the FF has been characterized, no irreparable damage has happened. Therefore, it may be employed in the production of transducers with a very exact characterization of the film since each piece of FF may react somewhat differently due to its variability. Second, the frequency at which the transmitter and receiver transducers work can be changed, among other things, based on the property being studied. For medical imaging, it is important to distinguish between echoes generated by two adjacent walls, such as the thickness of a vein. The most common method for addressing this issue is to create transducers that can work at high frequencies. So, in the time domain, the two echoes are separated, and the thickness can be found by measuring the time between the echoes and knowing how fast sound travels in the medium. This method has a few problems. For example, the production

of the transducer gets more expensive and complicated as the operating frequency increases.

There is another method for getting the same information. Using transducers with low operating frequencies, the echoes overlap in the time domain, but in Fourier space, a pattern of interference from both echoes can be observed. The matrix transfer technique and the inverse problem solution can be used to estimate the properties of the material, such as its thickness, attenuation, and so on. To be effective, this strategy requires two key elements. First, the piezoelectric material must be able to work as a pulse-echo (PVDF is thrown out). Second, the accuracy of the results depends on the bandwidth, so a broadband signal is needed to look at a wide range of the interference pattern. FF meets both criteria. Taking advantage of their unique characteristics and the paucity of literature on FF piezoelectric behavior in water immersion. It is motivating to look into the possibility of making hydrophones and compare them to ones that are already on the market. This will help improve the design, which can be made better, and find a market niche where the FF would be seen as the best option.

## 1.2 General Objectives

The main objective of this thesis focuses on the study of FF from two different points of view. First, delve into the purely mechanical aspects and then use them for transducer construction. To achieve these objectives for this thesis, two FF made with polypropylene from the company Emfit are used, HS03 and HS06.

- Objective 1. Characterize the FF mechanical and piezoelectric properties and understand its response to an underwater load.
  1. Extract FF mechanical properties using the Non-Contact Resonant ultrasound spectroscopy technique.
  2. Understand how thickness resonances vary with the outer medium and report an explication in the case of an anomalous thickness resonance modification.
- Objective 2. Manufacture FF transducers for water immersion and resonant pulse-echo spectroscopy.
  1. Study the emission and the reception band of the HS03 and HS06 FF independently.
  2. Design, fabricate, and test a robust transducer optimized to operate in water immersion and explore different aperture geometries.
  3. Study the FF reception band beyond the frequencies used for the pulse-echo operation.
- Objective 3. Proof of Concept. Delve into the FF reception band in water immersion.
  1. Design and manufacture a FF hydrophone with different aperture geometries.
  2. Compare the FF hydrophone results with the consolidated technology of ferroelectric polymer film PVDF.
- Objective 4. Develop pulse-echo resonant technique for quantitative echography.
  1. Manufacture human tissue phantoms and taking measurements to extract their properties.
  2. Use the simulated annealing algorithm for this technique.

This thesis aims to explore the FF possibilities and enhance their features, which make the material unique, in order to contribute to scientific knowledge at the same time as the industrial field. So this thesis lays some of the foundations for FF usability in water immersion.

### 1.3 Piezoelectricity & piezoelectric materials

This thesis focuses on the ferroelectret material from two different points of view. First, look into the electromechanical properties and how they work, and second, how to use them to make transducers that can be submerged in water.

But first, I would like to start with a short introduction of the general scope, continue with a description of ferroelectret materials, and end up with the possible applications for the industry. The foundation of this and many other theses is the physical principle of piezoelectricity, which is the relationship between pressure or squeeze, derived from the Greek word "piezo," and electricity. This phenomenon was demonstrated for the first time in 1880 by the brothers Pierre and Jacques Curie [4] although René Just Haüy and Antoine César Becquerel suspected of it some decades before. Since this discovery, many researchers have been attracted by the piezoelectric properties [5][6][7][8][9] and the search to develop new, higher-performance materials. Some of the typical and most studied piezoelectric materials are:

- **Ceramic, lead zirconate titanate (PZT) [10].** This material is by far the most studied and used in industry. The reason is the good piezoelectric coefficients combined with the ease of manipulation to create specific geometries to prioritize resonant modes like thickness and radial modes or length and width expander modes.
- **Ferroelectric polymer.** The most used is polyvinylidene fluoride (PVDF) discovered by Dr. Heiji Kawai in 1969 [11], and it is recognized by its flexibility, which makes the material very versatile when choosing active element geometry or establishing the active elements with a developable surface added to the lack of lateral mode resonances. The  $d$  coefficients are low, unlike the  $g$  coefficients; this phenomenon makes the material suitable to use as a receiver, for example, hydrophones [12][13][14].
- **Composites.** A composite is a material composed of two phases, in the case of piezoelectric materials. It is usually a ceramic and a polymer or a single crystal and a polymer. The origin is in PennState years 70 or 80, introduced by Wallace Smith, and Newham [cita]. The geometry can vary alternate sheets (2-2), pillars in a matrix (1-3), saturated "sponge" 3-3, and particles in an array (0-3).  
The primary advantage of this technique is the versatility with which piezoelectric elements be arranged in the matrix. As well as the ability to use different polymers as the matrix to optimize the acoustic impedance depending for the application. [15].
- **Ferroelectret.** This material is made of polymer with a significant piezoelectric coefficient  $d_{33}$ , discovered/invented by Kirjavainen and coworkers in 1989 [16] [17]. It presents a cellular structure composed of internally charged voids typically filled with air, although other gases can be used. Finally, on the top and bottom, there are usually electrodes to operate the film.

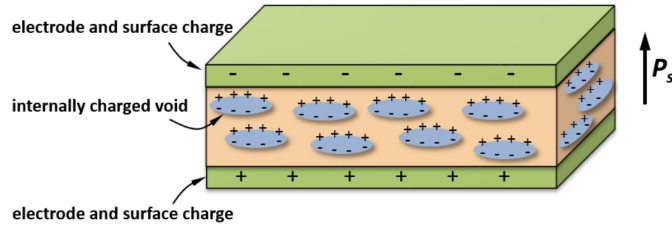


FIGURE 1.1: Schematic of ferroelectret material where  $P_s$  is the polarization direction [18]

- **Single crystals.** Lead Magnesium Niobate-Lead Titanate (PMN-PT) was the first single-crystal growth in 1990. The main advantage of this material is the electromechanical coupling factor  $k_{33} > 0.92$  and the piezoelectric coefficient, which is more than five times that of PZT ceramics. [19][20]. As a drawback, the high sensitivity is achieved only in one specific direction as a consequence of the high level of anisotropy.

## 1.4 Ferroelectrets

The electret is a dielectric material with a quasi-permanent electric charge [21], so it is the electrostatic equivalent of a permanent magnet, and ferroelectrets are a class of electret material. Quasi-permanent refers to the charge decay time being longer than the experiment investigation time. Ferroelectret is a cellular structure filled with gas and surrounded by a matrix polymer. The voids that compose the cellular structure can store positive and negative charges and form a permanent dipole moment, as can be observed in figure 1.1. The combination of the anisotropic cellular structure and the internal dipoles results in a strong piezoelectric effect.

Material	$d_{33}$ ( $pC/N$ )	Notes	Ref
PP	306	Stretching	[22]
	130	Foaming	[23]
	590		[24]
	330	Foaming	[6]
	300	Foaming	[25]
	650	Stretching $CaC_3$	[26]
	1400	Two compact PP skin layers	[27] [28]
	350	Two compact PP skin layers	[29]
	215	two compact PP skin layers	[29]
	580	Biaxial stretched	[30]
	1440	Three-layer of stretched filler-loaded PP	[30]
	2100	Five layer of stretched filler-loaded PP	[30]
PET	175	Stretching filler loaded PP followed by biaxial stretching	[31]
	23	Foaming	[32]
PTFE	500	Foaming with $CO_2$ following by biaxial stretching	[33]
	300	Cellular PTFE core and two compact PTFE skin layers	[34]
IXPP	1700	Cellular PTFE core and two compact PTFE skin layers	[34]
	140	Foaming with $CO_2$ followed by biaxial stretching	[35]
	100	Foaming followed by biaxial stretching	[36]
	308	Foaming followed by 200% stretching	[37]
	400	Foaming	[38] [39]

TABLE 1.1: Types of polymers ferroelectret and its piezoelectric coefficient  $d_{33}$ .

The first ferroelectret material was made with polypropylene, but due to the high interest in the material, other polymers were rapidly investigated to hold the cellular structure with the polarized voids. It can be highlighted some ferroelectrets with strong piezoelectric coefficient  $d_{33}$  as it can be observed in table 1.1

Polypropylene was used to produce the first ferroelectret material, but as interest in the material grew, alternative polymers were soon studied to hold the cellular structure with the polarized gaps. As a result, as noticed in the table 1.1, certain ferroelectrets with a high piezoelectric coefficient  $d_{33}$  can be emphasized.

PVDF is the piezoelectric material with the most significant resemblance to ferroelectret, compared to all of the previously stated materials. The main features that make both materials unique are their low elastic modulus, which grants them flexibility, the predominance of thickness mode resonances, and the lack of other resonance modes. Despite this, the differences make the materials suitable for different applications, precisely the piezoelectric coefficients, where ferroelectret is much higher than PVDF, and the acoustic impedance, where ferroelectret is much lower than PVDF.

Properties	P(VDF-TrEE) Thickness 100 $\mu\text{m}$	Cellular PP Thickness 58 $\mu\text{m}$
Density ( $\text{g}/\text{cm}^3$ )	1.79	0.33
Piezoelectric coefficient $d_{33}$ ( $\text{pC}/\text{N}$ )	20	300
Thickness-extension resonance frequency (MHz)	12.3	0.73
Electromechanical coupling factor	0.23	0.06
Elastic stiffness $c_{33}$ ( $\text{N}/\text{m}^2$ )	$10.8 \times 10^9$	$1.3 \times 10^6$

TABLE 1.2: Comparative table of some properties of PVDF vs Cellular PP [40].

Due to their unique properties, ferroelectrets are superior to other piezoelectric materials in several applications. Some instances include:

- **Energy harvesting.** There are three methods of transduction for harvesting kinetic energy: electromagnetic, electrostatic, and piezoelectric. I will quickly discuss the piezoelectric approach and explain why ferroelectrets play a significant role. Beyond the use of batteries, there is a significant demand for supplying energy to wearable electronic gadgets. [41][42][43][44]. The typical approach to harvesting kinetic energy is using PZT ceramics, which have suitable dielectric and piezoelectric properties. Another approach is the use of PVDF, which presents a low elastic modulus that makes the material very flexible and attachable to the majority of surfaces. However, the problem with the PZT is its high elastic modulus, which makes it challenging to accommodate the ceramic to the human body. In addition, PZT piezoelectrics are very brittle. In contrast, PVDF presents low piezoelectric coefficients. Ferroelectret properties are suitable for energy harvesting, showing good piezoelectric coefficients, flexibility, softness, and high compressibility. The energy that is passively generated by the human body, such as breathing, arm motion, and blood pressure, is presented in figure 1.2. As it is expected, the largest sources of energy are footwalls and arm motion, but these are very dependent on the lifestyle of the user, unlike the others like breathing or blood pressure. [45].

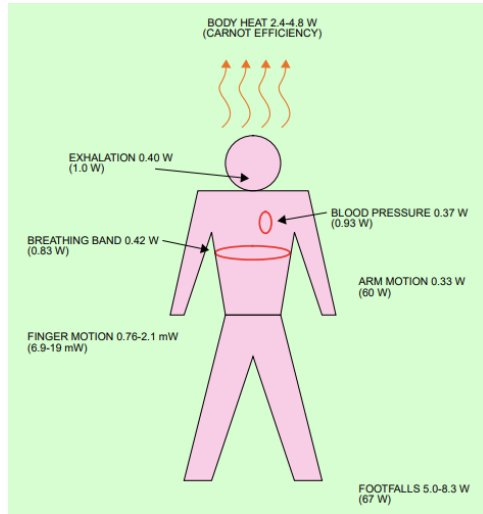


FIGURE 1.2: Power from body-driven sources; total power for each action is included in parenthesis [46]

- **Flexible wearable sensors** are a new technology that integrates sensors into wearables, such as clothes, rings, bracelets, etc., to provide smart functionalities. [47][48]. The FF is suitable for this purpose thanks to its high flexibility feature.
- **Air coupled transducers for NDT**. The low Young's modulus and density grant a very low acoustic impedance to the ferroelectret, which is favorable for the transmission of ultrasonic waves from the transducer to air. For this reason, it can be used as an active element for this purpose and applied in different applications [49] [50]. For example, in this paper [51] the ferroelectret is used to manufacture transducers for NDT wood-based materials.



FIGURE 1.3: Nondestructive testing of a piece of wood using air-coupled transducers in transmission operation [51].

- **Pressure sensors.** Softness and high compressibility added to the good sensitivity enable to produce this technology [52][53][54][55]. One example is the heart rate variability and sleep tracker from the company Emfit. The sensor is placed under the mattress and responds to micro pressure changes caused by the patient's heartbeat and respiration [56][57].

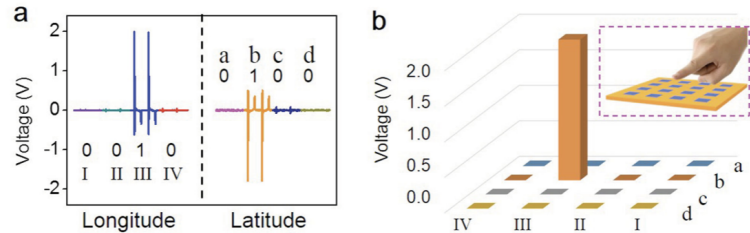


FIGURE 1.4: Position sensing. a) The voltage data plot harvested from the eight-channel electrodes when pixel (III-b) was subjected to a force. b) Histogram depiction derived from the case of (a), inset schematic represents the action of pressing the pixel (III-b) [58]

- **Biomedical sensors.** This application is especially convenient when combined with the wearable feature. For example, the paper [59] reports real-time and continuous human pulse monitoring for medical assessments and diagnosis. [60][61]

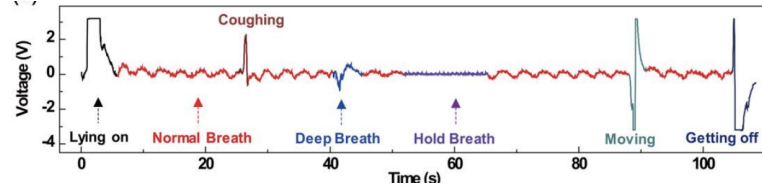


FIGURE 1.5: Electric response of the sleeping monitor to successive motions [62]



FIGURE 1.6: Heart rate variability and sleep tracker based on ferroelectrets by Emfit

#### 1.4.1 Ferroelectret fabrication

There are two methods to produce the cellular structure for the ferroelectrets, stretching and foaming. Foaming techniques require a polymer film to introduce

gases inside, such as  $CO_2$ ,  $Ar$ ,  $N_2$ , etc.; in this way, voids are formed (Fig 1.7 step 0)[63]. The stretching technique requires a polymer composite film with small solid particles and stretching it to form voids via decohesion/delamination around the solid particles (Fig 1.7 step 1) [63]. Finally, the polymer void heights are adjusted together with the elastic properties thanks to a gas-diffusion expansion process.

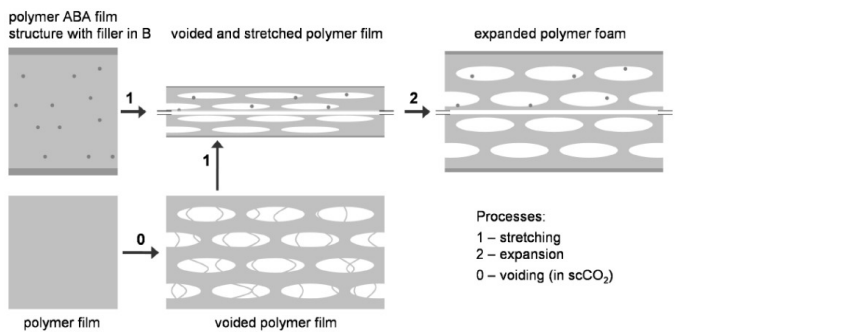


FIGURE 1.7: . Production of a cellular structure by stretching a filler-loaded polymer (process 1) or foaming by a physical blowing agent (supercritical carbon dioxide, CO<sub>2</sub>) [25]

Once the polymer film has the inner cellular structure, it is metalized on one or both film surfaces, depending on the application. The electrodes can be glued, deposited by a sputtering technique, or attached under vacuum to the film. The average thickness of the electrodes is around 50 nm. The electrical charging of the cellular structure film is the last and most important step. There are many ways to do this, but corona discharge and direct contact charging are the most common. Figure 1.9 shows the contact charging method, which involves applying a high electric voltage between both electrodes.

On the other hand, corona discharge does not need electrodes, although one electrode on the ground is preferred for better contact. For this method, a high voltage is applied between the ground and a needle that is a few centimeters above the cellular structure. The corona discharge can be applied in different gas atmospheres and temperatures [64] [65], which enables the possibility to adjust the polarization process. If we compare both methods, the main difference is that while contact charging creates the internal field directly by the high electric field between the electrodes, corona charging creates the internal field by the deposited surface charges. Due to its versatility, corona discharge is more accurate for the industry.

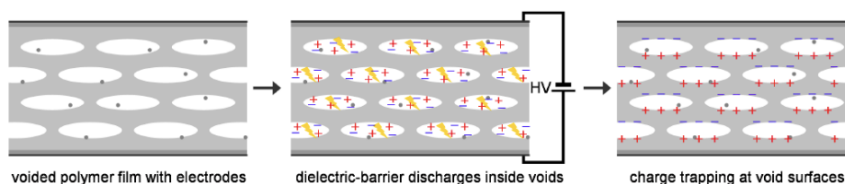


FIGURE 1.8: Schematic sketch of a cellular polymer film (left picture), the charge generation by dielectric-barrier discharges inside the voids (middle picture) and the trapping of charges of different polarities at the upper and lower void surfaces (right picture) [25].

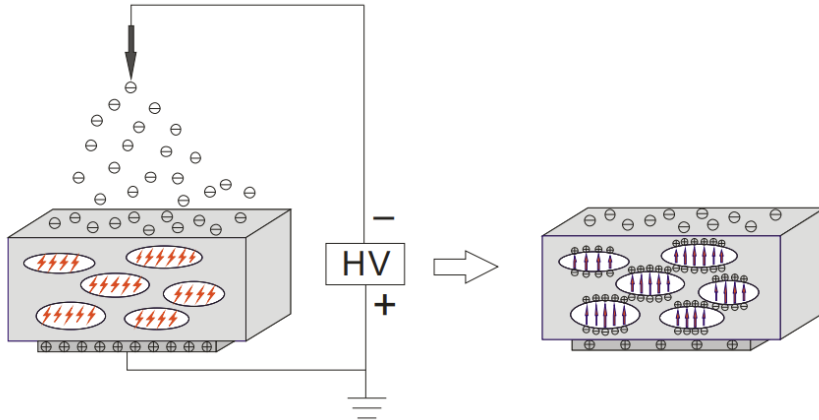


FIGURE 1.9: Negative tip-to-plane corona charging [66].

#### 1.4.2 Ferroelectret piezoelectric response

Ferroelectret piezoelectricity is made possible by the quasi-permanent dipole moments on the cellular structure (see the previous section) and the ease with which the thickness can be changed by pressure signals, whether they are acoustic or not. Furthermore, this process is reversible, so it can go from mechanical to electrical or electrical to mechanical. This feature enables pulse-echo operation for the transducers constructed with FF. Fig 1.10 shows both cases mentioned before.

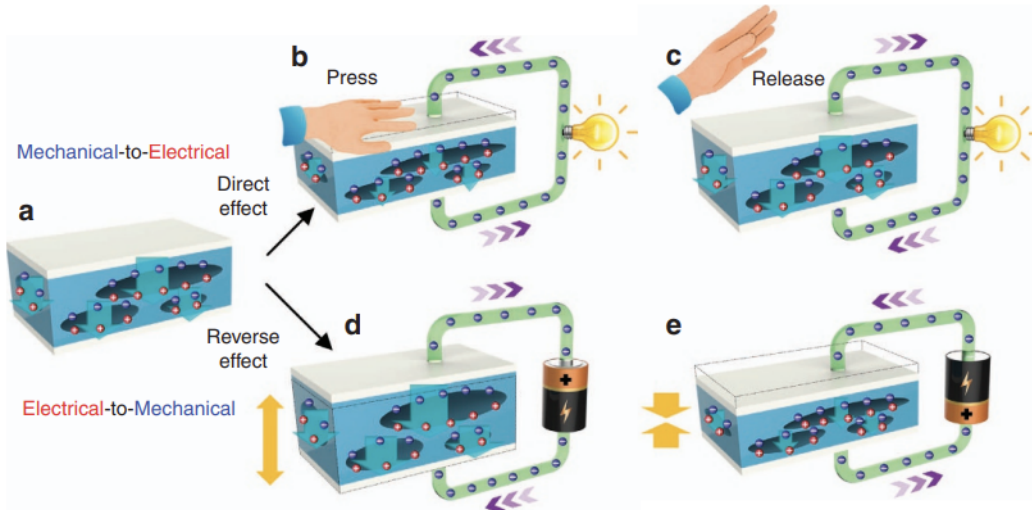


FIGURE 1.10: Energy Conversion Mechanisms of FENG. (a) Charge distribution and giant dipoles of the ferroelectret nanogenerator (FENG) after micro plasma discharging, showing that the upper and lower surfaces of voids are oppositely charged. (b,c) Direct electromechanical interaction effect. (b) Pressed by a human hand on the surface of FENG. (c) Pressure is released, and giant dipoles restore their original sizes. (d,e) Reverse electromechanical interaction effect. (d) Giant dipoles further expand as positive potential is applied. (e) Giant dipoles shrink as negative potential is applied. [67]

The piezoelectricity effect comes from the variations in the film thickness under mechanical pressure, as it was mentioned previously. So the shape of the void affects

how stiff the film is. Changing the shape of the void changes the elastic stiffness and the amount of mechanical force needed to get the same electrical response. Summarizing the piezoelectric activity is related to the film's elastic stiffness. This phenomenon is a crucial factor at the time of FF construction since optimizing the sensitivity is needed to achieve a specific void geometry where the elastic stiffness is minimum, as shown in figure 1.11.

Piezoelectric stability depends basically on three factors:

- The charges housed in the dipoles, whose stability can be affected by the presence of an electric or magnetic field
- The temperature, which is a limiting factor since it depolarizes the film.
- Environmental factors such as the melting temperature of the polymer, humidity, and radiation, among others, Can damage the stability of the cellular structure.

In general, FF is not as robust as piezoceramics.

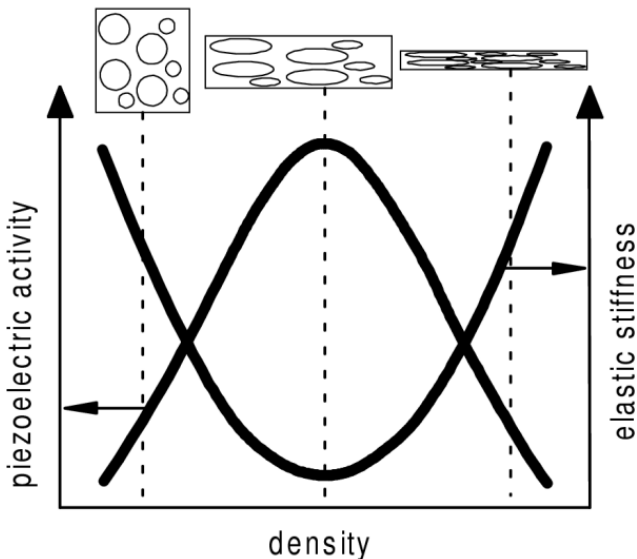


FIGURE 1.11: Schematic dependence of the piezoelectric activity and the elastic stiffness on sample density and cross sections of the corresponding cellular structures [68]

Finally, the rest of the section describes two models that can explain the piezoelectricity and elastic characteristics of cellular structures in ferroelectrets. In 2005, Tuncer came up with two geometric models, truss-like and eye-shaped, to explain how cellular structures work. Geometrical shapes are presented in figure 1.12. The length of the void,  $a$ , and the height of the void,  $b$ , are both described by the same set of coordinates. Tuncer developed a mathematical background to explain the behavior, with the following principal conclusions: If the effective Young's modulus of the structure is called  $E_e$  and  $E_s$  is the Young's modulus of the solid material, the effective Young's modulus is described as  $E_e/E_s$  and it decreases with the increasing  $a/b$  ratio. The volume fraction (ratio between cellular and bulk material) for the range between 0.15 and 0.85 for eye-like shapes shows a lower elastic modulus than truss-like cells, and for the range where the volume fraction is lower than 0.15 or higher than 0.85, the opposite.

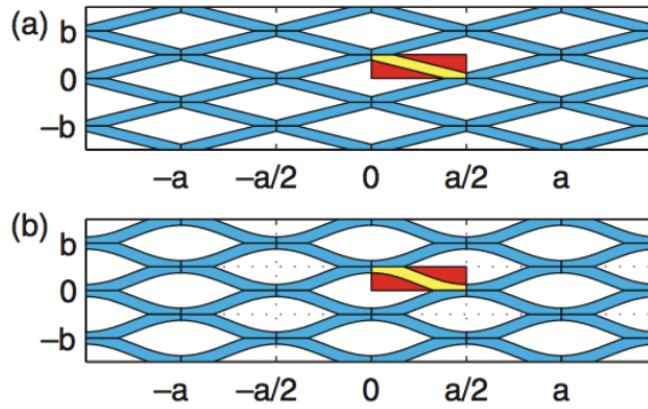


FIGURE 1.12: Schematic representation of: (a) truss-like and (b) eye-shaped geometrical structures [69]

In addition, there are numerous papers that mathematically describe the mechanical properties of the ferroelectret. There are different hypotheses. One of the most relevant is the sandwich structure, which separates the film thickness into three layers with different properties [70][71]. The first and third layers refer to the visible faces where the electrodes are, and there is no cellular structure, and the second layer is where the cellular structure is found.

The piezoelectricity model is graphically shown in figure 1.13, and it consists of parallel polymeric and gaseous layers interspersed between the electrodes.  $\sigma_i$  is the charge density on the interface of each layer,  $\epsilon_1$  and  $\epsilon_2$  are the permittivities,  $E_i$  is the electric field in the  $i$  layer,  $S_i$  is the thickness of the  $i$  layer, and  $V$  is the voltage applied between the electrodes. This model can calculate the  $d_{33}$  coefficient as [72].

$$d_{33} = \frac{\epsilon_2 \epsilon_1 \sigma}{c_{33}} \frac{ss_1}{s_2 (\epsilon_2 s_1 + \epsilon_1 s_2)^2} \quad (1.1)$$

Where  $c_{33}$  coefficient is the elastic modulus,  $s$  is the film thickness, and  $\sigma$  is the sum of all  $\sigma_i$  values. Also, it's important to note that the piezoelectric coefficient stays proportional to the charge density ( $\sigma$ ) in a linear way.

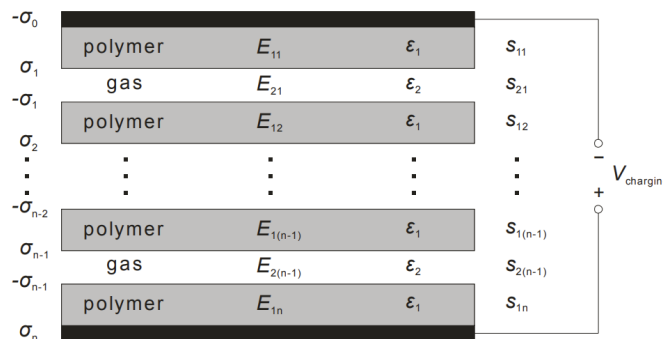


FIGURE 1.13: Model based on charged parallel polymeric and gaseous layers [70]



## Chapter 2

# Thickness resonance

### 2.1 String analogy $\lambda/4$ and $\lambda/2$

In the papers generated for this thesis, thickness resonance frequencies are commonly employed. This section calculates these frequencies by analogy with a standing wave on a string; thus, only one spatial dimension is employed.

First, the wave equation is solved:

$$v^2 \frac{\partial^2 y}{\partial x^2} = \frac{\partial^2 y}{\partial t^2} \quad (2.1)$$

Where  $v$  is the wave velocity and  $y(x, t)$  is the amplitude with position and time dependence. The solution for the wave equation is:

$$y = A \sin(kx \pm wt) \quad (2.2)$$

The "-" solution indicates the wave is traveling to the right, and the "+" solution indicates the wave is traveling to the left.  $A$  is half the peak-to-peak maximum amplitude,  $k$  is the wave vector, and  $w$  is the angular velocity. The total amplitude of the string is the sum of waves traveling to the right and the left so:

$$y(x, t) = A \sin(kx - wt) + A \sin(kx + wt) \quad (2.3)$$

Using the trigonometric sum to product identity  $\sin a + \sin b = 2 \sin\left(\frac{a+b}{2}\right) \cos\left(\frac{a-b}{2}\right)$  the equation 2.3 can be retyped as:

$$y(x, t) = 2A \sin(kx) \cos(wt) \quad (2.4)$$

To calculate the resonance frequencies, we can differentiate four different cases according to the boundary conditions:

- **String with two fixed ends.** The analogy consists of: both mediums next to the sample have a higher impedance than the sample itself. So  $Z_1 > Z_s$  and  $Z_2 > Z_s$ . The boundary conditions are  $y(0, t) = 0$  and  $y(l, t) = 0$

$$y(0, t) = 2A \underbrace{\sin(k \times 0)}_0 \cos(wt) = 0 \quad (2.5)$$

$$y(l, t) = 2A \underbrace{\sin(kl)}_0 \cos(wt) = 0 \quad (2.6)$$

$\sin kl = 0$  if  $kl = n\pi$  so, substituting  $k$  by  $2\pi/\lambda$  and  $\lambda = v/f$  we can clear the frequency  $f = \frac{nc}{2l}$  for  $n = 1, 2, 3, \dots$

- **String with left fixed end.** The analogy consists of: the impedance of medium one is higher than the sample, and medium two is lower than the sample. So  $Z_1 > Z_s > Z_2$ . The boundary conditions are  $y(0, t) = 0$  and  $|y(l, t)| = 2A$ .

$$y(0, t) = 2A \underbrace{\sin(k \times 0)}_0 \cos(wt) = 0 \quad (2.7)$$

$$|y(l, t)| = |2A \underbrace{\sin(kl)}_{1 \text{ or } -1} \cos(wt)| = 2A \quad (2.8)$$

the condition to  $|\sin(kl)| = 1$  is  $kl = \frac{\pi}{2}(2n - 1)$  for  $n = 1, 2, 3, \dots$ . Solving for the frequency,  $f = \frac{c}{4l}(2n - 1)$ .

- **String with right fixed end.** The analogy consists of: The impedance of medium one is lower than the sample, and medium two is higher than the sample. So  $Z_1 < Z_s < Z_2$ . Due to the symmetry of the boundary conditions, the resonance frequencies are the same that the previous case.  $f = \frac{c}{4l}(2n - 1)$
- **String with no fixed ends.** The analogy consists of: Both mediums next to the sample have a lower impedance than the sample itself. So  $Z_1 > Z_s < Z_2$ . For this case, we introduce a phase in the wave equation solution.

$$y(x, t) = A \sin\left(kx - wt + \frac{\pi}{2}\right) + A \sin\left(kx + wt + \frac{\pi}{2}\right) \quad (2.9)$$

$$y(x, t) = 2A \sin\left(kx + \frac{\pi}{2}\right) \cos(wt) \quad (2.10)$$

The boundary conditions are  $|y(0, t)| = 2A$  and  $|y(l, t)| = 2A$ .

$$y(0, t) = |2A \underbrace{\sin\left(k \times 0 + \frac{\pi}{2}\right)}_{1 \text{ or } -1} \cos(wt)| = 2A \quad (2.11)$$

$$y(0, t) = |2A \underbrace{\sin\left(kl + \frac{\pi}{2}\right)}_{1 \text{ or } -1} \cos(wt)| = 2A \quad (2.12)$$

the condition to  $|\sin(kl + \frac{\pi}{2})| = 1$  is the same than  $|\cos(kl)| = 1$  which it becomes  $kl = n\pi$ . if we solve for the frequency, the resonances are:  $f = \frac{nc}{2l}$  for  $n = 1, 2, 3, \dots$ . The resonance frequencies are found at the same values than the case where both ends were fixed. This is a consequence of the boundary conditions symmetry.

## 2.2 Transmission and reflection at single interface

We solve the wave equation for both mediums. On the left, there are two waves: the incident and the reflected. On the right, there is one wave, the transmitted.

$$\vec{P}(x, t) = \begin{cases} \vec{P}_1(x, t) = I e^{i(k_1 x - wt)} + A_r e^{-i(k_1 x + wt)} & \text{for } x \leq 0 \\ \vec{P}_2(x, t) = A_t e^{i(k_2 x - wt)} & \text{for } x \geq 0 \end{cases} \quad (2.13)$$

The boundary conditions are:

$$\begin{cases} \vec{P}_1(0, t) = \vec{P}_2(0, t) \\ \vec{v}_1(0, t) = \vec{v}_2(0, t) \end{cases} \quad (2.14)$$

Applying the first boundary condition

$$I e^{-iwt} + A_r e^{-iwt} = A_t e^{-iwt} \quad (2.15)$$

$$I + A_r = A_t \quad (2.16)$$

Applying the second boundary condition, we can calculate the velocity as,

$$\rho \frac{\partial v_x}{\partial t} = \frac{\partial P}{\partial x} \quad (2.17)$$

$$\frac{\partial P_1}{\partial x} = \frac{I}{e^{wt}} i k_1 e^{i k_1 x} - \frac{A_r}{e^{wt}} i k_1 e^{-i k_1 x} \quad (2.18)$$

$$\rho_1 \frac{\partial v_x}{\partial t} = \frac{I}{e^{wt}} i k_1 e^{i k_1 x} - \frac{A_r}{e^{wt}} i k_1 e^{-i k_1 x} \quad (2.19)$$

$$\int \partial v_x = \int e^{-wt} \left( \frac{i k_1}{\rho_1} (I e^{i k_1 x} - A_r e^{-i k_1 x}) \right) \partial t \quad (2.20)$$

$$v_x = -\frac{i k_1}{\rho_1 w} (I e^{i k_1 x} - A_r e^{-i k_1 x}) e^{-wt} \quad \text{for } x \leq 0 \quad (2.21)$$

We can replace  $\frac{k_1}{w} = \frac{2\pi/\lambda_1}{2\pi f} = \frac{1}{\lambda_1 f} = \frac{1}{c_1 f} = \frac{1}{c_1}$  and solving for velocity in the second medium  $x \geq 0$

$$\begin{cases} v_x = -\frac{i}{\rho_1 c_1} (I e^{i k_1 x} - A_r e^{-i k_1 x}) e^{-wt} & \text{for } x \leq 0 \\ v_x = -\frac{i}{\rho_2 c_2} A_t e^{i k_2 x} e^{-wt} & \text{for } x \geq 0 \end{cases} \quad (2.22)$$

Applying the second boundary condition we get:

$$\frac{1}{\rho_1 c_1} (I - A_r) = \frac{1}{\rho_2 c_2} A_t \quad (2.23)$$

we replace  $\rho c = Z$  and sum the equations from the boundary conditions:

$$\begin{cases} I + A_r = A_t \\ Z_2(I - A_r) = Z_1 A_t \end{cases} \quad (2.24)$$

If we assume the incident wave amplitude is 1 then, we solve for  $A_t$  and  $A_r$

$$A_r = \frac{Z_2 - Z_1}{Z_2 + Z_1} \quad (2.25)$$

$$A_t = \frac{2Z_2}{Z_2 + Z_1} \quad (2.26)$$

## 2.3 Transmission and reflection at two interface

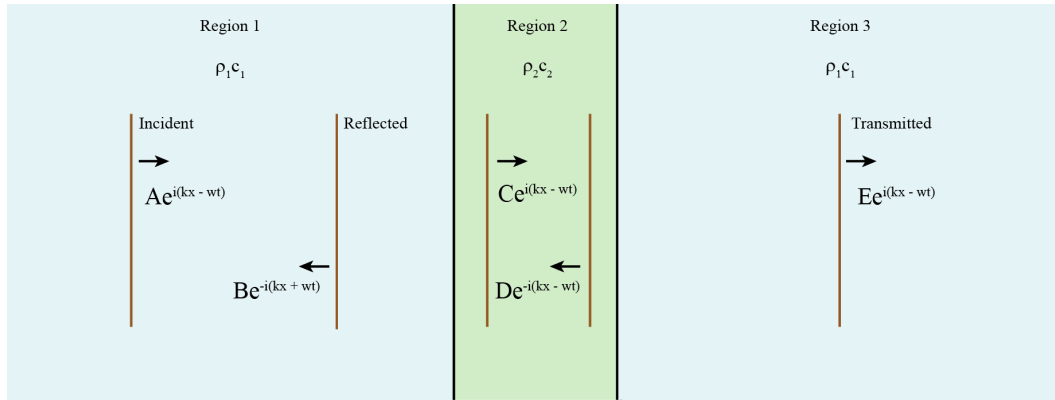


FIGURE 2.1: Scheme, where each wave is shown as a vertical line, with its mathematical equation next to it, and the direction of propagation is shown by an arrow.

The general wave equation is:

$$c^2 \left( \frac{\partial^2 P}{\partial x^2} + \frac{\partial^2 P}{\partial y^2} + \frac{\partial^2 P}{\partial z^2} \right) = \frac{\partial^2 P}{\partial t^2} \quad (2.27)$$

But since we are interested only in the propagation along the "x" axis, the wave equation becomes:

$$c^2 \frac{\partial^2 P}{\partial x^2} = \frac{\partial^2 P}{\partial t^2} \quad (2.28)$$

The solution is:

$$P(x, t) = A e^{i(kx \pm wt)} \quad (2.29)$$

The "-" sign means the wave velocity is positive, and the "+" sign indicates the wave velocity is negative. The peak-to-peak amplitude is A.

The wave equation is solved for each region (1, 2, and 3). The wave travels only to the right in region 3

$$\vec{P}(x, t) = \begin{cases} \vec{P}_1(x, t) = A e^{i(k_1 x - wt)} + B e^{-i(k_1 x + wt)} & \text{for } x \leq 0 \\ \vec{P}_2(x, t) = C e^{i(k_2 x - wt)} + D e^{-i(k_2 x + wt)} & \text{for } 0 \leq x \leq l \\ \vec{P}_3(x, t) = E e^{i(k_1(x-l) - wt)} & \text{for } x \geq l \end{cases} \quad (2.30)$$

We are interested in calculating the transmission coefficient, defined as the ratio between the amplitude of the source and transmitted waves E/A, and the reflection coefficient, defined as the ratio between the amplitude of the source and reflected waves B/A. To calculate these quantities, boundary conditions are applied. At  $x = 0$  and  $x = l$ , pressure and velocity quantities are the same on both sides of the barrier.

$$\begin{aligned}\vec{P}_1(0, t) &= \vec{P}_2(0, t) \quad \text{and} \quad \vec{u}_1(0, t) = \vec{u}_2(0, t) \\ \vec{P}_2(l, t) &= \vec{P}_3(l, t) \quad \text{and} \quad \vec{u}_2(l, t) = \vec{u}_3(l, t)\end{aligned}\quad (2.31)$$

First, we apply the boundary condition  $\vec{P}_1(0, t) = \vec{P}_2(0, t)$

$$Ae^{-i\omega t} + Be^{i\omega t} = Ce^{-i\omega t} + De^{i\omega t}$$

$$\boxed{A + B = C + D} \quad (2.32)$$

The velocity is related to the pressure by:

$$\rho \frac{\partial u_x}{\partial t} = \frac{\partial P}{\partial x} \quad (2.33)$$

We calculate  $u_x$

$$\frac{\partial \vec{P}_1(x, t)}{\partial x} = \frac{A}{e^{wt}} ik_1 e^{ik_1 x} - \frac{B}{e^{wt}} ik_1 e^{ik_1 x} = \rho_1 \frac{\partial u_x}{\partial t} \quad (2.34)$$

$$\frac{\partial u_x}{\partial t} = \frac{ik_1}{\rho_1 e^{wt}} (A e^{ik_1 x} - B e^{-ik_1 x}) \quad (2.35)$$

$$\partial u_x = e^{-wt} \left( \frac{ik_1}{\rho_1} (A e^{ik_1 x} - B e^{-ik_1 x}) \right) \partial t \quad (2.36)$$

$$\int \partial u_x = \int e^{-wt} \left( \frac{ik_1}{\rho_1} (A e^{ik_1 x} - B e^{-ik_1 x}) \right) \partial t \quad (2.37)$$

$$u_x = -\frac{ik_1}{\rho_1 w} (A e^{ik_1 x} - B e^{-ik_1 x}) e^{-wt} \quad (2.38)$$

for  $x = 0$

$$u_{x=0} = -\frac{ik_1}{\rho_1 w} (A - B) e^{-wt} \quad (2.39)$$

Substituting  $\frac{k_1}{w} = \frac{2\pi/\lambda_1}{2\pi f} = \frac{1}{\lambda_1 f} = \frac{1}{c_1 f} = \frac{1}{c_1}$

$$u_{x=0} = -\frac{i}{\rho_1 c_1} (A - B) e^{-wt} \quad (2.40)$$

In the same way, we calculate the velocity at  $x = 0$  in region 2.

$$u_{2,x=0} = -\frac{i}{\rho_2 c_2} (C - D) e^{-wt} \quad (2.41)$$

Second, we apply the boundary condition  $\vec{u}_1(0, t) = \vec{u}_2(0, t)$

$$u_{2,x=0} = -\frac{i}{\rho_2 c_2} (C - D) e^{-wt} \quad (2.42)$$

$$\boxed{\frac{1}{\rho_1 c_1} (A - B) = \frac{1}{\rho_2 c_2} (C - D)} \quad (2.43)$$

In the same way, we apply the boundary conditions for  $x = l$

$$\boxed{Ce^{ik_2 l} + De^{-ik_2 l} = E} \quad (2.44)$$

$$\boxed{\frac{1}{\rho_2 c_2} (Ce^{ik_2 l} - De^{-ik_2 l}) = \frac{1}{\rho_1 c_1} E} \quad (2.45)$$

The four equations that result from applying the boundary conditions are easily expressed in matrix form as follows:

$$\begin{pmatrix} \rho_2 c_2 & \rho_1 c_1 e^{-ik_2 l} & -\rho_1 c_1 e^{ik_2 l} & 0 \\ 1 & -e^{-ik_2 l} & -e^{ik_2 l} & 0 \\ 0 & -\rho_1 c_1 & \rho_1 c_1 & \rho_2 c_2 \\ 0 & 1 & 1 & -1 \end{pmatrix} \begin{pmatrix} E \\ D \\ C \\ B \end{pmatrix} = A \begin{pmatrix} 0 \\ 0 \\ \rho_2 c_2 \\ 1 \end{pmatrix} \quad (2.46)$$

To solve the equation for the amplitudes, we have a matrix equation in the form:

$$QX = W \quad (2.47)$$

The inverse of a matrix  $Q^{-1}$  is defined as  $Q^{-1}Q = I$  where  $I$  is the identity matrix.

$$Q^{-1}QX = Q^{-1}W \quad (2.48)$$

$$IX = X = Q^{-1}W \quad (2.49)$$

To calculate the inverse of  $Q$ , we use the cofactor method.

$$Q^{-1} = \frac{\text{Adjoint of } Q}{\text{Determinant of } Q} \quad (2.50)$$

Where adjoint of  $A$  is obtained by first replacing each matrix element by its signed cofactor and transposing the resulting matrix.

$$\begin{pmatrix} E \\ D \\ C \\ B \end{pmatrix} = \frac{A}{\det Q} \begin{pmatrix} c_{11} & c_{12} & c_{13} & c_{14} \\ c_{21} & c_{22} & c_{23} & c_{24} \\ c_{31} & c_{32} & c_{33} & c_{34} \\ c_{41} & c_{42} & c_{43} & c_{44} \end{pmatrix} \begin{pmatrix} 0 \\ 0 \\ \rho_2 c_2 \\ 1 \end{pmatrix} \quad (2.51)$$

we calculate the determinant of  $Q$ :

$$\det Q = \rho_2 c_2 \times \text{adj}(q_{11}) + 1 \times \text{adj}(q_{21}) \quad (2.52)$$

$$\text{adj}(q_{11}) = (-1)^{1+1} \begin{vmatrix} -e^{-ik_2 l} & -e^{ik_2 l} & 0 \\ -\rho_1 c_1 & \rho_1 c_1 & \rho_2 c_2 \\ 1 & 1 & -1 \end{vmatrix} \quad (2.53)$$

$$\text{adj}(q_{11}) = \rho_1 c_1 (e^{-ik_2 l} + e^{ik_2 l}) + \rho_2 c_2 (e^{-ik_2 l} - e^{ik_2 l}) \quad (2.54)$$

$$\text{adj}(q_{21}) = (-1)^{2+1} \begin{vmatrix} \rho_1 c_1 e^{-ik_2 l} & -\rho_1 c_1 e^{ik_2 l} & 0 \\ -\rho_1 c_1 & \rho_1 c_1 & \rho_2 c_2 \\ 1 & 1 & -1 \end{vmatrix} \quad (2.55)$$

$$\text{adj}(q_{21}) = (\rho_1 c_1)^2 (e^{-ik_2 l} - e^{ik_2 l}) + \rho_1 c_1 \rho_2 c_2 (e^{ik_2 l} + e^{-ik_2 l}) \quad (2.56)$$

$$\begin{aligned} \det Q &= \rho_1 c_1 \rho_2 c_2 (e^{-ik_2 l} - e^{ik_2 l}) + (\rho_2 c_2)^2 (e^{-ik_2 l} - e^{ik_2 l}) \\ &\quad + (\rho_1 c_1)^2 (e^{-ik_2 l} - e^{ik_2 l}) + \rho_1 c_1 \rho_2 c_2 (e^{-ik_2 l} + e^{ik_2 l}) \end{aligned} \quad (2.57)$$

$$\det Q = (\rho_1 c_1 + \rho_2 c_2)^2 (e^{-ik_2 l} - e^{ik_2 l}) + 4\rho_1 c_1 \rho_2 c_2 e^{ik_2 l} \quad (2.58)$$

We use Euler identity  $e^{ix} = \cos x + i \sin x$

$$\begin{aligned} \det Q &= (\rho_1 c_1 + \rho_2 c_2)^2 (\cos(-k_2 l) + i \sin(-k_2 l) - \cos(k_2 l) - i \sin(k_2 l)) \\ &\quad + 4\rho_1 c_1 \rho_2 c_2 (\cos(k_2 l) + i \sin(k_2 l)) \end{aligned} \quad (2.59)$$

Remembering the trigonometric identities ( $\cos -x = \cos x$ ) and ( $\sin -x = -\sin x$ )

$$\begin{aligned} \det Q &= (\rho_1 c_1 + \rho_2 c_2)^2 (\cos(k_2 l) - i \sin(k_2 l) - \cos(k_2 l) - i \sin(-k_2 l)) \\ &\quad + 4\rho_1 c_1 \rho_2 c_2 (\cos(k_2 l) + i \sin(k_2 l)) \end{aligned} \quad (2.60)$$

$$\det Q = -2i \sin(k_2 l) ((\rho_1 c_1)^2 + (\rho_2 c_2)^2) + 4\rho_1 c_1 \rho_2 c_2 (\cos(k_2 l)) \quad (2.61)$$

There is a discrepancy between my calculations and Element of Acoustic. the sign of  $4\rho_1 c_1 \rho_2 c_2 (\cos(k_2 l))$  is negative according to Temkin and positive according to my calculations. Since we want to find the coefficients of transmission and reflection, we solve the matrix equation for B and E.

$$E = \frac{A}{\det Q} (\rho_2 c_2 c_{13} + c_{14}) \quad (2.62)$$

where  $c_{13}$  and  $c_{14}$  are calculated as:

$$c_{13} = (-1)^{3+1} \begin{vmatrix} \rho_1 c_1 e^{-ik_2 l} & -\rho_1 c_1 e^{ik_2 l} & 0 \\ -e^{-ik_2 l} & -e^{ik_2 l} & 0 \\ 1 & 1 & -1 \end{vmatrix} = \rho_1 c_1 + \rho_1 c_1 = 2\rho_1 c_1 \quad (2.63)$$

$$c_{14} = (-1)^{4+1} \begin{vmatrix} \rho_1 c_1 e^{-ik_2 l} & -\rho_1 c_1 e^{ik_2 l} & 0 \\ -e^{-ik_2 l} & -e^{ik_2 l} & 0 \\ -\rho_1 c_1 & \rho_1 c_1 & \rho_2 c_2 \end{vmatrix} = \rho_1 c_1 \rho_2 c_2 + \rho_1 c_1 \rho_2 c_2 = 2\rho_1 c_1 \rho_2 c_2 \quad (2.64)$$

The transmission coefficient  $E/A$  is:

$$\frac{E}{A} = \frac{4\rho_1 c_1 \rho_2 c_2}{-2i \sin(k_2 l) ((\rho_1 c_1)^2 + (\rho_2 c_2)^2) + 4\rho_1 c_1 \rho_2 c_2 (\cos(k_2 l))} \quad (2.65)$$

$$\frac{E}{A} = \frac{2}{2 \cos(k_2 l) - i \sin(k_2 l) \left( \frac{\rho_1 c_1}{\rho_2 c_2} + \frac{\rho_2 c_2}{\rho_1 c_1} \right)} \quad (2.66)$$

We are interested in the ratio of transmitted to incident intensities given by.

$$\alpha_t = \frac{|E|^2}{A} = \frac{EE^*}{A} \quad (2.67)$$

$$\alpha_t = \frac{4}{4 \cos^2(k_2 l) + \sin^2(k_2 l) \left( \frac{\rho_1 c_1}{\rho_2 c_2} + \frac{\rho_2 c_2}{\rho_1 c_1} \right)^2} \quad (2.68)$$

We calculate the Reflection coefficient:

$$B = \frac{A}{\det Q} (c_{43} \rho_2 c_2 + c_{44}) \quad (2.69)$$

$$c_{43} = (-1)^{4+3} \begin{vmatrix} \rho_2 c_2 & \rho_1 c_1 e^{-ik_2 l} & -\rho_1 c_1 e^{ik_2 l} \\ 1 & -e^{-ik_2 l} & -e^{ik_2 l} \\ 0 & 1 & 1 \end{vmatrix} \quad (2.70)$$

$$c_{43} = 2i\rho_2 c_2 \sin(k_2 l) + 2\rho_1 c_1 \cos(k_2 l) \quad (2.71)$$

$$c_{44} = (-1)^{4+4} \begin{vmatrix} \rho_2 c_2 & \rho_1 c_1 e^{-ik_2 l} & -\rho_1 c_1 e^{ik_2 l} \\ 1 & -e^{-ik_2 l} & -e^{ik_2 l} \\ 0 & -\rho_1 c_1 & \rho_1 c_1 \end{vmatrix} \quad (2.72)$$

$$c_{44} = 2i(\rho_1 c_1)^2 \sin(k_2 l) - 2\rho_1 c_1 \rho_2 c_2 \cos(k_2 l) \quad (2.73)$$

$$\frac{B}{A} = \frac{\sin k_2 l \left( \frac{\rho_1 c_1}{\rho_2 c_2} + \frac{\rho_2 c_2}{\rho_1 c_1} \right)}{\sin k_2 l \left( \frac{\rho_1 c_1}{\rho_2 c_2} + \frac{\rho_2 c_2}{\rho_1 c_1} \right) + 2i \cos k_2 l} \quad (2.74)$$

We are interested in the ratio of reflected to incident intensities given by:

$$\alpha_r = \frac{|B|^2}{A} = \frac{BB^*}{A} \quad (2.75)$$

Another method to calculate the coefficient of reflection in this particular case where attenuation is not taken into account is to just subtract the coefficient of transmission from one.

$$\boxed{\alpha_r = 1 - \alpha_t} \quad (2.76)$$

There are two trivial solutions for the coefficient of transmission.

- The first is when  $\rho_1 c_1 = \rho_2 c_2$ , which means that the wall properties are the same as the medium, so the analogy is that there is no wall and the solution of the equation 2.68 is 1.
- The second is the case where the wall becomes very thin, and the thickness is nearly 0, which means there is no wall and the coefficient of transmission becomes 1.

As shown in the figure 2.2, the coefficient of transmission through a wall with a certain acoustic impedance in a certain medium depends on  $k_2 l$ . The effects of frequency on transmission depend on the  $c_2$  and  $l$  of the wall. The larger the difference between the two characteristic impedances, the smaller the transmission coefficient. However, we can see that there are a lot of frequencies where  $\alpha_t = 1$ . These correspond to the characteristic frequencies of the region  $0 < x < l$  and are given by the equation 2.77.

$$\frac{wl}{c_2} = n\pi, \quad n = 0, 1, 2, \dots \quad (2.77)$$

Resonance is what makes it possible to get a perfect transmitter at certain frequencies, even though the difference between the two characteristic impedances is large.

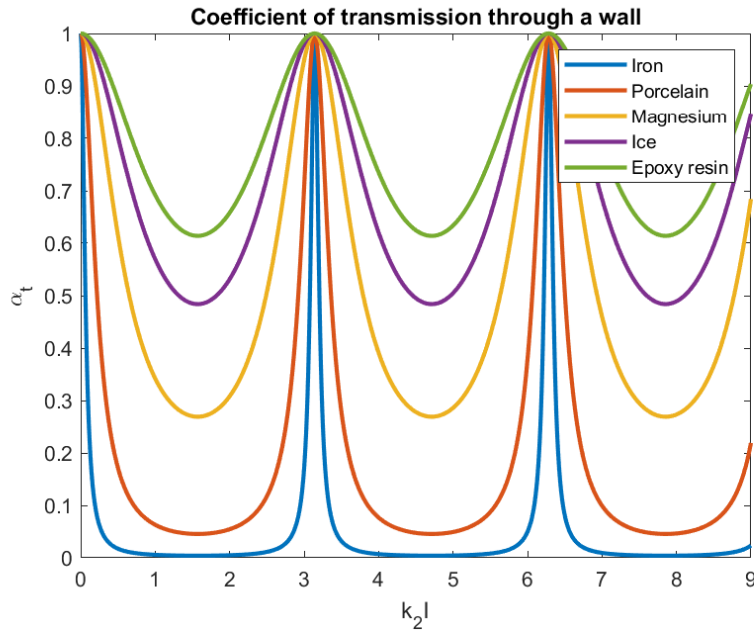


FIGURE 2.2: Coefficient of transmission through a wall made of different materials. The wall is immersed in water.

The interference ultrasound spectroscopy method, which is explained in Section XX, is based on fitting an experimental coefficient of reflection to a coefficient of reflection calculated in this section, along with an attenuation factor. Specifically, the cartilage phantoms prepared are the same case as the coefficient of reflection through a wall studied in this section, with the difference in attenuation as a function of frequency. The next figure shows the coefficient of reflection of the same materials as shown in figure 2.2.

As it was shown in figures 2.2 and 2.3 XX, the transmission/reflection coefficient depends on the speed of sound through the wall, the thickness of the wall, and the frequency of the acoustic wave. In the case of reflection as a difference of transmission, if the mismatch impedance between the medium and the wall is large, there is no situation where the coefficient of reflection becomes 1. The condition for obtaining the maximum amplitude of the reflected wave also changes.

$$\frac{wl}{c_2} = \pi \left( n + \frac{1}{2} \right) \quad (2.78)$$

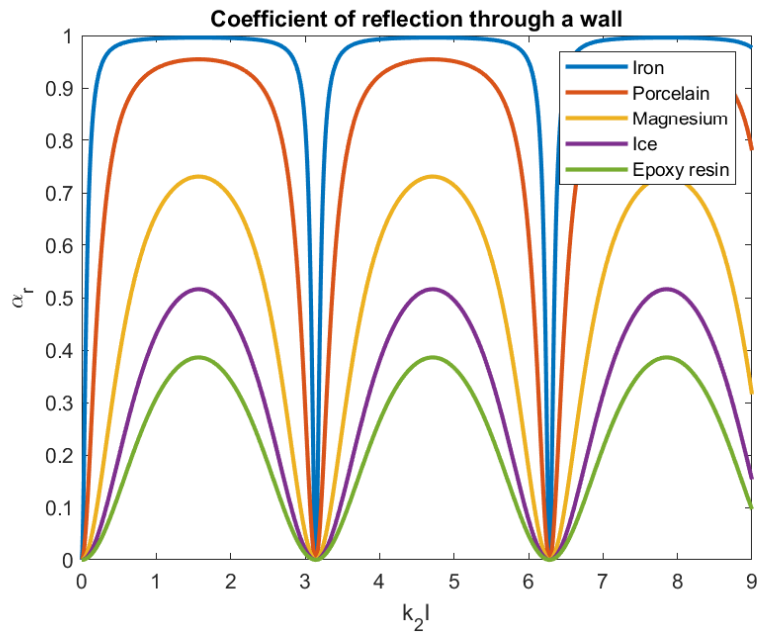


FIGURE 2.3: Coefficient of reflection through a wall made of different materials. The wall is immersed in water.

## 2.4 Transmission and reflection at n interface

By specifying the wave potentials in each layer and the boundary conditions (continuity of normal and shear stresses and displacements), the general problem of transmission through a layered medium is addressed by the transfer matrix method. This method is widely used in optics and acoustic to extract information from each layer [73][74][75][76].

It is presumed that the layers are viscoelastic and isotropic. At the interfaces between layers, normal and tangential displacements, as well as normal and shear stresses, must be continuous in order to meet the boundary criteria.

The following potential function may be used to represent the velocities and stresses in any layer:

$$\vec{P}_n(x, t) = A_n e^{i(k_n x - wt)} + B_n e^{-i(k_n x + wt)} \quad (2.79)$$

Where  $k_n$  is the wave number of the "n" layer,  $w$  is the angular frequency, And  $A_n$  and  $B_n$  corresponds to the pressure wave amplitude of the transmitted and reflected wave.

According to boundary conditions we can express the  $A_n$  and  $B_n$  coefficients in a matrix form as:

$$\begin{pmatrix} A_n \\ B_n \end{pmatrix} = \frac{1}{2Z_n} \begin{pmatrix} (Z_n + Z_{n+1})e^{i(wt + (k_n - k_{n+1})(nl_n + (n-1)l_{n+1}))} & (Z_n - Z_{n+1})e^{i(wt + (k_n + k_{n+1})(nl_n + (n-1)l_{n+1}))} \\ (Z_n - Z_{n+1})e^{i(wt - (k_n + k_{n+1})(nl_n + (n-1)l_{n+1}))} & (Z_n + Z_{n+1})e^{i(wt + (k_n + k_{n+1})(nl_n + (n-1)l_{n+1}))} \end{pmatrix} \begin{pmatrix} A_{n+1} \\ B_{n+1} \end{pmatrix} \quad (2.80)$$

Where  $Z_n$  is the acoustic impedance of the  $n$  layer. If the layered media contains N layers:

$$\begin{pmatrix} A_1 \\ B_1 \end{pmatrix} = [T] \begin{pmatrix} A_{N+1} \\ B_{N+1} \end{pmatrix} \quad (2.81)$$

Where  $[T]$  denotes the transfer matrix, and it is defined as the multiplication of the transfer matrix of each layer.



## Chapter 3

# Inverse problem

### 3.1 Algorithms, Simulated Annealing

Simulated annealing is a stochastic optimization method used to find the global optimum of a given function (error function) (see [77][78][79]). This algorithm is inspired by the slow cooling of metals when they reach the annealing temperature, and it mimics the internal structure change during this time as the temperature drops.

The analogy is made by showing how the system's internal energy function tends to move toward a minimum global state. For this comparison, the energy function becomes the objective function to optimize. The main idea of the algorithm is to calculate an objective function for both the actual and neighboring states and later change the current state of the neighboring state with a certain probability given by the following equation:

$$P(\Delta E) = e^{-\frac{|E(s) - E(s')|}{k_b T}} \quad (3.1)$$

Where  $k$  is the Boltzmann constant,  $T$  is the temperature, and  $E(s)$  is the objective function at the state  $s$ .

In the case of this thesis, this function is the least square error between the spectra that were calculated and those that were measured. One of the reasons to use this method is the significant number of variables in the calculated spectra, five variables for each layer which makes it computationally quasi-impossible to explore all the states of space. One of the main advantages of this method is that the starting state is relatively unimportant, as opposed to other methods in which the solution is heavily dependent on it. Also, this algorithm can avoid local minima, particularly at the start of the process when the temperature is still too high, and it can jump potential barriers to finding other local minima, which could eventually be the global minima (solution). From a mathematical point of view, it is proven that if the system's temperature drops slowly enough, the algorithm always finds the global minima [80][81]. However, from a practical standpoint, the time required to execute a perfect simulation is much greater than the time required to execute a significant number of simulations and make the statistics to ensure the global minimum (solution).

Figure 3.1 shows three attempts where the algorithm was executed, and every attempt is presented as a little sphere. At the start of the calculation, the temperature is at its highest, which lets the spheres (solutions) jump from one local minimum to another. However, as time goes on, the temperature goes down, which makes it harder for the spheres to "jump" over a significant potential barrier. Finally, the temperature freezes the spheres (solution), and they cannot move to another state. At this point, the optimal solution has been found as it is shown in figure 3.1. The SA algorithm does not always find the optimal solution. For this reason, it is

necessary to repeat the calculation several times to get the statistics. For example, in our case, if the optimal error function (solution) is greater than a certain threshold, the calculation is discarded, and the process is repeated.

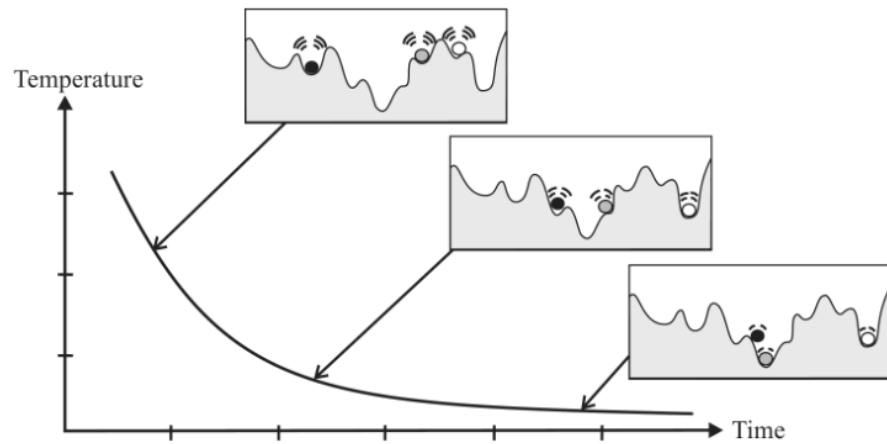


FIGURE 3.1: The image is from the book Simulated Annealing - Advances, Applications and Hybridizations [82]

## 3.2 Phantom Interferometry

The mathematical procedure shown in section 2.3 is used to obtain the calculated coefficient of reflection for each case with the specific phantom properties. Additionally, it includes the consideration of attenuation as a function of frequency. This last variable is responsible for the fact that all the peaks and valleys are not at the same y level, and as the frequency is increased, the peak-to-peak dB drop is reduced. Figure 2.3 does not contemplate the effect of attenuation, and therefore all the peaks and valleys are found at the same reflection coefficient value for all the frequencies. We have fabricated five cartilage phantoms with the same materials and procedures. The only difference between them is the thickness. The reflection coefficient of each phantom is measured five times with two different transducers: 1 MHz from Olympus model V314 and 5 MHz from Olympus, model A308S. So, there are 50 experimental measurements. The inverse problem algorithm is executed five times for each measurement. Suppose the objective function (error) is greater than a certain threshold once the calculation has finished. In that case, the solution is discarded, and the SA algorithm is repeated, so there are a minimum of 250 inverse problem calculations.

Although wrong solutions from the SA algorithm are discarded according to mathematical criteria, if we look at the visual solutions, it is obvious when they do not fit the experimental data, as shown in figure 3.2. This figure presents two different SA algorithm solutions for the experimental measurement of the Phantom 3 and the 5 MHz transducer. Also, it looks like there is not a local minimum solution that is close to the global minimum in this case. So, when the local minimum solution is found, the calculated and measured coefficients of reflection are very different.

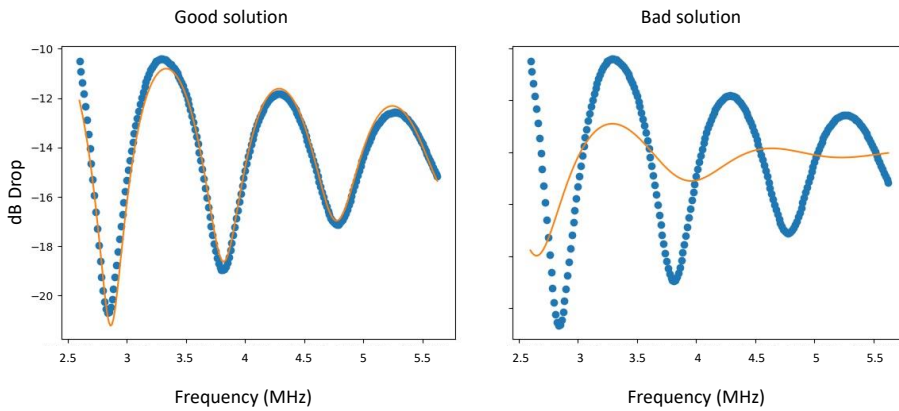


FIGURE 3.2: The image is from the book Simulated Annealing - Advances, Applications and Hybridizations [82]

The algorithm stops when the objective function reaches a predetermined value, but since the starting state is random and the algorithm is stochastic, the time needed for each calculation changes. To avoid very long calculations, the calculation stops when the temperature reaches a specific value, and it is supposed that the solution

state has ended up in local minima.

Figure 3.3 shows one measurement as blue dots for each phantom, with the 1 MHz transducer in the left column and the 5 MHz transducer in the right column. Also, it shows the inverse problem solution using the SA algorithm as a yellow line.

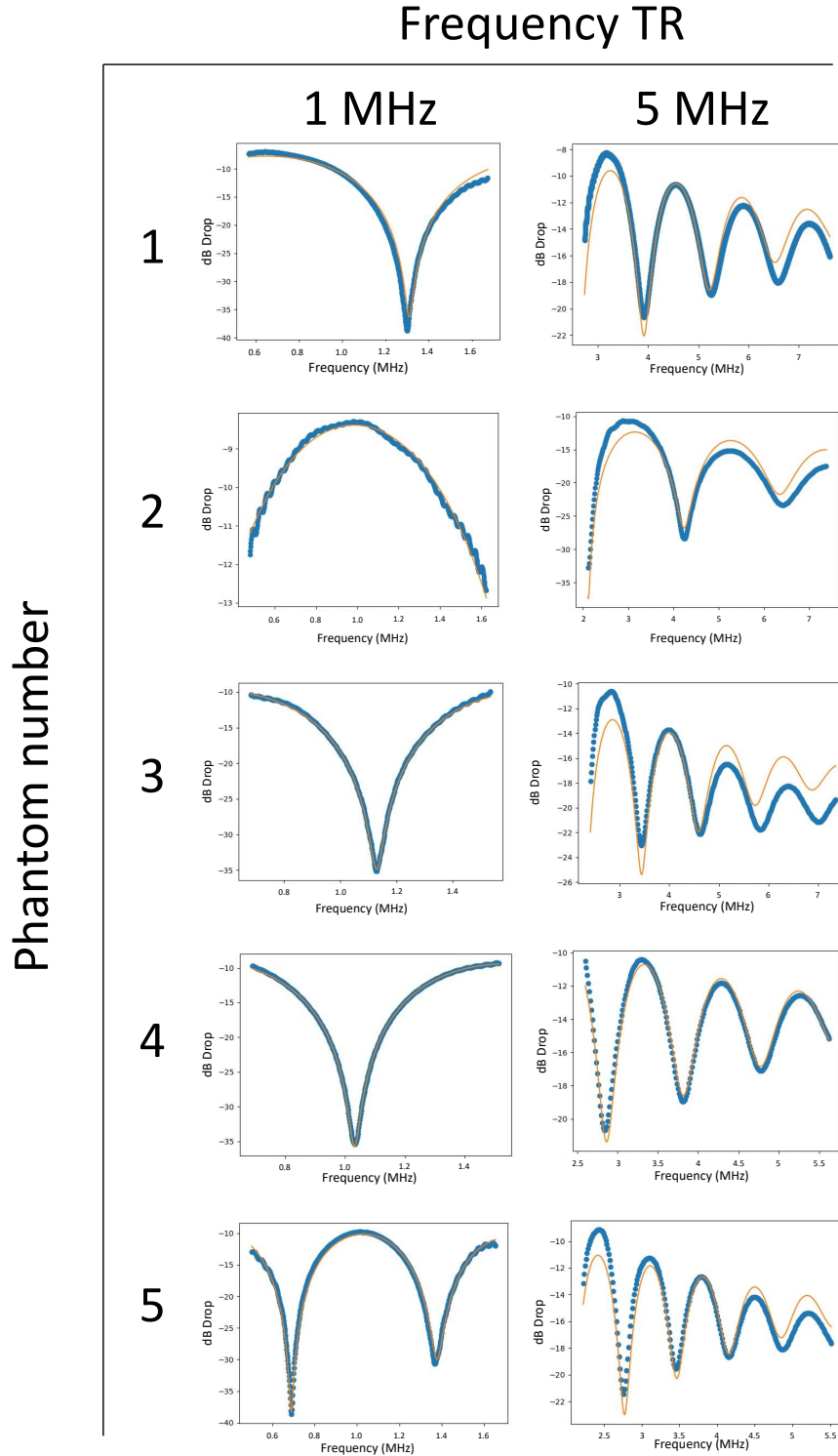


FIGURE 3.3: The blue dots represent the experimental data and the yellow line the solution of the inverse problem.

The inverse problem solution fits values which are:

- Eigen frequency:  $c/t$  where  $c$  is the ultrasound longitudinal velocity and  $t$  is the thickness of the sample.
- Impedance,  $Z = c\rho$  where  $\rho$  is the phantom density.
- $\frac{\rho}{att}$  where  $att$  is the attenuation.
- $att * t$
- Variation of the attenuation coef. with freq. assuming a power law:  

$$att = att_0 \left(\frac{f}{f_0}\right)^{efa}$$

We can use these values to figure out what the phantom properties are, but this method is not self-contained because it needs a known value to figure out the rest. In this study, the known value is the density, which was calculated with a scale and micrometer since the sample shape is a circle. The following table shows the phantom properties, from which we can conclude that the phantoms mimic cartilage tissue. This method is called quantitative echography because it can tell the difference between echoes from different tissues and measure distances like traditional echography. However, it can also calculate specific properties of the different tissues, which is a big plus. One drawback compared with traditional echography is that it is computationally very costly, and for this reason, it cannot be operated in real-time.

Phantom	Velocity (m/s)	Impedance (MRayl)	Attenuation @ 1 MHz (dB/cm)
Average	1819	2.1	4.94

All the values besides the thickness should be equal for all the phantoms since the fabrication material is the same. The variability between the phantoms is minimal but not zero. These differences can be attributed to the measurement error plus the error of the simulated annealing algorithm. The thickness, however, is different for all the phantoms. Also, it can be used to confirm that the SA algorithm works correctly by comparing the SA results to a micrometer measurement. Figure 3.4 depicts the thickness of each phantom as measured by a micrometer on the x-axis and ultrasound interferometry on the y-axis. The error bar on the x-axis is the standard deviation of five measurements. This error bar is different for all the phantoms, although they were all measured with the same micrometer. The reason is that both faces of each phantom are not completely parallel, so the thickness slightly depends on where the measurement was taken. The error bar on y is the standard deviation of the thickness calculated with the SA algorithm for the measurements with the 1 MHz and 5 MHz transducers.

In general, the thickness values measured by both methods are very similar, which suggests that this technique can be used to measure wall thickness in cases where the echoes are overlapped in time. However, this method is valuable for more than just figuring out distances. It can also be used to get the properties listed in the item list.

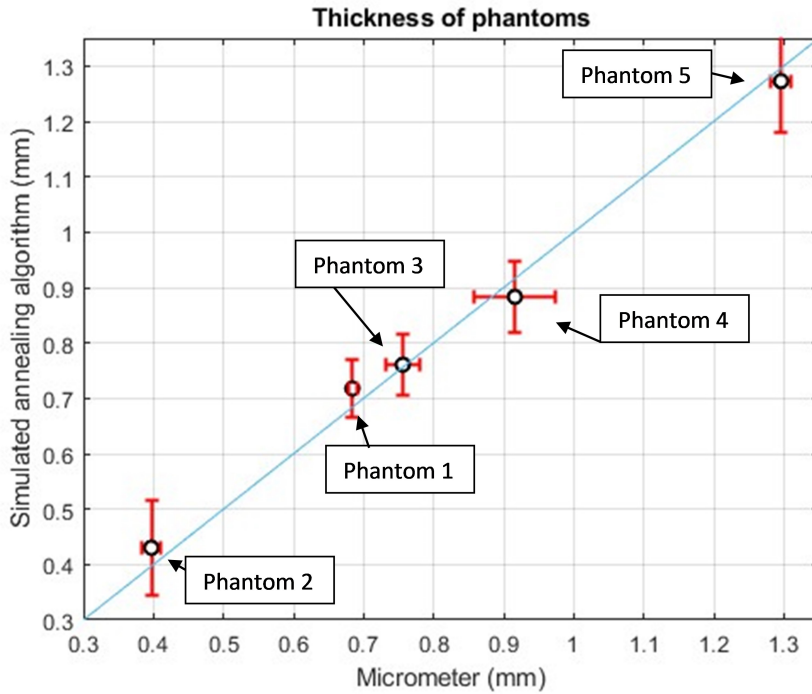


FIGURE 3.4: Thickness of the phantoms measured by two different methods, on y axis ultrasound spectroscopy is used and on the x axis a micrometer is used

If we compare the thinnest phantom, which is the second, with the thickest phantom, which is the fifth, we can appreciate significant differences. Figures 3.5 and 3.6 contain five measurements, each with a different color, to explore the variability in terms of the properties of the phantom. The time-domain signal for both phantoms measured with the 1 MHz transducer seems to overlap, especially in phantom 2. In Phantom 5, there are signs that two signals are overlapping, but it is still hard to tell which signal is which and figure out how thick the wall that originates the two echoes is. Instead, the frequency domain of the same signals reveals the interference pattern calculated in Section 2.3 and is used as input to solve the inverse problem with the SA algorithm. The interference pattern seems noisy at the beginning and end of the frequency limits; this is because we are trying to explore outside the transducer's frequency band. For the SA calculations, these parts are removed. For the 5 MHz transducer, the wavelength is smaller, so it is more sensitive to small distances. This can be appreciated in both examples: in Phantom 2, in the time domain, there are clear signs that two signals are involved, and in Phantom 5, both echoes are completely separated, and wall thickness can be calculated as usual in echography, which consists of calculating the time of flight between both echoes using the cross-correlation technique, for example. Other properties can be extracted, for example, by analyzing the relation between the peak-peak amplitudes of both echoes, the peak-peak amplitude of the first echo depending on the depth distance (time  $\mu\text{s}$ ), etc., but this is not the interest of this study. The frequency domain with the 5 MHz transducer in Phantom 2 shows four very similar measurements, and the blue one has the same pattern, but the peaks pointing down are sharper than the other. The fact that one measurement differs a little from the rest is reflected in the error bar in figure 3.4. Phantom 5, instead,

shows very similar measurements up to 5 MHz. Then, the coefficient of reflection of one measurement (yellow) keeps the same pattern, with the difference being that the dB drop grows more than the others.

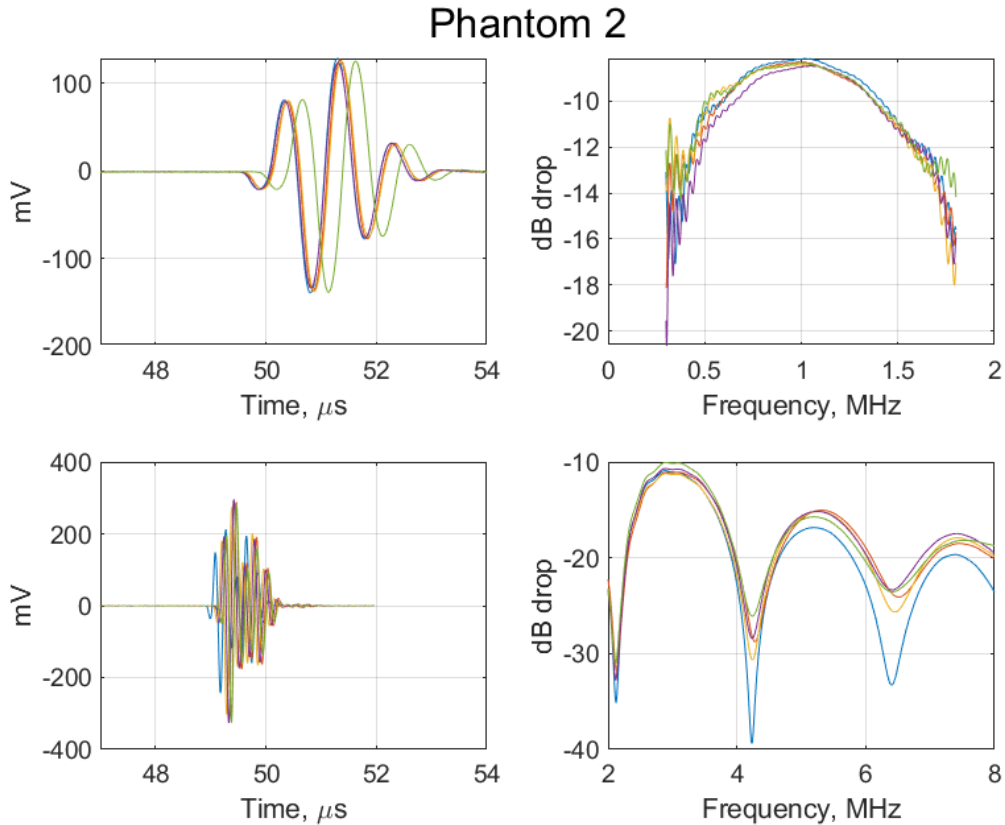


FIGURE 3.5: On the top left, echoes in time domain with the 1 MHz Transducer.  
 On the top right, coefficient modulus of reflection  
 On the bottom left, echoes in time domain with the 5 MHz Transducer.  
 On the bottom right, coefficient modulus of reflection

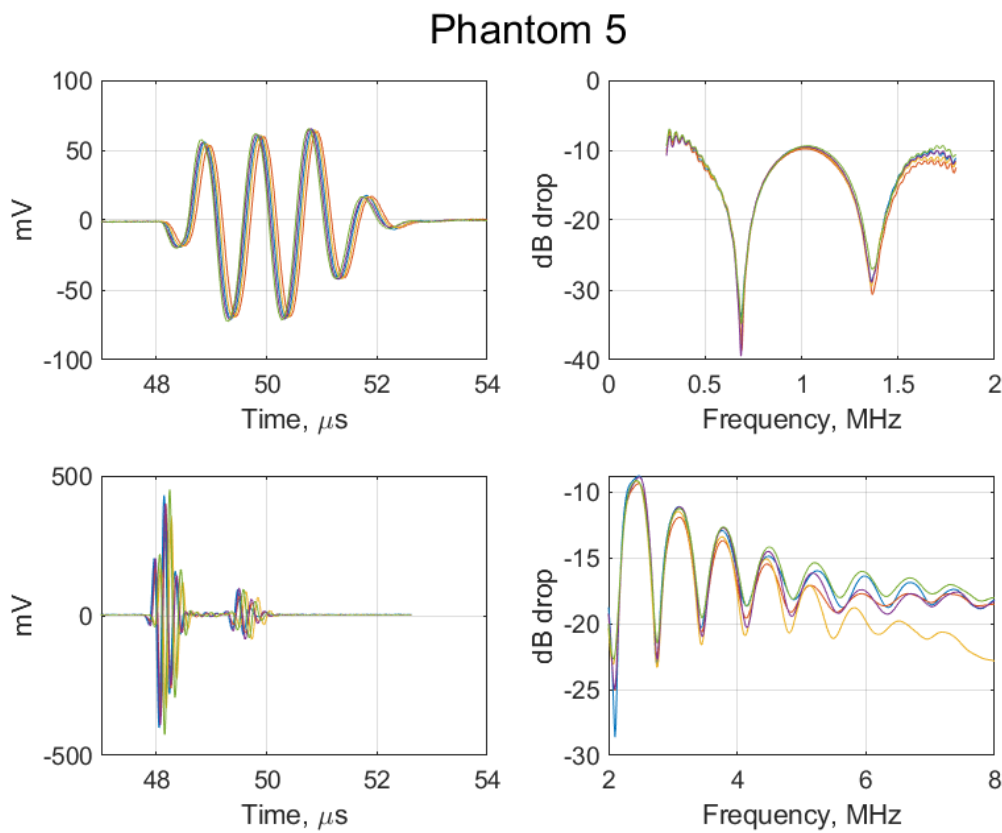


FIGURE 3.6: On the top left, echoes in time domain with the 1 MHz Transducer.

On the top right, coefficient modulus of reflection

On the bottom left, echoes in time domain with the 5 MHz Transducer.

On the bottom right, coefficient modulus of reflection

# Chapter 4

# Publications

## 4.1 Journals SCI

### 4.1.1 Paper 1, IEEE Transactions on Ultrasonics, Ferroelectrics, and Frequency Control, 2021.

The paper can be found at page [38](#) and the full reference is:

J. Q. Aguilar, M. Muñoz and T. G. Álvarez-Arenas, "Interpretation of the Thickness Resonances in Ferroelectret Films Based on a Layered Sandwich Mesostructure and a Cellular Microstructure," in IEEE Transactions on Ultrasonics, Ferroelectrics, and Frequency Control, vol. 68, no. 4, pp. 1245-1252, April 2021, doi: [10.1109/TUFFC.2020.3025358](https://doi.org/10.1109/TUFFC.2020.3025358).

### 4.1.2 Paper 2, Applied Sciences, 2021

The paper can be found at page [46](#) and the full reference is:

Quirce, Julio & Svilainis, Linas & Camacho, Jorge & Gómez Álvarez-Arenas, T.E.. (2020). Ferroelectret Ultrasonic Transducers for Pulse-Echo Water Immersion. Applied Sciences. [10.3390/app10248771](https://doi.org/10.3390/app10248771).

### 4.1.3 Paper 3, Polymers (Basel), 2021.

The paper can be found at page [60](#) and the full reference is:

Aguilar, Julio & Gómez Álvarez-Arenas, T.E.. (2021). Modification of Mechanical and Electromechanical Resonances of Cellular Ferroelectret Films Depending on the External Load. Polymers. [13. 3239](https://doi.org/10.3390/polym13193239). [10.3390/polym13193239](https://doi.org/10.3390/polym13193239).

### 4.1.4 Paper 4, IEEE Transactions on Ultrasonics, Ferroelectrics, and Frequency Control, 2022.

The paper can be found at page [79](#) and it is submitted, but not published yet.

# Interpretation of the thickness resonances in ferroelectret films based on a layered sandwich mesostructure and a cellular microstructure.

J. Quirce, M. Muñoz, T.E.G Álvarez-Arenas, *Member, IEEE*

**Abstract**—Transmission coefficient spectra of two ferroelectret films (showing several thickness resonances) measured with air-coupled ultrasound (0.2–3.5MHz) are presented and an explanation for the observed behavior is provided by proposing a film layered sandwich mesostructure (skin/core/skin) and by solving the inverse problem, using a simulated annealing algorithm. This permits to extract the value of the ultrasonic parameters of the different layers in the film as well as overall film parameters. It is shown that skin layers are thinner, denser and softer than core layers and also present lower acoustic impedance. Similarly, it is also obtained that the denser film also presents lower overall acoustic impedance. Scanning Electron Microscopy was employed to analyze the films cross-section, revealing that both denser films and film layers present more flattened cells and that close to the surface cells tends to be more flattened (supporting the proposed sandwich model). The fact that more flattened cells contributes to a lower elastic modulus and acoustic impedance can be explained, as it has been made previously by several authors, by the fact that the macroscopic film elastic response is furnished by cell micromechanics which is governed, mainly, by cell wall bending. Consistency of extracted parameters with trends shown by a simple model based on a honeycomb microstructure is discussed as well as the possibilities that this sandwich mesostructure and the associated impedance gradient could offer to improve the performance of FE films in ultrasonic transducers.

**Index Terms**— Ultrasonic transducers, ferroelectret film, cellular solids, thickness resonances, sandwich structure, inverse problem, mechanical properties.

## I. INTRODUCTION

FERROELECTRETS (FE) are permanently space charged cellular polymers that present piezoelectric response [1], [2]. Key to this behavior is the large porosity in the form of large and flattened pores in the film plane. These pores make possible both to entrap the electrical charge that build up macroscopic electric dipoles and to achieve an extremely low elastic modulus in the thickness direction that ease the film deformability in that direction. Both features give rise to the well-known piezoelectric response of these films. Hence, one

Submitted 10/06/2020. This work was supported in part by Financial support from Ministerio de Economía y Competitividad under grant DPI2016-78876-R, AEI/FEDER, UE.

Authors are with the Institute for Physical and Information Technologies, of the Spanish National Research Council, 28006 Madrid, Spain. ([j.quirce.aguilar@csic.es](mailto:j.quirce.aguilar@csic.es), [manuel.munoz@csic.es](mailto:manuel.munoz@csic.es), [t.gomez@csic.es](mailto:t.gomez@csic.es))

of the key issues in the optimization of the film electromechanical conversion capability is to strike the correct balance between cell and cell-wall shape and dimensions [3]–[10]. The other key feature is the efficient polarization of these films [11]–[13]. Another interesting feature is that they present a viscoelastic / poroelastic response [14], [15].

FE films are normally manufactured using a continuous biaxial orientation process (by stretching the film in two perpendicular directions), adding small particulate (to create lens-like voids) and subjecting it to a swelling process using a high-pressure gas injection technology [3], [5], [7], [16]. The swelling process alters the pore shape in a way that is critical to improve the electromechanical conversion capability [3]–[10]. Polarization is achieved by barrier discharge in the pores [17]. Main materials to produce FE are polypropylene (PP), polyethylene terephthalate (PETP) [10], FEP, cellular cyclo olefine (COC), polyethylene-naphthalate (PEN) [18]; main reason to modify the solid material has been to improve charge stability. FE films have been used for pressure sensors, tactile sensors [19], air-coupled transducers [20]–[25], energy harvesting [26]–[28], etc.

Recently it has been shown the possibility to use FE films to produce water immersion transducers for the frequency range 0.1–3.0 MHz [29], [30]. The main advantages are that FE films: i) present a very short response and a very large frequency bandwidth, ii) are flexible and conformable (which could permit to fabricate complex shapes [21], [22]), iii) present a reduced thickness and require thin backings. The main drawback is the reduced sensitivity which is the result of the lack of resonant response and the poor impedance matching of FE films to water. Improving transducer response demands improving sensitivity while keeping the large frequency bandwidth. This requires a better knowledge of the film properties and response in the frequency range of interest (0.1–3.0 MHz), which is much larger compared with conventional air-coupled FE transducers that operate around the first thickness resonance of the FE film (normally: 0.2 – 0.7 MHz).

Reference [31] studied thickness resonances of some FE films and found some anomalies that were explained by assuming that: i) velocity decreases with the frequency and ii) this decrease follows a stepwise shape between the first and the second resonances. The first assumption is quite reasonable provided that a quite large attenuation coefficient

value and a strong increase with the frequency were observed [31]. Quite on the contrary, the second one is quite an anomalous feature that was not further explained. Nonetheless, obtained fitting of theoretically calculated values into the experimental data was quite good. More recently, [32] has shown that similar distortions are found in the thickness resonance spectra of plant leaves and that this distortion can be explained by the layered structure of the leaves. However, solving this inverse problem (IP) can be extremely challenging. Reference [32] presented a method to solve it for the case of bilayer structures, based on the use of a Simulated Annealing algorithm and on the measurement of the transmission coefficient over a frequency range that fulfills two conditions: i) more than one thickness resonances are observed and ii) thickness resonances are completely damped out in the high frequency limit.

The objective of this paper is to obtain this kind of measurements in FE films, apply a modification of the procedure shown in [32] to solve this IP, analyze the capability of a sandwich model to reproduce the measured response, evaluate the meaning of the obtained parameters for the different layers in the FE film, its consistency with data that can be obtained by alternative methods and discuss the potential practical benefit that can be obtained from a ferroelectret film with a sandwich-like layered structure. Towards this end, the actual film structure is studied by analyzing Scanning Electron Microscopy (SEM) images and a symmetric layered mesostructured (three layers in a sandwich configuration) is proposed. In addition, and as it has been made previously by different authors, a cellular microstructure is assumed to provide an explanation for the extracted film parameters and the variations observed in them when comparing different films and different layers.

## II. MATERIALS

Two different types of polypropylene FE films obtained from EMFI have been studied, commercial names: HS03 and HS06. Nominal thicknesses are 70 and 90  $\mu\text{m}$ , for HS03 and HS06, respectively, while densities are 530 and 320  $\text{kg/m}^3$  for HS03 and HS06, respectively.

## III. METHODS

### A. Scanning Electron Microscopy (SEM) images.

Strips of 20 x 5 mm were cut out of the available sheets, put in liquid nitrogen and broke into two pieces. A thin film of gold was sputtered over the fracture and then examined using a Scanning Electron Microscope (SEM). Image analysis, performed using ImageJ, consisted on determining film thickness and mean value and standard deviation of different cell features. Ten pictures and between 100 and 120 measurements for each parameter were obtained for each film.

### B. Ultrasonic Measurements

Pieces of 4 x 4 cm were cut for the measurements: three pieces for each type of film. The ultrasonic set-up is shown in Fig. 1. The ultrasonic transmission coefficient spectra, both

magnitude and phase, at normal incidence were measured using air-coupled ultrasound in the frequency range 0.2-3.2 MHz. Four pairs of high-sensitivity, wideband, air-coupled transducers with center frequency 0.25, 0.65, 1.25 and 2.5 MHz designed and fabricated by our group were used. Transducers are flat, non-focused, and have circular aperture, (diameter of 25, 20, 15 and 15 mm, respectively) [33], [34]. Transmitter transducer was driven by a semicycle of square wave generated by a Olympus 4077 pulser-receiver (PR), with amplitude 400 V and tuned to the transducers centre frequency. Receiver transducer is placed in opposition at a distance between 100 and 10 mm. Receiver transducer is connected to the reception stage of the 4077 PR and the received signal is then transferred to a digital scope (Tektronix 5054), where the signal is digitized and stored. Finally, it is sent to a PC where Fast Fourier Transform (FFT) is extracted. First, signal received without sample in between the transducers and with 0 dB gain in the receiver stage of the 4077PR is stored. This signal is used to generate the reference magnitude and phase spectra. Then, sample is put in between transducers at normal incidence. Gain in the receiver stage of the 4077PR is set to 20 dB. This procedure is repeated with each pair of transducers. Overlap of the spectra is first checked to validate the measurements. Then, all spectra were concatenated and resampled ( $\Delta f=14 \text{ kHz}$ ).



Fig. 1. Experimental set-up for ultrasonic measurements: pulser-receiver, oscilloscope and three pairs of transducers (0.25, 0.65 and 1.25 MHz, from left to right, the 2.5 MHz pair is identical to the 1.25 MHz pair and is not shown). Transducers are mounted on an U-shaped holder that keeps them in the right position, a PVC cover protects transducers and measuring volume and provide a slot for the introduction of the sample in the right place and position.

### C. Data Extraction from Ultrasonic Transmission Coefficient Spectra.

A 1D layered model for the FE films is assumed with a sandwich structure (1: skin / 2: core / 3: skin), where skin layers are considered identical. The transmission coefficient spectra (magnitude and phase) for this sandwich structure were calculated using the transfer matrix method [35]-[42]. Material parameters are extracted by the solution of the IP as the set of layer parameters that minimize the error ( $\Delta$ ) between measured and calculated spectra:

$$\Delta = (\Delta M^2 + \Delta \varphi^2)^{1/2} \quad (1)$$

where  $\Delta M$  and  $\Delta \varphi$  are:

$$\Delta M = \left( \frac{\sum_N ((M_{exp} - M_{cal}) / M_{exp})^2}{N} \right)^{1/2} \times 100 \quad (2.a)$$

$$\Delta \varphi = \left( \frac{\sum_N ((\varphi_{exp} - \varphi_{cal}) / \varphi_{exp})^2}{N} \right)^{1/2} \times 100 \quad (2.b)$$

where  $M_{exp}$  and  $\varphi_{exp}$  are measured magnitude and phase spectra and  $M_{cal}$  and  $\varphi_{cal}$  are calculated magnitude and phase spectra. As explained in [32], parameters extracted for each layer are:

-  $f_{res} = v/t$ , where  $v$  is the ultrasound velocity and  $t$  the layer thickness. For isolated layers under symmetric boundary conditions, thickness resonances appear at  $(f_{res}/2) \times m$ , where  $m = 1, 2, 3, \dots$ . For isolated layers under asymmetric boundary conditions, thickness resonances appear at:  $(f_{res}/4) \times (2m - 1)$ , where  $m = 1, 2, 3, \dots$

- Acoustic impedance:  $Z$

- Attenuation coefficient  $\times$  thickness:  $\alpha \times t$

- Variation of attenuation with frequency:  $n$

Towards this end a power law is assumed [42]:

$$\alpha = \alpha_0 \left( \frac{f}{f_0} \right)^n \quad (3)$$

That is, four parameters are obtained for each layer. As we have three layers, but two of them are identical, the dimension of the space of search is eight. In addition, from these parameters the surface density ( $\rho_{surf}$ ) can also be obtained:

$$\rho_{surf} = Z / f_{res} \quad (4)$$

Moreover, the high frequency limit of the phase spectra can be used to determine the time of flight and the total thickness  $t^{Total}$  [32]. Hence, we can also work out effective velocity ( $v^{eff}$ ) and the volumetric density ( $\rho$ ) of the whole film:

$$v^{eff} = t^{Total} / \sum_{m=1}^3 (1/f_{res, m}) \quad (5)$$

$$\rho = \sum_{m=1}^3 \rho_{surf, m} / t^{Total} \quad (6)$$

where  $m$  denotes the layers in the sandwich. As  $t^{Total}$  and  $\rho$  can be determined from independent methods, estimations of these values (with  $\pm 10\%$  tolerance) are used to impose constraints to the search algorithm, through an adaptive penalization to the fitting quality or error ( $\Delta$ ), borrowed from evolutionary algorithms [44]. The search algorithm employed is the same as in [32]: modified constrained Simulated Annealing (SA) algorithm [44], [45]. The algorithm is run twenty times for each measured spectra with the purpose of determining: i) the existence of multiple solutions, ii) the variability/accuracy of the extracted parameters [32].

## IV. RESULTS

### A. SEM analysis.

Fig. 2 shows Scanning Electron Microscopy (SEM) pictures of the films cross-section. SEM images also revealed that film surfaces are non-porous. Results of the image analysis are shown in table I.

TABLE I.

PARAMETERS OF THE FILMS OBTAINED FROM SEM IMAGES. MEAN VALUE AND STANDARD DEVIATION.

Quantity	HS03	HS06
Film thickness (μm)	$70.4 \pm 1.8$	$77.0 \pm 2.6$
Outer layer thickness (μm)	$3.51 \pm 0.8$	$2.22 \pm 1.2$
Cell wall thickness: $t$ (μm)	$2.01 \pm 0.8$	$1.96 \pm 0.9$
Cell aperture: $w$ (μm)	$3.62 \pm 2.1$	$5.74 \pm 2.4$
Cell length: $D$ (μm)	$30.1 \pm 16.0$	$36.2 \pm 20.1$
Vertex angle: $\varphi$ (°)	$14.2 \pm 6.0$	$33.0 \pm 12.0$

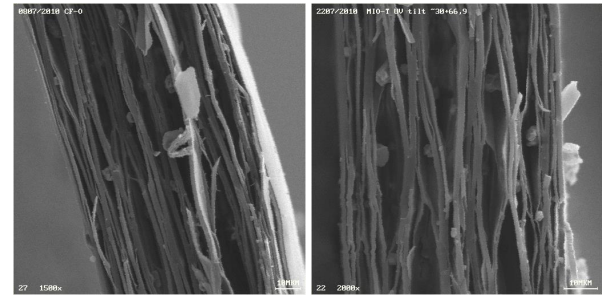


Fig. 2. Cross-section SEM images of the PP FE films studied. Left: HS03, right: HS06, showing cellular microstructure of the films composed of PP layers with lens-shaped cells. More flattened cells are observed in HS03, and cells tend to be more flattened in the section close to the film surface.

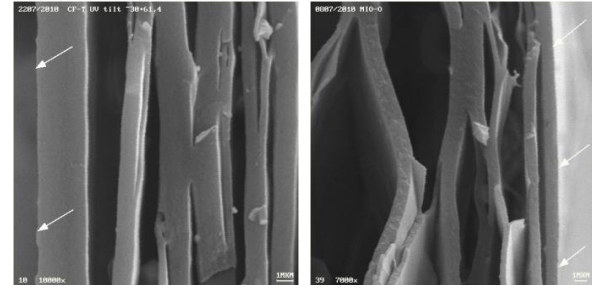


Fig. 3. Detail of the cross-section area close to the film surface (15 μm depth). White arrows indicate the film surface. Left: HS03; Right: HS06. Figures show the more flattened cell shape in the section close to the film surface.

Cell wall thickness is similar for both films and is slightly smaller than the thickness of the outer film layer. Cell length distribution is quite wide with comparable mean values in HS03 and HS06. In spite of the large variability, cell aperture and vertex angle are clearly larger in HS06. Fig. 2 also reveals that cells close to the surface tend to be more flattened. Fig. 3 shows some details of the section of the film close to the surface. Most likely, these features are specific of these films and the way they were fabricated and cannot be considered features to be found in all kinds of FE films. However, the fact that they are present here permits us to study if this subtle variation does have any measurable impact on the macroscopic response. If so, it could be possible to consider

the optimization of the macroscopic response of these films by the proper modification of their layered mesostructure.

### B. Ultrasonic Measurements

Figs. 4 and 5 show magnitude and phase spectra in HS03 and HS06 films, respectively. Dots represent measurements and solid line is the calculated spectra using the layers parameters extracted from the solution of the IP and assuming a symmetrical sandwich structure. As required by the method, two orders of the thickness resonances are observed, and the thickness resonances are completely damped out in the high frequency range ( $>1.8$  MHz and  $>2.8$  MHz for HS03 and HS06, respectively).

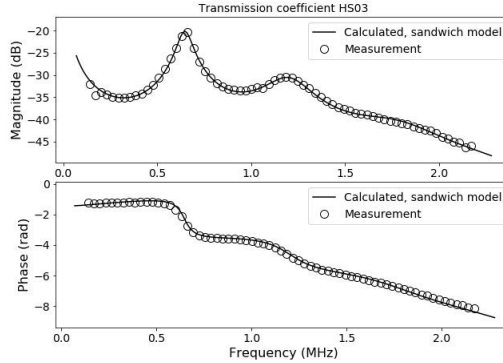


Fig. 4. Magnitude (up) and phase (down) spectra of the ultrasonic transmission coefficient at normal incidence for HS03 film in air. Dots: measurements. Solid line: calculated values using the sandwich model and the layer parameters obtained from the solution of the IP.

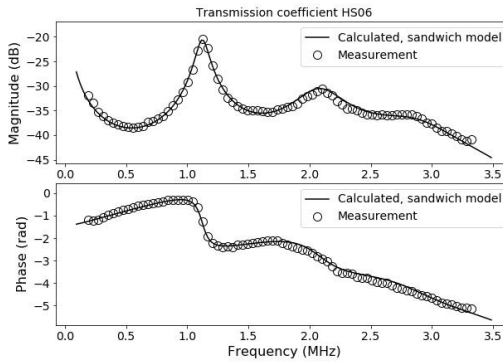


Fig. 5. Magnitude (up) and phase (down) spectra of the ultrasonic transmission coefficient at normal incidence for HS06 film in air. Dots: measurements. Solid line: calculated values using the sandwich model and the layer parameters obtained from the solution of the IP.

Table II lists some parameters that are obtained directly from the measured spectra. Multiple runs of the SA algorithm to solve the IP produced different results for HS03 and HS06. For HS03 two distinct solutions were found. However, error (1) of one of these solutions is clearly smaller ( $\Delta \sim 0.17$  and 0.6). Therefore, the solution with the best error was taken and the other disregarded as a local minimum. On the contrary, no multiple solutions were found for HS06, and all extracted

values gather around one single point in the space of search. In this case:  $\Delta \sim 0.4$ . Tables III and IV show the layer parameters extracted for one of the samples of the HS03 and HS06 films, respectively: mean values and standard deviation corresponding to run the SA algorithm 20 times for each measurement. Table V summarizes the overall film properties.

TABLE II.

EXPERIMENTAL VALUES OF RESONANCE ( $f_{res}^n$ ) AND ANTI-RESONANCE ( $f_{a-res}^n$ ) FREQUENCIES AND THE VALUE OF THE MAGNITUDE SPECTRUM FOR HS03 AND HS06 FILMS, OBTAINED FROM FIGS. 2 AND 3.

Order of resonance (n)	1	2	3
<b>HS03</b>			
$f_{res}^n$ (MHz)	0.638	1.190	--
Amplitude at $f_{res}^n$ (dB)	-20.1	-30.3	--
$f_{a-res}^n$ (MHz)	0.323	0.944	--
Amplitude at $f_{a-res}^n$ (dB)	-35.0	-33.7	
<b>HS06</b>			
$f_{res}^n$ (MHz)	1.120	2.096	$\sim 2.87$
Amplitude at $f_{res}^n$ (dB)	-20.9	-30.1	-36
$f_{a-res}^n$	0.550	1.610	2.48
Amplitude at $f_{a-res}^n$	-38.5	-35.5	-35.8

TABLE III.

MEAN VALUE AND STANDARD DEVIATION FOR THE LAYER PARAMETERS OF HS03. SA ALGORITHM IS RUN TEN TIMES

$f_{res}$ (MHz)	Z (MRayl)	$\alpha \times t$ (Np)	n	$\rho_{surf}$ (kg/m <sup>3</sup> )
<i>Skin layer</i>				
3.77 ± 0.14	0.044 ± 0.0003	(2.07 ± 0.03) $\times 10^{-2}$	2.0 ± 0.01	(1.16 ± 0.04) $\times 10^{-2}$
<i>Core layer</i>				
3.77 ± 0.30	0.050 ± 0.0004	(2.33 ± 0.18) $\times 10^{-2}$	2.1 ± 0.04	(1.35 ± 0.1) $\times 10^{-2}$

TABLE IV.

MEAN VALUE AND STANDARD DEVIATION FOR THE LAYER PARAMETERS OF HS06 PROBLEM. SA ALGORITHM IS RUN TEN TIMES.

$f_{res}$ (MHz)	Z (MRayl)	$\alpha \times t$ (Np)	n	$\rho_{surf}$ (kg/m <sup>3</sup> )
<i>Skin layer</i>				
10.8 ± 0.86	0.049 ± 0.004	(1.99 ± 1.8) $\times 10^{-3}$	2.0 ± 0.01	(4.63 ± 0.7) $\times 10^{-3}$
<i>Core layer</i>				
3.25 ± 0.21	0.075 ± 0.0014	(5.29 ± 1.9) $\times 10^{-3}$	2.8 ± 0.2	(2.31 ± 0.11) $\times 10^{-2}$

TABLE V.

OVERALL FILM PROPERTIES EXTRACTED FROM THE MEASURED SPECTRA AND (5) AND (6). MEAN VALUE AND STANDARD DEVIATION

Quantity	Film	
	<b>HS03</b>	<b>HS06</b>
Total thickness (μm)	69.3 ± 0.7	87.4 ± 0.8
Effective density (kg/m <sup>3</sup> )	530.0 ± 4.0	370.0 ± 7.8
Effective ultrasound velocity (m/s)	86.8 ± 0.7	177.0 ± 1
Effective elastic modulus (MPa)	3.98 ± 0.05	11.6 ± 0.25
Effective impedance (MRayl)	0.046 ± 0.0005	0.065 ± 0.0013

## V. DISCUSSION

SEM images in Fig. 2 show the inner cellular microstructure of the studied FE films and provide a clear representation of how the deformation in the film thickness direction is expected to take place: through the bending of the cell walls, mainly at the cell vertexes and at the curved section of the cell wall around the vertexes. In addition, the fact that cell aperture and vertex angle is not homogeneous along the film thickness can also be seen in Fig. 2. It is more likely to find less opened cells with very small vertex angle close to the film surface. This feature is surely the result of the fabrication route followed in these particular cases and cannot be considered a general property of all FE films; however it is interesting to study how this subtle modification may affect the macroscopy film response. The zoomed images in the section adjacent to the film surface (see Fig. 3) reveal cells with very reduced apertures and vertex angles (HS03: down to 0.5  $\mu\text{m}$  and 5°; HS06: down to 1  $\mu\text{m}$  and 9°, respectively), that rather than cells look more like slits or cracks. How deep does this feature penetrate into the film thickness is not easy to determine and can be expected to be variable, but it can be estimated to expand over a length of about 5-15  $\mu\text{m}$ . Given the fabrication procedure, this kind of anisotropy is not fully unexpected as this can be the result of the presence of a rather stiff boundary condition (non-porous surface layer) that restricts the deformability of adjacent cells during the process of stretching and inflating.

Thickness resonances (Figs. 4 and 5) appear in the transmission coefficient as a local maximum in the magnitude spectrum and as a step in the phase spectrum. The higher the frequency, the more reduced these effects are. This is due to the increase in the ultrasonic attenuation with the frequency. Phase spectra present negative values that correspond to the fact that ultrasound velocity in the film is lower than the ultrasound velocity in the air (~345 m/s). For high frequencies, phase spectra can be approximated to a straight line. This indicates that variation of velocity with the frequency is negligible, at least in this frequency range (>1.5 MHz for HS03 and >2.5 MHz for HS06).

Frequency location of the observed first two orders of the thickness resonances (Table II) does not follow the pure geometrical condition observed in homogeneous layers under symmetrical boundary conditions:

$$f_{res}^{(n)} = \frac{v}{2t} n, \quad n = 1, 2, 3, \dots \quad (7)$$

This deviation away from the expected response of a homogeneous film is small but clearly measurable. This was accounted for in a previous work [31], by assuming a variation in the velocity with the frequency. However, the high frequency phase spectrum measurement reveals that velocity does not change with the frequency. In addition, as  $f_{a-res}^{(1)} = \frac{1}{2} f_{res}^{(1)}$ , holds for both kinds of films (see Table II), velocity must be constant, also between  $f_{a-res}^{(1)}$  and  $f_{res}^{(1)}$ .

The sandwich model here proposed provides an excellent

fitting between calculated and measured spectra, even better than the one obtained before [31]. Two conclusions can be drawn: i) the sandwich model is able to reproduce very well the observed behavior and ii) the SA algorithm is able to solve this IP. Moreover, the multiple runs of the SA algorithm reveal that: i) no multiple solutions were found for HS06 and, although two solutions were found for HS03, it is possible to disregard one of them because it presents a significantly larger error; ii) the dispersion of the extracted material parameters is very low for all parameters (standard deviation below 10%). The main exception is  $\alpha \times t$  values for HS06, revealing a very low accuracy in this case; standard deviation of  $\rho_{surf}$  in the skin layer of HS06 is also slightly over the 10%.

Overall FE film thickness and density listed in table V are in good agreement with data obtained from conventional means, other authors and manufacturer data. Thickness data obtained from the ultrasonic technique also agrees with estimations obtained from SEM images (Table I and V), though HS06 thickness obtained from SEM images is smaller compared with both ultrasonic and micrometer measurements. In addition, effective ultrasonic velocity and elastic modulus also agree well with data published before. The very low value of the elastic modulus is the result of the porous structure and the fact that deformation of the film is expected to take place through bending of the pore walls. The lower elastic modulus of HS03 is then the result of the more flattened pore shape in HS03, that give rise to cells more deformable in the film thickness direction (Fig. 2). This can be explained by using different models that relate cell geometry and micromechanics with effective macroscopic elastic modulus. For example, the tetrakaidecahedron unit cell has been widely used for these purposes [46]. Later, [47], an elongated tetrakaidecahedron unit cell, more similar to the FE structure observed in Fig. 2, was proposed to study cellular solids. One of the simplest models is based on a hexagonal honeycomb structure [48]. This one and other similar structures have also been used to model FE films [8], [9], [49] and to study the relationship between fabrication route, film microstructure and macroscopic properties.

Fig. 6 shows the basic cell geometry for the elongated tetrakaidecahedron and for the hexagonal unit cells and an illustration of the cell deformation under uniaxial load. In spite of its radical simplicity, the hexagonal honeycomb model can be used to gain a basic understanding of the influence of the microstructure of the cellular solid in the macroscopic elastic response of the FE films. Equivalence between magnitudes in Table I and Fig. 6 are given by:  $\varphi = 180 - 2 \times \theta$ ,  $w = 2 \times l \times \cos \theta$ , and  $D = 2 \times l \times \sin \theta + h$ .

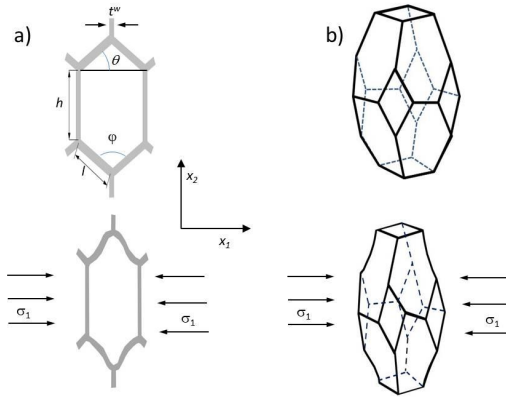


Fig. 6. Illustration of the unit cell and the deformation under uniaxial load of: a) hexagonal honeycomb cellular solid [39], b) tetrakaidecahedron-cellular solid [38].

Elastic modulus and density of the honeycomb are obtained from [48]:

$$\frac{E}{E_{solid}} = \left(\frac{t^w}{l}\right)^3 \frac{\cos\theta}{(h/l + \sin\theta)\sin^2\theta} \quad (8)$$

$$\frac{\rho}{\rho_{solid}} = \left(\frac{t^w}{l}\right) \frac{h/l+2}{2\cos\theta(h/l + \sin\theta)} \quad (9)$$

where  $E_{solid}$  is the Young modulus and  $\rho_{solid}$  the density of the cell wall material. It is clear that both the hexagon angle,  $\theta$ , and the ratio  $t^w/l$  play a significant role in the elastic modulus of the honeycomb. Hence, even this extremely simplified model can explain that denser films may also present a lower elastic modulus, due to the larger value of  $\theta$ . In general, this feature could appear counter-intuitive if the cellular microstructure is not taken into account.

As it is well known, this cellular microstructure of the FE films can also explain the differences observed in overall acoustic impedance of HS03 and HS06 films (table V). The larger density in HS03 (Table V) can be explained by this more flattened cell structure (Fig. 2), as this reduces the porosity. The lower impedance measured in HS03 is also explained in this way as the more flattened cell shape also significantly reduces the elastic modulus (Table V and (8)). The decrease in the elastic constant in the thickness direction with the increase of film density has already been reported in previous works (e.g. [5]-[9]) and explained in terms of the cellular microstructure. A similar effect was observed in [14].

As an example, Fig. 7 shows some calculations for  $E$  and  $\rho$  according to (8) and (9). Both the smaller density and the larger elastic modulus observed in HS06 can be explained by the fact that cells in HS06 are less flattened. This complex feature can be accounted for by the model in an extremely simple way: by assuming a smaller value of  $\theta$ .

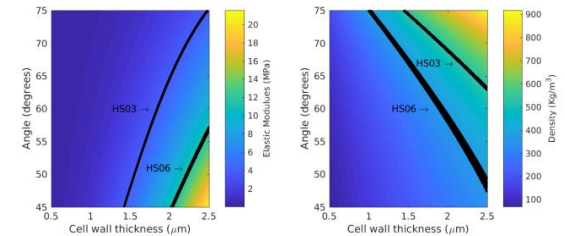


Fig. 7. Variation in the elastic modulus (left) and the thickness (right) of a polypropylene hexagonal honeycomb ( $L = 5.5\mu\text{m}$ ,  $h = 30\mu\text{m}$ ) with  $t$  and  $\phi$ . Assuming for the propylene:  $E = 1.33\text{ GPa}$  and  $\rho = 900\text{ kg/m}^3$ . The black lines represent obtained values for HS03 and HS06, line thickness correspond to the standard deviation (Table V).

Tables II and III reveal that a common feature in both types of films is that the acoustic impedance of the core layer is slightly larger. In parallel to what we considered before, we can now assume that this lower acoustic impedance in the skin layers is produced by a more flattened pore shape, which agrees with features revealed by SEM images (Figs. 2 and 3).

Unfortunately, and unlike the case of a one layer film [50], the ultrasonic method does not provide the thicknesses of each layer. Nonetheless, imposing some a priori conditions we can obtain an estimation of the possible range of variation. As a matter of fact we know that:

$$\rho_{PP} > \rho_{skin} > \rho_{core} \quad (10)$$

where  $\rho_{PP}$  is the density of the polypropylene. As  $\rho = \rho_{SUP}/t$ , then using the value of  $\rho_{SUP}$  from Tables II and III, and the limits in (10), we can obtain that the thickness of the skin layer must be within the range  $11\text{-}21\mu\text{m}$ , and  $5\text{-}12\mu\text{m}$ , for HS03 and HS06, respectively. These values are consistent with features revealed by SEM images. If we assume a mean value of  $15\mu\text{m}$  for the skin layer in HS03, then density and elastic modulus are:  $730\text{ kg/m}^3$  and  $9.9\text{ MPa}$ , for the skin layers, and  $344\text{ kg/m}^3$  and  $30.0\text{ MPa}$ , for the core layer, respectively. For HS06, if we assume a mean value of  $8\mu\text{m}$  for the skin layer, then density and elastic modulus of skin and core layers are:  $618\text{ kg/m}^3$ ;  $4.3\text{ MPa}$ , and  $317\text{ kg/m}^3$ ;  $18.0\text{ MPa}$ , respectively.

Finally, it is worth noting that none of the observed resonances correspond to resonances of the individual layers (Tables II, III and IV). Quite on the contrary, the explanation of the observed resonances is that they are produced by the whole cavity. We can make an approximate calculation of the frequency location of the first resonance of the whole cavity ( $f_{res}^{WC}$ ). This is given by:

$$f_{res}^{WC} = 1/(2 \sum_{n=1}^3 1/f_{res,n}) \quad (11)$$

where  $n$  denotes the layers in the sandwich: 1 and 3 for the skins and 2 for the core. Obtained  $f_{res}^{WC}$  from (11) is  $630\text{ kHz}$  and  $1.02\text{ MHz}$  for HS03 and HS06, respectively, very close to observed first order resonances (see Table II).

## VI. CONCLUSION

Inspired by the study of the thickness resonances in plant leaves [32], a layered sandwich mesostructure has been proposed to explain thickness resonances in FE films. This proposed mesostructure is consistent with the analysis of SEM images. It is shown that the IP can be solved using a SA algorithm and that this sandwich model provides an excellent representation of the measured spectra. The two studied films present skin layers thinner, denser and having lower acoustic impedance, compared with the core layers. These features can be explained by a cellular model assuming that cells in the skin layer are more elongated.

The fact that the observed subtle anisotropy in the film thickness direction induces a mesostructure that does have a measurable impact on the film macroscopic response can be of interest in the optimization of FE films for different applications. For example, provided that the flattened cells are more compressible, it could be of interest to prioritize the polarization of these cells. Alternatively, if for whatever reason, these parts of the film are more difficult to pole, then it would be convenient to minimize their presence. In addition, when considering the problem of matching the acoustic impedance of FE films to water or air, to take into account this sandwich structure and its impedance profile can also be beneficial. In particular, for skin layers that present lower acoustic impedance this can be exploited to improve the performance of air-coupled transducers by taking advantage of this extra capability to match impedances. Another possibility could be the increase of the frequency bandwidth by the convenient design of the thickness resonances of the different layers involved and their potential coupling. Finally, as in many cases FE films in transducers are operated in the non-linear regime [51], the areas of the film with more flattened cells may become more important as they are more likely to respond in a non-linear way. Future work will focus on the analysis of the electromechanical response of FE films to determine if it is possible to extract any information about the distribution of the  $d_{33}$  value across the film thickness and to study the possibility of improving FE transducers (air- and water- coupled) by engineering this layered structure.

## REFERENCES

- [1] A. Savolainen and K. Kijavainen, "Electrothermomechanical Film. Part I. Design and Characteristics", *J. Macromol. Sci. A*, Vol. 26, pp. 583-591, 1989,
- [2] G. M. Sessler and J. Hillenbrand, "Electromechanical response of cellular electret films," *Appl. Phys. Lett.*, vol. 75, no. 21, pp. 3405-3407, 1999.
- [3] M. Wegener, W. Wirges, J. Fohlmeister, B. Tiersch, and R. Gerhard-Multhaupt, "Two-step inflation of cellular polypropylene films: void-thickness increase and enhanced electromechanical properties," *J. Phys. D. Appl. Phys.*, vol. 37, no. 4, pp. 623-627, Feb. 2004.
- [4] A. Mohebbi, D. Rodriguez, "Energy absorption capacity of ferroelectrets based on porous polypropylene," *Polymer Engineering & Science*, vol. 58, no. 3, pp. 300-309, 2018.
- [5] P. Fang, W. Wirges, M. Wegener, L. Zirkel, and R. Gerhard, "Cellular polyethylene-naphthalate films for ferroelectret applications : foaming , inflation and stretching , assessment of electromechanically relevant structural features," *Polymer*, no. 043, pp. 1-9, 2008.
- [6] M. Sborikas and M. Wegener, "Cellular-foam polypropylene ferroelectrets with increased film thickness and reduced resonance frequency," *Appl. Phys. Lett.*, vol. 103, no. 25, p. 252901, 2013
- [7] M. Wegener, W. Wirges, R. Gerhard-Multhaupt, M. Dansachmüller, R. Schwödauer, S. Bauer-Gogonea, S. Bauer, M. Paajanen, H. Minkkinen, J. Raukola, "Controlled inflation of voids in cellular polymer ferroelectrets: Optimizing electromechanical transducer properties," *Appl. Phys. Lett.* vol. 84, pp. 392, 2004.
- [8] M. Wegener *et al.*, "Ferroelectrets: highly anisotropic electrically charged polymer foams for electromechanical transducer applications," *IEEE Ultrason. Symp. 2004*, vol. 62, no. c, pp. 1138-1141, 2004.
- [9] A. Mohebbi, F. Migri, A. Ajji, and D. Rodriguez, "Cellular Polymer Ferroelectret: A Review on Their Development and Their Piezoelectric Properties," *Adv. Polym. Technol.*, vol. 37, no. 2, pp. 468-483, 2018
- [10] M. Wegener, W. Wirges, and R. Gerhard-Multhaupt, "Piezoelectric Polyethylene Terephthalate (PETP) Foams Specifically Designed and Prepared Ferroelectret Films," *Adv. Eng. Mater.*, vol. 7, no. 12, pp. 1128-1131, 2005.
- [11] A. Mellinger, M. Wegener, W. Wirges, R. R. Mallepally, and R. Gerhard-Multhaupt, "Thermal and temporal stability of ferroelectret films made from cellular polypropylene/air composites," *Ferroelectrics*, vol. 331, pp. 189-199, 2006.
- [12] X. Zhang, J. Hillenbrand, and G. M. Sessler, "Thermally stable fluorocarbon ferroelectrets with high piezoelectric coefficient," *Appl. Phys. A*, vol. 84, no. 1-2, pp. 139-142, Apr. 2006.
- [13] E. Saarimäki *et al.*, "Novel heat durable electromechanical film: processing for electromechanical and electret applications," *IEEE Trans. Dielectr. Electr. Insul.*, vol. 13, no. 5, pp. 963-972, Oct. 2006.
- [14] M. Gaal, V. Bovtun, W. Stark, A. Erhard, Y. Yakymenko, and M. Kreutzbrück, "Viscoelastic properties of cellular polypropylene ferroelectrets," *J. Appl. Phys.*, vol. 119, no. 12, 2016.
- [15] T. E. G. Alvarez-Arenas, "Pressure sensitivity response of polymeric ferroelectret foam films," *2014 Int. IEEE Int. Symp. Appl. Ferroelectr. Int. Work. Acoust. Transduct. Mater. Devices*, pp. 8-11, 2014.
- [16] S. R. Anton, K. M. Farinholt, and A. Erturk, "Piezoelectret foam-based vibration energy harvesting," *J. Intell. Mater. Syst. Struct.*, vol. 25, no. 14, pp. 1681-1692, 2014.
- [17] X. Qiu, A. Mellinger, M. Wegener, W. Wirges, and R. Gerhard, "Barrier discharges in cellular polypropylene ferroelectrets: How do they influence the electromechanical properties?", *J. Appl. Phys.*, vol. 101, no. 10, pp. 104112, 2007.
- [18] P. Fang, M. Wegener, W. Wirges, R. Gerhard, L. Zirkel, "Cellular polyethylene-naphthalate ferroelectrets: Foaming in supercritical carbon dioxide, structural and electrical preparation, and resulting piezoelectricity," *Appl. Phys. Lett.*, vol. 90, no. 19, pp. 192908, 2007.
- [19] A. Kogler, R. Schwödauer, G. Buchberger, S. Bauer-Gogonea, S. Bauer, "Heteropolar Charging of Ferroelectrets for Flexible Keyboards and Tactile Sensors," *Ferroelectrics*, vol. 472, no. 1, pp. 90-99, 2014.
- [20] J. Döring, J. Bartusch, U. Beck, and A. Erhard, "EMFIT Ferroelectret Film Transducers for Non-Contact Ultrasonic Testing," in *ECNDT 2006*, pp. 1-10, 2006.
- [21] J. L. Ealo, F. Seco, and A. R. Jimenez, "Broadband EMFi-based transducers for ultrasonic air applications," *IEEE Trans. Ultrason. Ferroelectr. Freq. Control*, vol. 55, no. 4, pp. 919-929, 2008.
- [22] J. L. Ealo *et al.*, "Customizable field airborne ultrasonic transducers based on electromechanical film," *2008 IEEE Ultrason. Symp.*, pp. 879-882, Nov. 2008.
- [23] M. Gaal *et al.*, "Air-Coupled ferroelectret ultrasonic transducers applied to testing of fiber-reinforced polymers." in *12th International Conference of the Slovenian Society for Non-Destructive Testing*, 2013, pp. 43-49, 2013.
- [24] M. Gaal, J. Bartusch, E. Dohse, F. Schadow, and E. Köppé, "Focusing of ferroelectret air-coupled ultrasound transducers," *AIP Conf. Proc.* 1706, vol. 080001, p. 080001, 2016.
- [25] T. E. G. Alvarez-Arenas, "Air-coupled piezoelectric transducers with active polypropylene foam matching layers," *Sensors (Switzerland)*, vol. 13, no. 5, pp. 5996-6013, 2013.
- [26] S. R. Anton and K. M. Farinholt, "An evaluation on low-level vibration energy harvesting using piezoelectret foam," in *Proceedings of SPIE 2012 Smart Structures and Materials, Nondestructive Evaluation & Health Monitoring Conference, San Diego, CA, March 11-15*, vol. 836, 2012.
- [27] X. Mo, H. Zhou, W. Li, Z. Xu, J. Duan, L. Huang, B. Hu, and J. Zhou, "Piezoelectrets for wearable energy harvesters and sensors". *Nano Energy*, vol. 65, pp. 104033, 2019.

- [28] C. A Ray, S. R Anton, "Multilayer piezoelectret foam stack for vibration energy harvesting". *Journal of Intelligent Material Systems and Structures*, vol 28, no. 3, pp. 408-420, 2017.
- [29] T. E. G. Alvarez-Arenas and L. Diez, "Ferroelectret transducers for water immersion and medical imaging," *IEEE Int. Ultrason. Symp. IUS*, vol. 2016-Novem., pp. 4-7, 2016.
- [30] J. Q. Aguilar and T. E. G. Álvarez-Arenas, "Optimization of Ferroelectret Transducers for Pulse-Echo Water Immersion Operation," *IEEE Int. Ultrason. Symp. IUS*, vol. 2019-Octob, pp. 2604-2607, 2019.
- [31] T. E. G. Álvarez-Arenas, H. Calás, J. E. Cuello, a. R. Fernández, and M. Muñoz, "Noncontact ultrasonic spectroscopy applied to the study of polypropylene ferroelectrets," *J. Appl. Phys.*, vol. 108, no. 7, pp. 074110, 2010.
- [32] T. E. G. Álvarez-Arenas, D. Sancho-Knapik, J. J. Peguero-Pina, A. Gómez-Arroyo, and E. Gil-Pelegrín, "Non-contact ultrasonic resonant spectroscopy resolves the elastic properties of layered plant tissues," *Appl. Phys. Lett.*, vol. 113, no. 25, pp. 253704, 2018.
- [33] T. E. G. Álvarez-Arenas, "Acoustic Impedance Matching of Piezoelectric Transducers to the air," *IEEE Trans. Ultrason. Ferroelectr. Freq. Control*, vol. 51, no. 5, pp. 624-633, 2004.
- [34] T. E. G. Álvarez-Arenas, T. R. Shrout, S. J. Zhang, and H. J. Lee, "Air-Coupled Transducers Based on 1-3 Connectivity," in *IEEE International Ultrasonics Symposium*, 2012, pp. 2230-2233.
- [35] L. Knopoff, "A matrix method for elastic wave problems," *Bull.Seism. Soc. Am.* Vol. 54, pp. 431-438, 1964.
- [36] W. T. Thomson, "Transmission of elastic waves through a stratified solid medium," *J. Appl. Phys.*, vol. 21, pp. 89-93, 1950.
- [37] L. Brekhovskikh, Waves in layered media, Academic Press, 1960.
- [38] A.H. Fahmy, E.L. Adler, "Propagation of acoustic waves in multilayers: a matrix description," *Appl. Phys. Lett.*, vol. 20 pp. 495-497, 1973.
- [39] F. Fantosa and W. W. Symes, "The determination of a layered acoustic medium via multiple impedance profile inversions from plane wave responses," *Geophys. J. R. astr. Sov.*, vol. 81, no. 175-195, pp. 530-533, 1985.
- [40] A.H. Nayfeh, D.E. Chimenti, "Ultrasonic wave reflection from liquid-coupled orthotropic plates with application to fibrous composites," *J. Appl. Mech.*, vol 55, pp. 863-870, 1988.
- [41] J. Lekner, "Matrix methods in reflection and transmission of compressional waves by stratified media," *J. Acoust. Soc. Am.*, vol. 87, no. 6, p. 2319, 1990.
- [42] M. J. Lowe, "Matrix Techniques for Modeling Ultrasonic Waves in Multilayered Media," *IEEE Trans Ultrason Ferroelectr Freq Control*, vol. 42, no. 4, pp. 525-542, 1995.
- [43] T. T. L. Szabo and J. Wu, "A model for longitudinal and shear wave propagation in viscoelastic media," *J. Acoust. Soc. Am.*, vol. 107, no. 5, pp. 2437-2446, 2000.
- [44] J. Dréo, P. Siarry, A. Pétrowski, and E. Taillard, *Metaheuristics for hard optimization*. Methods and case studies. Springer, 2006, pp. 23-45 and pp. 217-220..
- [45] K.-L. Du and M. N. S. Swamy, *Search and Optimization by Metaheuristics. Techniques and algorithms inspired by nature*. Birkhäuser Basel, 2016, pp. 29-35.
- [46] A. N. Gent and A. G. Thomas, "The deformation of foamed elastic materials," *J. Appl. Pol. Sci.*, vol. 1, no. 1, pp 107-113, 1059.
- [47] R. M. Sullivan, L. J. Ghosn, and B. A. Lerch, "Application of an elongated kelvin model to space shuttle foams," *J. Spacecr. Rockets*, vol. 46, no. 2, pp. 411-418, 2009.
- [48] L. J. Gibson and M. F. Ashby, *Cellular Solids*, Cambridge Univ. Press (1997).
- [49] E. Tuncer, "Numerical calculations of effective elastic properties of two cellular structures," *J. Phys. D. Appl. Phys.*, vol. 38, no. 3, pp. 497-503, 2005.
- [50] T. E. G. Álvarez-Arenas, "Simultaneous determination of the ultrasound velocity and the thickness of solid plates from the analysis of thickness resonances using air-coupled ultrasound," *Ultrasonics*, vol. 50, no. 2, pp. 104-109, Feb. 2010.
- [51] V. Bovtun, J. Döring, J. Bartusch, M. Gaal, A. Erhard, M. Kreutzbrück, and Y. Yakimenko, "Enhanced electromechanical response of ferroelectret ultrasonic transducers under high voltage excitation," *Adv. Appl. Ceram.*, vol. 112, no. 2, pp. 97-102, 2013.



**Julio Quirce Aguilar** was born in Madrid, Spain. He received the B.S., M.S., degree in Physics and Nuclear Physics in 2015 and 2017 respectively from Autonoma de Madrid University. He is currently pursuing Ph.D dregree in ultrasonics transducers for medical and industrial application with the ITEFI, CSIC, Spain. His research interests focus on new materials, transducers design and fabrication.



**Manuel Muñoz** was born in Madrid in 1969. He received the PhD in Physics from the Universidad Autonoma de Madrid in 2002. He is tenured scientist at the Instituto de Tecnologías Fisicas y de la Información of the Spanish Research Council (CSIC). His research activities are focused on the design and characterization of micro and nanodevices for their applications in information technologies.



**Tomás Gómez Álvarez-Arenas**, is a Scientist in the Spanish National Research Council (CSIC). PhD in Physics from the Complutense University of Madrid. In 1996 joined as a postdoc the Center for Ultrasonic Engineering, Strathclyde University, Glasgow, Scotland. In 2000, joined the Institute of Acoustics of the CSIC, and then the Institute of Physical and Information Technologies, ITEFI-CSIC (2013). Since 2014 he is Head of the Sensors and Ultrasonic Technologies Department of ITEFI-CSIC. His research interest focuses on design, optimization and fabrication of piezoelectric transducers, the study of piezoelectric and ferroelectric materials, ultrasonic materials characterization, new materials for ultrasonic applications, solution of Inverse and Hard Optimization Problems and applications of ultrasonic techniques in NDT, medical diagnosis, food quality, industrial control, and agriculture sensing.



Article

# Ferroelectret Ultrasonic Transducers for Pulse-Echo Water Immersion

Julio Quirce <sup>1</sup>, Linas Svilainis <sup>2</sup> , Jorge Camacho <sup>1</sup> and Tomas Gomez Alvarez-Arenas <sup>1,\*</sup>

<sup>1</sup> Instituto de Tecnologías Físicas y de la Información, CSIC, 28006 Madrid, Spain;  
j.quirce.aguilar@csic.es (J.Q.); j.camacho@csic.es (J.C.)

<sup>2</sup> Department of Electronics Engineering, Kaunas University of Technology, LT-51368 Kaunas, Lithuania;  
linas.svilainis@ktu.lt

\* Correspondence: t.gomez@csic.es

Received: 10 November 2020; Accepted: 4 December 2020; Published: 8 December 2020



**Featured Application:** Ultrasonic transducers with a short impulse response and a wide frequency band response are desirable for ultrasonic imaging and quantitative echography where the spectral analysis of reflected pulses can reveal the inner structure of scatterers and different organs in medical imaging. Therefore, the featured application for the transducers here presented is for the resonant spectral echography technique that our group is introducing in applications for materials characterization and medical imaging for quantitative echography, with special focus on layered tissues, where this technique can reveal the presence of different layers and extract their properties; examples are the cornea, the artery wall, the skin, the pleura, etc.

**Abstract:** Ferroelectrets are thin and porous polymeric films with a cellular microstructure, high porosity, permanent polarization and piezoelectric response. They have been used for different applications, where one of the most interesting ones is for the fabrication of air-coupled ultrasonic transducers. More recently they have been tested as water immersion transducers, showing a promising wide bandwidth but limited sensitivity along with other technical problems. This paper investigates ultrasonic transducers for water immersion and pulse-echo operation based on ferroelectret films. Two different ferroelectret foams with different resonant frequencies, acoustic impedances and cellular structures were tried. Flat and spherically focused prototypes (radius of curvature of 22 and 35 mm) were produced and tested. Finally, different materials and methods were tried to provide a protective surface coating. Acoustic field measurements for the focused transducers confirm the possibility to efficiently focus the ultrasonic beam by the proposed fabrication method, with focal spot size of 1.86 mm at –6 dB. Results show that in spite of the reduced sensitivity (about –115 dB), some of the tried ferroelectret films provide a very wide band response (–6 dB band from 0.29 to 2.7 MHz) and short pulse duration (2–3 us) that can be of interest for different applications.

**Keywords:** ferroelectret films; ultrasonic transducers; pulse-echo transducers; water immersion transducers; ultrasonic medical imaging; ultrasonic NDT

## 1. Introduction

Ferroelectrets (FE) are polymeric foam films with elongated pores in the film plane that can be poled and present a piezoelectric response [1,2]. They have been widely researched and used. One of the most interesting uses of FE films is for air-coupled ultrasonic transducers, where flat and focused designs have been used in Nondestructive Tests NDT [3–5]. The very low impedance of this type of materials permits the construction of transducers without matching layers, though the response is

quite resonant and, hence, the bandwidth reduced, alternatively they have also been used as active matching layers [6].

Flat transducers were first tried for water immersion in [3,7] where they demonstrated a poor sensitivity but a very wide band response. Later, in [8], the use of matching layers was tried to increase both sensitivity and water resistance with limited success. In spite of the poor sensitivity, the large bandwidth together with other advantages, like the flexibility and the possibility to miniaturize the transducers, motivated further study of this application. In particular, the use of different FE materials, different protective coatings and focused designs to improve resolution.

In this work, we present the pulse-echo response in water immersion of transducers based on two different FE materials with the purpose of providing some insight into the path to improve FE material properties for water coupled ultrasonic transducers. Flat and spherically focused prototypes were fabricated and tested and the use of different thin polymeric coatings intended to protect the transducer surface without having any negative impact on either the sensitivity or the frequency bandwidth were tried. Transducer response in pulse-echo operation mode (both time domain and sensitivity in the frequency domain) was measured as well as the acoustic field distribution.

## 2. Materials and Methods: Transducers Design and Fabrication

The purpose of this work is to study the feasibility of using ultrasonic transducers based on FE films for pulse-echo water immersion. To this end, FE transducers were designed, fabricated and tested. Two different FE materials (HS03 and HS06) were used to make ultrasonic transducers that were then tested in pulse-echo mode in water immersion. For the FE material providing the best results, spherically focused transducers were then produced and tested. Finally, different techniques and materials were investigated with the purpose of providing further protection of the transducer radiating surface without affecting transducer performance.

### 2.1. Ferroelectret Materials

Two different polypropylene ferroelectret films were employed to produce and test water immersion transducers. Both materials were purchased from EMFI, their commercial names are: HS03 and HS06. The properties of these materials have been widely studied before (see, for example [9,10]). The main properties of the employed FE films are summarized in Table 1. These two materials permit determination of whether the resonant frequency of the film has any effect on the pulse-echo frequency band of the transducer when operated in water immersion and if the differences in the material impedance have any impact on the transducers' sensitivity. Furthermore, these two materials present a somewhat different microstructure; see [10], where pores in HS06 are more open giving rise to a lower material density and deformability in the thickness direction. It is of interest to determine what is the material microstructure that provides better water-coupled transducers is, as this information could be used to further engineer FE properties for this application.

**Table 1.** Properties of the ferroelectret FE films employed [10].

Material	Thickness ( $\mu\text{m}$ )	Density ( $\text{kg}/\text{m}^3$ )	$\lambda/2$ Resonant Frequency, Thickness Mode (MHz)	Impedance (MRayl)
HS03	70	530	0.638	0.046
HS06	90	370	1.120	0.065

### 2.2. Transducer Design and Fabrication Method

Flat and spherically focused transducers were tried. In all cases aperture was circular (15 mm diameter). Two different radii of curvature were tried for the spherically focused transducers: 22 and 35 mm. In all cases, the FE film is glued to a heavy backing block (brass) and provided with aluminum housing, ground connected for radio frequency RF shielding (see Figure 1).

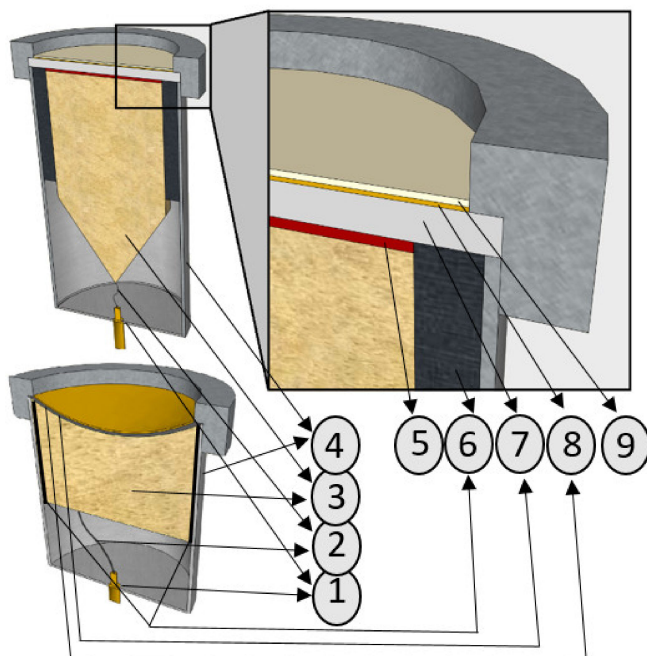


**Figure 1.** Transducer design for flat and spherically focused prototypes. 1: Connector, 2: wire, 3: backing block, 4: aluminum housing, 5: conductive tape, 6: insulating seal, 7: ferroelectret film, 8: Au coating, 9: Polymer coating.

The possibility of using matching layers for water-coupled FE transducers was studied in [8]. The purpose was to improve the transducer sensitivity and to provide a protection of the FE front surface and electrode. However, the main problem is that there are no available materials with the required properties to produce these matching layers. For the ferroelectret materials shown in Table 1, the required impedance for the matching layer is about 0.28 MRayl for one single matching layer and about 0.07 and 0.23 MRayl for a stack of two matching layers. Such low impedance materials can be found in porous materials like those presented in [11], however the open-cell nature of the pores of these materials makes it impossible to use them in water. Closed-cell porous materials were also tried as matching layers [12], but it is not easy to obtain close-cell porous materials with impedance below 0.3 MRayl; specially, considering that the pore size must be much smaller than the matching layer thickness. Finally, [8] revealed that the use of available materials produces a moderate improvement of the transducer sensitivity together with an unacceptable reduction in the transducers' frequency band. For this reason, the use of matching layers was discarded, however, methods to protect the transducer front surface and electrode that do not interfere with the frequency band nor reduce sensitivity have been considered in this work and are explained later.

Circles were cut out of the FE sheets, of diameter 15 mm, and glued to a brass backing block using double-sided electrically conductive tape. The front face of the FE circle is electrically connected to the cylindrical transducer housing (aluminum) that is connected to the ground electrode of the transducer. For the focused transducer, the backing block has a spherical shape. The FE film is pressed against the spherical surface, this permits the accommodation of the film to this curvature, though it also produces some wrinkles. The number and size of these wrinkles depend on the radius of the spherical backing block and the transducer aperture. The problem of adapting the flexible (but non-stretchable) ferroelectret film to non-developable surfaces has already been addressed in [13], where it was avoided by dividing the surface into small portions. When this is not possible some wrinkles may appear in the

film as is the case for spherically focused transducers. A similar effect has been observed previously in [14] for air-coupled spherically focused transducers.

The HS03 has one surface metalized with aluminum; this face is used as transducer external surface and the aluminum metallization can be used as ground electrode. The HS06 has no electroded surface. Therefore, in this case the outer surface is sputtered with gold. However, the stability of the aluminum electrode is very poor, and it can be easily removed with film manipulation or even when the transducer is operated in water. For this reason, in all cases a thin layer of gold was sputtered on the radiating surface, this electrode presents a much better resistance compared with the evaporated aluminum electrode. The Au-sputtering was performed using a Leica EM ACE200 coater with directional coating and coating time between 30 and 60 s.

Figure 2 shows a picture of some of the fabricated transducer prototypes. Wrinkles in the FE film can be seen in the focused designs, as well as the fact that there are more wrinkles and wrinkle size is larger in the transducer with the smaller radius.



**Figure 2.** Picture of transducer prototypes, from left to right: HS03 focused (radius of curvature: 22 mm), HS03 focused (radius of curvature: 35 mm), HS06 flat, HS03 flat.

### 2.3. Methods for Transducer Characterization

#### 2.3.1. Preliminary Transducer Verification: Pulse-Echo in Air

A first verification of the proper FE film behavior in the transducer was performed by measuring the transducer response in pulse-echo in air. As it is well known, the FE film glued to a backing block and operating in air is quite a resonant device and the resonant mode is the quarter wavelength thickness resonance of the FE film. Sensitivity (SNS) in pulse echo is measured as:

$$SNS = 20 \log \left( \frac{|FFT(s_{Rx})|}{|FFT(s_{Tx})|} \right) \quad (1)$$

where  $FFT$  denotes the Fast Fourier Transform,  $s_{Tx}$  is the signal applied to transducer terminals and  $s_{Rx}$  is the electrical signal generated in the transducer when the echo is received. In order to obtain these signals a temporal square gate is applied. In the first case the gate is located at  $t = 0$  s, while in the second case the gate is located at the time of arrival of the echo. We used an Olympus 4077 pulser-receiver PR in pulse-echo mode to drive the transducer with a half cycle square pulse, 400 V amplitude, 1.0 MHz center frequency, and to receive and amplify (40 dB) the received echo. Signals were digitized and stored using a Tektronix DPO oscilloscope.

The advantage of this way of verifying transducer fabrication is that it is simple and fast. Any lack of resonant response or a response more damped than expected or a significant deviation of the resonant frequency away from the expected value ( $\lambda/4$  thickness resonance) can easily be interpreted as defective design that can be attributed to a damaged FE film, or electrode, or to an imperfect binding

of the FE film to the backing block. Table 1 shows the value of the  $\lambda/2$  thickness resonance measured in [10] in free standing films, so the  $\lambda/4$  frequency is simply  $\frac{1}{2}$  of the  $\lambda/2$  resonant frequency shown in Table 1.

### 2.3.2. Transducer Characterization: Pulse-Echo Measurements in Water Immersion

The experimental set-up for pulse-echo measurements is shown in Figure 3; transducers and a flat steel block (53 mm thick) used as reflector were immersed in a water tank. The transducer is driven by the an Olympus 5058 pulser/receiver, the received echo is received through the receiver stage of the Olympus 5058 PR, filtered, amplified (40 dB) and then sent to an oscilloscope where the signal is digitized and stored. For the focused transducers, the reflector is located at the transducer focal distance, while for the flat transducer, the separation was 40 mm (which is close to the transition between near and far field).

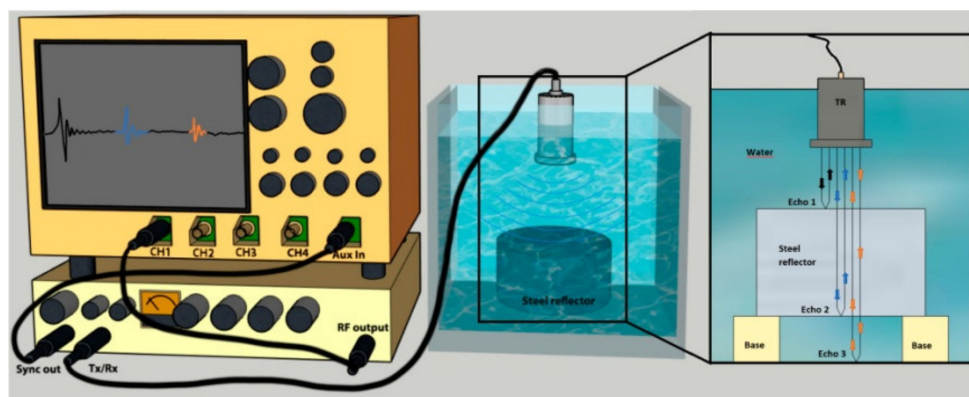


**Figure 3.** Experimental set-up for pulse-echo measurements.

### 2.3.3. Transducer Characterization: Acoustic Field Measurements in Water Immersion

An XYZ scanner DIS300 and a Difrascope pulse-echo ultrasound equipment were used, both from DASEL SL (Madrid, Spain). For each transducer, the acoustic field was measured over a rectangular grid, using a 1 mm diameter needle hydrophone (Precision Acoustics, Dorchester, Dorset, UK) connected to the reception stage of the pulse-receiver system. The excitation, acquisition and movement were synchronized by a rotary encoder in one of the scanner axes, with a resolution of 0.1 mm.

A single negative square pulse of  $-400$  V amplitude and 250 ns width was used for excitation, and a band-pass filter between 30 kHz and 5 MHz was applied on reception, along with averaging by 8 to improve signal to noise ratio. For each position of the measurement grid, the peak-to-peak value was registered, to build the normalized field plots. The time-of-flight between the transducer and the hydrophone was also registered, to account for measurement gap near the transducer surface. Measurement grid resolution was 1 mm for the flat transducer, 0.5 mm for the  $f = 35$  mm transducer, and 0.2 mm for the  $f = 22$  mm transducer. Signal processing and image reconstruction were performed in Matlab (Matworks Inc., Beltsville, MD, USA).

## 2.4. Methods for Radiating Surface Protection

Different techniques and materials were tried to provide an additional protection of the transducer surface while avoiding any reduction in either sensitivity or bandwidth: polymethylmethacrylate PMMA deposited by spin coating and polytetrafluoroethylene PTFE, varnish and acrylic lacquer (used for conformal coating for insulation and circuit boards environmental protection) deposited by spray coating, see Table 2.

**Table 2.** Coating material properties and method employed.

Material	Density (kg/m <sup>3</sup> )	Ultrasound Velocity (m/s)	Acoustic Impedance (MRayl)	Coating Method
PMMA	1150	2700	3.11	Spin coating
PTFE	2200	1400	3.10	Spray coating
Varnish	950 **	1800 *	0.95	Spray coating
Acrylic Lacquer	800 **	1800 *	0.88	Spray coating

\* Estimated.; \*\* According to manufacturer data.

PMMA powder was first dissolved in anisole (5%), deposited on transducer surface and then spin coated in two steps, first, 10 s at 1000 rpm and then 10 s at 2000 rpm. Continuity and uniformity of the coating were verified by observing the transducer surface under a microscope. The employed lacquer and varnish are UV fluorescent, so UV illumination was used to make the presence of the coating material clearer. All coatings were allowed to cure or dry for 24 h at room conditions. Thicknesses of the layers of coating were estimated from the frequency shift of the transducer thickness resonance, measured in pulse-echo in air, and from properties of the deposited materials (see Table 2).

### 3. Results

#### 3.1. Preliminary Verification of the FE Film Response

This preliminary verification is performed as explained in Section 2.4. This procedure was applied to uncoated flat and focused transducers to verify the proper integration of the FE layer in the transducer design and to coated flat transducers to determine the influence of the coating.

##### 3.1.1. Basic Design: Transducers without Surface Protection.

The resonant frequency in air of the HS03 and the HS06 transducers corresponds to the  $\lambda/4$  thickness resonance of the FE film. Hence, the resonant frequency is expected to be located close to 0.32 and 0.56 MHz, for HS03 and HS06, respectively (see Table 1). Measured SNS of the gold coated transducers operated in pulse-echo mode in air is shown in Figure 4.

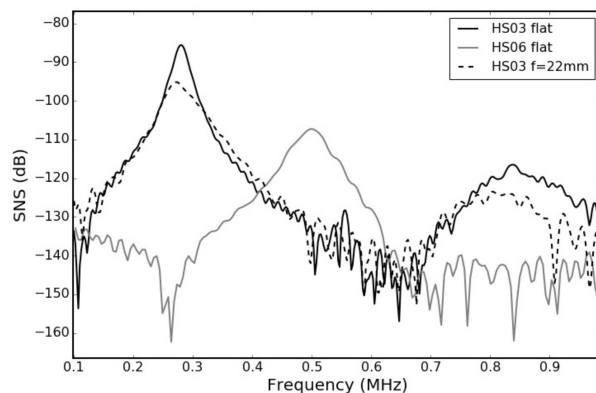


**Figure 4.** Au-sputtered transducers in pulse-echo response, air-coupled operation.

In all cases, the resonant response is clearly observed, however, the resonance is located at a lower frequency compared with the expected  $\lambda/4$  thickness resonant frequency (see Table 1). This is an expected result and is due to the effect of the layer of gold, as the gold loads the resonance and then shifts the resonant frequency towards lower values. Nonetheless, it can be confirmed that the thickness resonance is preserved and that the frequency shift is moderated. This deviation in the

resonant frequency (about 10%) is common in all Au coated transducers, this permits to estimate the thickness of the Au layer which is typically in the range 65–110 nm, for sputtering times between 30 and 60 s.

For the HS03 film the first two orders of resonances have been observed, revealing the effect of the increase in the ultrasound attenuation in the FE material with the frequency. For the HS06 film a lower sensitivity and more damped resonance is observed. This can be due to the increase in the attenuation with the frequency, or the higher impedance of this film (poorer matching to the air), or a reduced piezoelectric response compared with HS03, which could be due to a lower polarization level or to a lower piezoelectric constant that could be related to the different cellular structure of these two films, see [10].

For the HS03 focused transducer a similar resonant behavior is observed with the same resonant frequency, though it presents a somewhat lower peak SNS value that can be due to the wrinkles introduced in the FE film when it is glued to the spherical backing block. Figure 4 shows, as an example, the SNS in air of the HS03 transducer with the smaller radius of curvature.

### 3.1.2. Transducers with a Polymer Coating

HS03 transducers with different coatings were fabricated and the pulse-echo response in air compared before and after coating deposition. The purpose was to estimate the effect of the coating on the resonant response of the FE film: the thicker the coating, the larger the frequency shift and the lower the coating uniformity the larger the reduction in the resonance Q-factor. The measured SNS in pulse-echo mode in air, using the same equipment as in the previous section is shown in Figure 5. The frequency shift of the  $\lambda/4$  thickness resonance of the transducer operated in air in pulse-echo mode is shown in Table 3.

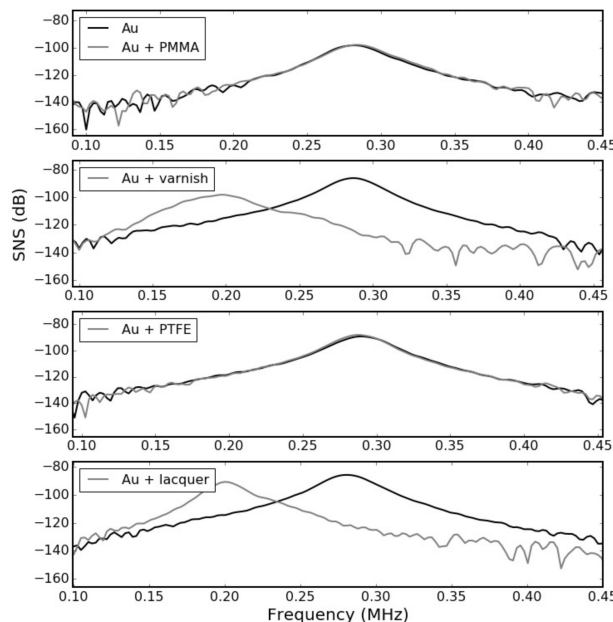


**Figure 5.** Sensitivity (SNS) vs. frequency for flat HS03 transducers with different coatings in pulse-echo mode in air.

**Table 3.** Frequency shift due to the coting and estimated coating thickness.

Coating	$\lambda/4$ Resonance (kHz)		Relative Variation (%)	Estimated Coating Thickness ( $\mu\text{m}$ )		
	Before Coating					
	After Coating					
PMMA	285.6	283.2	0.85	0.3		
PTFE	290.5	288.0	0.84	0.15		
Varnish	280.8	200.2	28.7	25		
Lacquer	285.0	200.0	29.8	26		

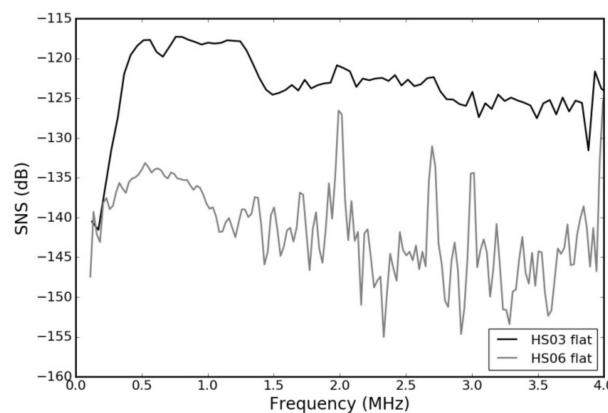
### 3.2. Water Immersion Response in Pulse-Echo Mode

All measurements presented in this section were performed as described in Section 2.3.2 of methods for transducer characterization.

#### 3.2.1. Frequency Domain Response

- Response of transducers made with different FE materials

The measured SNSs in pulse-echo mode in water immersion for flat HS03 and HS06 transducers without any coating (apart from the layer of sputtered Au) are shown in Figure 6. The response of the HS03-transducers is clearly better than that of the HS06-transducer. The sensitivity of the HS03 transducer is about 15 dB higher. The bandwidth of the flat transducers made with the HS06 film is narrower, more resonant and centered at a lower frequency (about 0.6 MHz). In addition, for frequencies over 1.2 MHz the signal to noise ratio is very poor and peaks observed for HS06 between 2 and 3 MHz are due to the noise. On the contrary, the HS03 transducer presents a wider frequency band: rather flat between 0.4 and 1.3 MHz. Between 1.5 and 4.0 MHz it is also flat but 6 dB below. Beyond 4.0 MHz, the signal to noise ratio becomes very low, in part due to the lower energy output of the pulser at those frequencies. The main drawback of these transducers is the reduced peak sensitivity that is about  $-117$  and  $-130$  dB for HS03 and HS06, respectively.

**Figure 6.** Pulse-echo sensitivity vs. frequency.

Due to the worse performance of HS06-transducers the rest of the study (performance of focused transducers and effect of surface coating) is limited to HS03-transducers.

- Response of focused transducers.

Figure 7 shows the measured sensitivity (SNS) for the flat and the spherically focused transducers with focal distance of 22 and 35 mm. The obtained response is pretty similar, so it can be concluded

that the effect of adapting the FE film to the spherical surface of the backing block has a limited effect on the transducer performance.

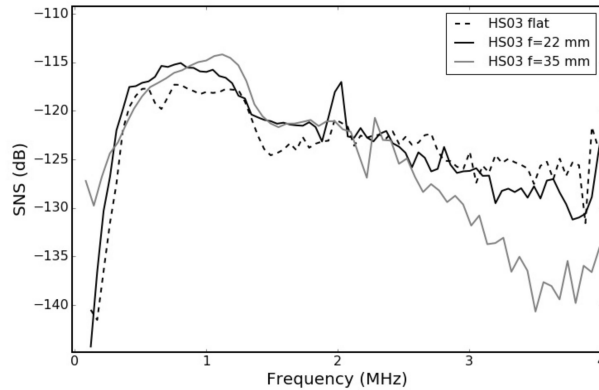


**Figure 7.** SNS vs. frequency for HS03 transducers in pulse-echo mode in water: flat and spherically focused (two focal distances: 22 and 35 mm).

- Response of transducers with different surface protection coatings.

Figure 8 shows the measured SNS vs. frequency for the HS03 flat transducers with different coatings. The response below 1.5 MHz is similar, but above 1.5 MHz the signal to noise ratio SNR is poorer in this case compared with the uncoated transducers.

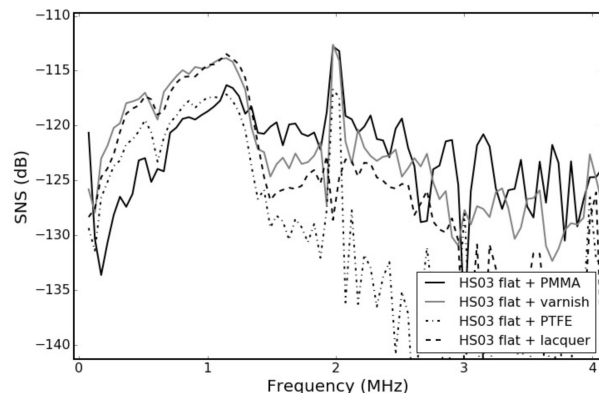


**Figure 8.** SNS vs. frequency for flat HS03 transducers in pulse-echo mode in water with different coatings.

### 3.2.2. Time Domain Response

All measurements presented in this section were performed as described in Section 2.3.2 of methods for transducer characterization.

- Flat and focused transducers.

The received echoes for the HS03 flat and focused transducers corresponding to the experimental set-up shown in Figure 3 are shown in Figure 9. For the flat transducer it is possible to see the first reflection from the water/steel surface (echo #1 in Figure 5) that appears at ~57 µs (Figure 9, top), and the first reverberation in this cavity (transducer-reflector), at ~115 µs (Figure 9, top). In addition, echoes from: (i) the back surface of the steel block (echo #2 in Figure 5), at ~75 µs (Figure 9, top), (ii) the bottom surface of the water tank (echo #3 in Figure 5), at ~87 µs (Figure 9, top), and (iii) reverberations

in those cavities can also be appreciated. For the focused transducers (focal distances of 22 and 35 mm) only the reflections from the front steel reflector surface (and reverberations in the transducer–reflector cavity) are observed as the other interfaces mentioned above are well out of focus. For the 22 mm radius of curvature transducer, the first reflection from the steel reflector front face (at  $\sim 29 \mu\text{s}$ ) plus two reverberations in the cavity between the transducer and the reflector can be observed (at  $\sim 57 \mu\text{s}$  and  $\sim 85 \mu\text{s}$ ).

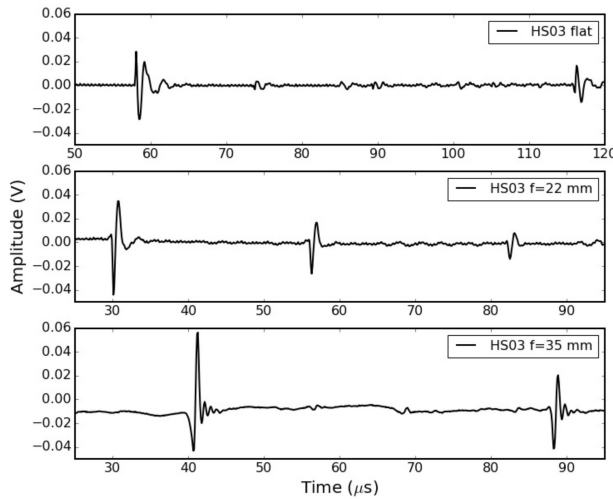


**Figure 9.** Response in the time domain in pulse-echo mode in water for the HS03 flat and focused transducers, radii of curvature of 22 and 35 mm.

- Transducers with coating.

The received echoes corresponding to the experimental set-up shown in Figure 5 for the HS03 flat transducers with different coatings are shown in Figure 10.

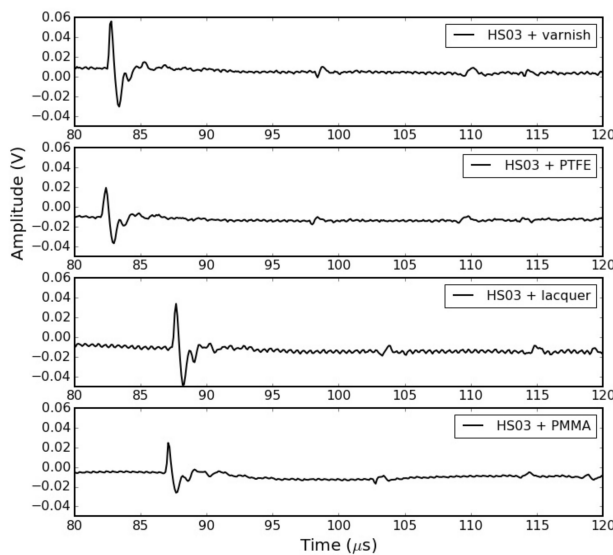


**Figure 10.** The response in the time domain in pulse-echo mode in water for HS03 transducers with different coatings (varnish, PTFE, lacquer and PMMA).

### 3.2.3. Acoustic Field

All measurements presented in this section were performed as described in Section 2.3.3.

The measured acoustic field (axial and transverse, at focal distance) distribution is shown in Figures 11–13 for HS03 transducers: flat and spherically focused with radii of curvature of 35 mm and 22 mm, respectively.

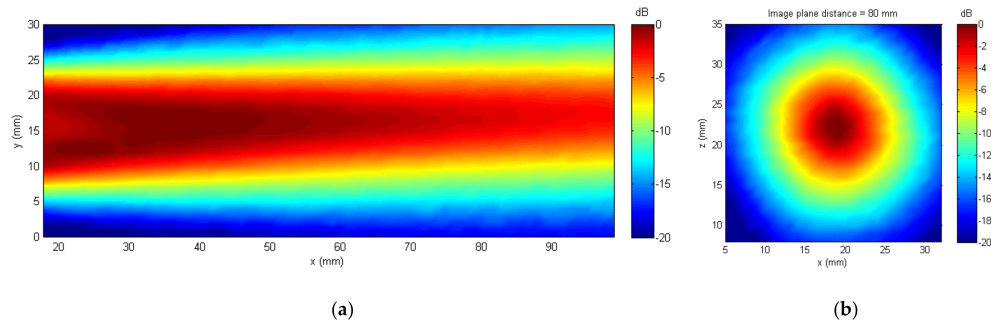


**Figure 11.** HS03 flat transducer acoustic field. (a) axial section, (b) transversal section.

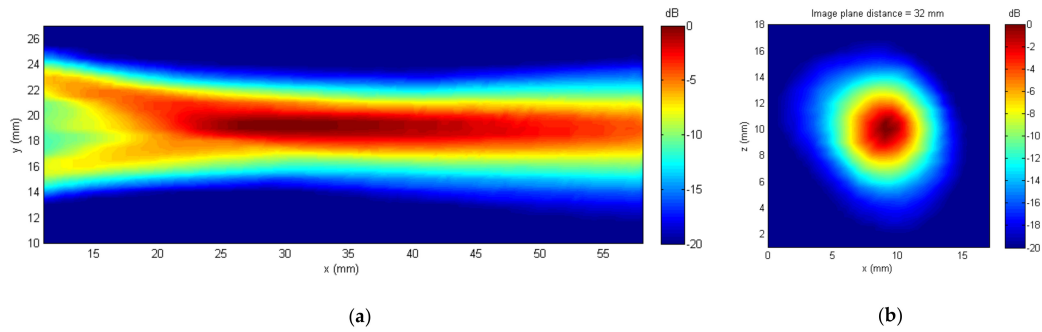


**Figure 12.** HS03 spherically focused transducer (radius of curvature 35 mm) acoustic field. (a) axial section, (b) transversal section.

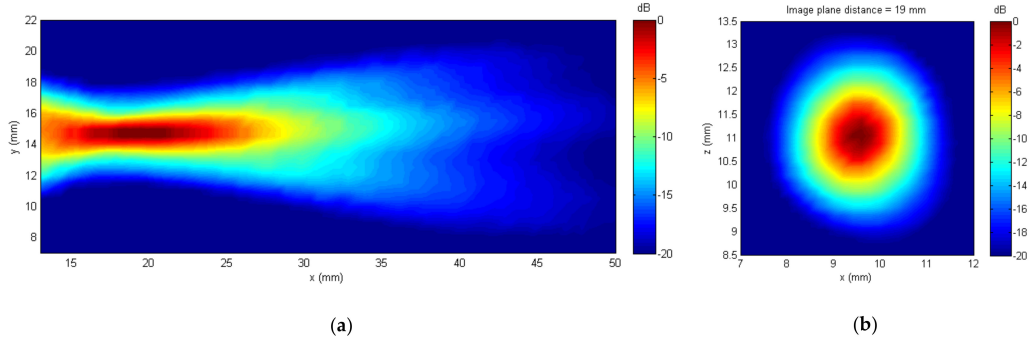


**Figure 13.** HS03 spherically focused transducer (radius of curvature 22 mm) acoustic field. (a) axial section, (b) transversal section.

The measured center frequency, focal distance and beam width at focus are shown in Table 4. In addition, the theoretical beam width ( $BW$ ) calculated according to Equation (2) is also shown.

$$BW = 1.02 F \lambda / (D) \quad (2)$$

where  $F$  is the focal distance,  $\lambda$  is the wavelength and  $D$  the transducer aperture diameter.

**Table 4.** Focal distance and beam width at focus.

Transducer (Radius Curvature)	Measured Center Frequency	Measured Focal Distance	Beam Width at Focus	
			Theoretical	Measured
22 mm	1.30 MHz	19 mm	1.67 mm	1.8 mm
35 mm	1.20 MHz	32 mm	2.88 mm	3.7 mm

#### 4. Discussion

The objective of this work was to test the possibility of using FE films to produce water immersion transducers for pulse-echo operation. Two different FE materials were employed: HS03 and HS06. The former has a lower resonant frequency, a more flattened pore structure (that makes the pores and the film more deformable in the thickness direction), and a lower acoustic impedance. Results with these two materials reveal that transducers produced with the HS03 film have a sensitivity about 15 dB better and a wider frequency bandwidth (Figure 6). Considering that the impedance of the HS06 film is better coupled to the water, this better response of the HS03 film could be related with either a better piezoelectric response of HS03 or a more efficient response of the cellular structure of HS03 when operated with a water load.

Water is a huge mechanical load for the FE film; hence, thickness resonances are expected to be completely damped out. As a matter of fact, no trace of the film thickness resonance is found in the pulse-echo response in water, where the film could be expected to operate in the lambda/2 thickness mode (Figure 6). This huge load imposed by the water is expected to produce a very large frequency bandwidth and a very low sensitivity. Pulse duration (under spike excitation) is about 2–3  $\mu$ s long (Figures 9 and 10), while the 6 dB frequency band expands from 0.29 up to 2.7 MHz (161%), and the 12 dB band expands up to 4.5 MHz (Figures 6 and 7). The main counterpart is the reduced sensitivity. The observed peak sensitivity values for the different prototypes are in the range of –114 to –118 dB (Figures 6–8). Nonetheless, even with this low sensitivity it was possible to observe the front and back echoes of a 53 mm thick steel block (see Figures 9 and 10).

Different techniques and materials were tried to provide protection for the radiating surface. The main idea is to provide a uniform and thin coating with acoustic properties similar to the water, so that the effect of this coating on the acoustic performance could be negligible. Measured response in pulse echo mode in water immersion revealed a somewhat better sensitivity (about 5 dB) for transducers with varnish and lacquer compared with PMMA and PTFE coted transducers. This can be due to the fact that the acoustic impedance of PMMA and PTFE coatings is expected to be higher than that of the water. However, the SNR of coated transducers seems to be poorer in coated transducers (Figures 7 and 8). This has to be confirmed in further studies.

Finally, we have shown that it is possible to produce spherically focused transducers, by using a backing block with a spherical surface and gluing the FE film to it. Adapting the FE film to the curved surface produces some wrinkles in the film, however the effect on the ultrasonic response is reduced (Figures 4 and 7) and no artifacts can be observed in the acoustic fields (Figures 11–13). SNS and the signal in the time domain (Figure 9) are very similar for flat and focused transducers. The measured acoustic field of the focused transducers revealed a field distribution very close to the expected one. For the transducer with a radius of curvature of 22 mm, the measured focal distance was 19 mm and the focal spot size was 1.8 mm. In this case the calculated focal spot size was 1.67 mm, very close to the measured value. For the transducer with a radius of curvature of 35 mm, the measured focal distance was 32 mm and the focal spot size was 3.7 mm. In this case the calculated focal spot size was 2.88 mm.

#### 5. Conclusions

This work shows the response of ferroelectret film-based transducers for pulse-echo operation in water. Two FE films were tried and the best results were obtained with the film (HS03) with the highest density and the lowest impedance. As the impedance matching is poorer for this film, the better

response must be due to a better piezoelectric response of the HS03 film. As expected, and due to the large load of the water, the thickness resonance of the film is completely damped out, giving rise to a poor sensitivity (around  $-115$  dB) and a very wide band response with a short signal duration. It has been shown that it is also possible to produce spherically focused transducers with a similar response compared with flat ones, but with the advantage of a better spatial resolution, with a focal spot size  $<2$  mm.

In spite of the reduced peak sensitivity, the huge bandwidth and the observed SNR values still permit to consider the use of this kind of transducers for different water immersion applications related to materials characterization, NDT and medical imaging, in applications where large bandwidth, moderate frequencies (0.5–4.0 MHz) and good axial resolution are required. In addition to the large frequency bandwidth and short signal duration, the FE transducers offer other advantages related to the flexibility of the material and the reduced size of the required backing block. Further studies are needed to determine if the transducer sensitivity can be improved. The first step can be to try techniques that have already been tested for FE air-coupled transducers. They include the use of a high voltage excitation to make the FE film work under the electrostrictive regime and the use of a bias voltage [15]. In addition, spread spectrum signals with programmable excitation spectral shape can be used to compensate the 10 dB spectral losses beyond 2.0 MHz, making received signals even more broadband [16]. In addition, further studies of transmission and reception sensitivity and frequency bands could be beneficial in order to optimize transducer design.

**Author Contributions:** Conceptualization, L.S. and T.G.A.-A.; methodology, T.G.A.-A. and J.C.; software, J.C.; validation, J.Q., and T.G.A.-A.; resources, T.G.A.-A., L.S., and J.C.; writing—original draft preparation, J.Q.; writing—review and editing, T.G.A.-A., L.S. and J.C.; funding acquisition, T.G.A.-A., J.C. and L.S. All authors have read and agreed to the published version of the manuscript.

**Funding:** This work was supported in part by Ministerio de Economía y Competitividad under grants ECERES (DPI2016-78876-R, AEI/FEDER, UE) and AIMUT (RTI2018-099118-A-I00, MCIU/AEI/FEDER, UE) and received partial funding (LS) from European Regional Development Fund (project No. 01.2.2-LMT-K-718-03-0026) under grant agreement with the Research Council of Lithuania (LMTLT).

**Conflicts of Interest:** The authors declare no conflict of interest and the funders had no role in the design of the study; in the collection, analyses, or interpretation of data; in the writing of the manuscript, or in the decision to publish the results.

## References

1. Savolainen, A.; Kijavainen, K. Electrothermomechanical Film. Part I. Design and Characteristics. *J. Macromol. Sci. A* **1989**, *26*, 583–591. [[CrossRef](#)]
2. Sessler, G.M.; Hillenbrand, J. Electromechanical response of cellular electret films. *Appl. Phys. Lett.* **1999**, *75*, 3405–3407. [[CrossRef](#)]
3. Kressmann, R. New Piezoelectric Polymer for Air-Borne and Water-Borne Sound Transducers. *J. Acoust. Soc. Am.* **2001**, *109*, 1412–1416. [[CrossRef](#)] [[PubMed](#)]
4. Bovtun, V.; Döring, J.; Bartusch, J.; Beck, U.; Erhard, A.; Yakymenko, Y. Ferroelectret Non-Contact Ultrasonic Transducers. *Appl. Phys. A Mater. Sci. Process.* **2007**, *88*, 737–743. [[CrossRef](#)]
5. Ealo, J.L.; Seco, F.; Jimenez, A.R. Broadband EMFi-based transducers for ultrasonic air applications. *IEEE Trans. Ultrason. Ferroelectr. Freq. Control* **2008**, *55*, 919–929. [[CrossRef](#)] [[PubMed](#)]
6. Álvarez-Arenas, T.E.G. Air-Coupled Piezoelectric Transducers with Active Polypropylene Foam Matching Layers. *Sensors* **2013**, *13*, 5996–6013. [[CrossRef](#)] [[PubMed](#)]
7. Álvarez-Arenas, T.E.G.; Diez, L. Ferroelectret transducers for water immersion and medical imaging. In Proceedings of the IEEE International Ultrasonics Symposium, IUS, Tours, France, 18–21 September 2016. [[CrossRef](#)]
8. Aguilar, J.Q.; Alvarez-Arenas, T.E.G. Optimization of Ferroelectret Transducers for Pulse-Echo Water Immersion Operation. In Proceedings of the 2019 IEEE International Ultrasonics Symposium (IUS), Glasgow, UK, 6–9 October 2019; pp. 2604–2607. [[CrossRef](#)]

9. Álvarez-Arenas, T.E.G.; Calás, H.; Cuello, J.E.; Fernández, A.R.; Muñoz, M. Noncontact ultrasonic spectroscopy applied to the study of polypropylene ferroelectrets. *J. Appl. Phys.* **2010**, *108*, 074110. [[CrossRef](#)]
10. Quirce, J.; Muñoz, M.; Alvarez-Arenas, T.E.G. Interpretation of the thickness resonances in ferroelectret films based on a layered sandwich mesostructure and a cellular microstructure. *IEEE Trans. Ultrason. Ferroelectr. Freq. Control* **2020**, in press. [[CrossRef](#)] [[PubMed](#)]
11. Alvarez-Arenas, T.E.G. Acoustic impedance matching of piezoelectric transducers to the air. *IEEE Trans. Ultrason. Ferroelectr. Freq. Control* **2004**, *51*, 624–633. [[CrossRef](#)]
12. Alvarez-Arenas, T.E.G.; Diez, L. Novel impedance matching materials and strategies for air-coupled piezoelectric transducers. In Proceedings of the 2013 IEEE SENSORS 2013-Proc, Baltimore, MD, USA, 3–6 November 2013. [[CrossRef](#)]
13. Ealo Cuello, J.L. Transductores Basados en Ferroelectretos para Aplicaciones Ultrasónicas en Aire. Ph.D. Thesis, University Politécnica de Madrid, Madrid, Spain, 14 December 2009.
14. Tang, J.; Tong, L.; Xiang, Y.; Qiu, X.; Deng, M.; Xuan, F. Design, fabrication and characterization of Emfi-based ferroelectret air-coupled ultrasonic transducer. *Sens. Actuators A Phys.* **2019**, *296*, 52–60. [[CrossRef](#)]
15. Bovtun, V.; Döring, J.; Bartusch, J.; Gaal, M.; Erhard, E.; Kreutzbruck, M.; Yakymenko, Y. Enhanced electromechanical response of ferroelectret ultrasonic transducers under high voltage excitation. *Adv. Appl. Ceram.* **2013**, *112*, 97–102. [[CrossRef](#)]
16. Svilainis, L.; Rodriguez-Martinez, A.; Chaziachmetovas, A.; Aleksandrovas, A. Ultrasound Transmission Spectral Compensation Using Arbitrary Position and Width Pulse Sets. *IEEE Trans. Instrum. Meas.* **2018**, *67*, 1778–1785. [[CrossRef](#)]

**Publisher's Note:** MDPI stays neutral with regard to jurisdictional claims in published maps and institutional affiliations.



© 2020 by the authors. Licensee MDPI, Basel, Switzerland. This article is an open access article distributed under the terms and conditions of the Creative Commons Attribution (CC BY) license (<http://creativecommons.org/licenses/by/4.0/>).



Article

# Modification of Mechanical and Electromechanical Resonances of Cellular Ferroelectret Films Depending on the External Load

Julio Quirce Aguilar and Tomás Gómez Álvarez-Arenas \*

ITEFI-CSIC, Serrano 144, 28006 Madrid, Spain; j.quirce@csic.es

\* Correspondence: t.gomez@csic.es

**Abstract:** Ferroelectret films are cellular polymers with electrically charged pores that exhibit piezoelectric response. Among other applications, ferroelectret films have been widely used as active elements in air-coupled ultrasonic transducers. More recently, they have also been tested in water immersion. They show a promising wide frequency band response, but a poor sensitivity produced by the disappearance of the electromechanical resonances. This paper studies in detail the modification of FE films response when put into water immersion, both the mechanical and the electromechanical responses (the latter in transmission and reception modes). The lack of electromechanical thickness resonances when the films are put into water is explained as the result of the different profile of the modification of the polarization vector along the film thickness imposed by the large mechanical load produced by the water. This different electromechanical response can also be the reason for the subtle modification of the mechanical thickness resonances that is also observed and analyzed.



**Citation:** Aguilar, J.Q.; Gómez Álvarez-Arenas, T. Modification of Mechanical and Electromechanical Resonances of Cellular Ferroelectret Films Depending on the External Load. *Polymers* **2021**, *13*, 3239. <https://doi.org/10.3390/polym13193239>

Academic Editors: Judith Martín-de León and Victoria Bernardo

Received: 30 August 2021  
Accepted: 21 September 2021  
Published: 24 September 2021

**Publisher's Note:** MDPI stays neutral with regard to jurisdictional claims in published maps and institutional affiliations.



**Copyright:** © 2021 by the authors. Licensee MDPI, Basel, Switzerland. This article is an open access article distributed under the terms and conditions of the Creative Commons Attribution (CC BY) license (<https://creativecommons.org/licenses/by/4.0/>).

## 1. Introduction

Ferroelectrets are cellular polymer films that contain flattened and elongated pores in the film plane with the capability that these pores can be electrically charged in a stable way [1,2]. Cellular porous solids are widely found in nature as this is a kind of hierarchical structure that provides many different design advantages and offer the possibility of combining different functionalities. They are also commonly found in medicine, both as organs that need to be studied and as a source of inspiration for the design of sensors. [3]. In addition, programmable materials based on cellular solids have also been proposed to recreate the essential features of biologically self-adaptive materials [4]. As a result of their cellular structure, ferroelectrets are thin and flexible polymeric films that exhibit piezoelectric properties. Different manufacturing techniques have been used, such as the two-step inflation technique [5], template-patterning techniques [6,7] and additive manufacturing techniques [8]. This cellular structure is designed so that the deformation of the material takes place through bending of the pore walls and the possibility of trapping electrical charge in the pores in a stable way is maximized [9]. This gives rise to very reduced elastic modulus, so relatively large deformations can be achieved. This feature together with the trapped electrical charge in the pore walls gives rise to a macroscopic piezoelectric response. Previous studies of ferroelectret materials have been oriented towards characterizing the films, modifying the cellular microstructure to maximize the piezoelectric response and stabilizing and optimizing the electrical charge trapped in the pores [5,10–16]. More recently, a new type of material combining conventional piezoelectricity (linked to microscopic charge distribution) and ferroelectret piezoelectric response (linked to macroscopic electrical dipoles trapped in the macroscopic pores) has been proposed and used as a biometric sensor [17].

Ferroelectrets have been used for many different applications including microphones [18], energy harvesting [19–21], wearable devices [22] and flexible and printable sensors (FLEPS) [23],

flexible touch pads and tactile sensors [24], and air-coupled ultrasonic transducers [25–33]. In the latter case, the main advantage is the extremely low acoustic impedance of these materials that facilitates the coupling to the air; they are normally operated using the thickness resonances of the films. In addition, the possibility to operate these films in the electrostrictive regime under high voltage excitation offers an important improvement of transducer efficiency [34,35]. Applications of FE-based air-coupled transducers have mainly been oriented towards non-destructive testing of materials. More recently, ferroelectret films have also been revealed as a promising candidate to produce transducers for liquid coupling and hydrophones. Applications in the low frequency range (below 100 kHz) have been studied in [36–38] while applications for wideband ultrasonic transducer for medical applications and hydrophones, involving a frequency range >200 kHz, have been proposed and studied in [39–41]. They present an extremely wideband response but a very low sensitivity compared with conventional transducers. In addition, they also present some abnormalities compared with the response of FE transducers for air-coupled ultrasonic applications that should be better understood in order to be able to improve their performance in water immersion applications—in particular, to improve sensitivity without compromising the bandwidth and to compensate the sensitivity loss when frequency increases.

Ref. [42] supposed a step forward, as it showed that air-loaded thickness resonances of these films can be better explained if a sandwich meso-structure together with a cellular microstructure is assumed. This conclusion is consistent with SEM images of the FE film structure. This approach permitted to justify the harmonic distortion of the thickness resonance spectra observed in these films.

The purpose of this paper is to study, simultaneously, both thickness resonances and electromechanical response (both as receiver and transmitter) of this type of material as well as the modifications in both of them when going from the well-known case of air-loaded films to the more unconventional case of water-loaded films, which is of interest for medical transducers and hydrophones, as suggested above. Given that the impedance of these materials is about 0.05 MRayl and impedance of water and air are 1.5 MRayl and  $4 \times 10^{-4}$  MRayl, respectively, the variation of boundary conditions when the film is in water or in air is remarkable.

Towards this end, two different FE films have been studied both in air and in water. First, we measured the transmission coefficient in water immersion at normal incidence and for a frequency band that, at least, covers the first order of the thickness resonances—in most cases, the first two orders. Similar measurements were performed in air for the same materials [15,42]; in the latter case, material parameters were extracted by assuming a sandwich structure for the film and solving the inverse problem. Observed resonances in air and in water have been compared and differences have been analyzed.

Then, the electromechanical response of the films is measured, both under air and water loads. Two different types of measurements were performed in this case. The first one consists of measuring the generated electric signal in the FE when an ultrasonic signal impinges on the film at normal incidence, while the second one consists of measuring the radiated ultrasonic signal when an electrical excitation is applied to the film (Tx mode). These measurements were performed both in water and in air. Responses of the film under these two different loading conditions are compared. Finally, an explanation for the observed differences is provided.

## 2. Materials and Methods

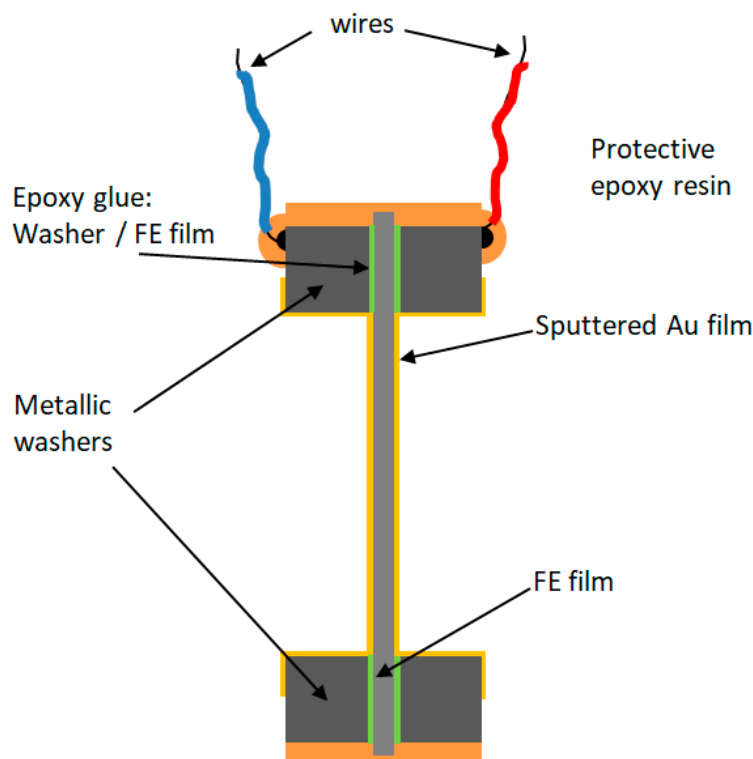
### 2.1. Materials

Two different ferroelectret (FE) films have been used for this study, both from EMFIT Ltd (Vaaejakoski, FINLAND), commercial names: HS03 and HS06. Properties of these films can be seen in Table 1 and in Refs. [15,41,42].

**Table 1.** Properties of the FE films employed [10].

Material	Thickness ( $\mu\text{m}$ )	Density ( $\text{kg}/\text{m}^3$ )	$\lambda/2$ Resonant Frequency, Thickness Mode (MHz)	Impedance (MRayl)
HS03	70	530	0.638	0.046
HS06	90	370	1.120	0.065

To facilitate sample handling and electrical connections for the measurement of the electromechanical response, samples were prepared by sandwiching the FE film between two metallic washers (outer diameter: 40 mm, inner diameter: 25 mm). The FE and the washers were glued using epoxy resin. Once glued, both free surfaces of the FE film and washer were Au sputtered (using a LEICA EM ACE200 sputtering LEICA, Wetzlar, Germany), for 60 s to ensure electrical conductivity between the washer and the surface of the FE film the washer is glued to. Finally, two wires were soldered to the washers and epoxy resin was applied to the edge of the washers and to cover the soldering points as protection and to facilitate the handling of the samples. The structure and composition of the samples so prepared is shown in Figure 1.

**Figure 1.** Schematic representation of the FE film preparation.

The samples resemble tambourines (see pictures in Figure 2). Two samples using HS03 film and one sample using HS06 film were prepared. In one of the HS03 samples, a film of adhesive tape (150  $\mu\text{m}$  thick) was glued to one of the faces of the FE film. Due to the very small thickness and impedance of the FE film (0.046 MRayl), the presence of this adhesive tape film is “seen” as very high impedance load (impedance of the adhesive tape ~1.7 MRayl). Hence, the observed thickness resonances of this sample in air are shifted closer to the quarter wavelength resonances, while for the other samples, we observe the half wavelength resonances of the free-standing film. On the contrary, when submerged in

water, as the impedance of the water is very close to the impedance of the adhesive tape, the response of the FE film with the adhesive tape is expected to be very similar to that of the free film (without adhesive tape).

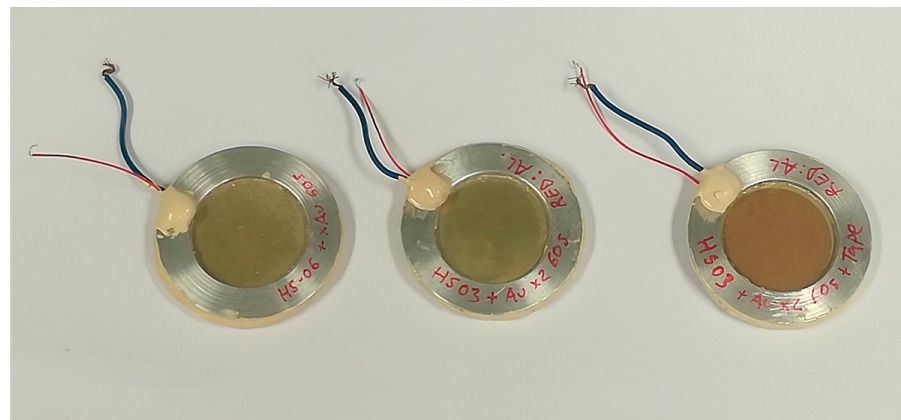


**Figure 2.** Picture of the prepared FE films for measurements. The HS03 sample with the adhesive tape is shown on the right; the brown adhesive tape can be seen on top of the Au layer.

The experimental set-up is shown in Figure 3. A couple of identical ultrasonic transducers are positioned in opposition and aligned and the sample to be measured is located in between them at normal incidence.

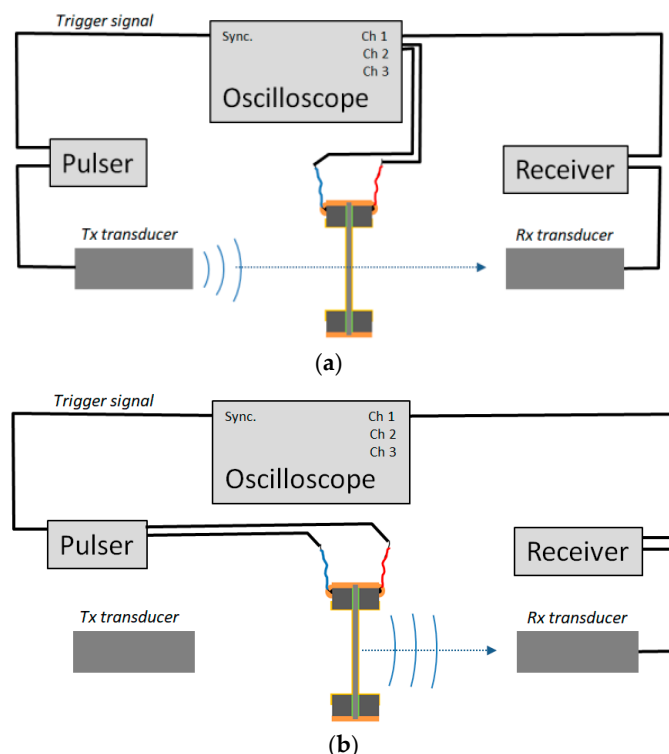


**Figure 3.** Experimental set-up. (a) Configuration for the measurement of both the transmission coefficient and the FE film and the film response in Rx mode; (b) configuration for the measurement of the FE film response in Tx mode.

Two different media, where both sample and transducers are immersed, have been used: water and air. When water immersion is used, a small water tank is used as shown in Figure 4.

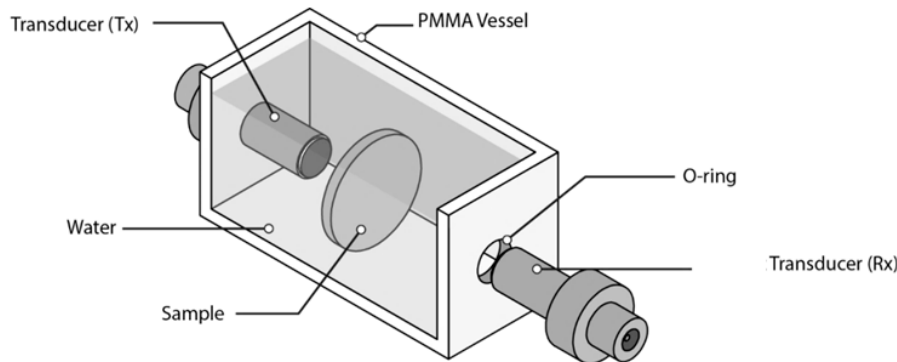


**Figure 4.** Water tank for water immersion measurements.

All measurements were performed at room conditions. For water immersion measurements, a pair of wide band transducers (Olympus, Olympus NDT Inc., Quebec, Canada, Ref #V303, 15 mm diameter, 1 MHz center frequency) have been employed. These transducers permit to cover the frequency range from 0.2 to 1.4 MHz. In some cases, it was of interest to expand the frequency range to higher frequencies. In these cases, a second pair of transducers, also from Olympus (Olympus NDT Inc., Quebec, Canada), centered at 2.25 MHz were used (15 mm diameter, Ref #C306). This permitted to expand the frequency range up to 3.0 MHz.

For air-coupled measurements, three pairs of air-coupled transducers manufactured at ITEFI-CSIC (Madrid, Spain) were used to cover a similar frequency range. The centre frequency of these three pairs of transducers is: 0.25, 0.65 and 1.1 MHz, respectively.

In all cases, the transmitter transducer was driven by using an Olympus pulser/receiver (5058PR), *pulser* in Figure 3. The same pulser was also used when the FE film was excited to measure its response in transmission (Tx) mode, as shown in Figure 3b. This pulser generates a wideband spike. Amplitude of the excitation was set to 200 V for air-coupled measurements and to 100 V for water immersion measurements. Gain in reception stage of the 5058 P/R (*receiver* in Figure 3) was between 0 and 10 dB for water immersion measurements and between 10 and 20 dB for air-coupled measurements; all filters in the receiver (5058PR) were off.

Without sample in between transducers, the fast Fourier transform (FFT) of the signal received in the scope ( $\text{FFT}(S_{ref})$ ) can be used to characterize the response of the system.  $\text{FFT}(S_{ref})$  is the result of the multiplication of the transfer functions (in frequency domain),  $TF$ , of the different elements present in the experimental set-up (i.e., *pulser*: electrical excitation, *Tx*: transmitter transducer, *Rx*: receiver transducer, *receiver*: electronics at reception, i.e., gain, matching impedance, etc.), and applying them to the input of the system: the signal provided by the pulser ( $[S_{pulser}]^*$ ):

$$\text{FFT}(S_{ref}) = \text{TF}(\text{receiver}) \times \text{TF}(\text{Rx}) \times \text{TF}(\text{fluid} - \text{gap}) \times \text{TF}(\text{Tx}) \times [S_{pulser}]^* \quad (1)$$

Alternatively:

$$\text{FFT}(S_{ref}) = \text{TF}(\text{receiver}) \times \text{TF}(\text{fluid} - \text{gap}) \times \text{TF}(\text{Tr})^2 \times [S_{pulser}]^*, \quad (2)$$

where  $\text{TF}(\text{Tr})^2 = \text{TF}(\text{Tx}) \times \text{TF}(\text{Rx})$ .

In addition,  $TF(receiver)$  can be split into two terms:

$$TF(receiver) = G \times TF(receiver^*), \quad (3)$$

where  $G$  is the gain in reception and  $TF(receiver^*)$  is the result of the electrical impedance matching between receiver transducer ( $Rx$ ) and the electronics in the receiver.

In some cases, Equation (2) can be further simplified. For example, for wide band transducers  $TF(Tx) \approx TF(Rx)$ . Under spike excitation and for pulser bandwidth much larger than transducers bandwidth, it can be assumed that  $[S_{pulser}]^* \approx cte = A$ , at least within the transducer's frequency band. Finally, for a receiver with flat frequency response,  $G$  in Equation (2), can be considered cte. Then Equation (3) can be simplified:

$$FFT(S_{ref}) = A \times G \times TF(Tr)^2 \times TF(fluid - gap) \times TF(receiver^*), \quad (4)$$

Three different measurements were performed for all of them the sample remained in the same position and the pulser configuration; that is,  $[S_{pulser}]^*$  was also kept unchanged:

1. the transmission coefficient of the FE sample,
2. the electrical voltage generated in the FE sample when an ultrasonic wave impinges on the it (electromechanical response in  $Rx$  mode),
3. the ultrasonic signal emitted by the FE sample when an electrical excitation is applied to it (electromechanical response in  $Tx$  mode).

## 2.2. Methods

### 2.2.1. Measurement of the Mechanical Response of the FE Sample: Transmission Coefficient

As explained before, the system is characterized by measuring  $FFT(S_{ref})$ . Then, the FE sample is put in between  $Tx$  and  $Rx$  transducers at normal incidence. All elements of the system remain unchanged with the exception of the gain in the receiver, which is increased. As in the previous case, the FFT of the signal in the receiver transducer,  $FFT(S_{sample})$ , is the result of the multiplication of the transfer functions (in frequency domain) of the different elements in the experimental set-up applied to the FFT of the input signal, which is the signal provided by the pulser:  $[S_{pulser}]^*$ :

$$\begin{aligned} FFT(S_{sample}) = & TF(receiver) \times TF(Rx) \times TF(fluid - gap 2) \times TF(sample) \times TF(fluid - gap 1) \\ & \times TF(Tx) \times [S_{pulser}]^* \end{aligned} \quad (5)$$

For films with thickness  $\ll$  distance between  $Tx$  and  $Rx$ , it can be assumed that:

$$TF(fluid - gap 1)TF(fluid - gap 2) = TF(fluid - gap), \quad (6)$$

So, Equations (2), (5) and (6) lead to:

$$FFT(S_{sample}) = TF(sample)FFT(S_{ref}), \quad (7)$$

then:

$$TF(sample) = \frac{FFT(S_{sample})}{FFT(S_{ref})}, \quad (8)$$

and  $TF(sample)$  is equal to the transmission coefficient of the film, the modulus (in dB) is obtained from:

$$20\log \left| \frac{FFT(S_{sample})}{FFT(S_{ref})} \right|, \quad (9)$$

### 2.2.2. Measurement of the Electromechanical Response: Rx Mode

Keeping the same experimental configuration, we measured the electromechanical response of the film in receiver mode. Following Figure 3a, this is obtained by measuring the FFT of the signal at channel 2 of the scope (i.e., the electrical voltage generated in the FE sample when the ultrasonic signal generated by *Tx* impinges on it).

The FFT of this signal,  $FFT(S_{FE-RX})$ , is given by:

$$FFT(S_{FE-RX}) = TF(receiver) \times TF(FE_{Rx}) \times TF(fluid - gap 1) \times TF(Tx) \times [S_{pulser}]^* \quad (10)$$

Moreover, if the sample is located in the middle of the fluid-gap:

$$TF(fluid - gap 1) = TF(fluid - gap 2) \approx TF(fluid - gap)^{1/2}, \quad (11)$$

Then Equation (4) is:

$$FFT(S_{ref}) = A \times G \times TF(Tr)^2 \times TF(fluid - gap) \times TF(receiver^*), \quad (12)$$

Then, with Equations (4) and (11), Equation (10) can be written as:

$$FFT(S_{FE-RX}) = A \times G \times TF(Tr) \times TF(fluid - gap)^{1/2} \times TF(FE_{Rx}) \times TF(receiver^*) \quad (13)$$

Then:

$$TF(FE_{Rx}) = \left( FFT(S_{FE-RX}) / \sqrt{FFT(S_{ref})} \right) \times 1 / \sqrt{A \times G \times TF(receiver^*)}, \quad (14)$$

That is:

$$TF(FE_{Rx}) \propto FFT(S_{FE-RX}) / FFT(S_{ref})^{1/2}, \quad (15)$$

and the modulus of  $TF(FE_{Rx})$  in dB is given by:

$$20\log|TF(FE_{Rx})| = 20\log \left| \frac{FFT(S_{FE-RX})}{FFT(S_{ref})^{1/2}} \right| - cte, \quad (16)$$

where:  $cte = 10\log(A \times G \times TF(receiver^*))$

The magnitude:  $20\log|TF(FE_{Rx})| + cte$  is defined as:  $20\log|TF(FE_{Rx})^*|$ . This is straightforwardly obtained from the measurements and represents the frequency profile of the FE sample response in Rx mode. Where  $S_{FE-RX}$  is the electric voltage measured at FE film terminals. In this configuration, the electrical voltage in the FE,  $FFT(S_{FE-RX})$ , is produced by the ultrasonic signal transmitted by the *Tx* transducer and the piezoelectric effect of the FE film.

### 2.2.3. Measurement of the Electromechanical Response: Tx Mode

Finally, we measured the electromechanical response of the film in transmission mode:  $FFT(S_{FE-TX})$ . Towards this end, the pulser output is connected to the FE film wires and the signal received at the receiver transducer (channel 1 of the scope in Figure 3b) is registered.

$$FFT(S_{FE-TX}) = TF(receiver) \times TF(Tr) \times TF(fluid - gap 1) \times TF(FE_{Tx}) \times [S_{pulser}]^*, \quad (17)$$

or:

$$FFT(S_{FE-TX}) = A \times G \times TF(FE_{Tx}) \times TF(fluid - gap)^{1/2} \times TF(Tr). \quad (18)$$

That is:

$$TF(FE_{Tx}) = \left( FFT(S_{FE-Tx}) / \sqrt{FFT(S_{ref})} \right) \times 1 / \sqrt{A \times G \times TF(receiver^*)}, \quad (19)$$

and the modulus of  $TF(FE_{Tx})$  in dB is given by:

$$TF(FE_{Tx}) \propto FFT(S_{FE-Tx}) / FFT(S_{ref})^{1/2}, \quad (20)$$

and the modulus of  $TF(FE_{Tx})$  in dB is given by:

$$20\log|TF(FE_{Tx})| = 20\log \left| \frac{FFT(S_{FE-Tx})}{FFT(S_{ref})^{1/2}} \right| - cte; \quad (21)$$

The magnitude:  $20\log|TF(FE_{Tx})| + cte$  is defined as:  $20\log|TF(FE_{Tx})^*|$ . This magnitude is straightforwardly obtained from the measurements and represents the frequency profile of the FE response in Tx mode:

$$20\log|TF(FE_{Tx})^*| = 20\log \left| \frac{FFT(S_{FE-Tx})}{FFT(S_{ref})^{1/2}} \right|, \quad (22)$$

### 3. Results

#### 3.1. FE Response in Air

Measurement of the modulus of the transmission coefficient and the modulus of the electromechanical response both in *Tx* and *Rx* mode in air for the samples HS03, HS03 + film and HS06 at normal incidence are shown in Figures 5–7, respectively. The repeatability of the measurements is typically within the range of the symbol size. Figures 5b, 6b and 7b show, in the same graph, both the *Tx* and *Rx* response. This is performed for convenience and there is no reason to expect the same response in *Tx* and *Rx* modes. Electromechanical measurements show a larger noise level below  $-35$  dB; this can be attributed to a reduced single to noise ratio. In a similar way, in some cases, a larger dispersion can be found at the limits of the transducer bandwidth; this is also due to a reduced signal-to-noise ratio, in this case produced by the reduced sensitivity of the transducer at the edge of its bandwidth.

The mechanical responses (Figures 5a, 6a and 7a) show the spectra of the transmission coefficient magnitude. These spectra clearly present the effect of the appearance of thickness resonances (located at the frequencies where the transmission coefficient presents a local maximum). Two orders of these resonances are shown in Figure 5a that correspond to the half wavelength resonances (shifted from the theoretically expected value due to the sandwich structure of the film as explained in Ref. [38]). Two orders of these resonances are also shown in Figure 6a. In this case, they correspond, approximately, to the quarter wavelength resonances due to the presence of the adhesive film. Finally, Figure 7a shows the first thickness resonance (half wavelength mode) for the HS06 sample. The electromechanical response follows a similar trend with the only exception of the second order resonance in Figure 5 that presents no electromechanical counterpart. These results are carefully discussed in the Discussion section.

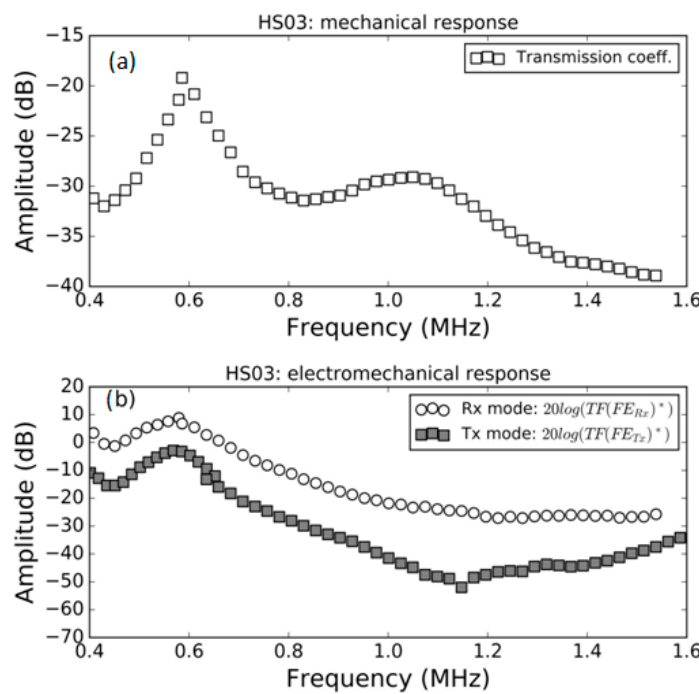


**Figure 5.** Measured response of the HS03 FE sample in air. (a) Modulus of the transmission coefficient vs. frequency (b) electromechanical response vs. frequency both in Tx and Rx mode, (see Equations (16) and (22)).

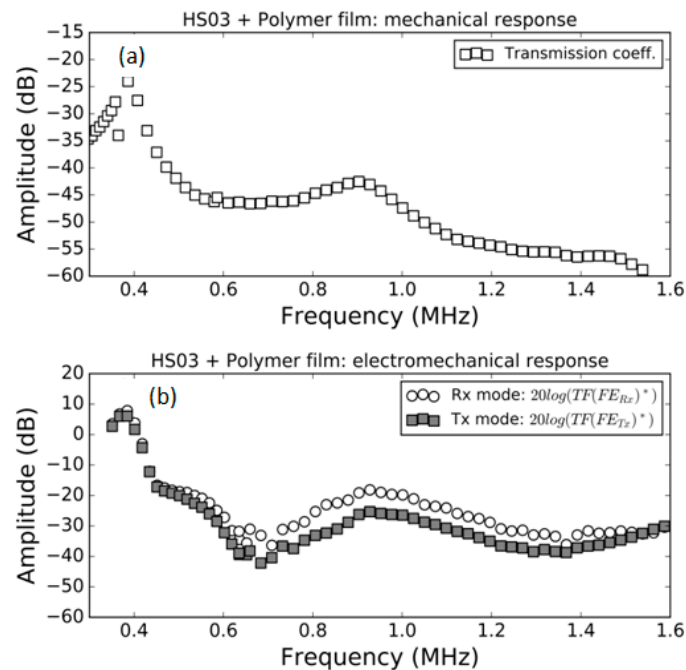


**Figure 6.** Measured response of the HS03 sample + film in air. (a) Modulus of the transmission coefficient vs. frequency; (b) electromechanical response vs. frequency both in Tx and Rx mode, (see Equations (16) and (22)).

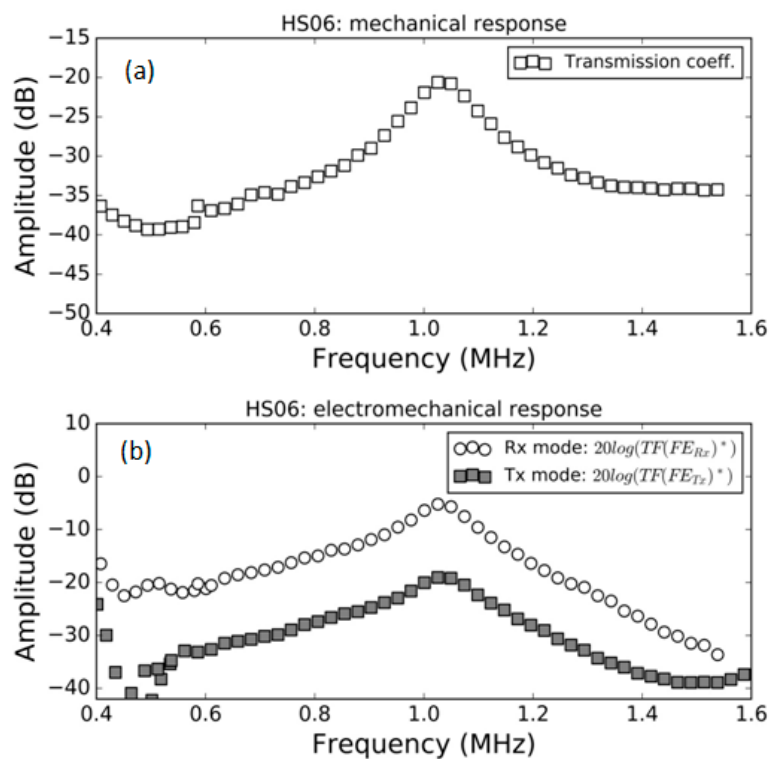


**Figure 7.** Measured response of the HS06 FE sample in air. (a) Modulus of the transmission coefficient vs. frequency; (b) electromechanical response vs. frequency both in *Tx* and *Rx* mode, (see Equations (16) and (22)).

### 3.2. FE Response in Water

Measurements of the modulus of the transmission coefficient and of the electromechanical response both in *Tx* and *Rx* mode in water for the samples HS03, HS03 + film and HS06 at normal incidence are shown in Figures 8–10, respectively. The repeatability of the measurements is typically within the range of the symbol size. Figures 8b, 9b and 10b show, in the same graph, both the *Tx* and *Rx* response. This is performed for convenience and there is no reason to expect the same response in *Tx* and *Rx* modes. Electromechanical measurements show a larger noise level below  $-35$  dB; this can be attributed to a reduced single-to-noise ratio.

The mechanical responses (Figures 8a, 9a and 10a) show the spectra of the transmission coefficient magnitude. These spectra clearly present the effect of the appearance of thickness resonances (where the transmission coefficient presents a local maximum). Two orders of these resonances are shown in Figure 8a that correspond to the half wavelength resonances (shifted due to the sandwich structure of the film, as explained in Ref. [38]). Two orders of these resonances are also shown in Figure 9a. In this case, they also correspond, approximately, to the half wavelength resonances due to the fact that the presence of water eliminates the effect of the adhesive film. Finally, Figure 10a shows the first thickness resonance (half wavelength mode) for the HS06 sample. Unlike in the previous case (air-coupled), the electromechanical response does not follow a similar trend and no electromechanical resonances appear in this case. These results are carefully discussed in the Discussion section.

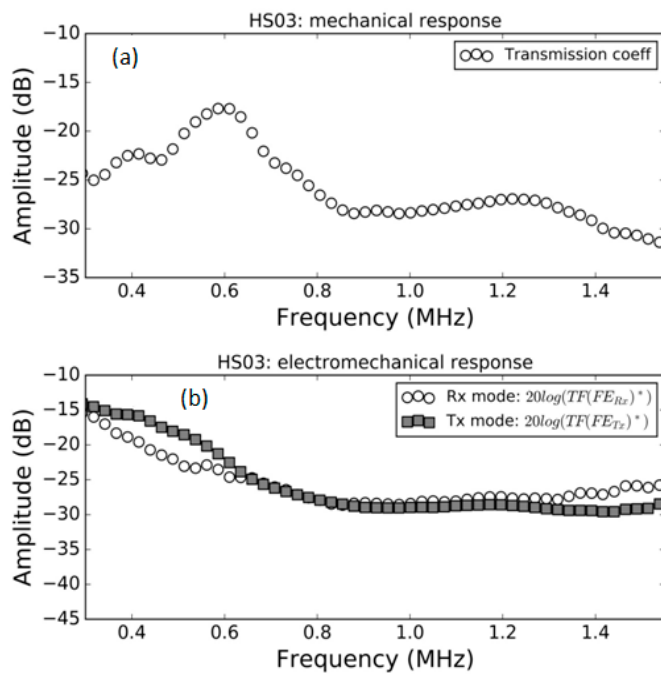


**Figure 8.** Measured response of the HS03 FE sample in water. (a) Modulus of the transmission coefficient vs. frequency; (b) electromechanical response vs. frequency both in *Tx* and *Rx* mode, (see Equations (16) and (22)).

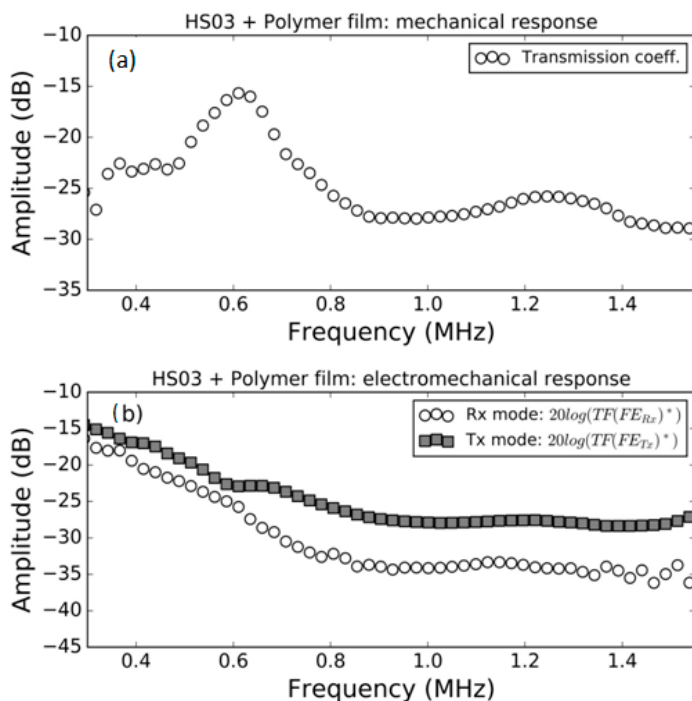


**Figure 9.** Measured response of the HS03 FE + adhesive film sample in water. (a) Modulus of the transmission coefficient vs. frequency; (b) electromechanical response vs. frequency both in *Tx* and *Rx* mode, (see Equations (16) and (22)).

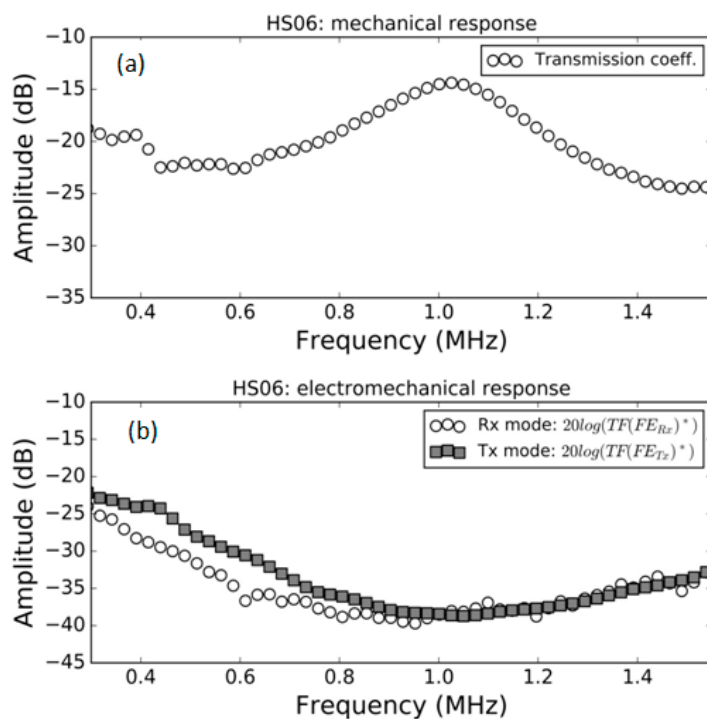


**Figure 10.** Measured response of the HS06 FE sample in water. (a) Modulus of the transmission coefficient vs. frequency; (b) electromechanical response vs. frequency both in Tx and Rx mode, (see Equations (16) and (22)).

#### 4. Discussion

##### 4.1. Discussion of the Modification of the FE Mechanical Response for Two Different External Loads: Air and Water

The mechanical response of the FE samples is studied through the analysis of the magnitude spectrum of the transmission coefficient for ultrasonic waves measured at normal incidence and in a frequency range that includes, at least, the first order thickness resonance of the FE film.

Transmission coefficient measurements of these films in air have been previously studied and reported (see Refs. [15,42]). The only difference in this case, compared with previously published results, is the presence of a sputtered Au layer. The results are shown in Figures 5a, 6a and 7a. The first thickness resonance appears at 0.59 and 1.03 MHz for HS03 and HS06, respectively. These values are slightly smaller than those previously reported (see Table 1). This is due to the presence of the sputtered Au layer. The presence of the adhesive tape film in the HS03 + film sample introduces as much larger load (compared with the load due to the Au layer). As consequence, the displacement towards lower frequencies and lower magnitude values is larger in this case, with the film response approaching a quarter wavelength thickness resonance response. This is similar to what was observed in Ref. [15] when a double-sided electrically conductive adhesive tape was attached to one of the FE film surfaces.

The spectra of the transmission coefficient of the FE samples are modified when water is used instead of air as the outer medium. For the HS03 sample (Figures 5a and 8a), the most significant change is the displacement of the second-order resonance from 1.05 MHz (in air) to 1.25 MHz (in water). In addition, resonances in air are sharper and the transmission coefficient level is, in general, lower. These latter modifications can be explained by the larger impedance mismatch between FE sample and external fluid in the case of air-coupled measurements, but the former modification is quite counterintuitive. Moreover,

the harmonic distortion observed in air (with the first order thickness resonance appear at 0.59 MHz and the second one at 1.05 MHz) is almost lost in water (first thickness resonance at 0.6 MHz and second at 1.25 MHz).

As expected, the influence of the adhesive tape film in the HS03 + film sample is almost negligible in water and measurements in water of the transmission coefficient of the HS03 sample (Figure 8a) and the HS03 + film sample (Figure 9a) are almost identical.

The transmission coefficient magnitude in HS06 measured in air is sharper and the overall level is lower compared with the measurements in water. As before, this can be explained by the larger impedance mismatch between the sample and the external fluid when this fluid is air. On the contrary no significant displacement of the resonant frequency is observed.

The modifications observed in the transmission coefficient when the air is replaced with water put forward the question of whether all the observed modifications can be fully explained by the change of the external fluid or if, on the contrary, the FE film undergoes any additional modification in its behavior. This is of interest especially for the HS03 sample where the displacement of the second order resonance towards higher frequency values when the air is replaced with water is difficult to explain by the mere action of the water load.

As this is of interest for this work, and for the potential use of these films for medical transducers and hydrophones, a more detailed analysis of this point has been performed. In particular, the studied films in [42], the same that we have used to fabricate the samples for this work, were used to measure transmission coefficient in water. For these samples, the transmission coefficient in air is well described by a theoretical model based on a layered structure, in particular, a sandwich structure. We have measured transmission coefficient measurements for these samples (HS03 and HS06), but in this case, in water. Then, we have used the same material parameters obtained in [42], from the air-coupled measurements, and used them to calculate the expected response in water. If the FE film remains unmodified, then the calculated transmission coefficient of the film in water using the material parameters obtained from air-coupled measurements should match the experimental measurements. If there is any difference, it can be concluded that the film response is modified when it is immersed in water.

Results are shown in Figures 11 and 12. These figures show the measured transmission coefficient in water—in this case, both magnitude and phase (open circles)—and the calculated transmission coefficient spectra in water assuming the FE film parameters obtained from measurements in air [42] (solid black line). It is clear that this calculated transmission coefficient fails to explain the measured response in water, so this fact supports the hypothesis that the film itself is modified when it is immersed in water. In addition, the figure also shows the prediction of the sandwich model when material parameters are recalculated for water (using the same procedure as in [42])—this is the dashed line. Clearly, the sandwich model is still able to reproduce the measured response in water, but the material parameters have to be changed. It can be seen from Figures 11 and 12 that this modification of the FE film is larger for the HS06 sample.

One remarkable feature is that in both cases the measured resonances in water appear at higher frequencies compared with the prediction obtained using the film parameters obtained from the air-coupled measurements and using water as outer medium.

It was verified that after water immersion films response in air-coupled measurements are the same as before immersion, without the need of any recovery time, so the mechanism for this modification must be reversible and operates without any delay. This together with the fact that FE surface is impervious support the hypothesis that this modification is not due to water percolation. Moreover, it was observed that the response in water is similar when other fluids are used instead of water (e.g., sunflower oil), so this discards any potential effect of the polar character of the water. In a similar way, as the sample is only submerged a few mm, the effect of hydrostatic pressure on the film must also be discarded.

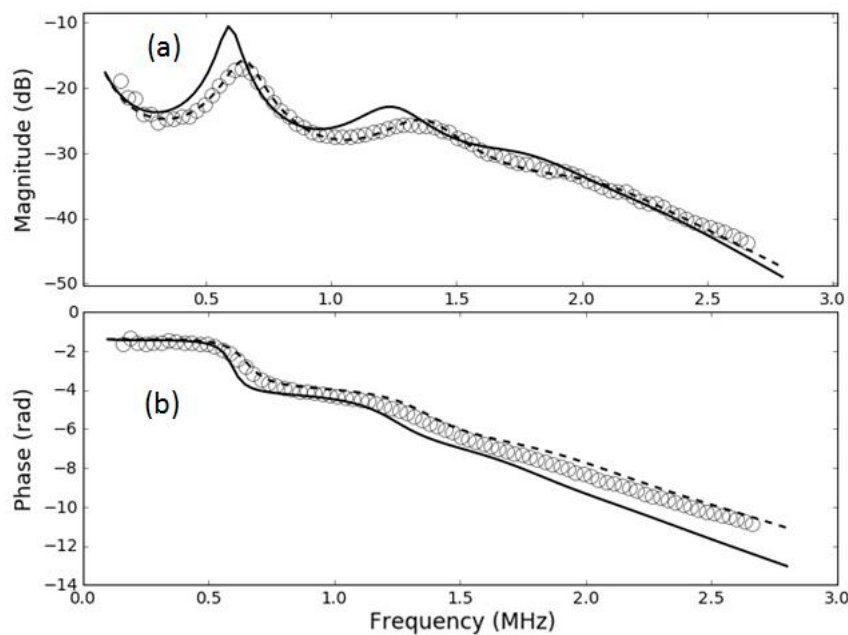


**Figure 11.** Magnitude (a) and phase (b) spectra of the transmission coefficient of the HS03 film in water immersion at normal incidence. Open circles: experimental data. Solid line: calculated response using film parameters obtained in [42]. Dashed line: calculated response using film parameters extracted from water immersion measurements.

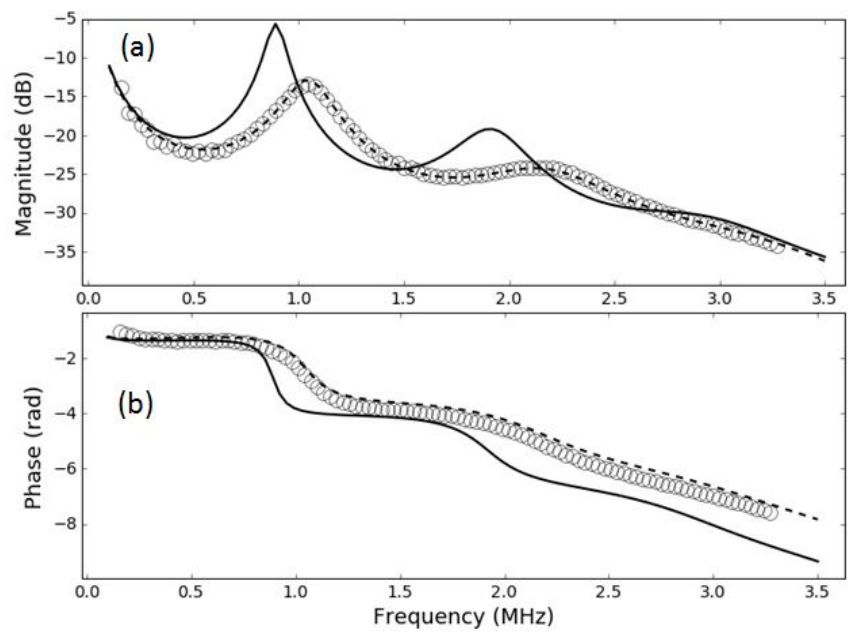


**Figure 12.** Magnitude (a) and phase (b) spectra of the transmission coefficient of the HS06 film in water immersion at normal incidence. Open circles: experimental data. Solid line: calculated response using film parameters obtained in [42]. Dashed line: calculated response using film parameters extracted from water immersion measurements.

#### 4.2. Electromechanical Response of the FE Films in Air and in Water

Unlike differences in the transmission coefficient, which required of a very detailed analysis to reveal the actual modification of the FE film response when the external fluid is changed (from air to water), the differences in the electromechanical response are evident.

In general, the variation with the frequency in the electromechanical response (both in  $T_x$  and  $R_x$  mode) in air follows the observed variation in the transmission coefficient. This is an expected result as at the resonant frequency of the film thickness mode, the strain and stress in the film is maximum due to the additive contribution of the reverberations within the film; therefore, it can be expected that the electromechanical conversion is also maximal at resonant frequencies. This response is observed in all cases, with the only exception being the second order resonance in the HS03 sample (Figure 5).

However, this behavior is completely different for samples in water. Thickness resonances of the FE samples are still present when the FE films are put in water (as can be seen Figures 8a, 9a and 10a), and this is a fully expected result given the large impedance difference between the FE films and the water. However, the electromechanical response does not follow the same trend as the transmission coefficient and the onset of mechanical resonances has no counterpart on the electromechanical response either in transmission or in reception mode.

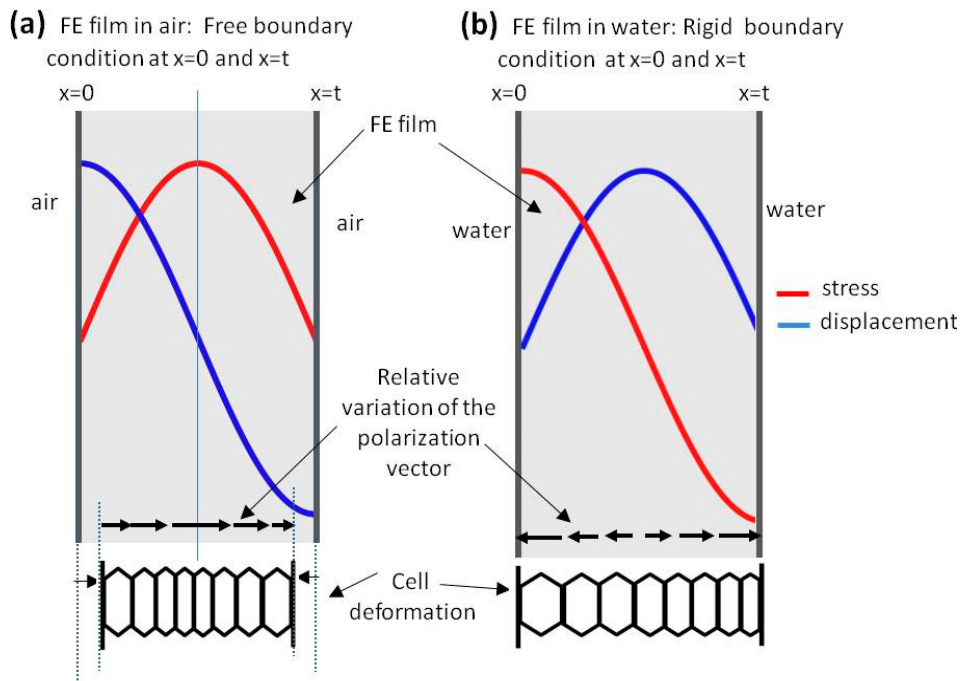
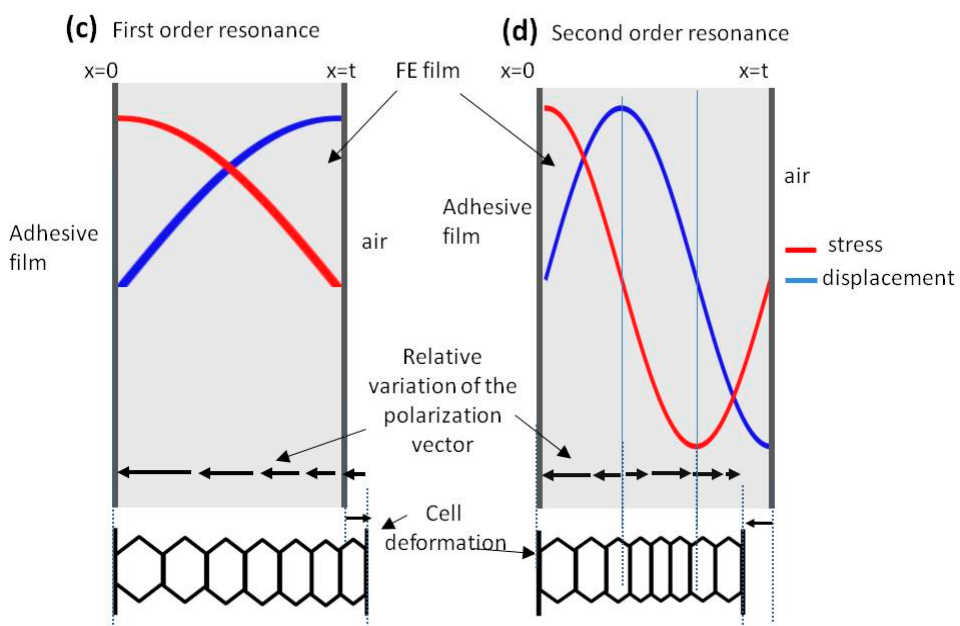
This can be attributed to the different nature of the boundary conditions in both cases (air and water) and the different modification of the polarization inside the material due to the resonances in the film. The situation is schematically explained in Figure 13.

Under air load, the impedance of the film is about 100 times larger than the impedance of the outer medium (air). Then, it can be assumed that the boundary conditions at the FE film surface are very close to those of a free boundary, i.e., maximal displacement and null stress. On the other hand, under water load, the impedance of the outer medium (water) is about 38 times the impedance of the film. Then, the boundary conditions at the FE film surface for the water-loaded case can be assumed to be very close to the rigid boundary condition, i.e., maximum stress and null displacement. Figure 13 schematically represents these two situations and the different pressure and displacement distribution across the film thickness produced by these different boundary conditions. In addition, cell deformation along the thickness is also depicted as well as the relative variation of the polarization vector.

As it can be seen in Figure 13a, the air-loaded case, the modification of the polarization in the FE cells is maximal at the center of the film and minimal on the surface, and the sign of the modification of the polarization vector is the same along the whole film thickness. Therefore, this results in a net variation of the mean polarization in the film. On the other hand, for the water-loaded case, the relative variation of the polarization inside the FE film has opposite signs in the two halves of the film (while polarization keeps the same direction in all the film in some part of the film it increases while in the other it decreases); therefore, it can be expected that the overall polarization modification is null. This explains the lack of electromechanical resonances in the water-loaded films.

The reason of the lack of the second order electromechanical resonance in Figure 5b is the same one that explains the lack of even piezoelectric thickness resonances in a piezoelectric plate and the reasoning is similar to that given for Figure 13b.

Quarter wavelength resonances are observed in the case of the film + adhesive tape in air (Figure 6b) or in the well-known case of air-coupled FE transducers (with a heavy backing). This resonant mode (Figure 6b) does present electromechanical resonances in both the first and the second order thickness resonances. This is explained in Figure 13c,d, where it is shown that under these conditions the net polarization modification along the FE film thickness is not null.

**1st half wavelength resonances in the FE film: symmetric boundary conditions**

**Quarter wavelength resonances in the FE film: asymmetric boundary conditions:  
Rigid boundary condition at  $x=0$  and free at  $x=t$** 


**Figure 13.** Representation of strain and stress, polarization variation and cell deformation distribution along the film thickness for different boundary conditions and resonance orders; (a) first half wave resonance with free boundary conditions; (b) first half wave resonance with rigid boundary conditions; (c) first quarter wavelength resonance; (d) second order quarter wave resonance.

## 5. Conclusions

This work shows that the response of thickness resonances and their associated electromechanical response in FE films is different in water and in air. The impedance of water is much larger than the impedance of the FE film; for this reason, boundary conditions at the FE surface are close to ideal rigid when the FE film is in water. This gives rise to a stress, displacement and polarization change distribution along the film thickness where the overall polarization modification is close to zero. On the contrary, when the film is in air, the impedance of the air is much lower than the impedance of the film and the boundary conditions are close to that of a free surface. Under these conditions, and for the uneven thickness resonance orders, the stress, displacement and polarization distribution along the film thickness gives rise to a net polarization variation. FE films under asymmetric conditions (quarter wavelength resonances) are close to this latter case, with the main difference that electromechanical resonances are observed for all orders of the mechanical resonances.

This difference in the ability of the film to couple mechanical into electrical energy, depending on the external fluid (that is on the boundary conditions), can also be the reason for the subtle differences observed in the transmission coefficient spectra.

**Author Contributions:** Conceptualization, J.Q.A. and T.G.Á.-A.; methodology, J.Q.A. and T.G.Á.-A.; validation, J.Q.A. and T.G.Á.-A.; formal analysis, J.Q.A. and T.G.Á.-A.; investigation, J.Q.A. and T.G.Á.-A.; resources, T.G.Á.-A.; data curation, T.G.Á.-A.; writing—original draft preparation, T.G.Á.-A.; writing—review and editing, T.G.Á.-A.; visualization, J.Q.A. and T.G.Á.-A.; supervision, T.G.Á.-A.; funding acquisition, T.G.Á.-A. All authors have read and agreed to the published version of the manuscript.

**Funding:** This work was supported in part by the Ministerio de Economía y Competitividad under Grant DPI2016-78876-R (AEI/FEDER, UE).

**Institutional Review Board Statement:** Not applicable.

**Informed Consent Statement:** Not applicable.

**Data Availability Statement:** The data presented in this study are available on request from the corresponding author and will also be publicly available in [www.us-biomat.com](http://www.us-biomat.com) (accessed on 29 August 2021).

**Conflicts of Interest:** The authors declare no conflict of interest and the funders had no role in the design of the study, in the collection, analyses, or interpretation of data; in the writing of the manuscript, or in the decision to publish the results.

## References

1. Savolainen, A.; Kirjavainen, K. Electrothermomechanical film. Part I. Design and characteristics. *J. Macromol. Sci. A-Chem.* **1989**, *26*, 583–591. [[CrossRef](#)]
2. Sessler, G.M.; Hillenbrand, J. Electromechanical response of cellular electret films. *Appl. Phys. Lett.* **1999**, *75*, 3405–3407. [[CrossRef](#)]
3. Gibson, L.; Ashby, M.F.; Brendan, A.H. *Cellular Materials in Nature and Medicine*; Cambridge University Press: Cambridge, UK, 2010; ISBN 9780521195447.
4. Restrepo, D.; Mankame, N.D.; Zavattieri, P.D. Programmable materials based on periodic cellular solids. Part I: Experiments. *Int. J. Solids Struct.* **2016**, *100–101*, 485–504. [[CrossRef](#)]
5. Wegener, M.; Wirges, W.; Fohlmeister, J.; Tiersch, B.; Gerhard-Multhaupt, R. Two-step inflation of cellular polypropylene films: Void-thickness increase and enhanced electromechanical properties. *J. Phys. D Appl. Phys.* **2004**, *37*, 623–627. [[CrossRef](#)]
6. Altafim, R.A.P.; Qiu, X.; Wirges, W.; Gerhard, R.; Basso, H.C.; Jenninger, W.; Wagner, J. Template-based fluoroethylenepropylene piezoelectrets with tubular channels for transducer applications. *J. Appl. Phys.* **2009**, *106*, 014106. [[CrossRef](#)]
7. Zhang, X.; Sessler, G.M.; Wang, Y. Fluoroethylenepropylene ferroelectret films with cross-tunnel structure for piezoelectric transducers and micro energy harvesters. *J. Appl. Phys.* **2014**, *116*, 074109. [[CrossRef](#)]
8. Dali, O.B.; Zhukov, S.; Rutsch, M.; Hartman, C.; von Seggern, H.; Sessler, G.M.; Kupnik, M. Biodegradable additive manufactured ferroelectret ultrasonic transducer with large output pressure. In Proceedings of the IEEE International Ultrasonic Symposium, Xi'an, China, 12–15 September 2021.
9. Qiu, X.; Wegener, M.; Wirges, W.; Zhang, X.; Hillenbrand, J.; Xia, Z.; Gerhard-Multhaupt, R.; Sessler, G.M. Penetration of sulfur hexafluoride into cellular polypropylene films and its effect on the electric charging and electromechanical response of ferroelectrets. *J. Phys. D Appl. Phys.* **2005**, *38*, 649–654. [[CrossRef](#)]

10. Wegener, M.; Wirges, W.; Gerhard-Multhaupt, R.; Bauer-Gogonea, S.; Paajanen, M.; Minkkinen, H.; Raukola, J.; Dansachmüller, M.; Schwodiauer, R.; Bauer, S. Controlled inflation of voids in cellular polymer ferroelectrets: Optimizing electromechanical transducer properties. *Appl. Phys. Lett.* **2004**, *84*, 392–395. [[CrossRef](#)]
11. Mellinger, A.; Wegener, M.; Wirges, W.; Mallepally, R.R.; Gerhard-Multhaupt, R. Thermal and Temporal Stability of Ferroelectret Films Made from Cellular Polypropylene/Air Composites. *Ferroelectrics* **2006**, *331*, 189–199. [[CrossRef](#)]
12. Saarimaki, E.; Paajanen, M.; Savijarvi, A.; Minkkinen, H.; Wegener, M.; Voronina, O.; Schulze, R.; Wirges, W.; Gerhard-Multhaupt, R. Novel heat durable electromechanical film: Processing for electromechanical and electret applications. *IEEE Trans. Dielectr. Electr. Insul.* **2006**, *13*, 963–972. [[CrossRef](#)]
13. Qiu, X.; Mellinger, A.; Wegener, M.; Wirges, W.; Gerhard, R. Barrier discharges in cellular polypropylene ferroelectrets: How do they influence the electromechanical properties? *J. Appl. Phys.* **2007**, *101*, 104112. [[CrossRef](#)]
14. Fang, P.; Wirges, W.; Wegener, M.; Zirkel, L.; Gerhard, R. Cellular polyethylene-naphthalate films for ferroelectret applications: Foaming, inflation and stretching, assessment of electromechanically relevant structural features. *e-Polymers* **2008**, *8*, 1–9. [[CrossRef](#)]
15. Álvarez-Arenas, T.E.G.; Calás, H.; Cuello, J.E.; Fernández, A.R.; Muñoz, M. Noncontact ultrasonic spectroscopy applied to the study of polypropylene ferroelectrets. *J. Appl. Phys.* **2010**, *108*, 074110. [[CrossRef](#)]
16. Mohebbi, A.; Mighri, F.; Ajji, A.; Rodrigue, D. Cellular Polymer Ferroelectret: A Review on Their Development and Their Piezoelectric Properties. *Adv. Polym. Technol.* **2018**, *37*, 468–483. [[CrossRef](#)]
17. Liu, B.; Han, L.; Pan, L.; Li, H.; Zhao, J.; Dong, Y.; Wang, X. Flexible Multiscale Pore Hybrid Self-Powered Sensor for Heart Sound Detection. *Sensors* **2021**, *21*, 4508. [[CrossRef](#)]
18. Sessler, G.M.; Hillenbrand, J. Novel Silicon and Polymer Sensors in Acoustics. In Proceedings of the SENSOR+TEST Conference, Nürnberg, Germany, 26–28 May 2009; pp. 9–14. [[CrossRef](#)]
19. Luo, Z.; Shi, J.; Beeby, S.P. Novel thick-foam ferroelectret with engineered voids for energy harvesting applications. *J. Phys. Conf. Ser.* **2016**, *773*, 012030. [[CrossRef](#)]
20. Zhang, Y.; Bowen, C.R.; Ghosh, S.K.; Mandal, D.; Khanbareh, H.; Arafa, M.; Wan, C. Ferroelectret materials and devices for energy harvesting applications. *Nano Energy* **2019**, *57*, 118–140. [[CrossRef](#)]
21. Zhang, X.; Pondrom, P.; Sessler, G.M.; Ma, X. Ferroelectret nanogenerator with large transverse piezoelectric activity. *Nano Energy* **2018**, *50*, 52–61. [[CrossRef](#)]
22. Ma, X.; Zhang, X.; Fang, P. Flexible film-transducers based on polypropylene piezoelectrets: Fabrication, properties, and applications in wearable devices. *Sens. Actuators A Phys.* **2017**, *256*, 35–42. [[CrossRef](#)]
23. Shi, J.; Beeby, S. Textile based ferroelectret for foot pressure sensor. In Proceedings of the IEEE International Conference on Flexible and Printable Sensors and Systems (FLEPS), Glasgow, UK, 8–10 July 2019; pp. 1–3. [[CrossRef](#)]
24. Buchberger, G.; Schwodiauer, R.; Arnold, N.; Bauer, S. Cellular ferroelectrets for flexible touchpads, keyboards and tactile sensors. *Proc. IEEE Sens.* **2008**, *2008*, 1520–1523. [[CrossRef](#)]
25. Sborikas, M.; Wegener, M. Cellular-foam polypropylene ferroelectrets with increased film thickness and reduced resonance frequency. *Appl. Phys. Lett.* **2013**, *103*, 252901. [[CrossRef](#)]
26. Kressmann, R. New piezoelectric polymer for air-borne and water-borne sound transducers. *J. Acoust. Soc. Am.* **2001**, *109*, 1412–1416. [[CrossRef](#)]
27. Wegener, M.; Tuncer, E.; Wirges, W.; Gerhard, R.; Dansachmuller, M.; Bauergogonea, S.; Schwodiauer, R.; Bauer, S. Ferroelectrets: Highly anisotropic electrically charged polymer foams for electromechanical transducer applications. *Proc. IEEE Ultrason. Symp.* **2004**, *62*, 1138–1141. [[CrossRef](#)]
28. Döring, J.; Bartusch, J.; Beck, U.; Erhard, A. EMFIT ferroelectret film transducers for non-contact ultrasonic testing. In Proceedings of the European Conference NDT, Berlin, Germany, 25–29 September 2006; pp. 1–10.
29. Ealo, J.; Seco, F.; Jimenez, A. Broadband EMFi-based transducers for ultrasonic air applications. *IEEE Trans. Ultrason. Ferroelectr. Freq. Control* **2008**, *55*, 919–929. [[CrossRef](#)]
30. Gaal, M.; Bartusch, J.; Döring, J.; Dohse, E.; Lange, T.; Hillger, W.; Kreutzbruck, M. Air-coupled ferroelectret ultrasonic transducers applied to testing of fiber-reinforced polymers. In Proceedings of the International Conference of the Slovenian Society for Non-Destructive Testing, Portorož, Slovenia, 4–6 September 2013; pp. 43–49.
31. Álvarez-Arenas, T.E.G. Air-coupled piezoelectric transducers with active polypropylene foam matching layers. *Sensors* **2013**, *13*, 5996–6013. [[CrossRef](#)] [[PubMed](#)]
32. Gaal, M.; Bartusch, J.; Dohse, E.; Schadow, F.; Köppé, E. Focusing of ferroelectret air-coupled ultrasound transducers. *AIP Conf.* **2016**, *1706*, 080001.
33. Tang, J.; Tong, L.; Xiang, Y.; Qiu, X.; Deng, M.; Xuan, F. Design, fabrication and characterization of Emfi-based ferroelectret air-coupled ultrasonic transducer. *Sens. Actuators A Phys.* **2019**, *296*, 52–60. [[CrossRef](#)]
34. Döring, J.; Bovtun, V.; Gaal, M.; Bartusch, J.; Erhard, A.; Kreutzbruck, M.; Yakymenko, Y. Piezoelectric and electrostrictive effects in ferroelectret ultrasonic transducers. *J. Appl. Phys.* **2012**, *112*, 084505. [[CrossRef](#)]
35. Bovtun, V.; Döring, J.; Bartusch, J.; Gaal, M.; Erhard, A.; Kreutzbruck, M. Enhanced electromechanical response of ferroelectret ultrasonic transducers under high voltage excitation. *Adv. Appl. Ceram.* **2013**, *112*, 97–102. [[CrossRef](#)]
36. De Medeiros, L.J.; Kamimura, H.A.S.; Altafim, R.A.P.; Carneiro, A.A.O.; Amorim, M.F.; Altafim, R.A.C. Piezoelectret-based hydrophone: An alternative device for vibro-acoustography. *Meas. Sci. Technol.* **2015**, *26*, 095102. [[CrossRef](#)]

37. Palitó, T.T.C.; Assagra, Y.A.O.; Altafim, R.A.P.; Carmo, J.P.; Altafim, R.A.C. Low-cost electro-acoustic system based on ferroelectret transducer for characterizing liquids. *Meas. J. Int. Meas. Confed.* **2019**, *131*, 42–49. [[CrossRef](#)]
38. De Luna, D.R.; Palitó, T.; Assagra, Y.; Altafim, R.; Carmo, J.; Carneiro, A.; de Sousa, J.V.A. Ferroelectret-based hydrophone employed in oil identification-A machine learning approach. *Sensors* **2020**, *20*, 2979. [[CrossRef](#)] [[PubMed](#)]
39. Álvarez-Arenas, T.E.G.; Diez, L. Ferroelectret transducers for water immersion and medical imaging. In Proceedings of the IEEE International Ultrasonic Symposium (IUS), Tours, France, 18–21 September 2016; pp. 4–7.
40. Aguilar, J.Q.; Álvarez-Arenas, T.E.G. Optimization of ferroelectret transducers for pulse-echo water immersion operation. In Proceedings of the IEEE International Ultrasonics Symposium (IUS), Glasgow, UK, 6–9 October 2019; pp. 2604–2607. [[CrossRef](#)]
41. Aguilar, J.Q.; Svilainis, L.; Camacho, J.; Álvarez-Arenas, T.E.G. Ferroelectret Ultrasonic Transducers for Pulse-Echo Water Immersion. *Appl. Sci.* **2020**, *10*, 8771. [[CrossRef](#)]
42. Aguilar, J.Q.; Munoz, M.; Álvarez-Arenas, T.E.G. Interpretation of the Thickness Resonances in Ferroelectret Films Based on a Layered Sandwich Mesosstructure and a Cellular Microstructure. *IEEE Trans. Ultrason. Ferroelectr. Freq. Control* **2021**, *68*, 1245–1252. [[CrossRef](#)] [[PubMed](#)]



# Application of Ferroelectret Films as Hydrophones: Flat and Cylindrical Geometries

J. Quirce, M.D. Fariñas, L. Svilainis, T.E.G Álvarez-Arenas, *Member, IEEE*

**Abstract**—The use of polypropylene ferroelectret films (FF) as active layers to manufacture hydrophones is studied. First, flat prototypes with apertures of 11 and 18 mm are built and tested in the frequency range from 0.1 to 8 MHz. For comparison purposes, similar hydrophones are fabricated using PVDF film. Similar sensitivity values are obtained at frequencies below 200 kHz for both FF and PVDF hydrophones. This result and the interest in testing FF response on non-flat surfaces motivate the fabrication and testing of cylindrical hydrophones (8 and 2 mm diameter). A similar 8 mm cylindrical PVDF hydrophone is also built following the same procedure for comparison purposes. Sensitivity obtained for PVDF and FF cylindrical hydrophones is similar. Finally, the ferroelectret hydrophone response is tested under hydrostatic pressure up to 7 bar (equivalent to a depth of 70 m) in such case a reduced and transient effect of the pressure on the hydrophone sensitivity is reported, though there is no significant alteration of the FF hydrophone response.

In conclusion, the paper shows that it is possible to fabricate ferroelectret hydrophones with different configurations, resistant to hydrostatic pressures that, in some cases, can be an interesting alternative to other conventional hydrophones. This opens the way for material optimization for this particular application.

**Index Terms**—Ultrasonic transducers, ferroelectret film, hydrophone.

## I. INTRODUCTION

FERROELECTRET films (FF) are soft material made of a cellular polymer matrix with separated and trapped stable electrical charges that present a measurable piezoelectric response (see Table I). FF can be manufactured with different polymers such as polytetrafluoroethylene [1], polyethylene-naphthalate [2], cyclo-olefin copolymers [3], polypropylene, among others and this technology have been used to develop some device applications like [4], [5]. For this work the FF used, was made of polypropylene by the company EMFIT,

Submitted 01/09/2022. This work was supported in part by Financial support from Ministerio de Economía y Competitividad under grant DPI2016-78876-R, AEI/FEDER, UE.

This work received partial funding (LS) from European Regional Development Fund (project No. 01.2.2-LMT-K-718-03-0026) under grant agreement with the Research Council of Lithuania (LMTLT)

J. Quirce, M.D. Fariñas and T.E.G Álvarez-Arenas were with the Institute for Physical and Information Technologies, of the Spanish National Research Council, 28006 Madrid, Spain. (e-mail: j.quirce.agular@gmail.com),(e-mail: md.farinias@csic.es),(e-mail: t.gomez@csic.es)

L. Svilainis, was with Electronics Engineering Department, Kaunas University of Technology, 51368 Kaunas, Lithuania (e-mail: au-thor@lamar.colostate.edu).

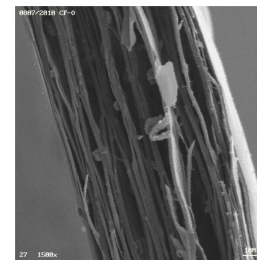


Fig. 1. cross-section SEM image of the ferroelectret polypropylene film HS03.

with a commercial name HS03 whose main mechanical properties are described in Table I and reported in [6]. Fig. 1 shows the cross-section SEM image of the particular FF used in this work. The pores that entrap the electrical charge and cause the elastic modulus to be very low in the thickness direction can be appreciated. Thanks to this feature the film is flexible and allows to cover developable surfaces [7]. In this paper the film flexibility is used to cover a cylindrical aperture for a hydrophone. Its low acoustic impedance about 0.046 MRayl makes the material suitable to be used as an active layer for air-coupled transducers [8], sensors... [9], [10]), as the acoustic impedance mismatch with the air is strongly reduced when compared to piezoelectric ceramics. Recently, the possibility to use FF polymers as active layer for water immersion transducers has been studied [11], [12]. As reported by Quirce et al. [13], the water is a significant mechanical load for the FF film when immersed. This significantly damps the thickness resonances and may suppress the piezoelectric resonance of the FF linked to the thickness resonance of the film. This phenomenon suggests the possibility of using this material for hydrophone construction since it points out to a flat frequency response with no upper limit linked to the appearance of thickness resonances as it happens with PVDF hydrophones. The main drawback lies on the reduced sensitivity. It should be noted that FF material has been used before for the construction of hydrophones for a different operational frequency range from 4 to 80 kHz [14], [15].

The hydrophone is a device made for measuring acoustic pressure under water, which was invented in 1929 by Reginald Fessenden. Hydrophones are widely used in many fields, such as underwater telecommunication [16], oilfield services [17], SONAR [18], military applications [19], fishing [20],

**TABLE I**  
MAIN PROPERTIES OF THE FF USED IN THIS WORK (HS03 EMFIT).

Comercial name	Density (Kg/m <sup>3</sup> )	Thickness (μm)	Elastic Modulus (MPa)	Thickness resonance freq. (MHz)	Impedance (MRayl)
Emfit HS03	550	70	3.98	0.65	0.046

underwater search and rescue [21], [22], and the most studied area: medical applications [23], [24].

There are a large number of piezoelectric materials that can be used as active layer for hydrophone construction. Ceramics, are the most common material for transmitter receiver transducer due to the piezoelectric coefficient and ease of fabrication, yet they are less common for hydrophones [25]. Polymers are more flexible than ceramics and the acoustic impedance is lower. The most studied one is Polyvinylidene fluoride (PVDF) which is the typical material for needle hydrophones [26]. Composites, although they present a wide bandwidth and good hydrostatic sensitivity, the manufacturing is expensive and difficult [27]. Ferroelectric single-crystals have also been used in different medical applications [28]. Finally fiber-optic hydrophones have been widely studied recently [29].

In general the frequency response of hydrophones is not completely flat. Therefore, in order to calculate the acoustic pressure waveform it is necessary to use hydrophone transfer function also known as calibration chart or just calibrated sensitivity used to convert the measured volts with the hydrophone into pressure. FF hydrophones are not an exception, and their frequency response is not flat either [11]–[13]. There are several methods to calculate the hydrophone sensitivity [30], for this work the FF hydrophone response is compared with a calibrated hydrophone used as reference. (substitution technique). Further details are explained in section IV.

28

## II. HYDROPHONE CONSTRUCTION

### A. Piston hydrophone

Fig. 2 shows the FF piston hydrophone design scheme used for this study. Two different sizes were manufactured. First, circular active layer with a diameter of 18 mm and height of 43 mm for FF hydrophone F18-1 and F18-2. Second, circular active layer diameter of 11 mm and height of 28 mm for hydrophones F11-1 and F11-2.

The inner design is similar for both sizes. On the right part on Fig. 2 a detailed section of the layer construction is shown. On the top, the gold layer is presented. The reason of adding gold by sputtering technique is to reinforce and prevent the degradation of the FF metallized electrode as it was observed previously when the FF was operating as transmitter [12]. The effect of the thin layer of gold on the hydrophone sensitivity response is negligible.

To quantify the thickness of the layer of gold, the spectra of the pulse-echo response of the hydrophone with and without gold and coupled into the air is both measured and calculated.

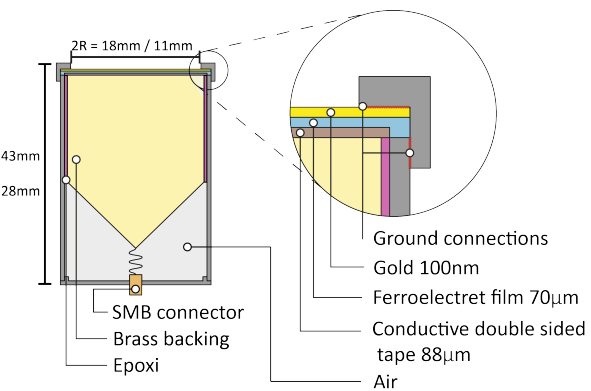


Fig. 2. FF piston hydrophone design.

It is well known that the pulse-echo response in air is pretty resonant and is dominated by the FF quarter wavelength resonance. Therefore, it is very sensitive to any load on the FF film and a measurable displacement of the resonant frequency towards lower frequencies is observed when the gold is sputtered on the FF surface. The thickness of the sputtered layer of gold can be inferred from this frequency shift of the FF resonant response measured in the pulse-echo response in air. This permitted us to estimate that the typical thickness of the layer of gold is 100 nm.

Leica-microsystems, model EM ACE600 sputter coater was used to deposit the layer of gold. Sputtering time was set to 40 s. Then the FF is glued to the brass backing with a 3M electrically conductive double-sided tape layer of 88 μm (see Fig. 2). Zig-zag red lines point the ground connection, to avoid the short-circuit a thin epoxy layer is placed between the housing and the brass backing. Finally the bottom lid is fitted with a SMB connector. Fig. 3 shows pictures of the FF hydrophones prototypes build and tested in this study. The gold color of the active layer is due to the sputtered layer of gold.



Fig. 3. 1- FF piston hydrophones manufactured for this study.

### *B. Cylindrical hydrophone*

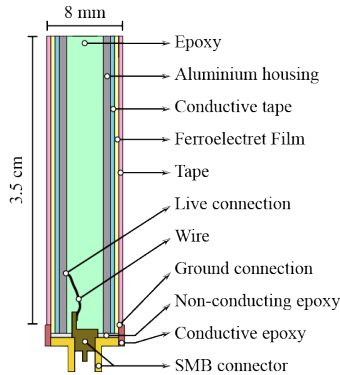


Fig. 4. FF cylindrical hydrophone design.



Fig. 5. From left to right, FF 8 mm diameter, PVDF 8 mm diameter, FF 4 mm diameter.

Hydrophones with cylindrical apertures have been commonly used in different cases [31]. Fig. 4 shows the design used for the FF cylindrical hydrophones constructed for this work. The FF is wrapped on a cylinder which dimensions are, 8 mm of diameter and 35 mm height for second hydrophone. FF is glued to the cylinder with double sided conductive tape and it does not complete the 360 degrees. The reason for that is to avoid the contact between both sides of the film that may short-circuit. The gap between the start and end of the FF rolled up is reinforced with tape to increase the sturdiness. The height of the cylinder (30 mm) was chosen based on the aperture size of the source transducers since smaller height would not cover all the acoustic field at focus distance and higher height makes the hydrophone bigger with no sensitivity advantage.

Fig. 5 shows some pictures of the fabricated cylindrical hydrophone prototypes using FF and PVDF.

## III. EXPERIMENTAL SETUP

### *A. Transmitters and reference hydrophone*

Several transmitters available in the laboratory were used to explore the reception band of the FF hydrophone in the

TABLE II  
TRANSMITTERS USED FOR THIS WORK.

Manufacturer	model	Frequency range MHz	Tx to Hydro Distance
Olympus-NDT	X1020	0.05 - 0.15	5 cm
CSIC	-	0.13 - 0.34	2.5 cm
Olympus-NDT	V1012	0.05 - 0.55	2.5 cm
Tecal	20-323	0.35 - 0.740	5 cm
Olympus-NDT	V314	0.75 - 1.25	10 cm
Olympus-NDT	A305S	1.3 - 3.2	10.4 cm
Olympus-NDT	A308S	3.3 - 7.5	10.3 cm

frequency range of interest. The transmitters used for this study and each frequency operative range are detailed in table II.

All commercial transmitters (Tx) apertures used for this work are around  $4.5 \text{ cm}^2$ . The different apertures sizes between the Tx are not critical for the objective of this work.

The FF hydrophone is placed at the natural focus distance from the source transmitter calculated as:  $d = a^2/\lambda$  where  $a$  is the radius of the aperture,  $\lambda = c/f$  where  $c$  is the ultrasound velocity and  $f$  is set at the Tx nominal center frequency.

A 4 mm needle hydrophone NH4000 and a DC coupler with power supply from Precision Acoustics Ltd (PA) was used as reference hydrophone for this study. Fig. 6 shows the PA hydrophone sensitivity vs frequency. The calibrated frequency response provided by the manufacturer is plotted with different colors to indicate the frequency range of the different transmitters (see table II) used to measure the FF hydrophone response.

### *B. Experimental setup*

Fig. 7 shows the scheme of the experiment setup. Metacrylate tank is filled with degassed water up to three quarters full.

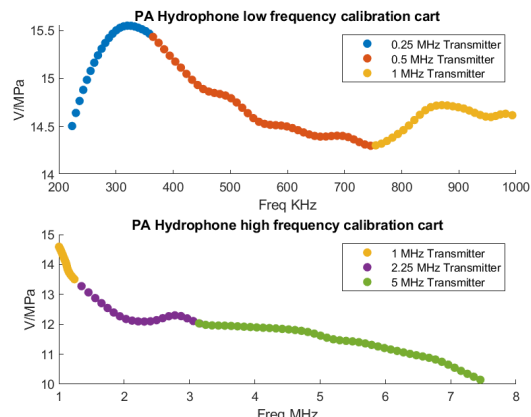
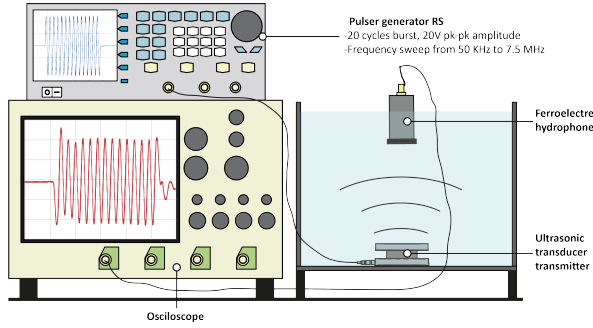


Fig. 6. The calibrated chart of NH4000 hydrophone from Precision Acoustic. The colors indicate the frequency range covered by each transmitter.



**Fig. 7.** Setup scheme of the experiment.

- 1 Inside of the tank both the transmitter connected to a pulser  
2 generator and the FF hydrophone / PA hydrophone connected  
3 to a oscilloscope are immersed.  
4 The 0.25 MHz, 0.5 MHz and 1 MHz transmitter distance  
5 concur with the natural focus. The 2.25 MHz and 5 MHz  
6 transmitter distance was fixed around 10 cm due to the water  
7 tank limitation size.

#### IV. METHOD FOR MEASURING HYDROPHONE RESPONSE

##### A. Alignment of the hydrophone and measurement

10 The hydrophone alignment is adjusted manually searching  
11 for the maximum amplitude of the peak - peak (pk-pk) signal  
12 hydrophone without average. Orthogonality between the trans-  
13 mittor and reference hydrophone is achieved by maximizing  
14 the echo from the reference hydrophone, whose active layer  
15 diameter is 4 mm, registered at the transmitter working in  
16 pulse-echo mode. The same procedure is used for the rest of  
17 the hydrophones.

18 This part of the experiment is quite delicate since the cal-  
19 culated FF hydrophone sensitivity continuity on the frequency  
20 limits partly depends on good alignment. The tone burst signal  
21 needs to be long enough to achieve the target frequency while  
22 avoiding the use of very long pulses that may cause the  
23 overlapping of echo signals and distort the pk-pk amplitude  
24 measurement. The complexity of the alignment increases with  
25 the tone burst frequency since the wavelength is shortened  
26 from 1 cm at 150 kHz to 200 μm at 7.5 MHz.

27 Once the Tx and the hydrophone are aligned, the signal  
28 is averaged four times to increase the SNR. The transmitter  
29 transducer is driven by a RS PRO SDG 1032X, sine-wave,  
30 tone burst of 20 V pk-pk amplitude. The number of cycles  
31 in the burst was 20, based to avoid the reverberation overlap  
32 with the water tank walls which is more problematic at low  
33 frequencies. The tone burst frequency is swept from the lower  
34 limit to the upper limit of the Tx bandwidth (see Fig. 6) with  
35 10 kHz steps for frequencies below 1 MHz, otherwise, the  
36 step was fixed to 50 kHz. At every step of the frequency  
37 sweep, the acoustic pressure signal generated by the Tx is  
38 received with the FF hydrophone / reference hydrophone with  
39 a SMB to BNC 1.5 m cable and digitized with the RTB2004  
40 Rohde & Schwarz oscilloscope with a sample rate of 2.5 GSa/s  
41 and 1 MΩ impedance termination. Then the desired pk-pk

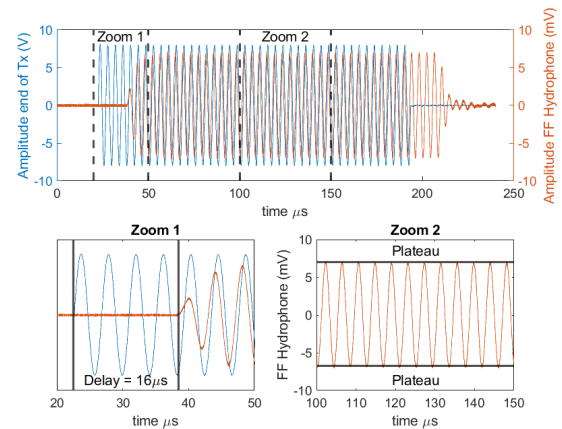


**Fig. 8.** Signal measured at the end of the Tx (Blue) and signal measured with the FF hydrophone F11-1.

amplitude measurement is obtained when the plateau region is achieved and all the crests and trough waves level match.

Fig. 8 presents an example of oscilloscope measurement during the measuring. The orange line is the sampled signal received with the FF hydrophone. The excitation signal to drive the Tx is presented with a blue line. Noteworthy the pk-pk amplitude is set at the pulser at 20 V but Fig. 8 shows 16 V, this is because the Tx is loaded when it is connected, and this load changes with the frequency but specially vary up when the Tx is replaced. No additional consideration needs to be done when the sensitivity is calculated, since the excitation signal to the transmitter is the same for the FF hydrophone and reference hydrophone.

Distance between the transmitter and the hydrophone is estimated in real time observing the time of flight with the cursor tool facility integrated in the oscilloscope as it is shown in the zoom 1 of Fig. 8. When the signals have been digitized a cross correlation method is used to calculate the time of flight and then the hydrophone transmitter distance [32]. No significant differences were found between time of flight and cross correlation methods. In addition, zoom 2 shows the region of interest where the plateau was achieved and the pk-pk amplitude measurement was taken.

## V. RESULTS AND DISCUSSION

### A. Sensitivity via substitution

To provide a first estimation of this new type of hydrophone we measured the ultrasound pressure field produced by some transducer with reference (calibrated) hydrophone and the evaluated FF hydrophone. The FF hydrophone sensitivity  $S_t(f)$  is calculated as

$$S_t(f) = \frac{FF\ hydrophone\ response(f, z)}{Pressure(f, z)} = \frac{R_t(f, z)}{\frac{R_r(f, z)}{S_r(f)}} = \frac{R_t(f, z) * S_r(f)}{R_r(f, z)}, \quad (1)$$

where  $S_r(f)$  is the reference hydrophone sensitivity detailed by the manufacturer and presented in Fig. 6.  $R_t(f, z)$  is the FF hydrophone frequency response at distance  $z$  measured in Volts and  $R_r(f, z)$  is the reference hydrophone frequency response measured in volts at distance  $z$ .

For this experiment a clean methacrylate tank filled with degassed water was used. The FF hydrophones were measured 22 °C. Previous studies have reported that FF response decreases with the temperature since the permanent polarization of the air gaps vanish [33] [34]. So the operating water temperature range goes from 5 °C up to 50 °C with better performance at low temperatures. Above 50 °C the risk of FF depolarization is too high and it could lead to irreversible damage of the hydrophone.

FF hydrophone sensitivity has not been measured in other liquid media.

### B. Signal-to-noise ratio

The noise floor of the oscilloscope with 1 MΩ input impedance limits the measurement of small acoustic signals. The lowest pressure that can be measured depends of the frequency since the FF hydrophone response is not flat. If the hydrophone sensitivity is assumed to be 0.2 V/MPa and the noise floor calculated as the RMS value of the measured signal exciting the emitting transducer is 77 µV leads to noise equivalent pressure:  $77 \mu\text{V} / (0.2 \text{ V} / \text{MPa}) = 388 \text{ Pa}$ . No mechanical damage have been observed when the FF hydrophone was operating under 56.6 kPa fields. Then the pressure threshold of the FF hydrophone is limited by the pressure upper limit of the reference hydrophone that is around 87.5 kPa or 700 mV.

### C. Piston hydrophone frequency response

Fig. 9a shows the end-of-cable sensitivity for the piston FF hydrophones with 10 kΩ load for the frequency range, 130 kHz up to 1 MHz. FF Hydrophone sensitivity drops drastically (from 6 V/MPa to 1.5 V/MPa in the frequency range from 130 kHz to 250 kHz. FF Hydrophone F11-1 and F11-2 present lower sensitivity than F18-1 and F18-2 since the aperture is 39% smaller.

FF hydrophone performance above 7.5 MHz has been explored in the congress paper [37]. It shows critical SNR and it becomes necessary to include a receiving stage where a certain gain must be applied. The final outcome is the result of concatenating the FF hydrophone response for each Tx frequency range showed in table II and Fig. 6. The ratio between the normalized acoustic pressure area and the aperture size used, must be constant to ensure continuity of the frequency response at the frequency limits of each Tx. As it is shown in Fig. 16, the ratio can not be constant due to the

TABLE III  
GAPS BETWEEN THE TRANSMITTERS BAND

0.25 MHz to 0.5 MHz	0.5 MHz to 1 MHz	1 MHz to 2.25 MHz	2.25 MHz to 5 MHz
772 mV/MPa	298 mV/MPa	35 mV/MPa	-64 mV/MPa

acoustic pressure field geometry and its variation according to the frequency. In addition, differences sizes of transmitter apertures could cause ratio modifications, but these differences are not significantly large to expect big variations of the ratio. Section G explains the axial pressure field generated by each Tx at the distance showed in table II.

Despite all the considerations explained to avoid the discontinuities at the frequency limit of the Tx, small manual corrections were applied to ensure the continuity of the hydrophone reception band. If sensitivity corrections are not applied there is a gap between bands of the consecutive transmitters, this gap is calculated as it is described in equation 2 and the gap values are shown in table III. Additionally, after the correction is applied, the sensitivity curves are smoothed using the locally estimated scatterplot smoothing, also known as "loess" method that is integrated in MATLAB 2022b with a span number of 0.23. For further details consult the MATLAB 2022b documentation.

### D. Cylindrical hydrophone sensitivity

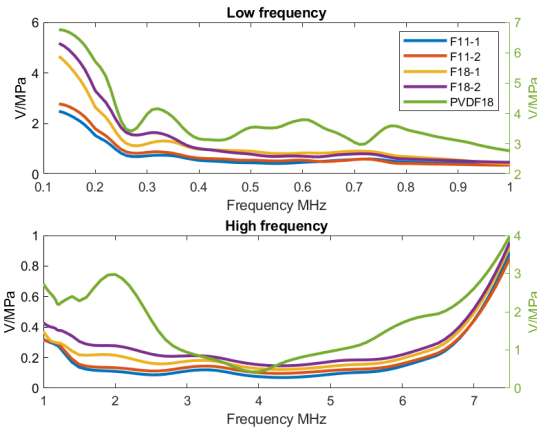
Cylindrical hydrophone frequency response has been explored from 60 kHz up to 450 kHz. PVDF and FF response is strong up to 7.5 MHz with better performance at high frequencies the PVDF and for lower frequencies the FF. As the excitation signal frequency increases, the wavelength becomes shorter and it complicates the interpretation of the received signal.

Fig. 10 shows the cylindrical hydrophone transverse plane operating inside of an acoustic field made up of sine monochromatic planar waves burst with 1 MHz frequency on the left image and 60 kHz on the right image. For 1 MHz, the piezoelectric material (FF / PVDF) surface of the hydrophone is receiving different amplitude pressures depending on the position, which makes the received signal not easy to interpret.

Nevertheless for 60 kHz the wavelength is 24.17 mm, much larger than the cylindrical hydrophone diameter, 8 mm, so it is assumed the acoustic pressure has the same value in the entire FF / PVDF surface. The sensitivity is 1.85 V/MPa and 0.83 V/MPa for the FF and PVDF respectively at 60 kHz.

Fig. 11 shows close sensitivity for the PVDF and FF of 8 mm diameter since 0 dB corresponds to close voltage values, 7.4 V and 6.2 V respectively. The cylindrical hydrophone with

$$\text{Gap} = \frac{\text{FF sensitivity (V) end of band}}{\text{Pressure by its transmitter at the end of band}} - \frac{\text{FF sensitivity (V) beginning of the next band}}{\text{Pressure originated by its transmitter at the beginning of the next band}} \quad (2)$$



**Fig. 9.** FF hydrophones frequency response.

On the top: Frequency range from 130 kHz up to 1 MHz  
On the bottom: Frequency range from 1 MHz up to 7.5 MHz  
High and low frequency chart sensitivity axis for FF hydrophones is located on the left and for the PVDF hydrophones is located on the right.

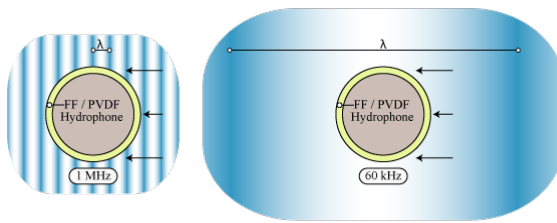


**Fig. 10.** Cylindrical hydrophones immersed in water with a sine wave one-dimensional monochromatic burst acoustic waves pressure. The sine-wave burst wavelength  $\lambda$  is 1.45 mm and 24.17 mm for the figure on the left and right respectively.

lower diameter exhibit a flatter frequency response. This is because the acoustic pressure variations along its surface is negligible in the frequency range studied.

#### E. Directivity

The cylindrical hydrophones can measure acoustic pressures from all the axial directions. This section reports the directivity pattern for the cylindrical FF hydrophone and PVDF cylindrical hydrophone. The hydrophone is located 7 cm from the Tx source and is rotated every 5 degrees from 0 up to 360 degrees around its axial axis taking special care to avoid tilt. The excitation pulse is a burst sinewave of 20 cycles, 10 V pk-pk amplitude and amplified x 50 with the Falco amplifier, the directivity is measured for two frequencies, 100 kHz (Tx X1020, table II) and 250 kHz (Tx CSIC, table II). The received

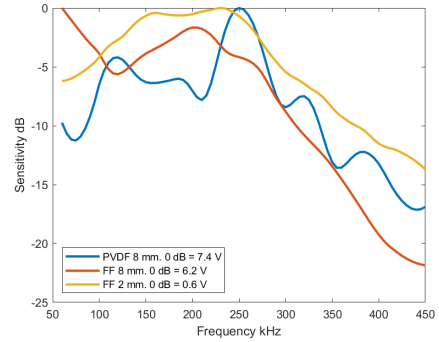


**Fig. 11.** Sensitivity comparison between PVDF and FF cylindrical hydrophone. The hydrophone is immersed in acoustic pressure field generated by the Tx from Panametrics NDT V1012 kHz 554380 videoscan with sine wave burst sweep from 60 up to 450 kHz in 5 kHz steps.

signal was digitized with the Rohde & Schwarz oscilloscope using an average of 20 signals and sample rate of 1.25 GSa/s.

Fig. 12 shows the 2D directivity. The length of the rectangle which conforms the active layer is a little bit shorter than the perimeter of the cylinder to avoid a shortcircuit between both faces of the film. This gap (the arch of the cylinder where there is not active layer) is 2.8 mm for the PVDF hydrophone and 0.8 mm for the FF hydrophone. The consequences of this gap can be appreciated as drop in sensitivity specially at 250 kHz since the wavelength is shorter and therefore more sensitive. This drop is also more intense for the PVDF hydrophone since the gap length is wider. For the FF hydrophone operating at 100 kHz hardly shows sensitivity variations even though at 250 kHz sensitivity drops 3 dB when the gap is facing the source.

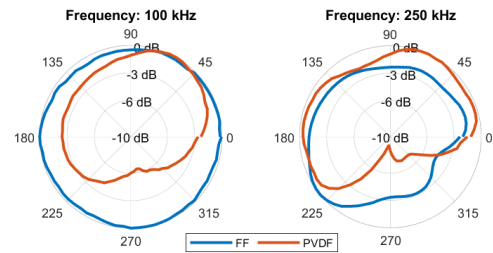


**Fig. 12.** Directivity Pattern response of the FF and PVDF hydrophones when are immersed in an acoustic field with a sine wave and frequency of 100 kHz in one case (left) and 250 kHz in the other case (right).

### 1 F. Hydrostatic pressure study

2 The objective of this section is to study the FF hydrophone  
 3 response when the hydrostatic pressure increases. This can  
 4 be of interest to validate the hydrophone performance and  
 5 endurance at different water depths. The experimental set-  
 6 up is similar to the one depicted in Fig. 7. In this case, the  
 7 water tank containing transducer and hydrophone is put in  
 8 a pressure chamber that is connected to an air compressor  
 9 that can be used to change the hydrostatic pressure in the  
 10 chamber from ambient pressure up to 7 bar. To perform this  
 11 experiment the 500 kHz commercial transducer (see table II) is  
 12 excited using a square wave half cycle with a period of 1350 ns  
 13 with a ultrascope pulser model USB-V4B-STD . The signal is  
 14 received with the hydrophone F18-2 and amplified 40 dBs with  
 15 the Phoenix amplifier model B2CH. The Pico oscilloscope  
 16 model 3206 was used to digitize at 2  $\mu$ s/div configuration.

Pressure pump can mimic depths ( $h$ ) from 0 m up to 50 m according to hydrostatic pressure equation modifying the external pressure ( $p_0$ ) from 1 bar to 6 bar.

$$p = \rho * g * h + p_0 , \quad (3)$$

where  $\rho$  is the water density,  $g$  is the gravitational acceleration,  $h$  is the depth and  $p_0$  is the external pressure mentioned before.

It is expected that due to the high compressibility of the ferroelectret the piezoelectric response may be modified.

Fig. 13 shows the normalized sensitivity cycle defined as the ratio between the sensitivity measured at specific pressure (x axis) divided by the sensitivity measured at atmospheric pressure. The errorbars are calculated as the standard deviation divided by the square of the number of points from the bandwidth.

The FF sensitivity improves with the hydrostatic pressure from 1 up to 3 bars. The pressure range, 3 up to 6 bars maintains the sensitivity stable. During the decompression the FF sensitivity decrease in a different way than the compression part, highlighting an improvement at atmospheric pressure when the cycle is completed.

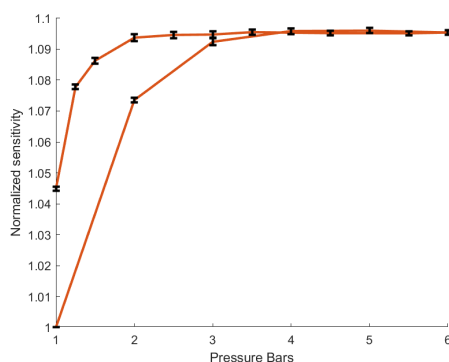


Fig. 13. Normalized sensitivity defined as sensitivity under certain pressure divided by sensitivity at atmospheric pressure, increasing from 1 up to 6 bar (lower red line) and then decreasing from 6 up to 1 bar again (top red line).

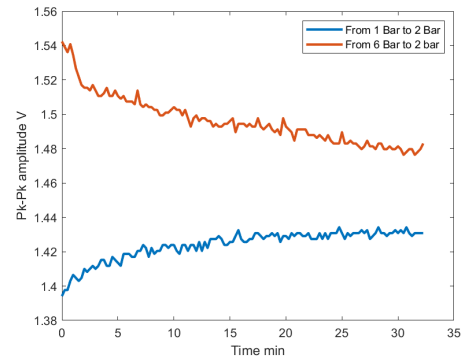


Fig. 14. FF hydrophone retarded response after pressure modification.

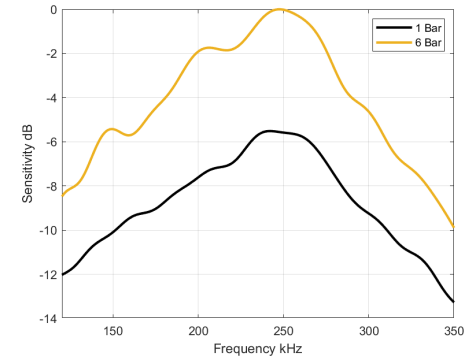


Fig. 15. FF frequency response at 1 and 6 Bar.

FF has a retarded response under hydrostatic pressure variations, Fig. 14 shows the time required to reach a stable sensitivity after a pressure modification. This phenomenon causes the sensitivity gap at atmospheric pressure before and after complete the pressure modification cycle. This gap is reduced over time until it disappears if the hydrophone is taken out of the water. This happens because during the compression and decompression the voids which compose the FF modify their size, specifically during the compression the voids are reduced and it can happen, some air bubbles escape from the cellular film, and during the decompression stage the lost air can not enter to inflate the FF since it is immersed.

Fig. 15 shows the frequency response of the hydrophone F18-2 at 1 and 6 bar. As it is shown in Fig. 13 the sensitivity improves considerably. The band geometry does not present significant changes. The Coefficient of Variation (CV) at 3 dB drop for the bandwidth is 6.5% and for the Q-factor 7.3%, also the CV at 6 dB drop for the bandwidth is 8% and the Q-factor 7.9%. Cellular structure does not show any signs of collapse after the hydro-static pressure cycle is completed and water does not percolate the polymer so the FF can be reused with similar performance.

### G. Acoustic pressure field

This section studies the relation between the aperture size of each hydrophone and the acoustic field geometry generated by each Tx (table II) used for the FF hydrophone frequency response showed in Fig. 9 at Tx-hydrophone distance.

The acoustic field is simulated with Field II [35], [36] using a similar bandwidth than the Tx, approximately around 70%.

Fig. 16 shows the theoretical normalized lateral pressure field drop measured in dBs for each Tx used for this work at the axial distance detailed in Table II simulated with Field II. Since all the Tx apertures are circular the elevation pressure profile and the lateral pressure profile are the same for any axial distance.

Smaller hydrophone aperture can measure higher pressure relative to their aperture size because the main lobe shape of the pressure field is wider than the hydrophone aperture which explains the FF hydrophone F18-1 and F18-2 sensitivity are not 1.6 times better than F11-1 and F11-2 hydrophones although the aperture size is 1.6 times larger. Also it explains the sensitivity differences between the two aperture size for low frequencies and high frequencies.

The 0.25 MHz, 0.5 MHz and 1 MHz transmitter distance concur with the natural focus. The 2.25 MHz and 5 MHz transmitter distance was fixed around 10 cm due to the water tank limitation size.

## VI. CONCLUSIONS

The results obtained in this work demonstrate the possibility to produce piston and cylindrical hydrophones using the FF as active layer with an operation frequency range from 130 kHz up to 7.5 MHz and from 50 kHz up to 450 kHz respectively. FF mechanical properties make possible manufacture hydrophones with different aperture geometries in a very simple way which is an advantage for applications where no standard hydrophone apertures are available.

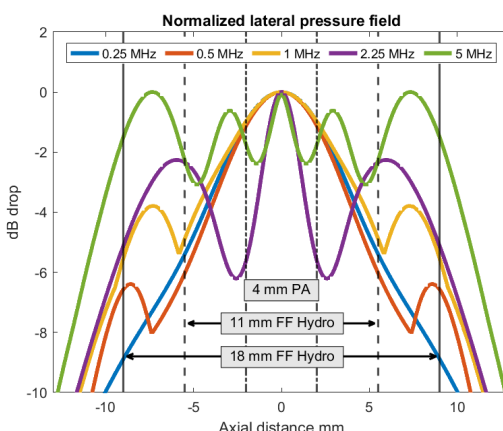


**Fig. 16.** Normalized lateral pressure field for each transmitter at distance indicated in table II. Arrows illustrate the diameter of the aperture size of the hydrophones used.

SNR may become a problem for these applications where frequencies above 7.5 MHz are needed but, a low noise preamplifier can extend the operating frequency range up to 13 MHz.

Due to the very low FF impedance (see table I) the backing block size can be drastically reduced with the same operation performance.

The design and manufacturing for both models is simple, also the materials are cheap and accessible which makes the FF hydrophones low-cost.

PVDF hydrophone sensitivity is higher than FF in the whole frequency range, specially for high frequencies (>1 MHz). Although, response flatness of FF is better than PVDF specially at low frequencies (<1 MHz). For example, the indicator blabla show FF is X time flatter than PVDF.

Pulse-echo operation can be performed with the piston design presented with no extra modifications. This might become an advantage over other commercial hydrophones, in scenarios where these features are required.

FF can be immersed in water up to 50 m with no irreversible damage. Since the frequency response does not vary up its geometry with the hydrostatic pressure, the sensitivity reported in Fig. 9 can be used for different depths setting a sensitivity offset which it is the y axis of Fig. 13.

Cylindrical hydrophones directivity pattern shows both hydrophones has better performance at low frequencies and FF does not present any sensitivity drop at 100 kHz.

For future work a FF hydrophone with wider directivity can be design as result of the combination of both designs presented in this work.

## REFERENCES

- [1] Z. Xia, R. Gerhard-Multhaupt, W. Künstler, A. Wedel, and R. Danz, "High surface-charge stability of porous polytetrafluoroethylene electret films at room and elevated temperatures," *J. Phys. D: Appl. Phys.*, vol. 32, 9 1999.
- [2] P. Fang, W. Wirges, M. Wegener, L. Zirkel, and R. Gerhard, "Cellular polyethylene-naphthalate films for ferroelectret applications: Foaming, inflation and stretching, assessment of electromechanically relevant structural features," *E-Polymers*, 2008.
- [3] E. Saarimäki, M. Paajanen, A. M. Savijärvi, H. Minkkinen, M. Wegener, O. Voronina, R. Schulze, W. Wirges, and R. Gerhard-Multhaupt, "Novel heat durable electromechanical film: Processing for electromechanical and electret applications," in *12th ISE*, Salvador, Brazil, 2005, pp. 220-223..
- [4] Y. Zhang, C. R. Bowen, S. K. Ghosh, D. Mandal, H. Khanbareh, M. Arafa, and C. Wan, "Ferroelectret materials and devices for energy harvesting applications," *Nano Energy*, vol. 57, 2019.
- [5] S. Yong, J. Shi, and S. Beeby, "Wearable textile power module based on flexible ferroelectret and supercapacitor," *Energy Technol.*, vol. 7, 2019.
- [6] T. E. G. Álvarez Arenas, H. Calás, J. E. Cuello, A. R. Fernández, and M. Muñoz, "Noncontact ultrasonic spectroscopy applied to the study of polypropylene ferroelectrets," *J. Appl. Phys.*, 2010.
- [7] J. L. Ealo, F. Seco, and A. R. Jiménez, "Broadband emfi-based transducers for ultrasonic air applications," *IEEE Trans. Ultrason. Ferroelectr. Freq. Control*, 2008.
- [8] K. J. Vössing, M. Gaal, and E. Niederleithinger, "Air-coupled ferroelectret ultrasonic transducers for nondestructive testing of wood-based materials," *Wood Sci. Technol.*, vol. 52, 2018.
- [9] S. Noh, C. Yoon, E. Hyun, H. N. Yoon, T. J. Chung, K. S. Park, and H. C. Kim, "Ferroelectret film-based patch-type sensor for continuous blood pressure monitoring," *Electron. Lett.*, vol. 50, 2014.
- [10] C. Sinha, D. Mandal, K. Roy, S. Jana, S. K. Ghosh, B. Mahanty, Z. Mallick, and S. Sarkar, "Three-dimensional mof-assisted self-polarized ferroelectret: An effective autopowered remote healthcare monitoring approach," *Langmuir*, vol. 36, 2020.

- [11] T. E. Alvarez-Arenas and L. Diez, "Ferroelectret transducers for water immersion and medical imaging," in *IEEE IUS*, Tours, France, 2016, pp. 1-4.
- [12] J. Q. Aguilar and T. G. Alvarez-Arenas, "Optimization of ferroelectret transducers for pulse-echo water immersion operation," in *IEEE IUS*, Glasgow, UK, 2019, pp. 2604-2607.
- [13] J. Quirce, L. Svilainis, J. Camacho, and T. G. Alvarez-Arenas, "Ferroelectret ultrasonic transducers for pulse-echo water immersion," *Appl. Sci. (Switz.)*, 2020.
- [14] L. J. Medeiros, H. C. Basso, R. A. Altafim, H. A. Kamimura, A. A. Carneiro, and R. A. Altafim, "Multi-layer piezoelectret hydrophone for ultrasonic applications," in *IEEE IUS*, Dresden, Germany, 2012, pp. 1-4.
- [15] L. J. D. Medeiros, H. A. Kamimura, R. A. Altafim, A. A. Carneiro, M. F. Amorim, and R. A. Altafim, "Piezoelectret-based hydrophone: An alternative device for vibro-acoustography," *Meas. Sci. Technol.*, 2015.
- [16] M. Chitre, S. Shahabudeen, and M. Stojanovic, "Underwater acoustic communications and networking: Recent advances and future challenges," *Mar. Technol. Soc. J.*, vol. 42, 2008.
- [17] N. Goujon, H. Hori, K. Liang, and B. K. Sinha, "Applications of piezoelectric materials in oilfield services," *IEEE Trans. Ultrason. Ferroelectr. Freq. Control*, vol. 59, 2012.
- [18] S. G. Schock, A. Tellier, J. Wulf, J. Sara, and M. Ericksen, "Buried object scanning sonar," *IEEE J. Ocean. Eng.*, vol. 26, 2001.
- [19] C. G. Fox, W. E. Radford, R. P. Dziak, T.-K. Lau, H. Matsumoto, and A. E. Schreiner, "Acoustic detection of a seafloor spreading episode on the juan de fua ridge using military hydrophone arrays," *Geophys. Res. Lett.*, vol. 22, pp. 131-134, 1995.
- [20] S. A. Holt, "Distribution of red drum spawning sites identified by a towed hydrophone array," *Trans. Am. Fish. Soc.*, vol. 137, 2008.
- [21] J. Zhao, L. Zhang, N. Li, and L. N. Zheng, "The design and research of intelligent search and rescue device based on sonar detection and marine battery," in *IEEE ICCNEA*, Xi'an, China, 2017, pp. 383-387.
- [22] J. E. Dusek, M. S. Triantafyllou, and J. H. Lang, "Piezoresistive foam sensor arrays for marine applications," *Sens. Actuators A: Phys.*, vol. 248, 2016.
- [23] T. Giesecke and K. Hyynen, "Ultrasound-mediated cavitation thresholds of liquid perfluorocarbon droplets in vitro," *Ultrasound Med. Biol.*, vol. 29, 2003.
- [24] C. Chandrana, J. Talman, T. Pan, S. Roy, and A. Fleischman, "Design and analysis of mems based pvd ultrasonic transducers for vascular imaging," *Sensors (Basel)*, vol. 10, 2010.
- [25] P. A. Lewin and R. C. Chivers, "Two miniature ceramic ultrasonic probes," *J. Phys. E: Sci. Instrum.*, vol. 14, 1981.
- [26] B. Fay, G. Ludwig, C. Lankjaer, and P. A. Lewin, "Frequency response of pvd needle-type hydrophones," *Ultrasound Med. Biol.*, vol. 20, 1994.
- [27] M. Avellaneda and P. J. Swart, "Calculating the performance of 1-3 piezoelectric composites for hydrophone applications: An effective medium approach," *J. Acoust. Soc. Am.*, vol. 103, 1998.
- [28] J. Chen and R. Panda, "Review: Commercialization of piezoelectric single crystals for medical imaging applications," in *IEEE IUS*, Rotterdam, Netherlands, 2005, pp. 235-240.
- [29] S. Atique, D. Betz, B. Culshaw, F. Dong, H. S. Park, G. Thursby, and B. Sorazu, "Detecting ultrasound using optical fibres," *J. Opt. (India)*, vol. 33, 2004.
- [30] Ultrasonic Exposimetry. Marvin C. Ziskin and Peter A. Lewin, Editors CRC Press, Inc., Boca Raton, FL, 1993. xiiq-457 pp.
- [31] L. K. Wang, H. Du, G. Wang, and L. Qin, "A cylindrical hydrophone with built-in amplifier," in *IEEE ICMA*, Changchun, China, 2009, pp. 4080-4084.
- [32] L. Svilainis, "Review on time delay estimate subsample interpolation in frequency domain," *IEEE Trans. Ultrason. Ferroelectr. Freq. Control*, vol. 66, 2019.
- [33] P. Fang, M. Wegener, W. Wirges, R. Gerhard, and L. Zirkel, "Cellular ferroelectrets: Foaming in supercritical carbon dioxide, structural and electrical preparation, and resulting piezoelectricity," *Appl. Phys. Lett.*, 2007.
- [34] X. Zhang, G. Cao, Z. Sun, and Z. Xia, "Fabrication of fluoropolymer piezoelectrets by using rigid template: Structure and thermal stability," *J. Appl. Phys.*, vol. 108, 2010.
- [35] J. A. Jensen and N. B. Svendsen, "Calculation of pressure fields from arbitrarily shaped, apodized, and excited ultrasound transducers," *IEEE Trans. Ultrason. Ferroelectr. Freq. Control*, vol. 39, 1992.
- [36] J. A. Jensen, "Field: A program for simulating ultrasound systems," *Med. Biol. Eng. Comput.*, vol. 34, 1996.
- [37] J. Q. Aguilar, T. G. Alvarez-Arenas and L. Svilainis, "Ferroelectret Hydrophone," in *IEEE IUS*, Xi'an, China, 2016, pp. 1-4.



**Julio Quirce Aguilar** was born in Madrid, Spain. He received the B.S., M.S., degree in Physics and Nuclear Physics in 2015 and 2017 respectively from Autonoma de Madrid University. He is currently pursuing Ph.D dregree in ultrasonics transducers for medical and industrial application at the Instituto de Tecnologías Físicas y de la Información of the Spanish Research Council (CSIC).

His research interests focus on piezoelectric transducers design, fabrication and test, ultrasonic NDT, ferroelectret films electromechanical properties and new materials.



**Lola Fariñas** received the B.S.E. degree from the University of Alcalá, Spain, in 2009, and the M.S. and Ph.D. on Biomedical Engineering from the Technical University of Madrid, Spain, in 2011 and 2016, respectively. In 2016, she was a visiting postdoctoral fellow in the Organismal and Evolutionary Biology department at Harvard University, USA. In 2018, she joined the Food Technology department at Universitat Politècnica de Valencia, Spain. She is currently a Juan de la Cierva - Incorporacion postdoctoral fellow at the Sensors and Ultrasonic Technologies department from the Institute of Physical and Information Technologies at Spanish National Research Council (ITEFI-CSIC). Her research interests are focused on new applications of ultrasound in complex materials characterisation, including applications in agriculture sensing, Non-Destructive Testing or industrial quality monitoring and manufacturing control.



**Linas Svilainis** (Senior Member, IEEE) received the Ph.D. degree from the Kaunas University of Technology, Lithuania, in 1996.

Since 2009, he is currently a full-time Professor with the Department of Electronics Engineering, Kaunas University of Technology. His current research interests include ultrasound electronics and signal processing, large scale LED video displays, electromagnetic compatibility, and EMI protection of electronic systems.



**Tomás Gómez Álvarez Arenas** is a Scientist in the Spanish National Research Council (CSIC). PhD in Physics from the Complutense University of Madrid. In 1996 joined as a postdoc the Center for Ultrasonic Engineering, Strathclyde University, Glasgow, Scotland. In 2000, joined the Institute of Acoustics of the CSIC, and then the Institute of Physical and Information Technologies, ITEFI-CSIC (2013). Since 2014 he is Head of the Sensors and Ultrasonic Technologies Department of ITEFI-CSIC. His research

interest focuses on design, optimization and fabrication of piezoelectric transducers, the study of piezoelectric and ferroelectric materials, ultrasonic materials characterization, new materials for ultrasonic applications, solution of Inverse and Hard Optimization Problems and applications of ultrasonic techniques in NDT, medical diagnosis, food quality, industrial control, and agriculture sensing.

## **4.2 IEEE International Ultrasonics Symposium (IUS) publications**

### **4.2.1 IUS 2019, Glasgow, UK.**

The paper can be found at page [89](#) and the full reference is:

J. Q. Aguilar and T. Gómez Álvarez-Arenas, "Optimization of Ferroelectret Transducers for Pulse-Echo Water Immersion Operation," 2019 IEEE International Ultrasonics Symposium (IUS), 2019, pp. 2604-2607, doi: [10.1109/ULTSYM.2019.8926178](https://doi.org/10.1109/ULTSYM.2019.8926178).

### **4.2.2 IUS 2021, Xi'an, China.**

The paper can be found at page [93](#) and the full reference is:

J. Q. Aguilar, T. G. Álvarez-Arenas and L. Svilainis, "Ferroelectret Hydrophone," 2021 IEEE International Ultrasonics Symposium (IUS), 2021, pp. 1-4, doi: [10.1109/IUS52206.2021.9593895](https://doi.org/10.1109/IUS52206.2021.9593895).

### **4.2.3 IUS 2021, Xi'an, China.**

The paper can be found at page [97](#) and the full reference is:

J. Quirce, T. G. Alvarez-Arenas and L. Svilainis, "Calibration of Air-Coupled Ultrasonic Transducers," 2021 IEEE International Ultrasonics Symposium (IUS), 2021, pp. 1-4, doi: [10.1109/IUS52206.2021.9593482](https://doi.org/10.1109/IUS52206.2021.9593482).

2019 IEEE International Ultrasonics Symposium (IUS)  
Glasgow, Scotland, October 6-9, 2019

# Optimization of Ferroelectret Transducers for Pulse-Echo Water Immersion Operation

Julio Quirce Aguilar<sup>1</sup>, Tomás Gómez Álvarez-Arenas Member, IEEE<sup>1</sup>  
*Ultrasonic and Sensors Technologies Dept.*

<sup>1</sup>*Instituto de Tecnologías Físicas y de la Información, CSIC,  
C/Serrano 144, Madrid 28035, Spain.  
j.quirce.aguilar@gmail.com, t.gomez@csic.es*

**Abstract**—The adaptation and optimization of polypropylene ferroelectret (FE) films as the main piezoelectric element for water immersion ultrasonic transducers is studied. One of its main features is that they present a very wide band response so they can be an alternative for certain medical applications, especially those demanding intermediate frequencies and reduced size. The main problems of using this kind of materials are the poor sensitivity and the weak bonding of the metallization to the FE film that is easily degraded when entre in contact with water. The objective of this work is to optimize FE transducers for pulse-echo water immersion, while preserving the bandwidth, by: i) protecting the surface and ii) improving the impedance matching to the water.

Metallization degradation produced by water has been quantified, then, main materials requirements to produce matching layers for this application are reviewed and potential materials to produce them proposed. A procedure to reinforce the metallization while preserving the electromechanical film response is proposed (based on Ar sputtering) and first prototypes of transducers with a single matching layer are proposed, built and characterized.

**Keywords**—Transducer, Ferroelectret, Matching Layer, Water immersion.

## I. INTRODUCTION

The electromechanical polymeric film called ferroelectret was introduced in the late 80's (see Refs. [1], [2] and [3]). It is a cellular polymer filled with air that can be electrically charged [4], where the cells end up comprising electric dipoles oriented along the thickness direction (see figure 1. c) that can be rather stable. Thanks to the very low elastic modulus of this cellular structure this material presents a measurable piezoelectric response. Different applications of this material have been proposed, such as air-coupled transducers [5], [6] and [7], active matching layers [8], wearable sensors [9], energy harvesting [10]. They have also been tested as transducers for water immersion and medical imaging [11], where the very wide band response obtained at intermediate frequencies and the possibility to miniaturize the transducer are quite promising features for different medical applications.

The main problems in using FE films for water immersion transducers are that the sensitivity is too low, and the FE

metallization is easily degraded. This metallization is obtained by evaporation of a thin film of Al, and it has poor stability when film is bended, touched or enter in contact with water. This fact gives rise to two main problems: i) film manipulation must be performed very carefully, ii) water immersion where water is in direct contact with the Al metallized surface is not possible as the conductivity is rapidly degraded. In both cases electrical conductivity in the outer transducer electrode is lost. Two main solutions can be adopted to deal with this problem: i) to apply a wear plate or some impedance matching layers, ii) to apply a more resistant conductive coating. Option 1, specially the use of impedance matching layers, can be considered the most convenient, as the use of impedance matching layers is required to solve the problem of acoustic impedance mismatch between the ferroelectret film and the water. However, the Al coating can be degraded even in the process of attaching or fixing the matching layers or the wear plates, therefore, it is necessary to identify a suitable process to stabilize the outer electrode before any further manipulation.

## II. MATERIALS

The FE film used in this study is produced by the company EMFIT. Characterization of the films is performed by the non-contact ultrasonic resonant spectroscopy method presented in Ref. [12]. Thickness is 70 um, density 550 Kg/m<sup>3</sup> and it presents a halfwave resonance at 645 kHz. One side of the film is metalized (Al) and the other one it is not. Figure 1 shows both sides and a micrograph of the cross-section, obtained by SEM of the fractured section immersed in liquid nitrogen.



Fig. 1. Metalized side of ferroelectret (left), Non metalized side (center), Cross-section SEM micrograph (right).

This work funded by The Spanish Government supported this research under grant DPI2016-78876-R (AEI/FEDER, UE).

2019 IEEE IUS  
Glasgow, Scotland, October 6-9, 2019

For the matching layers and wear plate epoxy resin loaded with microspheres were used. Two kind of microspheres, were tested: the first one with density = 30 kg/m<sup>3</sup> and diameter 50~85 µm and the second one with density = 70 kg/m<sup>3</sup> and diameter 15~30µm. The first one allows us to achieve lower densities (and hence lower acoustic impedances) although the diameter of the microspheres is higher, and this may limit the capability to produce thin layers out of this material and, therefore, to tune these layers to high frequencies.

Finally, to reinforce the Al electrode, gold was deposited over the Al film by a conventional sputtering technique.

### III. TRANSDUCER DESIGN AND FABRICATION.

Figure 2 shows a cross section of the proposed transducer design. The cable is welded from the SMB connector fitted on the back of the transducer (1) to the vertex of the brass cone (2) backing ending with cylindrical shape (3). The backing is glued to the housing using nonconductive epoxy (4). Then the FE film (5) is cut using a puncher to get a circular piece with larger diameter, 20mm, than the cylindrical brass backing. The FE is glued with a thin film of adhesive (6) to the backing (3). To make the mass connection we place an aluminum crown (8). One matching layer/ wear plate is shown in the design (7).

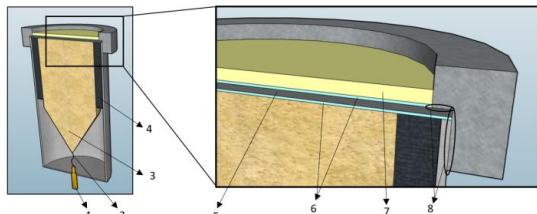


Fig. 2. Cross section view of transducer design (left) and detail of the connections (right)

### IV. MATCHING LAYER DESIGN

The required impedance of each layer in a N-stack of quarter-wavelength matching layers to obtain optimum transmission is calculated by Eq. (1), where  $Z$  denotes the acoustic impedance of a layer and the subindex is the order of this layer in the stack. In this case,  $Z_1$  is the ferroelectret layer and  $Z_N$  is water.

$$Z_n = \sqrt{Z_{n-1} Z_{n+1}}, n = 1, 2, 3, \dots N \quad (1)$$

Hence, for or one ML, the required impedance of the quarter-wavelength layer is given by Eq. (2), while for a stack of two matching layers, the required impedances are shown in Eqs. (3) and (4).

$$Z_{ML} = \sqrt{Z_{FE} Z_{water}} = 0.26M Rayl \quad (2)$$

$$Z_{ML1} = \sqrt{Z_{FE} Z_{ML2}} = 0.14M Rayl \quad (3)$$

$$Z_{ML2} = \sqrt{Z_{ML1} Z_{water}} = 0.46M Rayl \quad (4)$$

MLs were manufactured by mixing a low viscosity epoxy resin with microbubbles (apparent density of 30 kg/m<sup>3</sup>). Highest possible load of microbubbles were achieved by

adding a mass concentration of 12%-15%, beyond that level of load it was not possible to achieve an homogeneous mixture using conventional mixing methods. The composite is placed in a mould and let to cure for 16 h. Once cure, the sample was removed, polished and characterized by the same non-contact resonant ultrasonic spectroscopic technique. Velocity, attenuation coefficient and impedance were obtained. Velocity figure is used to calculate the thickness of the final matching layer. We always tune the matching layers to 1 MHz. Lowest achieved impedance was about 0.8 M Rayl, still too high for this application. Nonetheless, the samples were used to produce and attach the matching layers to check the consistency of the whole process.

### V. TRANSDUCER CHARACTERIZATION.

Transducers were characterized by three different techniques: Firstly, by analyzing the surface vibration by a laser vibrometer (Polytech), that scans the transducer surface and provides surface displacement with time.

Secondly, by measuring the pulse-echo response in air, mainly to determine the integrity of the metallization and the effect of any reinforcement of this metallization.

Thirdly, by pulse-echo in water immersion. In this case, a steel reflector located at 43mm using the Olympus pulser / receiver model 5072P/R, frequency: 1 MHz, pulse amplitude: 400 V, damping 40 ohm, gain: 59 dB, Low Pass Filter: 10 MHz. Depending on the orientation of the transducer the signal response change being the biggest one when the radiating area is parallel to the steel reflector. In this work, normal incidence is used so, in order to place the transducer in the optimum position a two-axis support has been designed with two steppers controlled by Arduino UNO through MATLAB taking the amplitude signal information from the oscilloscope. The stepper model used is 28BYJ-48 with a stride angle of 5.625°/64. Figure 3 shows a schematic of the positioning device.

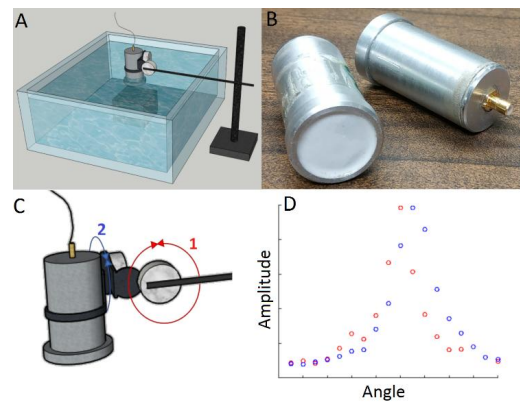


Fig. 3. Schematic representation of the experimental set-up for positioning the produced prototype transducer for water immersion pulse-echo characterization.

## VI. RESULTS AND DISCUSSION

### A. Analysis of electrode degradation.

The influence of the electrode degradation in contact with water was studied and quantified. Transducers with and without matching layers/wear plates and Au reinforcement were put in water for 7 hours and the echo received from a steel reflector at 2 cm recorded. Figure 5 shows the evolution of the normalized peak to peak amplitude of the echo with time of immersion for two different cases (no protection and one matching layer). The fast degradation of the electrode of the unprotected transducer is clearly seen.

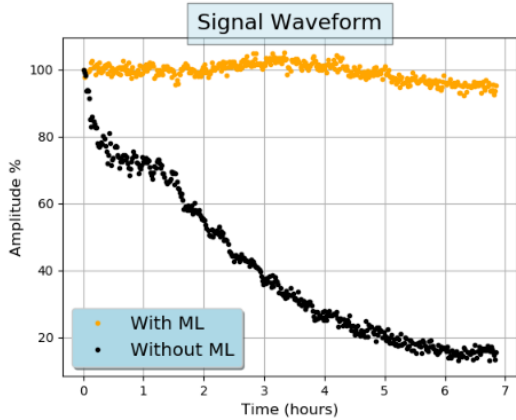


Fig. 4. Variation with time of immersion of the normalized echo amplitude for two prototype transducers: Transducer with unprotected Al metallization and transducer with one matching layer

### B. Surface vibration displacement.

Mapping of the surface vibration with the laser vibrometer were performed in order to verify the homogeneous gluing of the FE film to the substrate and of the matching layers. Figure 5. shows the measured amplitude along one surface diameter. Pulse excitation was used.

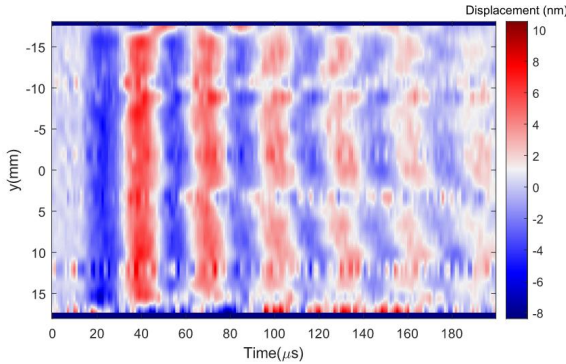


Fig. 5. Time evolution of the transducer surface displacement measured along one of the radiating surface diameters. Pulse excitation

### C. Al electrode reinforcement with Au.

The stability of the electrical charge trapped in the pores of the ferroelectret film cellular structure is quite poor and easily affected by variations in temperature or ambient pressure [13].

Therefore, the ferroelectret film electrical polarization is easily lost during the process of applying another conductive coating. However, good results were obtained when an electrically conductive coating was applied to the radiating surface of the transducer before applying any wear plate or matching layers, that is, under these conditions the coating is applied directly over the Al electrode. A custom sputtering deposition system (at ISOM CSIC-UPV) was used to deposit a thin layer of gold on the Al electrode. Sputtering time was changed from 80 to 60 s to achieve different thicknesses of the Au layer. The current intensity applied was always 30 mA and the deposition was performed under a stable atmosphere of Ar after a pre-vacuum of  $10^{-4}$  mbar. By this procedure, it was possible to achieve both a recovery of the electrode conductivity (in the case of already degraded electrodes) and a full electrode integrity against contact with water or any glue employed to fix matching layers. In addition, transducer performance was not affected by the sputtering process, so we conclude that the ferroelectret polarization is not compromised during the sputtering process.

The thickness of the Au layer deposited and the preservation of the film polarization after the deposition is determined from the measurement of the spectral response of the transducer in pulse-echo mode operated in air. In the case of air-operation the ferroelectret film response corresponds to a quarter wavelength resonance and is very sensitive to any mass deposited on the front face. In particular, the thickness resonant frequency shifts towards lower values as the deposited mass increases. For a large amount of added mass there can also be a decrease of sensitivity. Clearly, any loss of trapped dielectric charge in the ferroelectret foam will show up as a decrease of the transducer sensitivity. These measurements were performed using an Olympus 5058 PR and a digital scope Tektronix 5054. Results for the transducer without Au and transducers after 30 s sputtering time and 60 s sputtering time are shown in Fig. 6.

Quantification of the thickness of the Au layer deposited, the measured transducer response is compared with the calculated one, where the thickness of the Au layer is used as a fitting parameter. Results are shown in Fig. 7. Comparison of Figs. 6 and 7 reveals that the thickness of the Au layer sputtered is about 80 nm.

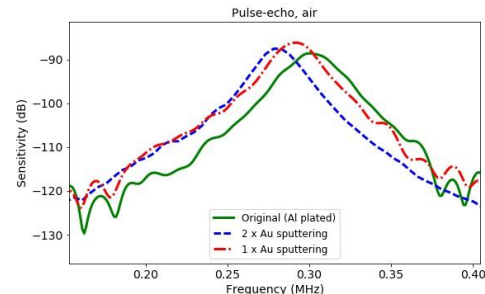


Fig. 6. Measured spectra of the pulse-echo response of the transducer in air. Original transducer and transducers with 1x 30 s sputtering of Au, and 2x 30 s sputtering of Au.

2019 IEEE IUS  
Glasgow, Scotland, October 6-9, 2019

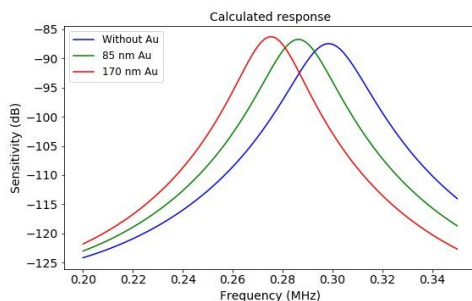


Fig. 7. Calculated spectra of the pulse-echo response of the transducer in air with different layers of Au deposited.

#### D. Influence of matching layers.

In addition to provide a protection to the outer electrode, matching layers are expected to improve sensitivity and modify bandwidth. Although achieved matching layer materials impedance is still very large, it is of interest to determine how do they affect the transducers.

Figure 8 shows a comparison of a transducer with and without matching layer.

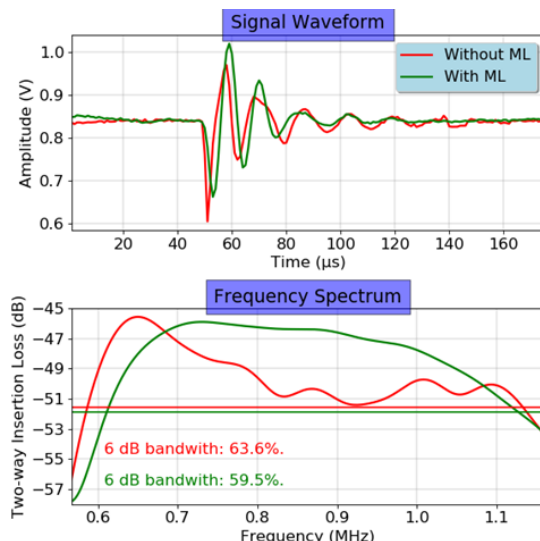


Fig. 8. Measured pulse-echo response in water immersion of transducers with and without matching layer. Up: impulse response. Bottom Spectra. The +40 dB Gain in the pulser receiver are not considered in the figure, so actual peak sensitivity is about -96 dB.

#### VII. CONCLUSIONS

The main drawbacks to use ferroelectret transducers in water immersion are the poor sensitivity and the poor stability of the transducer response. In this paper, we have verified that this poor stability is due to the Al electrode degradation when

it enters in contact with water. Several prototypes of ferroelectret based transducers for water immersion have been produced and tested. Laser vibrometry scanning of the radiating surface revealed a quite homogeneous response that validates the fabrication routes employed for this prototype. Moreover, we have shown that it is possible to deposit an extra layer of Au (by sputtering) whose effect on transducer response is minimal but that provides efficient protection of the Al electrode. Finally, the requirements for matching layer have been reviewed and some materials have been fabricated trying to meet these requirements by using syntactic foams. However, achieved impedances are still well beyond the expected values. Nonetheless, prototype transducers have been built employing these matching layers and it has been possible to improve the frequency band, though no significant improvement of the sensitivity has been achieved.

#### REFERENCES

- [1] Kirjavainen, K. Electromechanical film and procedure for manufacturing the same. U.S. Patent 4654546, 1987.
- [2] A. Savolainen, K. Kirjavainen. Electrothermomechanical film. Part I. Design and characteristics. *J. Macromol. Sci. Chem.* vol. 26, 1989, , pp. 583-591
- [3] G. M. Sessler, and J. Hillenbrand,. Electromechanical response of cellular electret films. *Appl. Phys. Lett.* vol. 75, 1999, pp. 3405–3407
- [4] M. Lidner, S. Bauer-Gogonea, S. Bauer, M. Paajanen, J. Raukola, Dielectric barrier microdischarges: Mechanism for the charging of cellular piezoelectric polymers. *J. Appl. Phys.* vol. 91, 2002, pp. 5283–5287
- [5] R. Kressmann, New piezoelectric polymer for air-borne and waterborne sound transducers. *J. Acoust. Soc. Am.* vol. 109, 2001, pp. 1412–1416.
- [6] V. Bovtun, J. Doring, J. Bartusch, A. Erhard, Y. Yakymenko, Ferroelectret non-contact ultrasonic transducers. *Appl. Phys. A*, vol. 88, 2007, 737–743.
- [7] J. Ealo, F. Seco, A. Jimenez, Broadband emfi-based transducers for ultrasonic air applications. *IEEE Trans.. Ultrason. Ferroelectr. Freq. Ctrl.* vol. 55, 2008, pp. 919–929.
- [8] T. E. G. Álvarez-Arenas, Air-coupled piezoelectric transducers with active polypropylene foam matching layers, *Sensors*, vol. 13, no. 5, pp. 5996–6013, 2013.
- [9] X. Ma, X. Zhang, P. Fang,, Flexible Film-Transducers Based on Polypropylene Piezoelectrets: Fabrication, Properties, and Applications in Wearable Devices. *Sensors and Actuators A: Physical*. vol. 256. 2017.
- [10] J. Shi, Y. Sheng, S. Beeby, An easy to assemble ferroelectret for human body energy harvesting. *Smart Materials and Structures*. vol. 27. 2018.
- [11] T. E. G. Alvarez-Arenas and L. Diez, Ferroelectret transducers for water immersion and medical imaging, *IEEE Int. Ultrason. Symp. IUS*, 2016.
- [12] T. E. Gómez Álvarez-Arenas, H. Calás, J. E. Cuello, A. R. Fernández, and M. Muñoz, Noncontact ultrasonic spectroscopy applied to the study of polypropylene ferroelectrets. *J. Appl. Phys.*, vol. 108, no. 7, p. 074110, 2010.
- [13] T. E. G. Alvarez-Arenas, “Pressure Sensitivity Response of Polymeric Ferroelectret Foam Films ..,” in *2014 Joint IEEE International Symposium on the Applications of Ferroelectric, International Workshop on Acoustic Transduction Materials and Devices & Workshop on Piezoresponse Force Microscopy*, 2014.

# Ferroelectret Hydrophone

Julio Quirce Aguilar

*Instituto de Tecnologías Físicas y de la información (ITEFI)  
Consejo Superior de Investigaciones  
científicas  
Madrid, Spain  
j.quirce.aguilar@csic.es*

Tomás Gómez Álvarez-Arenas

*Instituto de Tecnologías Físicas y de la información (ITEFI)  
Consejo Superior de Investigaciones  
científicas  
Madrid, Spain  
t.gomez@csic.es*

Linas Svilainis

*Electronics Engineering Department  
Kaunas University of Technology  
Kaunas, Lithuania  
linas.svilainis@ktu.lt*

**Abstract**—Ferroelectret films are soft cellular solids capable to trap dielectric dipoles within the pores. These dipoles together with the large material compressibility give rise to a measurable piezoelectric response. They have been used to produce air-coupled ultrasonic transducers (200 kHz to 600 kHz) and recent works have shown the possibility to use them in water immersion. The main advantage is the large bandwidth and the main drawback is the poor sensitivity. This suggests the possibility of using these materials for wide-band reception, in particular, to make hydrophones. Due to the very low acoustic impedance of ferroelectret films (about 0.08 MRayl), thickness resonances under water immersion are completely damped out. Therefore, unlike conventional PVDF hydrophones, no upper frequency limit in the frequency band of the FE film hydrophone is expected due to these resonances, being the only limit the attenuation in the material.

Present work is aimed to study the response of FE film as hydrophone and to explore the frequency range of the reception band in water immersion operation.

**Index Terms**—ferroelectret, hydrophone, water immersion.

## I. INTRODUCTION

Ferroelectret (FE) films were developed in the 80's by Kirjavainen and co-workers [1] [2] in Finland, leading the way towards different applications such as air-coupled transducers [3] [4], wearable sensors [5], or energy harvesting [6]. The most studied and developed FE film is the cellular polypropylene, with high piezoelectric  $d_{33}$  coefficient, superior than polyvinylidene fluoride (PVDF) film and comparable to some ceramics like lead zirconate titanate (PZT) [7]. After the high-voltage is applied to the FE film, it generates charges that are trapped inside of the voids located in the interior of the film originating electric dipoles with strong piezoelectric response. The interior of the FE film behave as cellular structure that can be modeled as honeycomb [8]. The FE film used for this study is cellular polypropylene which fundamental characteristics are described in table I [9]. These characteristics make the material very flexible, being suitable

This work was partially supported (LS) by European Regional Development Fund (project No. 01.2.2-LMT-K-718-03-0026) under grant agreement with the Research Council of Lithuania (LMTLT) and by the Ministerio de Economía y Competitividad under Grant DPI2016-78876-R (AEI/FEDER, UE).

for applications where curved active layer surface is required [10].

Prototypes of a circular plane piston hydrophone based on FE film are presented in this work for measurements in the frequency range from 0.2 MHz to 13 MHz. Since the acoustic impedance of the film is very low (0.08 MRayl) and stiffness too, the natural resonance in water immersion operation, half wavelength  $\lambda/2$ , should be observed at 650 kHz but water pressure dumped the resonances. Thanks to this phenomenon the FE film results a good candidate to be used as active layer for hydrophones.

Transducers for water immersion based on FE films have been proposed and tested before [9] [11] [12] [13]. Also ferroelectret based hydrophone for the frequency range 4 up to 100 kHz were developed previously [14] [15]. The objective of the present work is to study the response of FE films as hydrophones and to explore the frequency range of the reception band in water immersion operation.

Table I  
MAIN PROPERTIES OF THE FE FILM USED

Commercial name	Density (Kg/m <sup>3</sup> )	Thickness (μm)	Elastic Modulus (MPa)	Thickness resonance freq. (MHz)
Emfit HS03	550	70	3.98	0.65

## II. MATERIALS AND METHODS

HS03 FE film (from EMFIT corp.) were used for this study. The fundamental characteristics are listed in Table I. The FE film has one metalized side coated by aluminum that was additionally reinforced with 85 nm of gold deposited by sputtering to protect against water degradation. The other side is not metalized. It was glued to the brass backing which served as second, "hot" electrode. Three FE film hydrophones prototypes were developed for this work, two had 254 mm<sup>2</sup>, 18 mm diameter active FE film layer, one glued to the brass backing with conductive double sided tape and the second with the cyanoacrylate. Third FE film hydrophone prototype had 95 mm<sup>2</sup>, 11 mm diameter active FE film layer and it was glued with conductive double sided tape.

### A. Hydrophone Design and Manufacturing

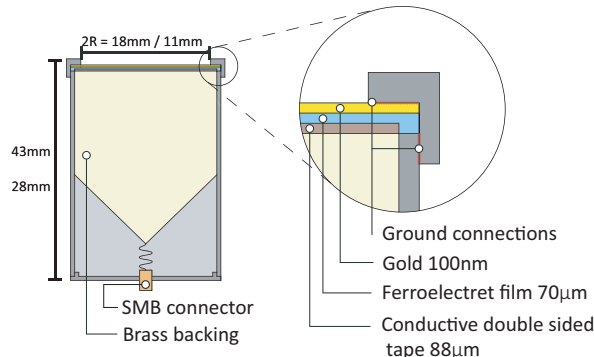


Figure 1. Cross section scheme of the FE film hydrophone prototype design.

Fig. 1 shows a cross section of the FE film hydrophone prototype design. The hydrophone was mounted in a aluminum housing with a back SMB connector (Fig. 2). The brass backing block was glued to the housing wall with epoxy resin. Fig. 1 also shows the layer construction. From bottom to top, the first layer was the glue used to attach the FE film to the brass baking, cyanocrylate was used for one prototype and conductive double sided tape for the two other prototypes. The next layer was the FE film, in this work we used HS06 and HS03 from Emfit corp. HS06 does not present enough sensitivity to be used as hydrophone, so this film was rejected [12].

Previous studies [11] reported that metallization degrades when the film is immersed in water. To avoid this issue, 85 nm gold layer was located between the film and the medium by using a sputtering technique.



Figure 2. FE film hydrophone prototypes employed for this study.

### B. Data Acquisition

The acoustic pressure amplitude of three FE film hydrophones prototypes for the frequency range from 0.2 MHz to 13 MHz was measured using five commercial transducers as transmitters with nominal center frequency: 250 kHz Olympus

NDT V1012, 500 kHz Olympus M2008, 2.25 MHz Olympus-NDT C306, 5 MHz Olympus A308S and 10 MHz Olympus NDT V311. Also Two calibrated commercial hydrophones (from Preccision Acoustics, ML4X50 and 2812) were used to measure the acoustic pressure amplitude generated by the Tx at the same distance where the FE film hydrophone prototypes were located.

Five transmitters were used because single transducer for such wide range does not exist. The procedure for the acoustic pressure amplitude measurement at each frequency was as follows.

The transmitter (one of the commercial transducers used) was placed at the bottom of the water tank pointing towards the water surface, calibrated hydrophone is located opposite Tx (see Fig. 3). Transmitter was excited with a of 20 cycles and 20 Vpp amplitude sine wave toneburst, using a DG1032 (made by RIGOL) signal generator. The signal received by the calibrated hydrophone was sampled using the RTB2004 oscilloscope (made by Rohde & Schwarz). The measured signal amplitude was converted to pressure using the probe's calibration cart (mV vs. Pa). Then, the probe was replace by the FE film hydrophone prototype taking the special care to keep the same distance between the transmitter and the hydrophone (to avoid the acoustic pressure variation with distance). The pk-pk amplitude observed with the hydrophone prototype is digitalized with the oscilloscope and using the pressure data obtained with the probe, the FE film hydrophone prototype calibration cart is generated.

The frequency range from 8 MHz to 13 MHz, which was measured using 10 MHz central frequency transducer required special care. Attenuation in water increases with frequency, so signal to noise ratio (SNR) becomes too low in this range. Excitation signal amplitude was increased using 20 dB Falcon power amplifier (toneburst shape was not affected).

Additionally, the FE film hydrophone prototype signal was amplified by using 56 dB amplifier (pulser/receiver 5072PR made by Olympus). These modifications were taken into account in amplitude calculation.

The calibrated sensitivity frequency response of the FE film hydrophone prototype for the full frequency range (Fig.4) was obtained by concatenating the five measurements. It should be noted that the transition regions do not always overlap and small corrections were applied. The reason for discrepancies can be attributed to the positioning errors or impedance mismatch of additional amplifiers used. The calibrated sensitivity in mV/Pa can be converted to dBmV/Pa or other convenient units.

### III. RESULTS

The calibrated sensitivity frequency response for three FE film hydrophone prototypes is presented in Fig. 4. The FE film hydrophones with 18 mm active layer diameter can be operated from 0.1 MHz to 13 MHz and the one with 11 mm diameter active layer provide lower range, from 0.1 MHz to 7.5 MHz. The difference in sensitivity between the 18 mm aperture prototypes is below 1% up to 4.1 MHz.

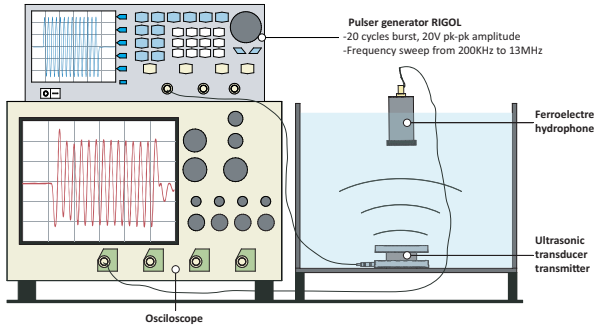


Figure 3. Experimental set-up for FE film hydrophone prototype calibration.

Beyond this frequency, the cyanoacrylate attachment exhibits higher sensitivity. It should be noted that there is an approximately 30 dB/decade sensitivity droop. The hydrophone design when using the cyanoacrylate attachment has a smoother response at high frequencies.

The 18 mm aperture hydrophones were able to receive signals above 13 MHz but the SNR was not sufficient to be usable. It should be noted that low excitation voltage (20 Vpp) and no receiving amplifier were used in frequency range up to 8 MHz. Furthermore, amplitude estimation was based on the oscilloscope measurements. If sine wave correlation [16] or at least narrowband filtering were used then SNR would have been significantly higher. Even at frequencies above 8 MHz, signal amplitude was just 20 Vpp. Better SNR would have been obtained with higher voltages. It should be noted that cable and oscilloscope impedance mismatch were not taken into account. Otherwise, frequency response would have been much smoother. The differences between the three types of prototypes can be explained by the aperture size and the method used to attach the active layer to the backing.

The FE film hydrophone prototype with small active area (11 mm) has lower sensitivity. Despite that, with all the aforementioned improvements it is feasible to expect that the miniature hydrophone can be constructed.

#### IV. CONCLUSIONS

The present work reports a method to fabricate ferroelectret-based wideband hydrophones for a frequency range up to 13 MHz. It was shown how such hydrophone can be calibrated. Experiments indicate that even 11 mm aperture can be used if lower frequency range is required. It can be assumed that even miniature FE hydrophone can be produced. The main drawback of the FE hydrophone prototype is the poor sensitivity and the active element degradation during long period of immersion operation.

For applications where higher frequencies (above 8 MHz) are required, poor sensitivity may become a problem. Then use of a low noise preamplifier may become necessary.

Unlike conventional hydrophones, the FE film hydrophone can

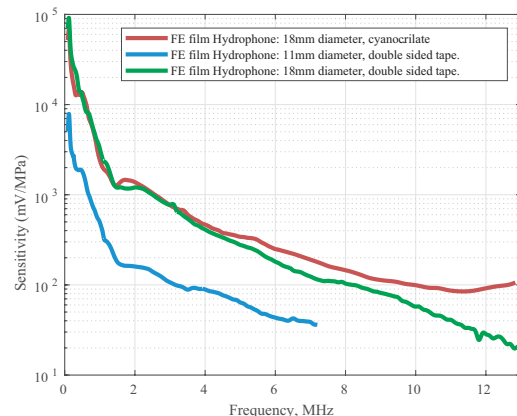


Figure 4. Frequency response of the calibrated reception sensitivity for the three FE film hydrophone prototypes.

also be used as broadband transmitter or even in pulse-echo mode without any modifications.

#### REFERENCES

- [1] A. Savolainen and K. Kirjavainen, "Electrothermomechanical film.: Part I. Design and characteristics," *Journal of Macromolecular Science: Part A - Chemistry*, 1989.
- [2] G. M. Sessler and J. Hillenbrand, "Electromechanical response of cellular electret films," *Applied Physics Letters*, 1999.
- [3] R. Kressmann, "New piezoelectric polymer for air-borne and water-borne sound transducers," *The Journal of the Acoustical Society of America*, 2001.
- [4] T. E. Álvarez-Arenas, "Air-coupled piezoelectric transducers with active polypropylene foam matching layers," *Sensors (Switzerland)*, 2013.
- [5] X. Ma, X. Zhang, and P. Fang, "Flexible film-transducers based on polypropylene piezoelectrets: Fabrication, properties, and applications in wearable devices," *Sensors and Actuators, A: Physical*, 2017.
- [6] J. Shi, S. Yong, and S. Beeby, "An easy to assemble ferroelectret for human body energy harvesting," *Smart Materials and Structures*, 2018.
- [7] J. Döring, J. Bartusch, U. Beck, and A. Erhard, "EMFIT Ferroelectret Film Transducers for Non-Contact Ultrasonic Testing," *Materials Research*, pp. 1–10, 2006.
- [8] S. Iyer, M. Alkhader, and T. A. Venkatesh, "On the relationships between cellular structure, deformation modes and electromechanical properties of piezoelectric cellular solids," *International Journal of Solids and Structures*, 2016.
- [9] T. E. Gómez Alvarez-Arenas, H. Calás, J. E. Cuello, A. R. Fernández, and M. Muñoz, "Noncontact ultrasonic spectroscopy applied to the study of polypropylene ferroelectrets," *Journal of Applied Physics*, 2010.
- [10] J. L. Ealo, F. Seco, C. Prieto, A. R. Jiménez, J. Roa, A. Koutsou, and J. Guevara, "Customizable field airborne ultrasonic transducers based on electromechanical film," in *Proceedings - IEEE Ultrasonics Symposium*, 2008.
- [11] J. Q. Aguilar and T. Gomez Alvarez-Arenas, "Optimization of Ferroelectret Transducers for Pulse-Echo Water Immersion Operation," in *2019 IEEE International Ultrasonics Symposium (IUS)*, vol. 2019-Octob. IEEE, oct 2019, pp. 2604–2607. [Online]. Available: <https://ieeexplore.ieee.org/document/8926178/>
- [12] J. Quirce, M. Muñoz, and T. Alvarez-Arenas, "Interpretation of the thickness resonances in ferroelectret films based on a layered sandwich mesostructure and a cellular microstructure," *IEEE Transactions on Ultrasonics, Ferroelectrics, and Frequency Control*, 2020.
- [13] T. T. Palitó, Y. A. Assagra, R. A. Altafim, J. P. Carmo, and R. A. Altafim, "Low-cost electro-acoustic system based on ferroelectret transducer for characterizing liquids," *Measurement: Journal of the International Measurement Confederation*, 2019.

- [14] L. J. De Medeiros, H. A. Kamimura, R. A. Altafim, A. A. Carneiro, M. F. Amorim, and R. A. Altafim, “Piezoelectret-based hydrophone: An alternative device for vibro-acoustography,” *Measurement Science and Technology*, 2015.
- [15] D. R. De Luna, T. T. Palitó, Y. A. Assagra, R. A. Altafim, J. P. Carmo, R. A. Altafim, A. A. Carneiro, and V. A. De Sousa, “Ferroelectret-based hydrophone employed in oil identification-A machine learning approach.” *Sensors (Switzerland)*, 2020.
- [16] L. Svilainis, V. Dumbrava, and D. Kybartas, “Evaluation of the ultrasonic preamplifier noise voltage density,” *Journal of Circuits, Systems, and Computers*, vol. 23, pp. 1–13, 2014.

# Calibration of Air-Coupled Ultrasonic Transducers

Julio Quirce  
 Instituto de Tecnologías Físicas y de la  
 Información (ITEFFI)  
 Consejo Superior de Investigaciones  
 Científicas  
 Madrid, Spain  
 j.quirce.agUILar@csic.es

Tomas Gomez Alvarez-Arenas  
 Instituto de Tecnologías Físicas y de la  
 Información (ITEFFI)  
 Consejo Superior de Investigaciones  
 Científicas  
 Madrid, Spain  
 t.gomez@csic.es

Linas Svilainis  
 Electronics Engineering Department,  
 Kaunas University of Technology  
 Kaunas, Lithuania  
 linas.svilainis@ktu.lt

**Abstract**—Air-coupled ultrasonic transducers working at frequencies over 100 kHz have been widely used in the past for NDT applications and are a very attractive alternative when test specimens cannot enter in contact with water. In these cases, and in order to determine transducer performance it is sufficient to measure transducer two-way insertion loss and signal to noise ratio. However, in the recent years, new applications are being developed for different fields. In these novel uses, the precise knowledge of the actual amplitude of the pressure field is demanded. However, such measurements are not simple nor straightforward. This work presents a simple procedure to measure the transducer sensitivity in transmission mode (Pa/V) and in reception mode (V/Pa) using mixed water-coupled air-coupled procedure that can be easily implemented in any ultrasonic lab. As an application example, the procedure is applied to 0.65 MHz wide band transducers. The transmission and reception sensitivities are presented here. As verification of the technique, the combined transmission-reception sensitivity is then calculated and compared with direct measurements

**Keywords**—air-coupled transducers, transducer calibration

## I. INTRODUCTION

Advances in air-coupled piezoelectric transducers design operating over 100 kHz over the last 30 years have made possible to mitigate, in a significant way, the typical problems related to the strong acoustic impedance mismatch between air and solid materials, namely, the poor sensitivity and the reduced bandwidth [1-10]. Novel transducers design (including optimization techniques), novel impedance matching approaches and novel impedance matching layer materials made these advances possible. As a result, an increasing number of problems in non-destructive testing (NDT) applications have been solved by using air-coupled ultrasonic techniques. For these applications, transducers are normally operated in through transmission or pitch-catch or pulse-echo. Hence it has been sufficient to characterize transducer response by measuring the two-way insertion loss and the signal to noise ratio. In general, it has not been necessary to determine the actual pressure level in the air produced by the ultrasonic transducers.

Enabled by these advances in air-coupled transducers technology, new applications are being developed. Some of them, for example in air-coupled excited elastography demand the precise determination of the actual pressure level provided by the transducers ([11] and [12]). However this can be a complex problem ([13] and [14]). The conventional technique used to characterize transmitter transducers based on the measurement of the transducer surface by the laser vibrometry is not a good approach as the magnitude of interest in this case is the value of the pressure field at some point in the air. Hence, this is an indirect method as the

pressure field is calculated from the data about transducer surface displacement. On the other hand, microphones in this frequency range are not common or are expensive.

This paper presents a simple technique that can be easily implemented in an ultrasonic laboratory. It is based on the use of a calibrated hydrophone immersed in water and on the operation of the transducer under air-coupled conditions; a simple procedure to precisely control location of transducer, hydrophone and water level and to measure water-gap and air-gap distances is also presented. This is very important in order to properly account for pressure amplitude modification due to attenuation, diffraction and reflection.

Once characterized the transmitter sensitivity of a given transducer, this transducer can be used to calibrate the sensitivity of other transducers (with similar frequency band) in reception mode by using a completely air-coupled set-up. The method proposed also includes a verification procedure. This is based on the calculation of the combined transmission-reception sensitivity, which is obtained by multiplying transmitter and receiver sensitivity and the comparison of this result with the transmission-reception sensitivity that can be directly measured using a pitch-catch or pulse-echo configuration.

The experimental set-up to carry out these measurements is described in detail and the procedure is applied to 0.65 MHz air-coupled transducers produced at ITEFI-CSIC. These transducers have been extensively used in NDT applications and for water content determination of wine leaves.

## II. MATERIALS AND EXPERIMENTAL SET-UP

### A. Air-coupled transducers employed for the study.

The proposed procedure is applied to two identical air-coupled transducers with centre frequency at 0.65 MHz and fabricated at ITEFI-CSIC. Transducer aperture is circular and flat with a diameter of 15 mm, centre frequency is 0.65 MHz and they can be operated from 400 to 950 kHz with a peak transmission reception sensitivity of -31 dB. Picture of these transducers is shown in Fig. 1. In order to obtain a conventional characterization of these transducers, pulse-echo and through transmission response were first measured. Results are shown in Fig. 2 and 3, for the response in pulse-echo mode and in Fig. 4 and 5 for the response in through transmission mode. For these measurements an Olympus 5077 Pulser receiver was used, with a semicycle square wave excitation, 100 V excitation and 0 dB gain in reception.

This work was partially supported (LS) by European Regional Development Fund (project No. 01.2.2-LMT-K-718-03-0026) under grant agreement with the Research Council of Lithuania (LMTLT) and by the Ministerio de Economía y Competitividad under Grant DPI2016-78876-R (AEI/FEDER, UE)



Fig. 1. Air-coupled transducers employed for this study.

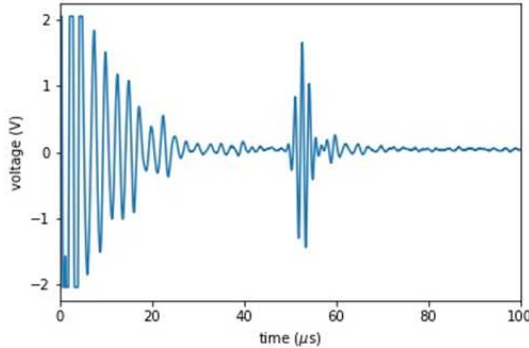


Fig. 2. Response in pulse-echo mode in air of one of the transducers: time domain.

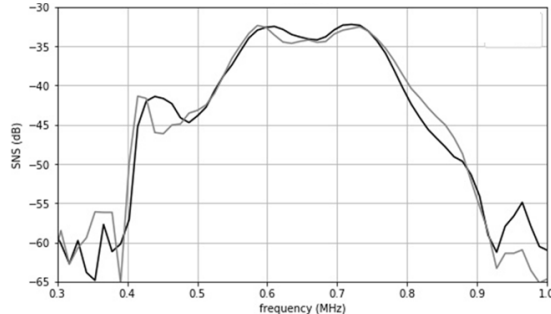


Fig. 3. Sensitivity (SNS) band of both transducers in pulse-echo mode

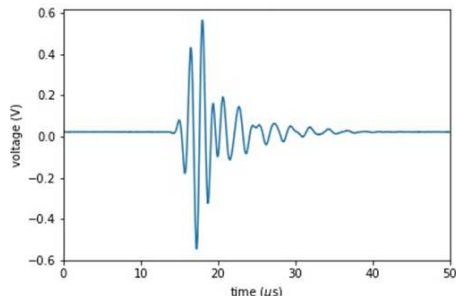


Fig. 4. Transducers response in through transmission mode in air: time domain

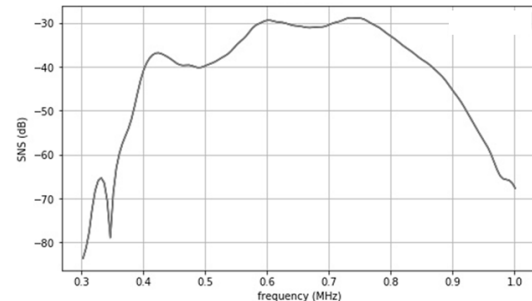


Fig. 5. Sensitivity (SNS) band of both transducers in through-transmission mode

### B. Transmission sensitivity measurement

The proposed experimental set up for the calibration of air-coupled transducer in transmission mode is shown in Fig. 6.

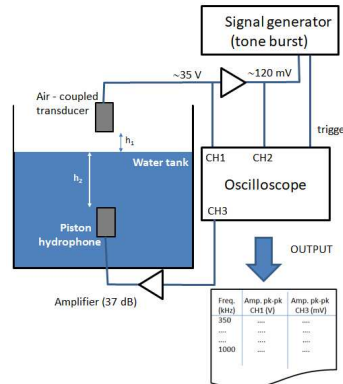


Fig. 6. Experimental set-up for transducer calibration in transmission mode.

In the experimental set-up shown in Fig. 6, the transmitter transducer is located above a water tank, looking downwards, providing normal incidence on the water surface and at a distance  $h_1$ . Inside the water tank a Precision Acoustics (PA) piston hydrophone (ML4X50), NPL calibrated, same aperture as the transmitter transducer, is located looking upwards with its surface parallel to the water surface (at a distance from water surface:  $h_2$ ). This hydrophone is calibrated in the frequency band 0.1-1.0 MHz. The hydrophone output is connected to an Olympus preamplifier (whose actual gain was previously accurately determined: 37 dB) and then connected into a Tektronix scope (channel 3).

A Rigol function generator (DG1032Z) is used to generate a tone burst: 20 cycles long and 120 mV amplitude. Then, this signal is amplified using a E&I 1040L power amplifier up to 35 V. This signal is connected (in parallel) to both the transmitter transducer terminals and to the oscilloscope, Tektronix 5054 (Channel 1). The voltage in the transmitter transducer is kept low to avoid non-linear effects. Tone burst frequency is swept from 0.3 up to 1.0 MHz in 10 kHz steps. At each step, the signal amplitude at both transducer terminals and after the Olympus preamplifier is measured by the scope and stored in the PC included in the Tektronix scope.

First step is to verify the proper positioning of transducer, water surface and hydrophone as well as the actual distances ( $h_1$  and  $h_2$ ). Received signal in the hydrophone for a tone burst at 670 kHz is shown in figure 7.

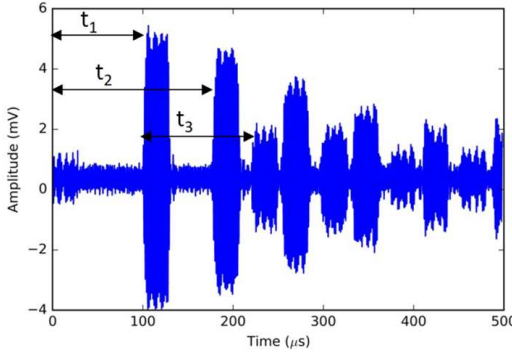


Fig. 7. Received signal in hydrophone in experimental set-up shown in Fig.6. Multiple reverberations in air-gap and water gap can be seen.

$$\begin{aligned} t_1 &= \frac{h_1}{v_{air}} + \frac{h_2}{v_{water}} \\ t_3 &= t_1 + 2 \frac{h_1}{v_{air}} \quad t_2 = t_1 + 2 \frac{h_2}{v_{water}} \end{aligned} \quad (1)$$

What we observe in Fig.7 is the multiple reverberations of the tone burst in the air- and the water-gaps. The large amplitude of these reverberations and the moderate decay with time, permit to verify that incidence on water surface is normal and that the hydrophone surface is placed parallel to the water surface. In addition, it is possible to estimate the distances  $h_1$  and  $h_2$  from time of flight measurements indicated in Fig. 6 to verify that they correspond to the values directly measured in the experimental set-up (Eq. 1).

Once transmitter transducer is calibrated, this calibrated transducer is used to calibrate other transducers in reception mode. The experimental set up is shown in Fig. 8

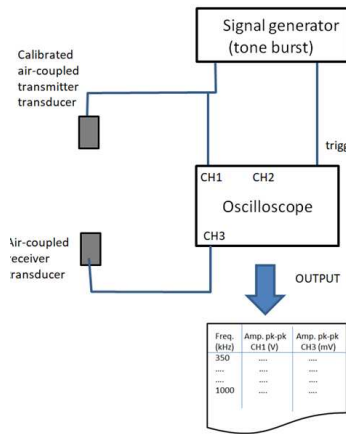


Fig. 8. Experimental set-up for transducer calibration in reception mode using a calibrated transmitter

### III. RESULTS

#### A. Transmitter sensitivity ( $Tx_{SNS}$ )

Transmitter sensitivity for the two identical air-coupled transducers used for this study were first measured following the procedure previously described (Fig. 6). Results appear in Fig. 9.

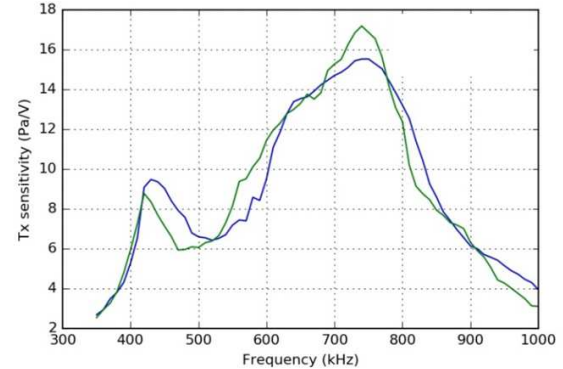


Fig. 9. Transducer sensitivity band in transmission mode ( $Tx_{SNS}$ ).

#### B. Receiver sensitivity ( $Rx_{SNS}$ )

Then, one of these transducers was used to calibrate the other one in reception mode and vice versa using the procedure outlined before (Fig. 8). Results are shown in Fig. 10.

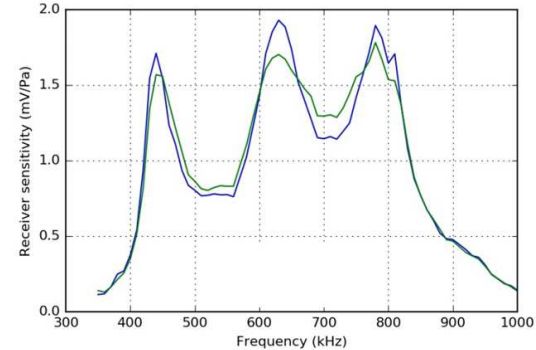


Fig. 10. Transducer sensitivity band in reception mode ( $Rx_{SNS}$ )

#### C. Combined transmission-reception sensitivity ( $Tx_{SNS} \times Rx_{SNS}$ )

Combined transmission reception sensitivity ( $Tx_{SNS} \times Rx_{SNS}$ ) can be worked out from:  $Tx_{SNS} \times Rx_{SNS} = Tx_{SNS} \times Rx_{SNS}$ , where  $Tx_{SNS}$  and  $Rx_{SNS}$ , appear in Figs. 9 and 10, respectively. Alternatively, this magnitude can be directly measured either in through transmission mode (using two transducers, see Fig. 5) or in pulse-echo mode (for one single transducer, see Fig. 3). This alternative measurement can be used as verification of the results obtained by the procedure here proposed.

Fig. 11 shows the comparison of  $Tx_{SNS} \times Rx_{SNS}$  obtained from  $Tx_{SNS} \times Rx_{SNS}$  (blue and green) with the direct measurement of  $Tx_{SNS} \times Rx_{SNS}$  in through transmission mode using both transducers (red), while Fig. 12 shows the

comparison of  $Tx_{SNS} \times Rx_{SNS}$  (blue and green) with a direct measurement of  $Tx_{SNS}-Rx_{SNS}$  in through transmission mode using both transducers (yellow and black).

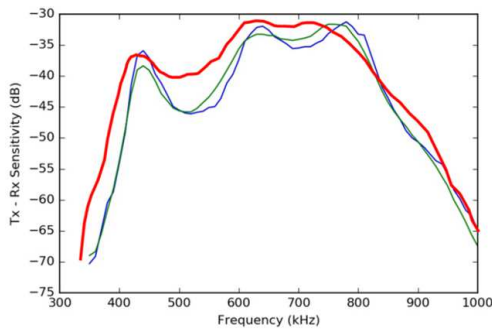


Fig. 11. Combined transmission-reception sensitivity band ( $Tx_{SNS} \times Rx_{SNS}$ ), blue and green, with direct measurement in through transmission configuration (red)

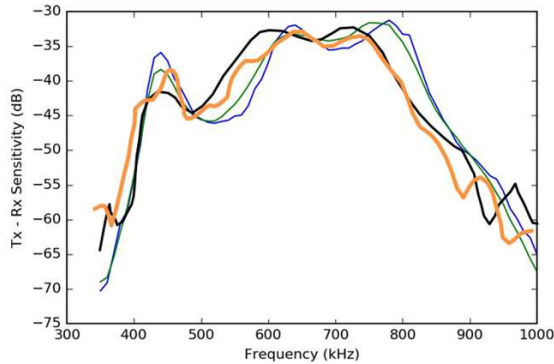


Fig. 12. Combined transmission-reception sensitivity band ( $Tx_{SNS} \times Rx_{SNS}$ ), blue and green, with direct measurement in pulse-echo configuration (black and orange)

#### IV. CONCLUSIONS

A simple and low-cost method to characterize transmission sensitivity of air coupled transducers has been presented. The calibrated transmitter can be used to measure the sensitivity of other transducers in reception mode. The method has been applied to characterize 0.65 MHz air-coupled transducers in transmission and in reception mode. Combined transmission-reception sensitivity have been calculated and compared with direct measurements in transmission and pulse-echo with good agreement. Results are of interest for applications demanding a precise

knowledge of the pressure level generated by an air-coupled transducer (medical applications) or for the further optimization of air-coupled transducers.

#### REFERENCES

- [1] G. Hayward and A. Gachagan, "An evaluation of 1-3 connectivity composite transducers for air-coupled ultrasonic applications," *J. Acoust. Soc. Am.*, vol. 99, no. March 1995, pp. 2148–2157, 1996.
- [2] I. Ladabaum, X. Jin, H. T. Soh, A. Atalar, and B. T. Khuri-Yakub, "Surface micromachined capacitive ultrasonic transducers," *IEEE Trans. Ultrason. Ferroelectr. Freq. Control*, vol. 45, no. 3, pp. 678–90, Jan. 1998.
- [3] T. Gomez Alvarez-Arenas *et al.*, "Low-Impedance and low-loss customized materials for air-coupled piezoelectric transducers," in *IEEE International Ultrasonics Symposium*, 2001, vol. 0, no. 1, pp. 1077–1080.
- [4] T. Gudra and K. J. Opielinski, "Influence of acoustic impedance of multilayer acoustic systems on the transfer function of ultrasonic airborne transducers," *Ultrasonics*, vol. 40, no. 1–8, pp. 457–463, 2002.
- [5] M. Toda, "New type of matching layer for air-coupled ultrasonic transducers," *IEEE Trans. Ultrason. Ferroelectr. Freq. Control*, vol. 49, no. 7, pp. 972–979, 2002.
- [6] T. E. Gomez-Alvarez Arenas, "Acoustic Impedance Matching of Piezoelectric Transducers to the air," *IEEE Trans. Ultrason. Ferroelectr. Freq. Control*, vol. 51, no. 5, pp. 624–633, 2004.
- [7] S. P. Kelly, G. Hayward, and T. E. G. Alvarez-Arenas, "Characterization and assessment of an integrated matching layer for air-coupled ultrasonic applications," *IEEE Trans. Ultrason. Ferroelectr. Freq. Control*, vol. 51, no. 10, pp. 1314–1323, 2004.
- [8] T. E. G. Alvarez-Arenas, T. R. Shroud, S. J. Zhang, and H. J. Lee, "Air-Coupled Transducers Based on 1-3 Connectivity," in *IEEE International Ultrasonics Symposium*, 2012, pp. 2230–2233.
- [9] T. E. G. Alvarez-Arenas, "Air-coupled piezoelectric transducers with active polypropylene foam matching layers," *Sensors (Switzerland)*, vol. 13, no. 5, pp. 5996–6013, 2013.
- [10] A. M. Ginel and T. G. Alvarez-Arenas, "Air-coupled Transducers for Quality Control in the Food Industry," *IEEE Int. Ultrason. Symp* 2019, pp. 803–806, 2019.
- [11] H. Nguendou Kenhagho, F. Canbaz, T. E. Gomez Alvarez-Arenas, R. Guzman, P. Cattin, and A. Zam, "Machine Learning-Based Optoacoustic Tissue Classification Method for Laser Osteotomes Using an Air-Coupled Transducer," *Lasers Surg. Med.*, vol. 53, no. 3, pp. 377–389, 2021.
- [12] Z. Jin *et al.*, "In-vivo 3D corneal elasticity using air-coupled ultrasound optical coherence elastography," *Biomed. Opt. Express*, vol. 10, no. 12, p. 6272, 2019.
- [13] A. Gachagan, G. Hayward, S. P. Kelly, and W. Galbraith, "Characterization of Air-Coupled Transducers," *IEEE Trans. on Ultrason., Ferroelectr., Freq. Control* vol. 43, no. 4, 1996.
- [14] M. Almqvist, A. Holm, H. W. Persson, and K. Lindström, "Characterization of air-coupled ultrasound transducers in the frequency range 40 kHz-2 MHz using light diffraction tomography," *Ultrasonics*, vol. 37, no. 8, pp. 565–575, 2000.

## 4.3 International Congress on Ultrasonics (ICU)

### 4.3.1 ICU 2019, Bruges, Belgium.

The paper can be found at page 102 and the full reference is:

Andrius Chaziachmetovas, Linas Svilainis, Julio Quirce, and Tomas Gomez Alvarez-Arenas , "Ultrasonic ferroelectret transducer excitation study", Proc. Mtgs. Acoust. 38, 045030 (2019) <https://doi.org/10.1121/2.0001176>

### 4.3.2 ICU 2019, Bruges, Belgium.

The paper can be found at page 108 and the full reference is:

Jorge Camacho, Giovanni Ortiz, Julio Quirce, Alba Martin-Ginel, and Tomás Gömez Álvarez-Arenas , "Miniaturized sector array with additive-manufactured mirror for low diameter pipe inspection", Proc. Mtgs. Acoust. 38, 030014 (2019) <https://doi.org/10.1121/2.0001179>

**Ultrasonic ferroelectret transducer excitation study**

Andrius Chaziachmetovas, Linas Svilainis, Julio Quirce, and Tomas Gomez Alvarez-Arenas

Citation: *Proc. Mtgs. Acoust.* **38**, 045030 (2019); doi: 10.1121/2.0001176

View online: <https://doi.org/10.1121/2.0001176>

View Table of Contents: <https://asa.scitation.org/toc/pma/38/1>

Published by the [Acoustical Society of America](#)

---

**ARTICLES YOU MAY BE INTERESTED IN**

**Arbitrary position and width pulse sequences - novel spread spectrum signals for ultrasonic measurements**  
Proceedings of Meetings on Acoustics **38**, 055016 (2019); <https://doi.org/10.1121/2.0001167>

**Numerical modeling of ultrasonic wave propagation in CFRP radii**  
Proceedings of Meetings on Acoustics **38**, 045031 (2019); <https://doi.org/10.1121/2.0001181>

**A method for undersea gas bubbles detection from acoustic image**  
Proceedings of Meetings on Acoustics **39**, 070003 (2019); <https://doi.org/10.1121/2.0001263>

**Qualitative analysis of a 2D multiphysics model for vibration induced heating at closed defects**  
Proceedings of Meetings on Acoustics **38**, 022007 (2019); <https://doi.org/10.1121/2.0001183>

**Gas-coupled transducers for pulse-echo operation**  
Proceedings of Meetings on Acoustics **38**, 045032 (2019); <https://doi.org/10.1121/2.0001191>

**Acoustic metamaterial capsule for reduction of stage machinery noise**  
The Journal of the Acoustical Society of America **147**, 1491 (2020); <https://doi.org/10.1121/10.0000857>

---



**POMA** Proceedings  
of Meetings  
on Acoustics

**Turn Your ASA Presentations  
and Posters into Published Papers!**





Volume 38

<http://acousticalsociety.org/>

## 2019 International Congress on Ultrasonics

Bruges, Belgium

3-6 September 2019

### Physical Acoustics: PSP (1/3) Presentation 5

## Ultrasonic ferroelectret transducer excitation study

**Andrius Chažiachmetovas and Linas Svilainis***Department of Electronics Engineering, Kaunas University of Technology, Kaunas, 51368, LITHUANIA;  
andrius.chaziachmetovas@ktu.lt; linas.svilainis@ktu.lt***Julio Quirce and Tomas Gomez Alvarez-Arenas***Institute of Physical and Information Technologies, Spanish National Research Council, Madrid, SPAIN;  
j.quirce@csic.es; t.gomez@csic.es*

Investigation of the new type ferroelectret transducer excitation is presented. The conventional ultrasonic transducers made from piezoelectric ceramics, but the power efficiency change to mechanical efficiency is limited, furthermore the acoustic impedance is not compatible with the test medium. These drawbacks can be avoided using ferroelectret transducers. It should be noted that the efficiency of ferroelectret transducers increases significantly when the excitation voltage exceeds 500-1000 V. However, such excitation voltages are difficult to achieve: conventional active components (transistors) can only withstand a voltage up to 1700 V; when required excitation voltage is up to 2000 V active component voltage can go beyond therefore switch should be capable to withstanding beyond 2 kV. The investigation of high voltage (up to 2 kV) excitation of ferroelectret transducers is presented. Spectrum of the signals generated, transduction efficiency dependence on applied voltage and its' polarity were studied. An analysis of the spatial pressure distribution for both single-element and multi-element transducers is presented.

Published by the Acoustical Society of America



## 1. INTRODUCTION

Broadening of the ultrasound application areas requires the development of the specific transducers with different requirements (cost, durability, disposable character, etc.). Use of noncontact ultrasound is an attractive field in applications related to NDT, human-machine interfaces, haptics, etc. Air-coupled ultrasound is also an offering ease of measurement setup, absence of mechanical contact with test object and no need for liquid couplant, which can damage the test sample. While piezoelectric materials are widely used for ultrasonic transducers, this material presents some problems for air-coupled ultrasound transmission and reception in air due its high acoustical impedance. Piezoelectric ceramics requires complicated technological operations, especially when it comes to multi-element transducers, so cost for ultrasonic transducers is high. *Ferroelectret films* (FF) have low acoustic impedance,  $<0.1$  MRayl<sup>1</sup>, so offer much better match to air in noncontact ultrasound applications, though they may present other problems related to the lack of electrical charge stability and low electrical impedance among other factors. FF's are made as permanently charged nonpolar space-charge electrets, they exhibit piezoelectric response and mechanical flexibility. Essential, that FF's provide hopes for transducer cost reduction: array transducer can be produced by gluing the FF on PCB traces, forming "hot" electrode<sup>2</sup>. Yet, there are some technological problems associated: FF thickness is typically between 30  $\mu\text{m}$  and 150  $\mu\text{m}$ , non-conductive glue will decrease the electrical coupling of the "hot" electrode. *Ferroelectret* (FE) materials also exhibit the electrostriction effect: inverse transfer constant for electrostriction follows square law to the excitation voltage, while piezoelectricity effect does not depend on the excitation voltage<sup>3</sup>. Excitation voltage should exceed 500 V in order the electrostriction effect to become significant. Excitation of 500 V<sup>4</sup> or even 1000 V<sup>5</sup> is relatively easy to achieve since transistors with 1.7 kV breakdown are available, but there is a challenge<sup>6</sup> to get up to 2 kV excitation since breakdown voltage should be higher than 2 kV. Special pulser topology has to be devised if both excitation polarities are needed.

Air-coupled transducer parameter investigation is presented in this study. FE material based transducer was investigated. Transducer's efficiency depends on its construction: hot electrode must be as close as possible to FE material in order to maximize the electrical field interaction. Therefore various technologies for hot electrode attachment were studied. Since acoustic pressure spatial pressure distribution on the transducer surface defines the resulting field, this spatial distribution was also investigated for single element and multielement transducer. The amount of energy transferred into acoustic pressure depends on electrical input impedance, which was analyzed. Due to high input impedance, transducer has to be excited using extremely high voltage in order to get sufficient acoustic output. Excitation up to 2 kV, causing nonlinearities both in transducer response and propagating media were investigated.

## 2. METHODOLOGY

Low frequencies, used in air-coupled ultrasound, prevent the efficient use of step-up transformer for transducer excitation<sup>6</sup>. Excitation electronics, capable of 2 kV positive or negative excitation was developed. Sample transducers have been manufactured using 65  $\mu\text{m}$  EMFIT film HS-03-20BRAL1<sup>7</sup> mounted on FR4 PCB (Fig.1). EMFIT film was glued on the PCB copper which was used as "Hot" electrode. Whole PCB was 40 mm x 40 mm, "Hot" electrode size was 20 mm x 20 mm, all copper was removed around "Hot" electrode to prevent high voltage breakdown<sup>6</sup> at the edges (Fig.1 center). Aluminum coating of EMFIT served as ground and it was connected to opposite side of PCB using conductive copper foil (WE 3003310A 40  $\mu\text{m}$ ). Opposite side was a copper ground (Fig. 1 right) except 10 mm diameter keep-out around "Hot" electrode solder point. BNC connector was soldered on opposite side of PCB.



*Figure 1: Single element transducer (left) and PCB: EMFIT side (center), connector side (right).*

The multielement (2x2, 10 mm x 10 mm each) transducer was manufactured following same topology (Fig.2).

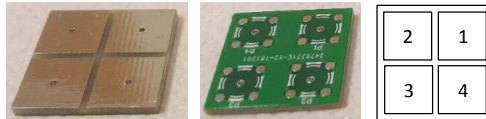


**Figure 2: Multielement transducer PCB: EMFIT (left), connector side (center) and numbering (right).**

The conductive textile (WE 33050 100  $\mu\text{m}$ ) as “Hot” electrode for segment 1 and 2 was used and conductive copper foil (WE 3003310A 40  $\mu\text{m}$ ) was used for segments 3 and 4 in order to avoid electrical field decrease due to non-conductive gluing to PCB copper. SMA connectors in order to save space were used. Small 3 mm diameter piece of FF as acoustic field spatial distribution measurement sensor was used.

### 3. RESULTS AND DISCUSSION

Transducers’ impedance was measured using WK6500B impedance analyzer. Measurements were compensated for connector impedance to have bare EMFIT response and converted into series real and imaginary parts (Fig.3).

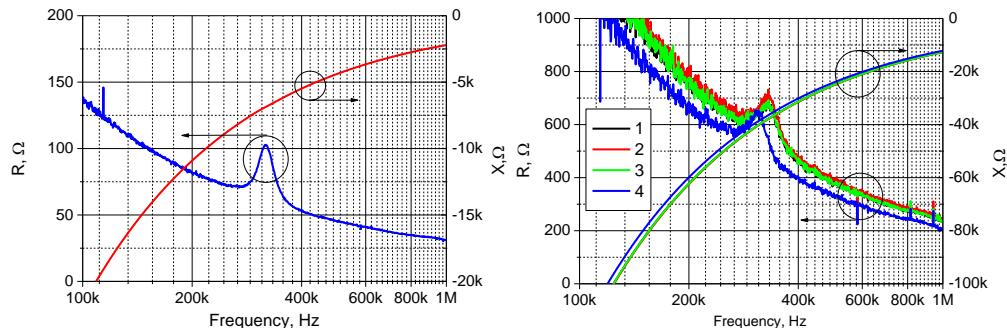


**Figure 3: Electrical impedance of test transducers: single element (left) and multielement (right).**

Impedance measurement results indicate that the real part (representing transduction) is severely tampered by capacitance: impedance ratio is 1:100. The majority of energy exerted for excitation will be wasted. Furthermore, after conversion into parallel form, such impedance corresponds to 500 k $\Omega$  for large transducer and 2 M $\Omega$  for multi element. The use of conductive patches<sup>8</sup> was studied. Spatial pressure distribution for 2x2 element transducer when every element was driven by 320 kHz 5 periods rectangular 300 V toneburst is presented in Fig. 4.

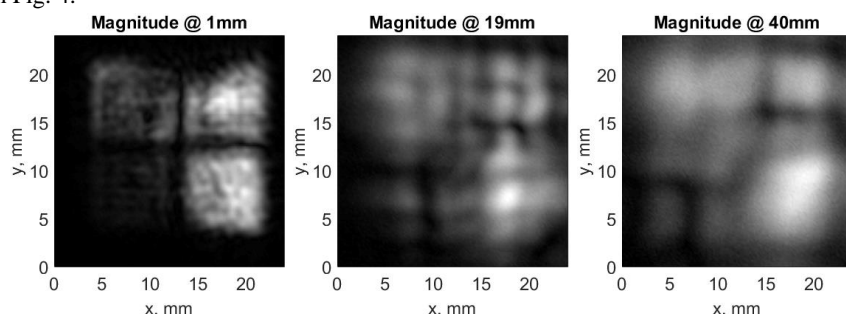


**Figure 4: Spatial pressure distribution at 320 kHz for 2x2 element transducer when using 300 V excitation: at 1 mm (left), 19 mm (center) and 40 mm (right) distance.**

It can be seen, that the use of patches, attached using conductive glue, provides uneven coupling so transmission efficiency varies. No difference on segments between textile (1, 2 in Fig. 2) and copper foil (3,4 in Fig. 2) was noted. Spatial pressure distribution of single element transducer excited by 320 kHz five periods rectangular 300 V toneburst is presented in Fig. 5.

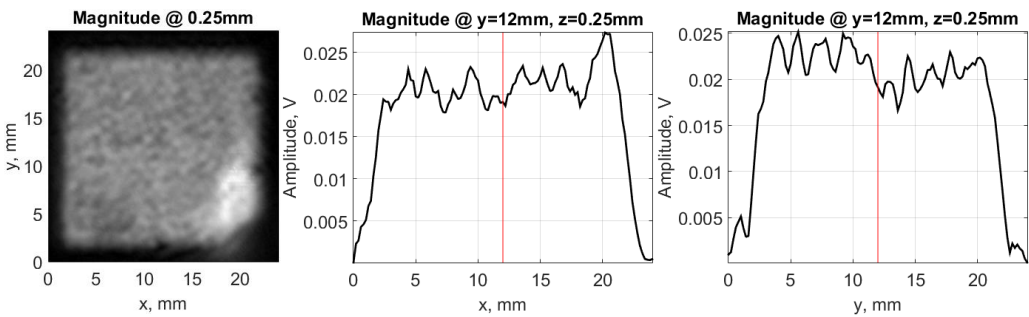


**Figure 5:** Pressure distribution at 320 kHz for single element transducer when using 300 V excitation at 0.25 mm: C-scan (left), slice along x at  $y=12$  mm (center) and slice along y at  $x=12$  mm (right).

In this case the FF was directly glued on PCB electrode. Radiation of whole transducer surface is even. Light artefact, seen at the lower right edge is created by signal leak through aluminum coating that was damaged due to rubbing during FF application. Pressure distribution along transducer axis for a single element transducer when excited by negative 320 kHz 5 periods rectangular 300 V and 1000 V toneburst is presented in Fig. 6.

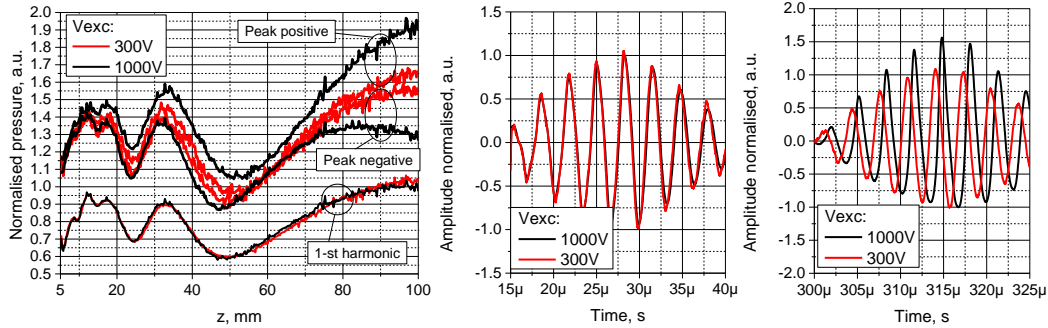


**Figure 6:** Received signal variation along the distance from transducer (left) and signals at 5 mm (center) and 100 mm (right) distance for negative excitation using 300 V and 1000 V.

It can be noted that the air nonlinearity builds up during propagation time, so signal received at 100 mm distance has difference between peak positive and peak negative pressure. The first harmonic was extracted using sine wave correlation<sup>6</sup> within the 25  $\mu$ s window, as indicated in Fig. 6 above. Spectral shape changes of the signal were received at 100 mm distance (end of near zone is 95 mm) from a single element transducer driven by a single rectangular pulse (duration matched to 320 kHz) of varying voltage with a different polarity in Fig. 7 is presented. Note, that acoustic response in Fig. 7 (left) is normalized to excitation voltage. In case of linear response, it should have been equal for both 100 V and 2 kV. Response for 2 kV is higher thanks to increased electrostriction<sup>3</sup> interaction, it is parabolic, see Fig. 7 (right).

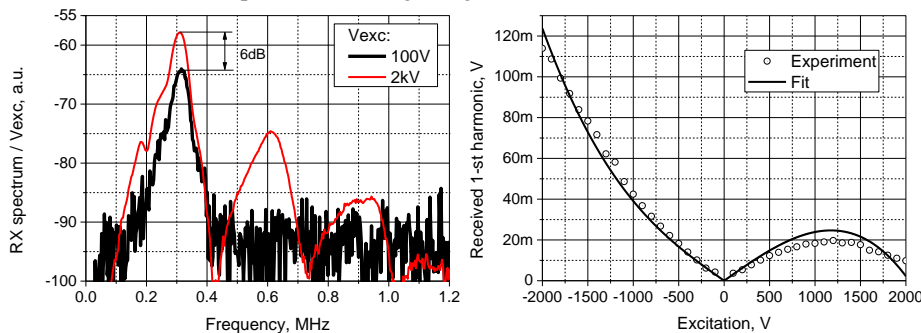


**Figure 7:** Spectrum (left) of signal registered and first harmonic amplitude relation to excitation voltage amplitude and polarity (right).

It can be seen that the air nonlinearity prevents the significant rise of first harmonic already at the end of near zone. Therefore, gain in a first harmonic amplitude is just 6 dB. Results were fitted (Fig. 7 right) using assumption of electrostrictive effect, presented in<sup>3</sup>.

## 4. CONCLUSION

Despite of good matching to air, the ferroelectret films have large electrical input impedance. This creates the need for high voltage excitation, which in turn creates the additional burden for excitation electronics. Air-coupled measurement is usually carried out at some distance to prevent the multiple reflections. Investigation has indicated that the use of high instantaneous power (acoustic pressure) signals is related to air nonlinearity and higher harmonics build up even using 1000 V excitation. Thin aluminum coating, used to maintain the low acoustic impedance, is not durable so any rubbing immediately results in electrode damage.

## ACKNOWLEDGEMENTS

This work was supported by the Research, Development and Innovation Fund of Kaunas University of Technology (grant No. PP-91F/19) and ECERES grant DPI2016-78876-R-AEI/FEDER, UE from the Spanish State Research Agency (AEI) and the European Regional Development Fund (ERDF/FEDER).

## REFERENCES

- <sup>1</sup> J. Hillenbrand, G. M. Sessler, Piezoelectricity in cellular electret films, IEEE Transactions on Dielectrics and Electrical Insulation, **7** 2000, 537 - 542.
- <sup>2</sup> A.J. Martin, et al., EMFi-Based Ultrasonic Sensory Array for 3D Localization of Reflectors Using Positioning Algorithms, IEEE Sensors Journal, **15** 2015, 2951-2962.
- <sup>3</sup> V. Bovtun, et al., Enhanced electromechanical response of ferroelectret ultrasonic transducers under high voltage excitation, Advances in Applied Ceramics: Structural, Functional and Bioceramics, **112** 2013, 97-102.
- <sup>4</sup> L.Svilainis, A.Chazachmetovas, V.Dumbrava, Half bridge topology 500 V pulser for ultrasonic transducer excitation, Ultrasonics, **59** 2015, 79-85.
- <sup>5</sup> L Svilainis, A Chazachmetovas, V Dumbrava, Efficient high voltage pulser for piezoelectric air coupled transducer, Ultrasonics, **53** 2013, 225-231.
- <sup>6</sup> A. Chazachmetovas, T. E. Gómez Álvarez-Arenas, L. Svilainis, Comparison of Direct and Transformer Drive High Voltage Ultrasonic Pulser Topologies, IEEE IDAACS, **2** 2017, 1105-1110.
- <sup>7</sup> T. E. Gómez Álvarez-Arenas, et al. Noncontact ultrasonic spectroscopy applied to the study of polypropylene ferroelectrets, Journal of Applied Physics, **108** 2010, 074110.
- <sup>8</sup> J. L. Ealo, J. C. Prieto, F. Seco, Dynamic response estimation of multilayer ferroelectret-based transducers using lumped-element electromechanical models, IEEE IUS, 2009, 2754-2757.

**Miniaturized sector array with additive-manufactured mirror for low diameter pipe inspection**

Jorge Camacho, Giovanni Ortiz, Julio Quirce, Alba Martin-Ginel, and Tomás Gömez Álvarez-Arenas

Citation: *Proc. Mtgs. Acoust.* **38**, 030014 (2019); doi: 10.1121/2.0001179

View online: <https://doi.org/10.1121/2.0001179>

View Table of Contents: <https://asa.scitation.org/toc/pma/38/1>

Published by the [Acoustical Society of America](#)

---

**ARTICLES YOU MAY BE INTERESTED IN**

[Advances in air-coupled ultrasonic transducers for non-destructive testing](#)

Proceedings of Meetings on Acoustics **38**, 030003 (2019); <https://doi.org/10.1121/2.0001072>

[Calcium sulfate setting monitoring with ultrasonic backscattering analysis](#)

Proceedings of Meetings on Acoustics **38**, 020009 (2019); <https://doi.org/10.1121/2.0001093>

[Water surface displacement induced by acoustic radiation pressure of focused ultrasound acting on air-water interface](#)

Proceedings of Meetings on Acoustics **38**, 045025 (2019); <https://doi.org/10.1121/2.0001145>

[Phase Coherence Imaging: Principles, applications and current developments](#)

Proceedings of Meetings on Acoustics **38**, 055012 (2019); <https://doi.org/10.1121/2.0001201>

[Acoustic characterization of hidden thin \(adhesive\) layers](#)

Proceedings of Meetings on Acoustics **38**, 055010 (2019); <https://doi.org/10.1121/2.0001131>

[Evaluation of a multiple scattering sensor for water-in-oil emulsion monitoring](#)

Proceedings of Meetings on Acoustics **38**, 055007 (2019); <https://doi.org/10.1121/2.0001090>

---



**POMA** Proceedings  
of Meetings  
on Acoustics

**Turn Your ASA Presentations  
and Posters into Published Papers!**





## 2019 International Congress on Ultrasonics



Bruges, Belgium

3-6 September 2019

### Engineering Acoustics: NAS+NTD (2/2): NDT Presentation 1

## Miniaturized sector array with additive-manufactured mirror for low diameter pipe inspection

**Jorge Camacho***Departamento de Sensores y Sistemas Ultrasónicos, Consejo Superior de Investigaciones Científicas,  
Madrid, 28006, SPAIN; j.camacho@csic.es***Giovanni Ortiz, Julio Quirce, Alba Martín-Ginel and Tomás Gómez Álvarez-Arenas***CSIC, Madrid, SPAIN; giovanni1805@gmail.com j.quirce.aguilar@gmail.com, a.ginel@csic.es,  
t.gomez@csic.es;*

The ultrasonic inspection of low diameter pipes remains challenging, particularly in the power industry where new heater exchanger designs include tight curvatures and severe access restrictions. Moreover, advances in welding techniques require performing not only normal-incidence corrosion maps typical in pipe inspection, but also the more complex weld evaluation procedures that require oblique incidence at different propagation angles and modes.

This work presents the design, fabrication and preliminary characterization of a miniaturized sector array for low diameter pipe inspection, with 7.8 mm exterior diameter, 8 sector elements and 2.0 MHz center frequency. A 45° reflector cone was developed by additive manufacturing for obtaining normal incidence at the pipe wall. The additive manufacturing technique allows to easily testing different mirror geometries at low cost, giving more flexibility to the design and validation process.

The experimental results include the analysis of the pulse-echo temporal and frequency response of the array elements, and the inspection of a 25 mm thickness ring to assess the feasibility of using this device in corrosion mapping applications.

---

Published by the Acoustical Society of America



## 2019 INTERNATIONAL CONGRESS ON ULTRASONICS BRUGES, BELGIUM, 3-6 SEPT 2019

### I. Introduction.

The inspection of low diameter pipes is of increasing interest in the power generation industry, mainly for the condition evaluation of boilers and heat exchangers during manufacturing and in service. While several solutions exist for ultrasonic automatic inspection from the outside of the pipe [1], access limitations of pipe clusters heavily restrict their use. On the contrary, the interior of the pipe offers a constant and homogeneous geometry that can be used to guide the movement of a transducer, with the additional difficulty of designing and manufacturing a miniaturized ultrasonic device.

Most current ultrasonic inspection devices for low diameter pipes are based on the Internal Rotary Inspection System (IRIS) concept [2], where a single element transducer propagates a beam in the axial direction of the pipe and a 45° rotary mirror redirects it to the wall with normal incidence. Usually, a water driven turbine is used to rotate the mirror, taking advantage of the own pressure of the water used for ultrasound coupling. Alternatively, some devices include an external drive mechanism for the mirror rotation [3].

To avoid the rotary motion, phased-array probes can be used. If the array elements are located around the tube axis no mirror is required, as the beams are directed to the pipe wall with normal incidence [4]. The main drawback of this approach is that the elements must be distributed cylindrically, which complicates transducer design and manufacturing. Alternatively, a flat circular array with elements in the radial direction can be used. A cone mirror is required in this case to redirect the beams towards the pipe wall with normal or oblique incidence, covering the 360° of the tube circumference with no rotational movement while still using a planar array design [5].

The device developed in this work follows the last approach. A 7.8 mm exterior diameter, 8 sector elements and 2.0 MHz center frequency array was developed, along with a cone mirror to obtain normal incidence at the pipe wall. Additive manufacturing was used for the mirror and the holding device, which enables low cost and fast prototyping for system validation.

### II. Methodology.

#### II.1 Array design and manufacturing.

1-3 connectivity piezocomposite disks (5 mm diameter) made of PZT5A fibers (250  $\mu\text{m}$  diameter) randomly embedded in an epoxy resin matrix, with ceramic volume fraction of 65% and acoustic impedance of 15 MRayl. Flat surfaces are plated (CuSn) and they are poled in the thickness direction and operated in thickness mode (resonant frequency 2.0 MHz). All arrays are kerfless arrays with 8 elements (see Fig. 1) [6, 7]. The different elements are obtained by cutting the metallization of the back electrode (100  $\mu\text{m}$  wide and 100  $\mu\text{m}$  depth). In addition, a 10 mm long backing made of epoxy resin loaded with alumina particles, 5 $\mu\text{m}$  diameter (50% weight), with acoustic impedance of 4 MRayl was added to increase bandwidth, and a wear plate at the front face, to protect the piezoelectric element, made of silver loaded epoxy resin (150  $\mu\text{m}$ , 6 MRayl).

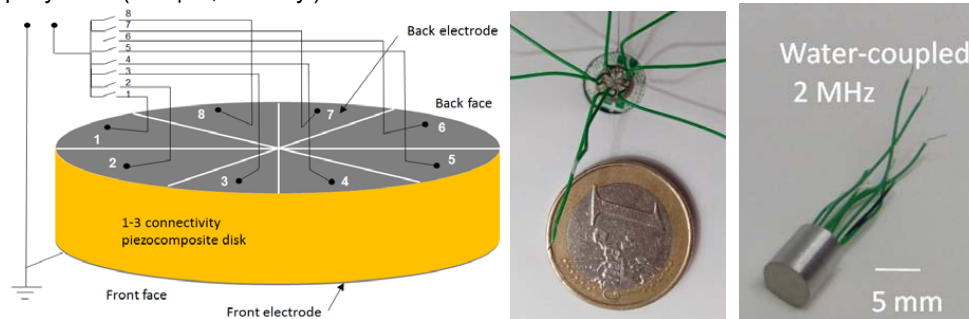


Figure 1 – Pictures of the array design and manufacturing process

## II.2 Mirror design and manufacturing.

For achieving normal incidence at the pipe wall a 45° cone and 12 mm diameter was designed, along with three supports and a holding ring for the circular array (Figure 2). All parts were manufactured in polylactide (PLA) material with a Legio 3D printer (Leon3D, Valverde de la Virgen, Spain).

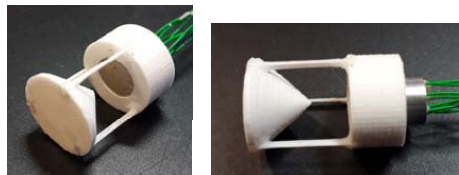


Figure 2- Different views of the sector array and the reflector cone.

## II.3 Experimental set-up.

A SITAU-111 (Dasel SL, Madrid, Spain) 128 channel phased array system was used for excitation and signal reception, with a custom developed Matlab (Mathworks Inc., MA, USA) interface for data acquisition and display. In the first experiment, a 100 mm aluminum block was used as reflector for the array without the cone mirror (Figure 3.a). The eight array elements were sequentially excited and the received signals stored for sensitivity and bandwidth analysis. In a second experiment, the cone mirror was used to inspect a ring of 50 mm interior diameter and 25 mm thickness (Figure 3.b), with the objective of evaluating the feasibility of measuring wall thickness in corrosion mapping applications. A SDS1204X-E oscilloscope (Siglent, Guangdong, China) was used for registering the excitation signal, in order to calculate frequency response of the array elements.

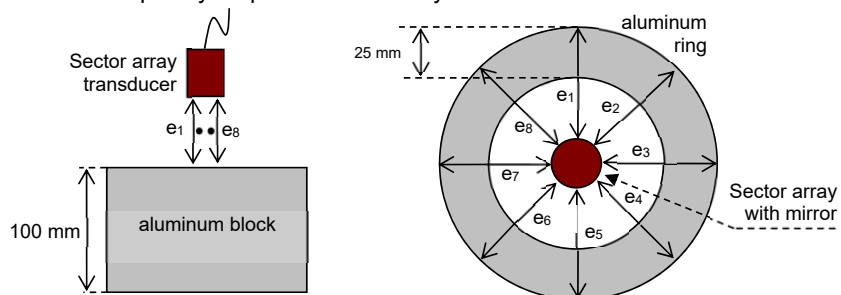


Figure 3 – Schematic representation of (a) experiment 1 for array characterization and (b) experiment 2 for mirror device testing.

## III. Results and discussion.

### III.1 Array characterization.

Figure 4 shows the elements pulse-echo sensitivity (SNS) against frequency, obtained from

$$SNS(dB) = 20 \cdot \log_{10} \left| \frac{FFT(V_{RX})}{FFT(V_{TX})} \right| \quad (1)$$

where  $V_{RX}$  is the received echo and  $V_{TX}$  the excitation pulse. For comparison, all the plots are normalized to the maximum response of element 6, the one with best sensitivity.

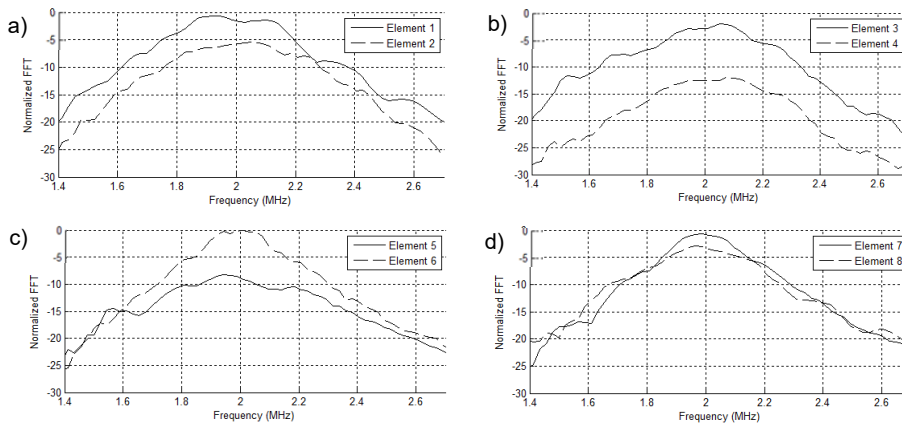


Figure 4 – Sensitivity plots for elements (a) 1,2 (b) 3,4 (c) 5,6 and (d) 7,8

Table 1 – Measured parameters

Element number	Sensitivity (dB)	Center frequency (MHz)	Bandwidth (%)	Element number	Sensitivity (dB)	Center frequency (MHz)	Bandwidth (%)
1	-0.7	1.9	69	5	-8.3	1.9	85
2	-5.4	2.1	61	6	0	2.0	57
3	-2.1	2.1	65	7	-0.7	2.0	59
4	-12.0	2.1	72	8	-2.9	2.0	73

Table 1 shows the parameters measured for the eight array elements. Center frequency variations are negligible, while sensitivity differences are within -6 dB except for elements 4 and 5. The average bandwidth is 68%.

### III.2 Mirror testing.

Figure 5 shows the B-Scan obtained from the aluminum ring, with a time window showing the entry echo of the inner surface and the back-wall echo of the outer surface. A time-gain-compensation of 0.7 dB/mm was applied to display both echoes with similar amplitude, and the sensitivity measured in experiment 1 (Table 1) was used to equalize the elements amplitude response. For all channels the time distance between echoes corresponds with the component thickness, and acceptable signal-to-noise ratio was obtained in all cases.

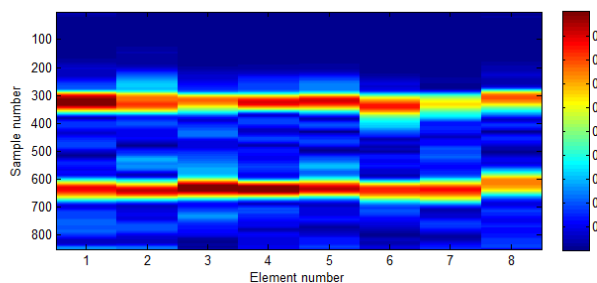


Figure 5 – B-Scan of the cylinder showing the internal and external wall echoes.

### IV. Conclusions.

The feasibility of developing a miniaturized array probe for the inspection of small diameter pipes with the resources available at the USTG lab was demonstrated. The manufactured prototype has acceptable performance, being its main limitation the relatively low center frequency for this kind of applications. This limitation will be addressed in future designs using

J. Camacho et al.

Miniaturized sector array with additive-manufactured mirror for low-diameter pipe inspection

higher frequency piezocomposites. Additive manufacturing has proven to be a valuable tool for fast prototyping, providing enough precision for the first feasibility tests of the device.

**Acknowledgements:** This work is supported by the projects RTI2018-099118-A-I00 founded by MCIU/AEI/FEDER, UE, and grant (DPI2016-78876-R-AEI/FEDER, UE)

#### References

- [1] Michael Moles, Ed Ginzel, Phased Array for Small Diameter, Thin-Walled Piping Inspections, 18th World Conference on Nondestructive Testing, 16-20 April 2012, Durban, South Africa.
- [2] Birchall M., Sevcic N., 1992, "Heath exchangers and boiler tube thickness measurement by ultrasonic internal rotary inspection system (IRIS)". Proceedings of the 13 th World conference on Non-Destructive Testing, Vol. 1, São Paulo/SP, Brazil, pp 816-822;
- [3] Z. Chen, K. Chan, J. Huggins, Tom Malkiewicz, Ultrasonic Inspection of Steam Generators at CANDU Power Plants,
- [4] H. C. L. Vos, R. Schepers and J. A. Vogel, "An ultrasonic circular array transducer for pipeline and borehole inspection," IEEE 1988 Ultrasonics Symp. Proc., Chicago, IL, USA, 1988, pp. 659-662 vol.2.
- [5] J. Poguet, A. Garcia, J. Vazquez, J. Marguet, F. Pichonnat, "Phased Array technology Concepts, probes and applications", 8th European Congress on Non Destructive Testing, June 17-21, 2002, Barcelona, Spain.
- [6] T. G. Alvarez-Arenas and L. Diez, "Air-coupled and water immersion sectorized array transducers for industrial and medical endoscopy," 2017 IEEE International Ultrasonics Symposium (IUS), Washington, DC, 2017, pp. 1-4.
- [7] T. G. Alvarez-Arenas and L. Diez, "Ultrasonic single element and sectorized array transducer with omnidirectional 2D field distribution for non-contact human-machine interface and eco-location", Electronika ir Electrotechnika, 23(4), pp. 51-55, 2017



## Chapter 5

# Conclusions and Future work

### 5.1 Conclusions

During the last decade, previous works have demonstrated that FF can be used as an active layer for ultrasonic air-coupled transducers. Over the last five years, there have been some attempts to use the same material for ultrasonic water-coupled transducers, which is where this thesis focuses.

The main conclusions of this thesis refer to the fundamental properties of FF, in particular, the unexpected fact that the FF's mechanical resonances, when immersed, do not change, but their piezoelectric resonances disappear, which is critical for the design and fabrication of this type of ultrasonic transducers. And fabrication procedures for ultrasonic transducers and hydrophones that can play an important role in a market where PVDF is the most common material.

An essential part of this work deal with the extraction of the FF properties by using a non-contact resonant ultrasound spectroscopy technique. The HS03 and HS06 FF results have been reported in two directions (Objective 1).

The mechanical and electromechanical properties have been studied in detail, and their use to manufacture different FF transducers, such as spherically focused, cylindrical, and circular apertures. This concludes that we can enhance the transducer's performance by using the previously extracted information and foresee the FF limitation when designing a sensor or transducer that uses this material as the active layer.

The impact of the microstructure and mesostructure of the FF in their mechanical and electromechanical response has been intensely investigated thanks to this technique. Thickness resonances in the transmission coefficient spectra have been measured and calculated, and the fitting of the calculated values and measured ones are excellent, and it allows the extraction of the properties of the FF. Moreover, the FF is immersed in two outer mediums, air, and water, to determine how this can affect the FF response. The main conclusion related to this fact is that FF can be understood as a sandwich model of three layers. The first and third, also called skin in the published papers, share the same properties: higher bulk modulus and density and smaller acoustic impedance than the core, and smaller thickness. This conclusion is validated according to the cross-section SEM images of the FF used.

Properties of the cellular structure, such as elongation of the internal voids, have been satisfactorily mathematically described by a simple hexagonal honeycomb structure, which allows a deeper understanding of the FF internal mechanism and enhances its properties for transducer construction. This technique could also be helpful to characterize FF made with other cellular polymers, as was described in the introduction.

Thanks to the mechanical properties studied and the manufacturing of the transducers with different geometrical apertures, the FF is suitable to use as an active layer for transducer construction in these applications where aperture geometry is not conventional. Additionally, in the case of the focused spherical aperture transducer, we have reported the same frequency response as the circular aperture but with better spatial resolution. This conclusion can be extended to the fact that we have reported a very detailed scheme design for the HS03 and HS06 FF transducers, which can be used for other FF (mentioned in the introduction) with no extra modifications beyond the FF replacement.

One of the main contributions of this thesis is that we report that electromechanical thickness resonances disappear in underwater operation, and we provide an explanation for that, which leads us to the idea of producing hydrophones out of this material. As a result, when the film is immersed, the faces in contact with water experience maximum stress and minimum displacement. This fact limits the pulse-echo operation performance in transducers with this active layer, despite the  $d_{33}$  piezoelectric factor of the HS03 being good enough to perform -46 dB sensitivity and 63.6 % bandwidth at a 6 dB drop under these conditions.

The unexpected disappearance of electromechanical resonances reported in the previous conclusions lead us to the unique idea of using this material as an active layer for hydrophones to take advantage of the lack of resonances which will not limit the upper-frequency response of the hydrophone. From this idea, the entire manufacturing process of the hydrophone has been developed in this work.

Also, we thought it appropriate to compare the frequency response of the reception stage of two hydrophones with the same construction design, one with an active layer of HS03 FF and the other with PVDF, to conclude that PVDF reports better sensitivity for all frequencies, but especially those that are superior to 1 MHz. FF sensitivity is quite similar to PVDF at low frequencies and offers a larger and flatter bandwidth for both cases, 3 dB drop and 6 dB drop.

The PVDF hydrophone bandwidth is limited because, at high frequencies, resonances appear contrary to the FF, where that limit does not exist. In this case, attenuation marks the limit since this increases with the frequency and, therefore, the sensitivity drops. This last conclusion opens up the way to design a novel FF material that attenuates less as the frequency increases. In that case, the frequency bandwidth would have no upper limit for the reception.

Based on the results of the study not yet published about interference ultrasound spectroscopy, we have demonstrated that the technique is a powerful tool to determine distances in a non-intrusive way for the one-layer case. It was possible to demonstrate that the precision of this method is approximately the same as using a micrometer. Further research is needed to test if the technique can distinguish different layers in a stack with impedance similar to human tissues and if the impedance difference between one layer and another is minimal. In this direction, the medical industry's technology could be highly interested in doing diagnostic imaging. Also, it is necessary to add the limits that we found of the technique and need research on it. On the one hand, high bandwidth is needed to measure the interference. On the other, for every new layer considered in the calculation, the number of possible solutions increases exponentially, so the inverse problem becomes computationally challenging to solve.

The significance of the results and conclusions for objective number four have been constrained due to the amount of work required to achieve the prior objectives.

From this thesis, two different research and industry lines are opened. First, improve the interference ultrasound spectroscopy technique to implement quantitative echography into ultrasound diagnostic imaging equipment. Second, integrate a preamplifier inside the FF hydrophone housing and provide a calibration cart according to the standards to commercialize this technology as a hydrophone.

## 5.2 Future work

The future work will answer some unknowns mentioned in the papers produced during this thesis.

On the one hand, it will be interesting to conduct a similar study of the mechanical properties along the thickness direction with the piezoelectric coefficient  $d_{33}$  to investigate the piezo activity distribution when the film operates in both mediums, air and water, and transmitting and receiving.

On the other hand, from the point of view of fabrication, different approaches will be worthwhile to be considered, in particular it is of interest to mention two of them:

- Adding another FF as an active layer at the end of the hydrophone orthogonal to their axes to complement the directivity. In this way, the directivity would increase to a half-sphere pattern instead of cylindrical.
- Fabrication of arrays. This idea comes from the facility to manipulate the FF and its high anisotropy, which allows minimal crosstalk. For this reason, is coherent to think that probably the cutting part of the fabrication process can be eliminated producing a kerfless array. This fact can also facilitate the mechanical focus in the case is needed.
- Transducer designed for pulse-echo can be made where the transmitting active layer would be different (For example, a piezoceramic) from the receiving active layer, which would be FF. Also it is possible to fabricate a stack of various FF or PVDF with FF and explore their piezoelectric response.
- Modify the process of the FF fabrication taking into account that the final use will be ultrasonic transducer water-coupled.

The interference ultrasound spectroscopy is the field where more future work can be done from a research point of view. Additional it has a large industrial and economic interest since a medical application can be developed based in this technology.

The following steps to evolve the idea that can end up with two different papers are:

- Test the quantitative echography technique for layered phantoms that mimic real tissues that do have in a natural way a layered structure.
- It is necessary to quantify the performance of this technique when the incident wave is not normal to the target tissue. It is necessary to observe the influence of the incident angle and explore the presence of shear waves (elastography).
- The FF transducers developed in this thesis meet the requirements to perform quantitative echography. So, it is necessary to compare the results that can be extracted with a commercial ultrasonic transducer against the FF transducer and modify the construction design to enhance their features for this purpose if needed.

## Chapter 6

# Conclusiones y Trabajo Futuro

### 6.1 Conclusiones

Durante la última década, trabajos anteriores han demostrado que el FF puede utilizarse como capa activa para transductores ultrasónicos acoplados al aire. En los últimos cinco años, se han realizado algunos ensayos para utilizar el mismo material en transductores ultrasónicos acoplados al agua, que es en lo que se centra esta tesis. Las principales conclusiones de esta tesis se refieren a las propiedades fundamentales del FF, en particular, al hecho inesperado de que las resonancias mecánicas del FF, cuando se sumerge, no cambian, y en cambio sus resonancias piezoelectricas desaparecen, lo cual es crítico para el diseño y la fabricación de este tipo de transductores ultrasónicos. También se reportan los procedimientos de fabricación de transductores ultrasónicos e hidrófonos que pueden jugar un papel importante en un mercado en el que el PVDF es el material más común.

Una parte esencial de este trabajo consiste en la extracción de las propiedades del FF mediante una técnica de espectroscopia ultrasónica resonante sin contacto. Los resultados de los FF de HS03 y HS06 se han reportado en dos direcciones (Objetivo 1).

Se han estudiado en detalle las propiedades mecánicas y electromecánicas, y su uso para fabricar diferentes transductores de FF, como los enfocados esféricamente, directividad cilíndrica o de apertura circular. Se concluye que se puede mejorar el rendimiento del transductor utilizando la información extraída anteriormente y que se puede prever las limitaciones de los FF a la hora de diseñar un sensor o transductor que utilice este material como capa activa.

El impacto de la microestructura y mesoestructura de los FF en su respuesta mecánica y electromecánica ha sido profundamente investigado gracias a esta técnica. Se han medido y calculado las resonancias de espesor en los espectros del coeficiente de transmisión. El ajuste de los valores calculados y los medidos es excelente, y permite extraer las propiedades del FF. Además, se sumerge el FF en dos medios distintos, aire y agua, para determinar cómo puede afectar las diferentes cargas a la respuesta del FF. La principal conclusión relacionada con este hecho es que el FF puede entenderse como un modelo de sandwich de tres capas. La primera y la tercera, también llamadas piel en los artículos publicados, comparten las mismas propiedades: mayor módulo de volumen y densidad y menor impedancia acústica que el núcleo además de menor espesor. Esta conclusión se valida de acuerdo con las imágenes SEM de la sección transversal del FF utilizado.

Las propiedades de la estructura celular, como la elongación de los huecos internos, se han descrito satisfactoriamente de forma matemática mediante una estructura simple de panal hexagonal, lo que permite una comprensión más profunda del mecanismo interno del FF y mejora sus propiedades para la construcción de transductores. Esta técnica también podría ser útil para caracterizar los FF

fabricados con otros polímeros celulares, tal y como se ha descrito en la introducción.

Gracias a las propiedades mecánicas estudiadas y a la fabricación de los transductores con diferentes aperturas geométricas, el FF es adecuado para ser utilizado como capa activa para la construcción de transductores en aquellas aplicaciones en las cuales la geometría de la apertura no es convencional. Además, en el caso del transductor cuya apertura está esféricamente enfocada, se ha reportado la misma respuesta en frecuencia que el transductor con apertura circular pero con mejor resolución espacial. Esta conclusión puede ampliarse al hecho de que hemos presentado un diseño de construcción muy detallado para los transductores hechos con HS03 y HS06 FF, que puede utilizarse para otros FF (mencionados en la introducción) sin modificaciones adicionales más allá de la sustitución del FF.

Una de las principales contribuciones de esta tesis es que se reporta que las resonancias electromecánicas de espesor desaparecen cuando el FF está funcionando inmerso en agua, y proporcionamos una explicación para ello, lo que nos lleva a la idea de producir hidrófonos con este material. Como resultado, cuando la lámina se sumerge, las caras en contacto con el agua experimentan una tensión máxima y un desplazamiento mínimo. Este hecho limita el rendimiento en el funcionamiento de pulso-eco en los transductores con esta capa activa, a pesar de que el factor piezoelectrónico  $d_{33}$  del HS03 es lo suficientemente bueno como para realizar una sensibilidad de -46 dB y un ancho de banda del 63,6 % con una caída de 6 dB en estas condiciones.

La inesperada desaparición de las resonancias electromecánicas señalada en las conclusiones anteriores nos lleva a la idea de utilizar este material como capa activa en hidrófonos para aprovechar la ausencia de resonancias que puedan limitar la respuesta en frecuencia superior del hidrófono. A partir de esta idea, en este trabajo se ha desarrollado todo el proceso de fabricación del hidrófono.

Asimismo, se ha considerado oportuno comparar la respuesta en frecuencia de la etapa de recepción de dos hidrófonos con el mismo diseño de construcción, uno con una capa activa de HS03 FF y otro con PVDF, para concluir que el PVDF reporta una mejor sensibilidad para todas las frecuencias, pero especialmente las superiores a 1 MHz. La sensibilidad del FF es bastante similar a la del PVDF a bajas frecuencias y ofrece un ancho de banda mayor y más plano para ambos casos, 3 dB de caída y 6 dB de caída.

El ancho de banda del hidrófono de PVDF está limitado porque, a altas frecuencias, aparecen resonancias al contrario que en el FF, donde ese límite no existe. En este caso, la atenuación marca el límite ya que ésta aumenta con la frecuencia y, por tanto, la sensibilidad disminuye. Esta última conclusión abre el camino para diseñar un nuevo FF que atenúa menos a medida que aumenta la frecuencia. En ese caso, el ancho de banda no tendría límite superior para la recepción.

Basándonos en los resultados del estudio aún no publicado sobre la espectroscopía de ultrasonidos de interferencia, hemos demostrado que la técnica es una potente herramienta para determinar distancias de forma no intrusiva para el caso de una capa. Se ha podido demostrar que la precisión de este método es aproximadamente la misma que la de utilizar un micrómetro. Es necesario seguir investigando para comprobar si la técnica puede distinguir las distintas capas en un apilamiento con una impedancia similar a la de los tejidos humanos y además si la diferencia de impedancia entre una capa y otra es mínima. En esta dirección, industria médica podría tener un gran interés en esta tecnología para realizar

diagnóstico por imagen. Además, es necesario añadir los límites que encontramos a la técnica y que necesitan ser investigados. Por un lado, se necesita un gran ancho de banda para medir las interferencias. Por otro, por cada nueva capa considerada en el cálculo, el número de posibles soluciones aumenta exponencialmente, por lo que el problema inverso se convierte en un reto computacional a resolver.

La importancia de los resultados y las conclusiones para el objetivo número cuatro se han visto limitadas debido a la cantidad de trabajo necesario para alcanzar los objetivos anteriores.

A partir de esta tesis, se abren dos líneas diferentes, una referida a la investigación y otra a la industria. Primero, mejorar la técnica de espectroscopía de ultrasonidos de interferencia para implementar ecografía cuantitativa en los equipos de diagnóstico por imagen de ultrasonidos. En segundo lugar, integrar un preamplificador dentro de la carcasa del hidrófono FF y proporcionar una carta de calibración según los estándares para comercializar esta tecnología como hidrófono.

## 6.2 Trabajo Futuro

El trabajo futuro responde a algunas incógnitas mencionadas en los trabajos realizados durante esta tesis.

Por un lado, es interesante realizar un estudio similar al de las propiedades mecánicas a lo largo de la dirección del espesor de la lámina de ferroelctreto con el coeficiente piezoeléctrico  $d_{33}$  para investigar la distribución de la actividad piezoeléctrica cuando la película opera en ambos medios, aire y agua, y también en transmisión y recepción.

Por otro lado, desde el punto de vista de la fabricación, merece la pena considerar diferentes enfoques, en particular es interesante mencionar dos de ellos:

- Añadir otra LF como capa activa en el fondo del hidrófono, ortogonal a sus eje principal, para complementar la directividad. De este modo, la directividad aumentaría hasta un patrón de media esfera en lugar de cilíndrico.
- Fabricación de arrays. Esta idea proviene de la facilidad para manipular la LF junto a su alta anisotropía, que permite un crosstalk mínimo. Por esta razón, es coherente pensar que probablemente la parte de corte del proceso de fabricación pueda ser eliminada produciendo un array kerfless. Este hecho también puede facilitar el enfoque mecánico en el caso de que fuera necesario.
- Se puede fabricar un transductor diseñado para pulso-eco en el que la capa activa transmisora sería diferente (por ejemplo, una piezocerámica) de la capa activa receptora, que sería la LF. También es posible fabricar un apilamiento de varias LF o PVDF con LF y explorar su respuesta piezoeléctrica.
- Modificar el proceso de fabricación de FF teniendo en cuenta que el uso final será fabricar un transductor ultrasónico acoplado al agua.

La espectroscopía ultrasónica de interferencia es el campo en el que más trabajo futuro se pueden realizar desde el punto de vista de la investigación. Además tiene un gran interés industrial y económico ya que se puede desarrollar una aplicación médica basada en esta tecnología.

Los siguientes pasos para evolucionar la idea que puede terminar con dos artículos diferentes son:

- Probar la técnica de ecografía cuantitativa para phantoms estratificados que imitan los tejidos reales que sí tienen de forma natural una estructura en capas.
- Es necesario cuantificar el rendimiento de esta técnica cuando la onda incidente no es normal al tejido objetivo. Es necesario observar la influencia del ángulo de incidencia y explorar la presencia de ondas de cizalla (elastografía).
- Los transductores basados en las LF desarrollados en esta tesis cumplen con los requisitos para realizar ecografía cuantitativa. Por ello, es necesario comparar los resultados que se pueden extraer con un transductor ultrasónico comercial frente al transductor de LF y modificar el diseño de construcción para mejorar sus características para este fin si fuera necesario.

# Bibliography

- [1] Maria Dolores Fariñas et al. "Monitoring Plant Response to Environmental Stimuli by Ultrasonic Sensing of the Leaves". In: *Ultrasound in Medicine and Biology* 40 (9 2014). ISSN: 1879291X. DOI: [10.1016/j.ultrasmedbio.2014.04.004](https://doi.org/10.1016/j.ultrasmedbio.2014.04.004).
- [2] Domingo Sancho-Knapik et al. "Ultrasonic spectroscopy allows a rapid determination of the relative water content at the turgor loss point: A comparison with pressure-volume curves in 13 woody species". In: *Tree Physiology* 33 (7 2013). ISSN: 0829318X. DOI: [10.1093/treephys/tpt052](https://doi.org/10.1093/treephys/tpt052).
- [3] T. E.G. Álvarez Arenas et al. "Non-contact ultrasonic resonant spectroscopy resolves the elastic properties of layered plant tissues". In: *Applied Physics Letters* 113 (25 2018). ISSN: 00036951. DOI: [10.1063/1.5064517](https://doi.org/10.1063/1.5064517).
- [4] Jacques Curie and Pierre Curie. "Développement par compression de l'électricité polaire dans les cristaux hémièdres à faces inclinées". In: *Bulletin de la Société minéralogique de France* 3 (4 1880). ISSN: 0150-9640. DOI: [10.3406/bulmi.1880.1564](https://doi.org/10.3406/bulmi.1880.1564).
- [5] Reiner Kressmann. "New piezoelectric polymer for air-borne and water-borne sound transducers". In: *The Journal of the Acoustical Society of America* (2001). ISSN: 0001-4966. DOI: [10.1121/1.1354989](https://doi.org/10.1121/1.1354989).
- [6] M. Wegener et al. "Ferroelectrets: Highly anisotropic electrically charged polymer foams for electromechanical transducer applications". In: 2004. ISBN: 0780384121. DOI: [10.1109/ULTSYM.2004.1417981](https://doi.org/10.1109/ULTSYM.2004.1417981).
- [7] Joachim Döring et al. "EMFIT Ferroelectret Film Transducers for Non-Contact Ultrasonic Testing". In: *Materials Research* (2006), pp. 1–10.
- [8] X. Zhang, J. Hillenbrand, and G. M. Sessler. "Thermally stable fluorocarbon ferroelectrets with high piezoelectric coefficient". In: *Applied Physics A: Materials Science and Processing* (2006). ISSN: 09478396. DOI: [10.1007/s00339-006-3573-5](https://doi.org/10.1007/s00339-006-3573-5).
- [9] Xunlin Qiu et al. "Barrier discharges in cellular polypropylene ferroelectrets: How do they influence the electromechanical properties?". In: *Journal of Applied Physics* (2007). ISSN: 00218979. DOI: [10.1063/1.2735410](https://doi.org/10.1063/1.2735410).
- [10] P. K. Panda and B. Sahoo. "PZT to lead free piezo ceramics: A review". In: *Ferroelectrics* 474 (1 2015). ISSN: 15635112. DOI: [10.1080/00150193.2015.997146](https://doi.org/10.1080/00150193.2015.997146).
- [11] Heiji Kawai. "The Piezoelectricity of Poly (vinylidene Fluoride)". In: *Japanese Journal of Applied Physics* 8 (7 1969). ISSN: 0021-4922. DOI: [10.1143/jjap.8.975](https://doi.org/10.1143/jjap.8.975).
- [12] K. C. Shotton, D. R. Bacon, and R. M. Quilliam. "A pvdf membrane hydrophone for operation in the range 0.5 MHz to 15 MHz". In: *Ultrasonics* 18 (3 1980). ISSN: 0041624X. DOI: [10.1016/0041-624X\(80\)90025-6](https://doi.org/10.1016/0041-624X(80)90025-6).

- [13] M. Platte. "A polyvinylidene fluoride needle hydrophone for ultrasonic applications". In: *Ultrasonics* 23 (3 1985). ISSN: 0041624X. DOI: [10.1016/0041-624X\(85\)90059-9](https://doi.org/10.1016/0041-624X(85)90059-9).
- [14] H. L.W. Chan et al. "Piezoelectric copolymer hydrophones for ultrasonic field characterization". In: *Review of Scientific Instruments* 62 (1 1991). ISSN: 00346748. DOI: [10.1063/1.1142306](https://doi.org/10.1063/1.1142306).
- [15] A. Safari. "Development of piezoelectric composites for transducers". In: *Journal de physique. III* 4 (7 1994). ISSN: 11554320. DOI: [10.1051/jp3:1994191](https://doi.org/10.1051/jp3:1994191).
- [16] A. Savolainen and K. Kirjavainen. "Electrothermomechanical film.: Part I. Design and characteristics". In: *Journal of Macromolecular Science: Part A - Chemistry* (1989). ISSN: 0022233X. DOI: [10.1080/00222338908051994](https://doi.org/10.1080/00222338908051994).
- [17] G. M. Sessler and J. Hillenbrand. "Electromechanical response of cellular electret films". In: *Applied Physics Letters* (1999). ISSN: 00036951. DOI: [10.1063/1.125308](https://doi.org/10.1063/1.125308).
- [18] Yan Zhang et al. "Ferroelectret materials and devices for energy harvesting applications". In: *Nano Energy* 57 (2019). ISSN: 22112855. DOI: [10.1016/j.nanoen.2018.12.040](https://doi.org/10.1016/j.nanoen.2018.12.040).
- [19] Seung Eek Park. "Relaxor based ferroelectric single crystals for electro-mechanical actuators". In: *Materials Research Innovations* 1 (1 1997). ISSN: 14328917. DOI: [10.1007/s100190050014](https://doi.org/10.1007/s100190050014).
- [20] Seung Eek Park and Thomas R. Shrout. "Characteristics of relaxor-based piezoelectric single crystals for ultrasonic transducers". In: *IEEE Transactions on Ultrasonics, Ferroelectrics, and Frequency Control* 44 (5 1997). ISSN: 08853010. DOI: [10.1109/58.655639](https://doi.org/10.1109/58.655639).
- [21] N. Behrendt et al. "Morphology and electret behaviour of microcellular high glass temperature films". In: *Applied Physics A: Materials Science and Processing* 85 (1 2006). ISSN: 09478396. DOI: [10.1007/s00339-006-3660-7](https://doi.org/10.1007/s00339-006-3660-7).
- [22] M. Wegener et al. "Controlled inflation of voids in cellular polymer ferroelectrets: Optimizing electromechanical transducer properties". In: *Applied Physics Letters* (2004). ISSN: 00036951. DOI: [10.1063/1.1641171](https://doi.org/10.1063/1.1641171).
- [23] Martynas Sborikas and Michael Wegener. "Cellular-foam polypropylene ferroelectrets with increased film thickness and reduced resonance frequency". In: *Applied Physics Letters* (2013). ISSN: 00036951. DOI: [10.1063/1.4850523](https://doi.org/10.1063/1.4850523).
- [24] M. Wegener et al. "Two-step inflation of cellular polypropylene films: Void-thickness increase and enhanced electromechanical properties". In: *Journal of Physics D: Applied Physics* (2004). ISSN: 00223727. DOI: [10.1088/0022-3727/37/4/013](https://doi.org/10.1088/0022-3727/37/4/013).
- [25] M. Wegener. "Piezoelectric polymer foams: transducer mechanism and preparation as well as touch-sensor and ultrasonic-transducer properties". In: vol. 7644. 2010. DOI: [10.1117/12.847245](https://doi.org/10.1117/12.847245).
- [26] Joachim Hillenbrand, Gerhard M. Sessler, and Xiaoqing Zhang. "Verification of a model for the piezoelectric d 33 coefficient of cellular electret films". In: *Journal of Applied Physics* 98 (6 2005). ISSN: 00218979. DOI: [10.1063/1.2058185](https://doi.org/10.1063/1.2058185).
- [27] X. Zhang, J. Hillenbrand, and G. M. Sessler. "Piezoelectric d33 coefficient of cellular polypropylene subjected to expansion by pressure treatment". In: *Applied Physics Letters* 85 (7 2004). ISSN: 00036951. DOI: [10.1063/1.1781388](https://doi.org/10.1063/1.1781388).

- [28] X. Zhang, J. Hillenbrand, and G. M. Sessler. "Improvement of piezoelectric activity of cellular polymers using a double-expansion process". In: *Journal of Physics D: Applied Physics* 37 (15 2004). ISSN: 00223727. DOI: [10.1088/0022-3727/37/15/015](https://doi.org/10.1088/0022-3727/37/15/015).
- [29] Xunlin Qiu et al. "Penetration of sulfur hexafluoride into cellular polypropylene films and its effect on the electric charging and electromechanical response of ferroelectrets". In: *Journal of Physics D: Applied Physics* 38 (4 2005). ISSN: 00223727. DOI: [10.1088/0022-3727/38/4/020](https://doi.org/10.1088/0022-3727/38/4/020).
- [30] Xunlin Qiu, Zhongfu Xia, and Feipeng Wang. "Piezoelectricity of single-and multi-layer cellular polypropylene film electrets". In: *Frontiers of Materials Science in China* 1 (1 2007). ISSN: 16737377. DOI: [10.1007/s11706-007-0013-1](https://doi.org/10.1007/s11706-007-0013-1).
- [31] S. R. Anton, K. M. Farinholt, and A. Erturk. "Piezoelectret foam-based vibration energy harvesting". In: *Journal of Intelligent Material Systems and Structures* (2014). ISSN: 15308138. DOI: [10.1177/1045389X14541501](https://doi.org/10.1177/1045389X14541501).
- [32] Michael Wegener et al. "Piezoelectric two-layer stacks of cellular polypropylene ferroelectrets: Transducer response at audio and ultrasound frequencies". In: *IEEE Transactions on Ultrasonics, Ferroelectrics, and Frequency Control* 52 (9 2005). ISSN: 08853010. DOI: [10.1109/TUFFC.2005.1516033](https://doi.org/10.1109/TUFFC.2005.1516033).
- [33] Werner Wirges et al. "Optimized preparation of elastically soft, highly piezoelectric, cellular ferroelectrets from nonvoided poly(ethylene terephthalate) films". In: *Advanced Functional Materials* 17 (2 2007). ISSN: 1616301X. DOI: [10.1002/adfm.200600162](https://doi.org/10.1002/adfm.200600162).
- [34] Xiaoqing Zhang et al. "Quasi-static and dynamic piezoelectric responses of layered polytetrafluoroethylene ferroelectrets". In: *Journal of Physics D: Applied Physics* 47 (1 2014). ISSN: 00223727. DOI: [10.1088/0022-3727/47/1/015501](https://doi.org/10.1088/0022-3727/47/1/015501).
- [35] P. Fang et al. "Cellular polyethylene-naphthalate ferroelectrets: Foaming in supercritical carbon dioxide, structural and electrical preparation, and resulting piezoelectricity". In: *Applied Physics Letters* 90 (19 2007). ISSN: 00036951. DOI: [10.1063/1.2738365](https://doi.org/10.1063/1.2738365).
- [36] Xiaoqing Zhang et al. "Low-cost, large-area, stretchable piezoelectric films based on irradiation-crosslinked poly(propylene)". In: *Macromolecular Materials and Engineering* 299 (3 2014). ISSN: 14387492. DOI: [10.1002/mame.201300161](https://doi.org/10.1002/mame.201300161).
- [37] X. Zhang et al. "Piezoelectric coefficients of cross-linked polypropylene films stretched at elevated temperatures". In: *Journal of Electrostatics* 69 (6 2011). ISSN: 03043886. DOI: [10.1016/j.elstat.2011.07.008](https://doi.org/10.1016/j.elstat.2011.07.008).
- [38] Xiaoqing Zhang et al. "Quasi-static and dynamic piezoelectric d 33 coefficients of irradiation cross-linked polypropylene ferroelectrets". In: *Journal of Materials Science* 44 (10 2009). ISSN: 00222461. DOI: [10.1007/s10853-009-3312-3](https://doi.org/10.1007/s10853-009-3312-3).
- [39] Xiaoqing Zhang et al. "Piezoelectric properties of irradiation-crosslinked polypropylene ferroelectrets". In: *Applied Physics Letters* 91 (18 2007). ISSN: 00036951. DOI: [10.1063/1.2803316](https://doi.org/10.1063/1.2803316).
- [40] Michael Wegener et al. *Voided Space-Charge Electrets ? Piezoelectric Transducer Materials for Electro-Acoustic Applications*. May 2004.

- [41] Y. Naruse et al. "Electrostatic micro power generation from low-frequency vibration such as human motion". In: *Journal of Micromechanics and Microengineering* 19 (9 2009). ISSN: 09601317. DOI: [10.1088/0960-1317/19/9/094002](https://doi.org/10.1088/0960-1317/19/9/094002).
- [42] Feng Qian, Tian Bing Xu, and Lei Zuo. "Piezoelectric energy harvesting from human walking using a two-stage amplification mechanism". In: *Energy* 189 (2019). ISSN: 03605442. DOI: [10.1016/j.energy.2019.116140](https://doi.org/10.1016/j.energy.2019.116140).
- [43] Rahul Shukla and Andrew J. Bell. "PENDEXE: A novel energy harvesting concept for low frequency human waistline". In: *Sensors and Actuators, A: Physical* 222 (2015). ISSN: 09244247. DOI: [10.1016/j.sna.2014.11.016](https://doi.org/10.1016/j.sna.2014.11.016).
- [44] Tom J. Kázmierski and Steve Beeby. *Energy harvesting systems: Principles, modeling and applications*. 2011. DOI: [10.1007/978-1-4419-7566-9](https://doi.org/10.1007/978-1-4419-7566-9).
- [45] Nan Wu et al. "Cellular Polypropylene Piezoelectret for Human Body Energy Harvesting and Health Monitoring". In: *Advanced Functional Materials* 25 (30 2015). ISSN: 16163028. DOI: [10.1002/adfm.201501695](https://doi.org/10.1002/adfm.201501695).
- [46] T. Starner. "Human-powered wearable computing". In: *IBM Systems Journal* 35 (3-4 1996). ISSN: 00188670. DOI: [10.1147/sj.353.0618](https://doi.org/10.1147/sj.353.0618).
- [47] Sheng Yong, Junjie Shi, and Stephen Beeby. "Wearable Textile Power Module Based on Flexible Ferroelectret and Supercapacitor". In: *Energy Technology* 7 (5 2019). ISSN: 21944296. DOI: [10.1002/ente.201800938](https://doi.org/10.1002/ente.201800938).
- [48] Junjie Shi et al. "Optimization a structure of MEMS based PDMS ferroelectret for human body energy harvesting and sensing". In: *Smart Materials and Structures* 28 (7 2019). ISSN: 1361665X. DOI: [10.1088/1361-665X/ab1ce2](https://doi.org/10.1088/1361-665X/ab1ce2).
- [49] Mate Gaal et al. "Focusing of ferroelectret air-coupled ultrasound transducers". In: 2016. ISBN: 9780735413535. DOI: [10.1063/1.4940533](https://doi.org/10.1063/1.4940533).
- [50] Joao L. Ealo, Fernando Seco, and Antonio R. Jimenez. "Broadband EMFi-based transducers for ultrasonic air applications". In: *IEEE Transactions on Ultrasonics, Ferroelectrics, and Frequency Control* (2008). ISSN: 08853010. DOI: [10.1109/TUFFC.2008.727](https://doi.org/10.1109/TUFFC.2008.727).
- [51] Konrad J. Vössing, Mate Gaal, and Ernst Niederleithinger. "Air-coupled ferroelectret ultrasonic transducers for nondestructive testing of wood-based materials". In: *Wood Science and Technology* 52 (6 2018). ISSN: 00437719. DOI: [10.1007/s00226-018-1052-8](https://doi.org/10.1007/s00226-018-1052-8).
- [52] S. Noh et al. "Ferroelectret film-based patch-type sensor for continuous blood pressure monitoring". In: *Electronics Letters* 50 (3 2014). ISSN: 00135194. DOI: [10.1049/el.2013.3715](https://doi.org/10.1049/el.2013.3715).
- [53] Chittaranjan Sinha et al. "Three-dimensional MOF-assisted self-polarized ferroelectret: An effective autopowered remote healthcare monitoring approach". In: *Langmuir* 36 (39 2020). ISSN: 15205827. DOI: [10.1021/acs.langmuir.0c01749](https://doi.org/10.1021/acs.langmuir.0c01749).
- [54] Y. Cao et al. "Understanding the dynamic response in ferroelectret nanogenerators to enable self-powered tactile systems and human-controlled micro-robots". In: *Nano Energy* 63 (2019). ISSN: 22112855. DOI: [10.1016/j.nanoen.2019.06.048](https://doi.org/10.1016/j.nanoen.2019.06.048).
- [55] Nan Wu et al. "Theoretical study and structural optimization of a flexible piezoelectret-based pressure sensor". In: *Journal of Materials Chemistry A* 6 (12 2018). ISSN: 20507496. DOI: [10.1039/c8ta00688a](https://doi.org/10.1039/c8ta00688a).

- [56] CONTACT-FREE SLEEP ANALYZER - *Emfit Ltd (Finland)*. URL: <https://emfit.com/>.
- [57] Shuwen Chen et al. "Noncontact Heartbeat and Respiration Monitoring Based on a Hollow Microstructured Self-Powered Pressure Sensor". In: *ACS Applied Materials and Interfaces* 10 (4 2018). ISSN: 19448252. DOI: [10.1021/acsami.7b17723](https://doi.org/10.1021/acsami.7b17723).
- [58] Qize Zhong et al. "Paper-Based Active Tactile Sensor Array". In: *Advanced Materials* 27 (44 2015). ISSN: 15214095. DOI: [10.1002/adma.201502470](https://doi.org/10.1002/adma.201502470).
- [59] Yao Chu et al. "Human Pulse Diagnosis for Medical Assessments Using a Wearable Piezoelectret Sensing System". In: *Advanced Functional Materials* 28 (40 2018). ISSN: 16163028. DOI: [10.1002/adfm.201803413](https://doi.org/10.1002/adfm.201803413).
- [60] Pedro Gonzalez-Losada et al. "Flexible ferroelectret for zero power wearable application". In: (June 2022), pp. 1–4. DOI: [10.1109/FLEPS53764.2022.9781488](https://doi.org/10.1109/FLEPS53764.2022.9781488).
- [61] Bo Wang et al. "Ultrasensitive cellular fluorocarbon piezoelectret pressure sensor for self-powered human physiological monitoring". In: *Nano Energy* 32 (2017). ISSN: 22112855. DOI: [10.1016/j.nanoen.2016.12.025](https://doi.org/10.1016/j.nanoen.2016.12.025).
- [62] Xiwei Mo et al. *Piezoelectrets for wearable energy harvesters and sensors*. 2019. DOI: [10.1016/j.nanoen.2019.104033](https://doi.org/10.1016/j.nanoen.2019.104033).
- [63] Abolfazl Mohebbi et al. *Current issues and challenges in polypropylene foaming: A review*. 2015. DOI: [10.1177/026248931503400602](https://doi.org/10.1177/026248931503400602).
- [64] Xia Zhong-fu et al. "Constant-current Corona Charging of Teflon PFA". In: *IEEE Transactions on Electrical Insulation* 26 (1 1991). ISSN: 00189367. DOI: [10.1109/14.68224](https://doi.org/10.1109/14.68224).
- [65] H. Von Seggern and J. E. West. "Stabilization of positive charge in fluorinated ethylene propylene copolymer". In: *Journal of Applied Physics* 55 (7 1984). ISSN: 00218979. DOI: [10.1063/1.333281](https://doi.org/10.1063/1.333281).
- [66] Peng Fang. *Preparation and investigation of polymer-foam films and polymer-layer systems for ferroelectrets*. URL: [https://www.researchgate.net/publication/291380898\\_Preparation\\_and\\_investigation\\_of\\_polymer-foam\\_films\\_and\\_polymer-layer\\_systems\\_for\\_ferroelectrets](https://www.researchgate.net/publication/291380898_Preparation_and_investigation_of_polymer-foam_films_and_polymer-layer_systems_for_ferroelectrets).
- [67] Wei Li et al. "Nanogenerator-based dual-functional and self-powered thin patch loudspeaker or microphone for flexible electronics". In: *Nature Communications* (2017). ISSN: 20411723. DOI: [10.1038/ncomms15310](https://doi.org/10.1038/ncomms15310).
- [68] Michael Wegener, Werner Wirges, and Reimund Gerhard-Multhaupt. "Piezoelectric polyethylene terephthalate (PETP) foams - Specifically designed and prepared ferroelectret films". In: *Advanced Engineering Materials* (2005). ISSN: 14381656. DOI: [10.1002/adem.200500177](https://doi.org/10.1002/adem.200500177).
- [69] Enis Tuncer. "Numerical calculations of effective elastic properties of two cellular structures". In: *Journal of Physics D: Applied Physics* (2005). ISSN: 00223727. DOI: [10.1088/0022-3727/38/3/023](https://doi.org/10.1088/0022-3727/38/3/023).
- [70] G. M. Sessler and J. Hillenbrand. "Electromechanical response of cellular electret films". In: *Applied Physics Letters* 75 (21 Nov. 1999), pp. 3405–3407. ISSN: 00036951. DOI: [10.1063/1.125308](https://doi.org/10.1063/1.125308).
- [71] Gerhard S. Neugschwandtner et al. "Piezo- and pyroelectricity of a polymer-foam space-charge electret". In: *Journal of Applied Physics* 89 (8 2001). ISSN: 00218979. DOI: [10.1063/1.1355719](https://doi.org/10.1063/1.1355719).

- [72] Shaoxing Qu and Yalin Yu. "Electromechanical coupling properties and stability analysis of ferroelectrets". In: *Journal of Applied Physics* 110 (4 2011). ISSN: 00218979. DOI: [10.1063/1.3626467](https://doi.org/10.1063/1.3626467).
- [73] John Lekner. "Matrix methods in reflection and transmission of compressional waves by stratified media". In: *Journal of the Acoustical Society of America* (1990). ISSN: NA. DOI: [10.1121/1.399077](https://doi.org/10.1121/1.399077).
- [74] A. H. Fahmy and E. L. Adler. "Propagation of acoustic surface waves in multilayers: A matrix description". In: *Applied Physics Letters* (1973). ISSN: 00036951. DOI: [10.1063/1.1654482](https://doi.org/10.1063/1.1654482).
- [75] Michael J. Lowe. "Matrix Techniques for Modeling Ultrasonic Waves in Multilayered Media". In: *IEEE Transactions on Ultrasonics, Ferroelectrics, and Frequency Control* (1995). ISSN: 08853010. DOI: [10.1109/58.393096](https://doi.org/10.1109/58.393096).
- [76] L Knopoff. "A Matrix Method for Elastic Wave Problems". In: *Bulletin of the Seismological Society of America* (1964). ISSN: 1943-3573.
- [77] V. Fabian. "Simulated annealing simulated". In: *Computers and Mathematics with Applications* 33 (1-2 1997). ISSN: 08981221. DOI: [10.1016/s0898-1221\(96\)00221-0](https://doi.org/10.1016/s0898-1221(96)00221-0).
- [78] Dimitris Bertsimas and John Tsitsiklis. "Simulated annealing". In: *Statistical Science* 8 (1 1993). ISSN: 08834237. DOI: [10.1214/ss/1177011077](https://doi.org/10.1214/ss/1177011077).
- [79] S. Kirkpatrick, C. D. Gelatt, and M. P. Vecchi. "Optimization by simulated annealing". In: *Science* 220 (4598 1983). ISSN: 00368075. DOI: [10.1126/science.220.4598.671](https://doi.org/10.1126/science.220.4598.671).
- [80] J. Dreo et al. *Metaheuristics for Hard Optimization*. 2006. DOI: [10.1007/3-540-30966-7](https://doi.org/10.1007/3-540-30966-7).
- [81] Bruce Hajek and Galen Sasaki. "Simulated annealing - to cool or not". In: *Systems and Control Letters* 12 (5 1989). ISSN: 01676911. DOI: [10.1016/0167-6911\(89\)90081-9](https://doi.org/10.1016/0167-6911(89)90081-9).
- [82] Sergio Ledesma, Jose Ruiz, and Guadalupe Garcí. *Simulated Annealing Evolution*. 2012. DOI: [10.5772/50176](https://doi.org/10.5772/50176).